Grain Boundary Engineering of Electrodeposited Thin Films

Alimadadi, Hossein

Publication date:
2013

Document Version
Publisher's PDF, also known as Version of record

Citation (APA):
Alimadadi, H. (2013). *Grain Boundary Engineering of Electrodeposited Thin Films*. Technical University of Denmark.

Grain Boundary Engineering of Electrodeposited Thin Films

by

Hossein Alimadadi

A thesis submitted in fulfillment of the requirements

for the degree of Doctor of Philosophy

Technical University of Denmark, 2012

Department of Mechanical Engineering

Technical University of Denmark

Denmark

Preface

This thesis is submitted as partial fulfillment of the requirement for the PhD degree at Technical University of Denmark (DTU). The work has been carried out at the Department of Mechanical Engineering, from August 2008 until February 2012 under the supervision of Associate Professor Karen Pantleon, Professor Marcel A.J. Somers and co-supervision of Dr. Alice Bastos da Silva Fanta. The project was funded by the Danish Research Council for Technology and Production Sciences (grant No. 274-07-0492). This work has been carried out in close collaboration with Center of Electron Nanoscopy (CEN) at Technical University of Denmark (DTU).

Hossein Alimadadi
February 2012

Acknowledgments

I would like to express my deepest gratitude to my PhD thesis supervisor Associate Professor Karen Pantleon for her guidance on the research presented in this thesis. I cannot thank her more for her constant support and valuable help during my PhD studies, especially the days that I was in great need. I have learned a lot from her and have appreciated each of many discussions that we had. *Thank you for your patience during these years. You have been a source of inspiration for me throughout this project due to your passion and dedication towards research.*

I am grateful to Professor Marcel Sommers for providing me an opportunity to do my PhD project in Materials and Surface Engineering section. His leadership has been very productive for making a multidisciplinary group which has helped me to broaden my research vision. Your involvement has been very helpful in this project. *Thanks for your understanding and providing peace and comfort as I followed a twisting path.*

My gratitude to Dr. Alice Bastos da Silva Fanta for her huge enthusiasm she has shown for different aspects of this work, from the very beginning to the very end. Note only I have learned a lot about EBSD and FIB from her but also her deep involvement in the project provided me with valuable input. *Thanks for your support, guidance and most important of all, your friendship.*

I am thankful of Professor Anthony D. Rollett and Professor Gregory S. Rohrer whom provided me the codes they have developed over years for 5 parameter grain boundary plane analysis; especial thank to Anthony D. Rollett for welcoming me in his group and supporting me afterwards.

I am thankful of Professor Stefan Zaefferer for introducing me to me ECCI and high resolution EBSD.

Dr. Philip Littlewood has helped me with the analysis of ion channeling images and reconstruction of the 3-dimensional data. I am thankful of him.

A thank you to Dr. Peter Torben Tang, Mikkel Ostergaard Hansen, and Cristian Ravn at IPU, who offered their experience when ever they I had a question. John C. Troelsen and Lars Pedersen are thanked for their help on many practical challenges.

I have learned a lot from Steffe S. Munch on metallography and sample preparation. I am thankful of him.

Flemming Bjerg Grumsen is thanked for his help with XRD measurements.

I have shared office with Thomas Strabo Hummelshj, Matteo Villa, Uffe Bihlet, Ole West, Saeed Baghsheikhi, and Freja Nygaard Jespersen; they have created an environment suitable for studies and breaks. They deserve a thank you.
Grethe Saugmann and Laila Leth were helpful with various practical issues; I am thankful.
I am so grateful to Trine Colding Lomholt for her friendship. She has introduced me to Danish culture and society and most importantly she was a friend in need.

I also want to express my kind gratitude to my family, especially my parents Hassan Alimadadi and Fatemeh-sadat Mirghavameddin, my brothers Meisam and Mehrzad for their support and love.
This work would have never finished if Negar Sadegh, my beloved wife, was not beside me. I do not know how to express my gratitude in words for her love and kindness. From bottom of heart, *Thank You.*

Hossein Alimadadi
February 2012

Abstract

Grain boundary engineering aims for a deliberate manipulation of the grain boundary characteristics to improve the properties of polycrystalline materials. Despite the emergence of some successful industrial applications, the mechanism(s) by which the boundary specific properties can be improved is not yet well-understood. This, at least partly, owes to the lack of robust characterization methods for analyzing the nature of grain boundaries including the grain boundary plane characteristics, until recently. In the past decade, significant improvements in the 2-dimensional and 3-dimensional analysis of the grain boundaries have happened. These improvements, for example by high-resolution imaging techniques and orientation imaging microscopy for additional crystallographic information, provide the possibilities for thorough characterization of the grain boundaries and based on that, it is possible to engineer new materials.

In this study, one of the most widely used electrolytes for electrodeposition is chosen for the synthesis of nickel films and based on thorough characterization of the boundaries the potentials in grain boundary engineering are outlined. The internal structure of the nickel films both in the as-deposited state and after thermal annealing is investigated and experimental methods for grain boundary characterization are accordingly applied to essentially different microstructures. Supplementary characterizations with X-ray diffraction, orientation imaging microscopy, and focused ion beam microscopy were applied.

Using additive free Watts electrolyte, coarse columnar microstructures with <211>, <100>, and <210> texture and fairly high fraction of twin boundaries are synthesized. In <210> textured nickel film, multiple twinning occurs which brings about an arrangement of the favorable boundaries that break the network of general grain boundaries. Successful dedicated synthesis of a <210> textured nickel film fulfilling the requirements of grain boundary engineered materials, suggests improved boundary specific properties. However, the <210> textured nickel film shows fairly low thermal stability and growth twins annihilate by thermal treatment at $600°C$. In contrast, for <211> oriented grains, growth nano-twins which are enveloped within columnar grains show a high thermal stability even after thermal treatment at $600°C$. In order to exploit the high thermal stability of nano-twins, the effect of different electrodeposition conditions and alloying cobalt on the strength of <211> texture and twin formation are studied.

Using the Watts electrolyte with a common sulfur-free additive, nano-crystalline nickel films with different characteristics in as-deposited state are synthesized as a function of the deposition conditions. The microstructure of thermally treated nano-crystalline nickel films, show low fraction of favorable boundaries. The grain size and texture development due to thermal treatment is studied too and it is argued that prior to the major grain growth strain energy minimization plays the major role in the microstructure evolution while after major grain growth interface energy minimization has the major role. Differences in as-deposited microstructural characteristics, brings about differences in grain size and grain boundary characteristics after thermal treatment. It is suggested that triple lines, at least partly, contribute to the observed differences and potentials for “Grain Boundary Junction Engineering” are outlined.

Keywords: Grain Boundary Engineering, Electrodeposition, Nickel, Grain Boundary, Nano-Twin, Nano-Crystalline, Thermal Stability.

Dansk resumé

"Grain boundary engineering" har til formål at manipulere korngrænsernes karakteristika bevidst for at forbedre egenskaber af polykrystalinske materialer. På trods af fremkomsten af nogle succesfulde industrielle applikationer, er mekanismerne for at forbedre materialernes egenskaber der afhænger af korngrænserne endnu ikke velkendte. Dette skyldes, i hvert fald delvist, indtil for nylig mangel på karateriseringsmetoder til at analysere arten af korngrænserne, herunder korngrænsefladernes karakteristika. I det sidste årti er der sket signifikante forbedringer af 2-dimensionel og 3-dimensionel analyse af korngrænser. Disse forbedringer, for eksempel høj-opløsnings teknikker til både at afbilde materialernes indre struktur og at analysere krystallografiske orienteringer, giver mulighed for grundig karakterisering af korngrænserne og dermed gør det muligt at fremstille materialer med skræddersyede egenskaber.

I dette projekt er en af de mest brugte elektrolytter til elektrokemisk deponering valgt til syntese af nikkelfilm, og baseret på grundig karakterisering af korngrænserne er potentialerne af "grain boundary engineerin" opridset. Den indre struktur af nikkelfilmene undersøges, både i den oprindelige tilstand lige efter deponering og efter varmebehandling, og eksperimentelle metoder til korngrænse karakterisering anvendes således på to i bund og grund forskellige mikrostrukturer. Supplerende karakterisering er også lavet med røntgen diffraktion, electron backscatter diffraction og "focused ion beam" mikroskopi.

Grove søjleformede mikrostrukturer med forskellige krystallografiske fortrinsorienteringer, som <211>, <100>, og <210>, og en ret høj andel af særlige korngrænser (tvillingsgrænser) blev syntetiseret ved at bruge Watts elektrolyt uden tilsætningsstoffer. I nikkelfilm med <210> kornorientering opstod "multiple twinning" der giver en favorabel placering af korngrænser som bryder netværket af almindelige korngrænser. Succesfuld dedikeret syntese af en nikkelfilm med <210> tekstur, der opfylder betingelserne for "grain boundary engineered" materialer indikerer forbedrede egenskaber der afhænger af korngrænserne. Nikkelfilmene med <210> tekstur har dog en relativ dårlig termisk stabilitet, og særlige korngrænser som resulterer fra tvillingsrelationer mellem kornene forsvinder ved varmebehandling ved $600°C$.

I modsætning til dette viser "growth twins", som dannes under film vækst med dimensionerne på nano-skalaen inde i søjleformede korn med <211> orientering, en høj termisk stabilitet selv efter varmebehandling ved $600°C$. For at kunne udnytte den høje termiske stabilitet af "nano twins" studeres effekten af forskellige elektrokemiske deponerings forhold samt legering af nikkel med kobolt.

Ved at bruge Watts elektrolyt med et almindeligt sulfurfrit tilsætningsstof er nanokrystallinske nikkel film med forskellige karakteristika i det deponerede tilstand syntetiseret som funktion af deponeringsforholdene. Mikrostrukturen af varmebehandlede nanokrystallinske nikkel film viser en lav brøkdel af favorable korngrænser. Kornstørrelsen og teksturudviklingen på grund af varmebehandling er også undersøgt og det diskuteres i relation til minimering af tøjningsenergi og minimering af grænsefladeenergi som gør sig gældende i forskellige stadier af kornvækst. Forskelle i de oprindelige mikrostrukturelle karakteristika som funktion af deponeringsprocessen giver forskelle i kornstørrelse og korngrænse karakteristika efter varmehandling. Det foreslås at “triple junctions” i korngrænse netværket, i hvert fald til dels, bidrager til de observerede forskelle, og potentialet for “grain boundary junction engineering” skitseres.

Contents

List of Figures

List of Tables

Chapter 1

Introduction

Grain boundaries and other inter-crystalline regions e.g. triple lines and quadruple nodes play a significant role in the properties of polycrystalline materials [1–3]. Traditional processing has been targeted to control the grain size, i.e. number of grain boundaries. However, more important than the number of grain boundaries, the key for designing and controlling functional properties is the grain boundary characteristics. Accordingly, the concept of grain boundary design/engineering has been proposed as a tool for deliberate manipulation of grain boundary characteristics to improve materials properties [4, 5]. In other words grain boundary engineering aims to increase the fraction of favorable boundaries above the level present in a random polycrystalline material and thereby, tailor the materials properties. Based on this concept, some industrial applications have emerged [6] and there is an increase in the research conducted in this field of materials science [7–10]. Traditionally grain boundary engineering was applied in low to medium stacking fault energy materials owing to the fact that twinning has a major role in the process of synthesis of desired boundaries and microstructure [11–13]. Furthermore, most of the studied grain boundary engineered materials were composed of relatively large grains in the range of tens to hundreds of microns [12].

At about the same time that grain boundary engineering was proposed, the concept of nano-crystalline materials (NcM) was developing [14, 15]. The notable improvement in mechanical properties, e.g. hardness and wear, by miniaturization of the microstructural features down to nano-meter was a driving force for extensive research in this field [16, 17]. Many scientific studies were conducted on different aspects of nano-crystalline materials and it is a continuing topic of high importance for improving materials properties [18–20]. Materials possessing a nano-twinned microstructure benefit from both of the mentioned concepts of materials properties improvement (GBE and NcM) [21–23]. In recent years some outstanding mechanical properties (e.g. high strength and ductility) and physical properties (e.g. high thermal stability and conductivity) for this class of materials have been reported [21, 24]. Nano-twinned microstructure are synthesized mainly with low stacking fault energy materials such as copper and stainless steel [25]. Since high density of twins in materials with relatively high stacking fault energy such as nickel cannot be achieved [25], they are less studied in this context.

More than a half of the overall nickel produced worldwide is used in the form of coatings. In addition, one of the most common metal plating processes is nickel electrodeposition [26]. High wear resistance, relatively high hardness, barrier properties, corrosion resistance, bright and leveled deposits, thick layers deposition, etc. makes nickel electrodeposition of practical importance for various application [26]. Functional, protective and decorative nickel coatings have been applied in industry [26]. Nickel films are also used in micro-electro-mechanical systems (MEMs), magnetic recording heads and ultra thin films for magnetic sensors [27, 28].

Thus electrodeposition of nickel is of high importance in industrial applications and there is an urge in discussing

(i) grain boundary engineering of nickel specially in sub-micron scales, and
(ii) nickel nano-twins in the context of grain boundary engineering.

The aim of the project is to address these two topics.

Electrodeposited nano-crystalline materials are manufactured under conditions far from equilibrium and hence, are meta-stable. In previous studies it has been shown that twinning plays a role in the microstructural evolution of electrodeposited nano-crystalline materials [29–31]. Accordingly, microstructural evolution of electrodeposited nano-crystalline nickel films is studied in this project in the context of GBE. Using the same material synthesis technique (electrodeposition) columnar microstructures comprising high fraction of twins are synthesized and investigated too, i.e. *growth twins* are studied.

Since by growth of nano-sized features of microstructure, the material properties alters notable, thermal stability of nano-crystalline and nano-twinned materials is of importance for practical applications [32–34]. Thus, thermal behavior of nano-crystalline material and nano-twins in electrodeposited films is also addressed. In other words, thermal treatment experiments are conducted both as a tool for manipulation of the microstructure (GBE) and for analysis of the thermal stability of the synthesized microstructures.

For characterization of the microstructure, X-ray diffraction (XRD), electron backscatter diffraction (EBSD), and focused ion beam (FIB) microscopy are utilized in a supplementary manner. Moreover, 3D-EBSD which is a technique based on serial sectioning using FIB and sequential 2D-EBSD is also applied to achieve a complete characterization of the grain boundaries. Especial emphasize is put on electron and ion microscopy on the cross-section of the films, because the microstructure of the films can be a function of the thickness [30, 35, 36].

Chapter 2

Electrodeposition

The major aim of this chapter is to briefly introduce electrodeposition as a method for synthesis of nano-structured materials. Accordingly, it is first introduced in comparison with other synthesis methods, and a general description of the process is provided afterwards. Special attention is paid to electrodeposition of nickel (section 2.3) and Watts electrolyte of nickel electrodeposition (section 2.4) to provide the background for the later chapters.

2.1 Electrodeposition and Synthesis of Nano-Structured Materials

Miniaturization of microstructural features down to a few tens of nanometers has improved some of the mechanical, physical and chemical properties of the materials [16, 17]. In addition, it has been shown that some inherent characteristics of the synthesis method influences the final properties of nano-structured material. For instance, there is a significant difference between thermal expansion of nano-crystalline material of the same composition and grain size, synthesized by electrodeposition and by inert gas condensation (the former brings about a fully dense material whilst the latter does not) [37]. Hence, to obtain desired material's properties it is of importance to note the advantages and disadvantages of different synthesis methods.

There are two main approaches to produce nano-structured materials: (i) Top-down methods, in which large precursor dimensions are processed down to nanometer size, e.g. ball milling. (ii) Bottom-up methods, in which atoms or clusters of a few atoms are adjoined and form a nanometer size feature, e.g. inert gas condensation [38]. Top-down methods are normally accompanied with significant deformation, whilst bottom-up methods bring about more chemical homogeneity and less defects [38].

The state of matter during the process is utilized for classification of the processes. All three states of matter (solid, liquid, and gas) are used for synthesis of nano-structured materials. Ball milling is one of the most common solid based processes; gas phase is utilized in CVD, PVD and inert gas condensation; and rapid solidification is a liquid based process [38]. Based upon the mentioned categories, electrodeposition is a bottom-up-liquid-phase method.

Electrodeposition has been found to be technologically feasible and an economically superior method for fabrication of nano-structured materials [39]. The parameters that govern the processes e.g. current density, temperature, agitation, electrolyte composition, etc. are relatively easy to control. Low operating temperature for the process is advantageous, as undesirable phenomena associated with high temperature methods are avoided [39]. In addition, utilizing a fairly simple experimental set-up, different types of materials such as pure metals, alloys and composites can be electrodeposited at high production rate and relatively low initial investment [37]. Due to the mentioned benefits, electrodeposition of nano-structured materials have found wide application [28, 40–42].

The most common electrodeposition process for production of nano-structured materials is cathodic metal deposition, in which single or complex ions from the electrolyte reduce to solid state on the surface of the cathode [39]. By careful selection of electrodeposition parameters, nucleation and growth of grains can be controlled such to obtained the desired microstructure and, hence, properties [37]. Electrodeposition is very often used for synthesis of films and coatings [40]. In this case, the thickness of the film, influences properties of the nano-crystalline material [32]. Accordingly, the properties of the nano-structured films can be significantly different from their bulk counterparts. Furthermore, the properties and microstructural characteristics of the films can be a function of their thickness, [30, 35, 36], and that requires a cross-sectional characterization to addresses the thickness dependence.

2.2 Basics of Electrodeposition

2.2.1 Thermodynamics of Electrodeposition

Electrodeposition is defined as film growth processes in which a metallic coating forms on a base material due to electrochemical reduction of metal ions from an electrolyte [26]. Cathode and anode are immersed in a vessel containing electrolyte and are connected to a power supply to make current flow possible, Figure 2.1. The main constituent of the electrolyte is the ions of the electrodepositing metal. Other than electrolyte, in the case of sacrificial anode (such as depicted in Figure 2.1) the metal cation concentration is maintained constant in the electrolyte by an oxidation reaction of the anode ($M_{(S)} \rightarrow M^{z+}_{(aq)} + ze^-$). The metallic cations are transferred to the cathode surface and undergo a reduction reaction ($M^{z+}_{(aq)} + ze^- \rightarrow M_{(S)}$) [26]. Hence, at the cathode, metallic ions are removed from the electrolyte and incorporated into the deposit. In practice there are other reduction reactions accompanying the metallic reduction reaction. The hydrogen evolution ($2H^+ + 2e^- \rightarrow H_2 \uparrow$) very often proceeds parallel to the electrodeposition of the metals[1]. Reduction of metallic ions on the cathode surface results in the deposition of certain mass (m), which can be calculated by Faraday's law [26].

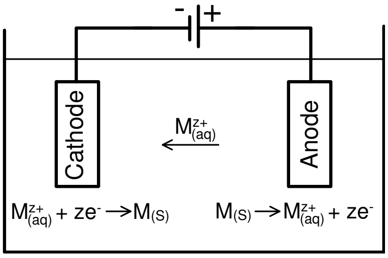

Figure 2.1: Schematic representation of electrodeposition set-up. There is a net flow of $M^{z+}_{(aq)}$ from the sacrificial anode to the cathode.

$$m = CE\frac{QM}{zF} \tag{2.1}$$

where CE is current efficiency[2]; Q, transferred charge; M, molar mass of deposited metal; z, number of valance electrons of the metal; and F, Faraday's number ($F = 96485\ C/mol$). The total transferred charged, Q, is calculated from:

$$Q = \int I.dt \tag{2.2}$$

where, I is the applied current and t is deposition time. Conducting the electrodeposition at constant current, the transfered charge can be calculated from: $Q = It$.

By immersion of the cathode into the electrolyte, an electrically charged double layer forms at the interface between the two; this double layer significantly influences the kinetics of electrodeposition [43]. When no current is passing through the set-up ($I = 0$) and the cathode and the electrolyte containing M^{z+} are at equilibrium state, a potential establishes between the two. The potential value is defined as the equilibrium potential of

---

[1] Oxygen reduction takes place in alkaline electrolytes: $O_2 + 2H_2O + 4e^- \rightarrow 4OH^-$

[2] CE has a value ranging from 0 to 1 and takes into account reactions other than main metallic ion reduction.

the process (E_{eq})[26]. E_{eq} is dependent on the activity of the electro-active species($a_{M^{z+}}$) in the electrolyte and the activity of the metal in solid phase (a_M); it is assessed by Nernst Equation [26]:

$$E_{eq} = E_0 + \frac{RT}{zF} ln(\frac{a_{M^{z+}}}{a_M}) \tag{2.3}$$

Where, E_0 is standard potential; R, gas constant (8.3145 J/mol K); T, the absolute temperature.

In order to initiate electrodeposition, it is necessary to shift the potential of the cathode to smaller values than E_{eq}. The power supply is the means to reduce the potential of the cathode. The difference between the potential during the electrodeposition and the equilibrium potential is called *overpotential*, η.

$$\eta = E(I) - E_{eq} \tag{2.4}$$

Overpotential is the thermodynamical driving force for electrodeposition and influences the extent of adsorption at the cathode, hence, the structure of the deposit. [26].

2.2.2 Kinetics of Electrodeposition

The actual processes of electrodeposition and formation of the deposit layer does not only depend on the thermodynamic driving force. In addition to the overall charge transfer of metallic ions, electrodeposition consist of four and each of them can be rate-determining [26]. These steps are:

1- Mass transfer of metallic ions (more precisely reducible species e.g. hydrated ions) to the cathode surface under the influence of diffusion, convection and (electric) migration from the bulk of electrolyte [26].

2- Dehydration (i.e. stripping the hydration sheath) or dissociation from the ligands of electro-active species; [26, 43].

3- Charge transfer at the cathode and adsorption of the reduced metal on the surface.

4- Incorporation of metal atoms (ad-atoms) into the crystal lattice of the deposit by their diffusion across the surface to active (growth) sites.

The listed steps are to provide a general grasp of the process. Some of these steps can be realized as single step (very often 2 & 3) or some of these steps can be divided into other sub-steps (e.g. in an electrodeposition process leading to a coherent deposit, step 4 is composed of nucleation and growth [43]).

The overall overpotential of the electrodeposition process is the sum of the overpotentials of the various steps, hence:

$$\eta = \eta_1 + \eta_2 + \eta_3 + \eta_4 \tag{2.5}$$

It is worth mentioning that the kinetics of the four steps are different and the slowest step governs the rate of the overall process [26].

2.2.3 Parameters Influencing the Electrodeposition Process

There are many parameters influencing the electrodeposition process, e.g. electrolyte chemical composition, current density, pH, temperature, agitation, electrode composition and surface conditions, etc. [26, 43]. More than being numerous, there is interdependence between these parameters which makes the study of their influence rather complicated. Having mentioned that, the influence and occasionally interdependence of some of the influencing parameters are shortly discussed in the following.

2.2.3.1 Electrolyte Composition

Electrodeposition can be accomplished in a simple solution containing salt(s) or soluble compound(s) of the depositing metal. However, the quality of the deposits obtained from single component solutions is so poor that in practice such a solution is rarely used for real applications. Instead, multi-chemical-component solutions (electrolytes) are most often used. The type of ions and their concentration in the electrolyte influence the deposit quality and properties. Moreover, controlling electrical conductivity of the electrolyte, adjusting pH, buffering the electrolyte, increasing metal dissolution at the anode, are some of the tasks that are served by addition of different chemical compounds [26]. More than the essential salts and chemical compounds that provide coherent deposits, the so-called 'additives' have major influence on the electrodeposition. Brightening the deposit, reducing grain size, increasing the applicable current density range, promoting leveling power, reducing stress, increasing electrolyte stability and reducing pitting, etc. are some of the benefits that correct choice of additives can provide [43–47]. Additives are often organic compounds or colloids [44].

Bright deposits, providing mirror finish surface without need of further treatment are of high importance for practical applications. This requires a smooth topography of the surface (very often realized by fine grains) and leveling of the topography on the cathodesurface [44]. The latter takes place when the deposition in the valleys is more pronounced than on the peaks (leveling) [44]. There is a defined concentration range at which any additive is effective [44] in the bulk of the electrolyte, it is $10^{-4} - 10^{-2}$ mol/lit. The mechanism of action of additives in a simplistic point of view is based upon the adsorption on the active growth sites of the cathode surface. Thus, the concentration of additives in the vicinity of the cathode is much higher than in the bulk of the electrolyte[3]. The adsorption on the growth sites, 'inhibits' the deposition, and increases the overall overpotential [26, 48]. The adsorption of the additives is selective, i.e. only molecules of a certain size, shape, and chemical structure can be adsorbed on the metal surface[4] [48]. The activity of an organic molecule depends on the presence of certain types of unsaturated bonds between atoms of carbon, nitrogen, oxygen or certain sulfur-containing radicals [49]. Furthermore, a suitable spacing between metal atoms on the surface of the deposit is required to hold the organic molecules [48]. This has two implications: (i) there are very rare cases that an organic compound acts as an effective additive for two different metals [48] (ii) adsorption of a particular additive is different on different crystallographic planes of a same metal.

It is worth mentioning that, due to decomposition of the additives and/or their incorporation into the deposit, the concentration of additives decreases as the processes of electrodeposition continues [43, 48].

2.2.3.2 Current Density & Electrode Potential

It has been pointed out that an overpotential the driving force for the process of electrodeposition. In practice the overall overpotential is controlled and varied by alteration of the electrode potential[5] or applied current density. Applied current density is the most practical measure for controlling the rate of the electrodeposition process and its value can be easily calculated from an ammeter reading of the current and measurement of the geometry of the cathode surface area (S_{geo}) [26]. Electrodeposition can be applied at a fixed current density (galvanostatic process) or altering the current density by different forms of waves (pulse electrodeposition). Furthermore, since there is a one-to-one correspondence between the applied current density and the cathode potential, an alternative to a galvanostatic process is to conduct the electrodeposition at a fixed cathodic potential (potentiostatic process).

In general, a higher current density brings about a higher overpotential. However, the relation between the two is not linear. A generic current density vs potential curve is shown in Figure 2.2. At high overpotentials mass transport of chemical species to the cathode becomes the rate controlling step of electrodeposition process [50]. In that case,

---

[3] It is worth mentioning that the action of additives is fairly complex and other than adsorption on the growth sites, at least 8 other mechanisms has been proposed [44] to explain the action of additives.

[4] The crystallography of the surface influences the adsorption too.

[5] Cathode potential is normally measured versus and standard electrode e.g. Calomel, silver chloride, etc.

further increase of the potential, hence, overall overpotential, does not yield an increase of current density. This upper limit of current density is called 'limiting current density' [50].

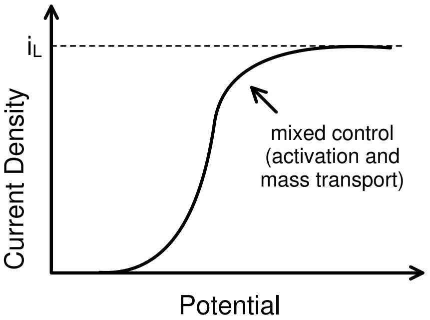

Figure 2.2: General current vs overpotential relationship; at high overpotential the limiting current density i_L is reached. The figure is adopted from [50].

2.2.3.3 Temperature

Temperature has a profound influence on the quality and properties of the deposit. In general, a higher temperature of the electrolyte is advantageous as it brings about higher solubility of the chemical compounds, higher conductivity, higher stability and lower tendency of passivation of the anode [26]. In contrast to the mentioned advantages, higher temperature of the electrolyte results in higher evaporation and reduction of the additives efficiency and lower inhibition. Lower inhibition normally bring about increase in grain size [51].

2.2.3.4 pH

Based upon operating pH, commercial electrodeposition electrolytes are categorized into acidic, neutral, and alkaline [43]. It is of high importance to avoid pH alteration of the electrolyte, during the electrodeposition [43]. Accordingly, all practical electrodeposition electrolytes have added acid, buffer, or alkali corresponding to their electrolyte type, to stabilize the pH. In acidic electrolytes, such as acidic copper in which sulfuric acid is a vital chemical in the electrolyte, high concentration of acid is beneficial for increasing conductivity and minimizing the pH change. For electrodeposition of nickel, it has been argued that H_2 gas evolution inevitably accompanies the process [27]. Thus, the pH in the vicinity of the cathode increases as the H^+ ions are reduced and form H_2 [27]. The value of pH in the vicinity of the cathode can differ from that of the bulk by several pH units [26]. Hence, buffering the electrolyte is of high importance to avoid formation of non-conductive hydroxides on the surface [52].

2.2.3.5 Substrate

Cathode prior to electrodeposition is the deposit ‘substrate’. Since, the substrate chemistry and properties are unlike the deposit, at very early stage of electrodeposition, the substrate has a significant influence [26]. For instance, hydrogen evolution on steel has a much lower overpotential in comparison with that of zinc. Thus, at a very early stage of electrodeposition of zinc on steel the current efficiency is significantly lower and after formation of very thin layer of zinc, current efficiency increases [26]. Similarly, hydrogen evolution on platinum is so strong that it inhabits formation of any deposit under many conditions, i.e. CE=0 [53].

Substrate influence on the deposit has been subdivided in 3 zones [54]: zone A, the deposit is influenced by the substrate, in zone C the growth conditions are expected to be largely controlled by the deposition parameters; and zone B is a transition zone from zone A to C. If the substrate is amorphous, then the nucleation of electrodeposit takes place randomly and zone A is unbiased by the substrate [54, 55]. Whereas a crystalline substrate may impose an influence on the orientation of the deposit (epitaxial growth) [54, 55]. Depending on the substrate and electrodeposition condition the thickness of zone A ranges from nanometers to a few tens of microns [26, 53].

2.2.3.6 Agitation of the Electrolyte

It is mentioned that, the first step of formation of the deposit is mass transfer of metallic ions to the cathode surface. It is predominantly achieved by convection, i.e. ion transport is enhanced due to stirring of the surrounding solution [43]. Even though ‘natural convection’ occurs due to convection currents in the electrolyte, in practice, ‘enhanced convection’ by various forms of agitation is applied to achieve high quality deposits. It is worth mentioning that the migration of ions due to a potential gradient between anode and cathode is small in comparison with convective mass-transport [43]. In absence of agitation, mass transport becomes the rate limiting step of the process at lower applied current density, i.e. agitation increases limiting current density [48].

2.3 Electrodeposition of Nickel

2.3.1 Electrolyte Composition

Nickel electrodeposition has a long history, starting with the ammonium sulfate solution developed by Adams in 1869 [26]. In the past years different electrolytes have been developed which provide different deposit characteristics and microstructure. Generally, most of the nickel electroplating electrolytes are comprising nickel sulfate, nickel chloride, and nickel sulfamate. To a lesser extent nickel acetate is used in some electrolytes [26]. In addition, boric acid, sodium chloride, sodium sulfate, magnesium sulfate, potassium fluoride, etc. are some other chemical compounds that often used as additives in nickel electrodeposition [26]. Three widely used electrolytes for nickel electrodeposition and their typical operating conditions are listed in Table 2.1.

Table 2.1: Three widely used nickel electrodeposition electrolytes composition and operating conditions [56].

	Watts	Conventional Sulfamate	Concentrated Sulfamate
	Electrolyte Composition, g/L		
$NiSO_4 \cdot 6\,H_2O$	225 to 300		
$Ni(SO_3NH_2)_2 \cdot 4\,H_2O$		315 to 450	500 to 650
$NiCl_2 \cdot 6\,H_2O$	37 to 53	0 to 22	5 to 15
	Operating Conditions		
Temperature,°C	44 to 66	32 to 60	norm. 60 or 70
Agitation	Air or mech.	Air or mech.	Air or mech.
Current density, A/dm^2	3 to 11	0.5 to 32	Up to 90
Anodes	Nickel	Nickel	Nickel
pH	3.0 to 4.2	3.5 to 4.5	3.5 to 4.5

Thousands of compounds are known for brightening nickel deposits just in sulfate-chloride electrolytes [44] which significantly alter the nickel electrodeposits properties. For instance, elongation of the electrodeposited nickel vary from 1.0% to 28% for different electrolytes [44].

The importance of electrodeposition of bright nickel for industrial applications cannot be overstated. The key to achieve bright nickel deposit is to combine class(I) and class(II) of brighteners [44]. Class(I), brings about only grain refinement, hence, results in bright deposits only on a well-polished substrate [43, 44]. It also increases the range of concentrations at which class(II) brighteners can be practically used [44]. Class(II) brighteners act as both brightener and leveler, such that near-mirror finish to the deposit is obtained even at very low concentrations. However, they often impose negative influence such as excessive brittleness and stress in the deposits in the absence of brighteners of class (I) [43, 44].

2.3.2 pH

Nickel electrodeposition is very sensitive to the pH of the electrolyte; at a pH higher than 5.6 nickel hydroxides precipitate near the cathode and are incorporated into the deposit, whilst at low pH hydrogen evolution reaction (HER) takes place profoundly, parallel to the nickel deposition [26]. Thus, there is normally a large difference between the pH at the bulk of the electrolyte and at that in the vicinity of the cathode, hence, nickel electrolytes must contain buffering agents. Boric acid is the predominant buffering agent; NH_4Cl, malic acid and other buffering systems such as acetic acid are also used [26, 52, 57].

2.3.3 Anode

Sacrificial soluble nickel anodes are almost always used during electrodeposition of nickel. Pure nickel anode is prone to passivation and formation of slurries, specially at relatively high pH [26]. To avoid this, small anodic current density, addition of activators to the electrolyte e.g. chlorides and fluorides and placing the anodes into suitable bags are common practice in industry [26].

Several types of commercially used anodes contain up to 0.01% of sulfur and also silicon, nickel oxide, carbon, etc. [26]. The film formed at the surface of these anodes during dissolution, impedes the precipitation of a slurry [26].

2.4 Watts Electrolyte

In 1916 Watts proposed an electrolyte comprising nickel sulfate, nickel chloride and boric acid as main constituents [58]. Watts electrolyte and its modified counterparts are the most widely used electrolyte for nickel electrodeposition today [59]. In a simplistic view, nickel sulfate is the main source of nickel ions; nickel chloride (Cl^-) improves anode dissolution and increases electrolyte conductivity and boric acid buffers the electrolyte [56]. However, a thorough study of this electrolyte has revealed more complex characteristics of it. For instance, it has been pointed out that Cl^- influences cathodic reactions as well as anodic reactions [59]. Details of chemical and electrochemical reactions in Watts electrolyte are discussed below.

2.4.1 Chemical and Electrochemical Reactions in Watts Electrolyte

The mechanism proposed for electrodeposition of nickel in Watts electrolyte is as follows: Saraby-Reintjes and Fleischmann have proposed two consecutive one-electron charge transfers, and participation of an anion, as follows [60]:

(1) $Ni^{+2} + X^- \rightarrow NiX^+$ (2) $NiX^+ + e^- \rightarrow NiX_{ads}$ (3) $NiX_{ads} + e^- \rightarrow Ni + X^-$

It has been postulated that X^- is OH^-, SO_4^{2-}, or Cl^-, however, there is experimental evidence that X^- is Cl^- [60]. In another study by Supicova et al., a three-step mechanism was proposed: (i) a chemical reaction preceding an electrochemical reaction, (ii) the occurrence of surface reactions with the adsorption of intermediates (iii) a reaction of the electro-active substance transported to the electrode by diffusion [60].

(1) $Ni^{+2} + H_2O \leftrightarrow Ni(OH)^+_{aq} + H^+$ (2) $Ni(OH)^+_{aq} \leftrightarrow Ni(OH)^+_{ads}$
(3) $Ni(OH)^+_{ads} + e^- \rightarrow NiOH$ (4) $NiOH + H^+ + e^- \rightarrow Ni + H_2O$

Karayannis and Patermarakis have divided the reactions in Watts electrolyte to (I) reaction common between Cl^- and SO_4^{2-}, (II) specific reactions of Cl^- and (III) specific reactions of SO_4^{2-} [59].

(I): $2H^+ + 2e^- \rightarrow H_2$
$Ni^{+2} + e^- \rightarrow Ni^+_{ads}$
$Ni^+_{ads} + e^- \rightarrow Ni$
$Ni^{+2} + Ni^+_{ads} + 2e^- \rightarrow Ni + Ni^+_{ads}$
(II): $Ni^+_{ads} + 2H_2O \rightarrow Ni(OH)_{2\ ads} + 2H^+ + e^-$
$Ni + 2H_2O \rightarrow Ni(OH)_{2\ ads} + 2H^+ + 2e^-$
$Ni(OH)_{2\ ads} + 2e^- \rightarrow Ni + 2OH^-$
(III): $Ni^+_{ads} + H^+ + e^- \rightarrow Ni^+_{ads} + H_{ads}$
$2H_{ads} \rightarrow H_2$
$Ni^+_{ads} + H_{ads} + e^- \rightarrow Ni + H_{inclusion}$

Other mechanisms have been proposed which are reviewed in [60]. It is noteworthy that the pH has been found to exert a larger influence than anions in adsorption at the cathode surface [60]. However there is still interdependence between pH and chemical species. For instance, it is argued that hydrogen evolution reaction which influences local pH directly modifies with chloride adsorption [53]. Adding to this complexity, Motoyama et al. take into account 10 different reactions which are involved in dissociation of boric acid which is the most influential chemical compound in regarding pH value at the cathode surface [27]. In addition to that, it is often pointed out that boric acid forms complexes with nickel ions which ease nickel ion discharge [61, 62]. Thus, boric acid also acts as a catalyst which lowers the overpotential of Ni electrodeposition [61, 62]. In a simplistic view, by neglecting all the interaction with other chemical species in the electrolyte and just focusing on boric acid reactions, it was found that at pH below 6, H_3BO_3 barely dissociates, and at higher pH, $HB_4O_7^-$ concentration start to increase at the expense of H_3BO_3 concentration [27], Figure 2.3.

In conclusion, the three-constituent in the Watts electrolyte, which at first appears a very simple system, is in fact extremely complex. It is close to a century that Watts electrolyte is invented and it is predominant electrolyte studied and used for electrodeposition of nickel [26]. Yet, not all the details of the process are well-understood. In the following some of the micro-structural characteristics of electrodeposited nickel films from the Watts electrolyte are discussed.

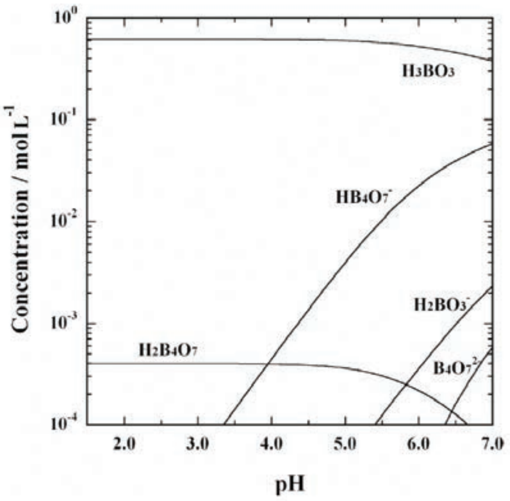

Figure 2.3: Concentration distribution of the soluble species from boric acid [27].

2.4.2 Characteristics of Deposits From Watts Electrolyte

Materials properties, structure and processing are interdependent and understanding the interrelation between these, is crucial to obtain the desired materials performance. The connection between properties, structure and processing is extensively studied for deposits obtained from Watts electrolyte. The electrochemistry of the process is investigated by voltammetry and impedance measurements [61, 63, 64] and the connection between the electrochemistry and certain microstructural characteristics is established [59, 65–67]. Similarly, mechanical properties (e.g. hardness, wear resistance) [56, 68, 69], physical properties (e.g. conductivity, brightness) [70–72] and chemical properties (e.g. corrosion resistance) [73, 74] of the deposits are linked to electrodeposition conditions and the deposits' structure. Since the characterization of the microstructure is a key to understand various properties, the microstructure is studied by various means in the past decades. Grain size, surface topography, defects density, preferred orientation are more often studied by Transmission Electron Microscopy (TEM), XRD, Scanning Electron Microscopy (SEM), etc. [69, 72, 75–77]. In is notable that TEM is extensively utilized for the characterization of the microstructure and it provided valuable pieces on information on microstructural characteristics. For instance, using a supposedly primitive TEM, growth twins were revealed in a nickel deposit more than 60 years ago (see Figure 1 in [78]) and onward number of publications on the microstructure of Watts nickel has increased. In a pioneering research [75], the texture of nickel deposit as a function of pH and applied current density is characterized, Figure 2.4. Based on that, the effect of modification of the electrolyte by pulse plating [79] or presence of additive (see Figure 2.6) on the texture is studied too. Since the texture of pure Watts electrolyte is very well linked with microstructural characteristics [75], a very strong background for further research is established for Watts electrolyte which is a huge advantage in studying it. Note that texture and microstructure of sulfamate electrolyte which is also widely used, have not been extensively investigated as a function of current density, pH, and bath additives [80].

It is pointed out that texture and common characteristics of the microstructure of each texture is described [75, 81]. In addition, different theories are proposed to explain the occurrence of different textures. Inhibition of different chemical species, relative surface energies of different crystallographic planes, and theories which resemble the plastic deformation texture formation, are the most notable ones [75, 82–84]. Though no general agreement is yet achieved on this topic, inhibition by different chemical species [75, 85] has gained most acceptance [79, 83, 86, 87].

It has been proposed that Watts nickel has four different fiber textures, Figure 2.4, namely, <110>, <210>, and <211>, are formed due to inhibition by H^+_{ads}, H_2, and colloidal $Ni(OH)_2$; And uninhibited growth brings about <100> fiber texture which has been called the 'free mode of growth'. All of these fiber textures have characteristic twins [75]. A

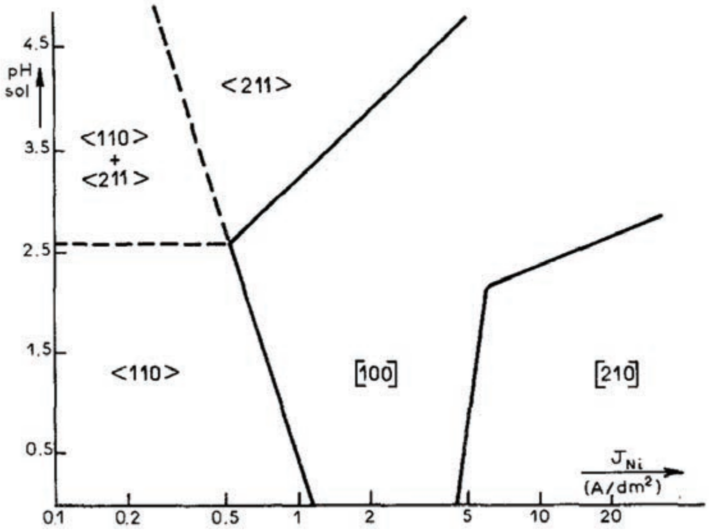

Figure 2.4: Stability of the various fiber textures of nickel electrodeposits versus pH of the Watts electrolyte and nickel current density [75].

<211> fiber texture twins are more or less parallel to the growth direction, Figure 2.5a;

those of <100> are inclined with respect in growth direction, twins in <110> oriented grains form a pseudo five-fold symmetry, and most complex of all, <210> oriented grains exhibit a 'helical' structure consisting of a compact connection by edges of tetrahedra with conservation of a common crystallographic direction of <210> type [75, 81, 88].

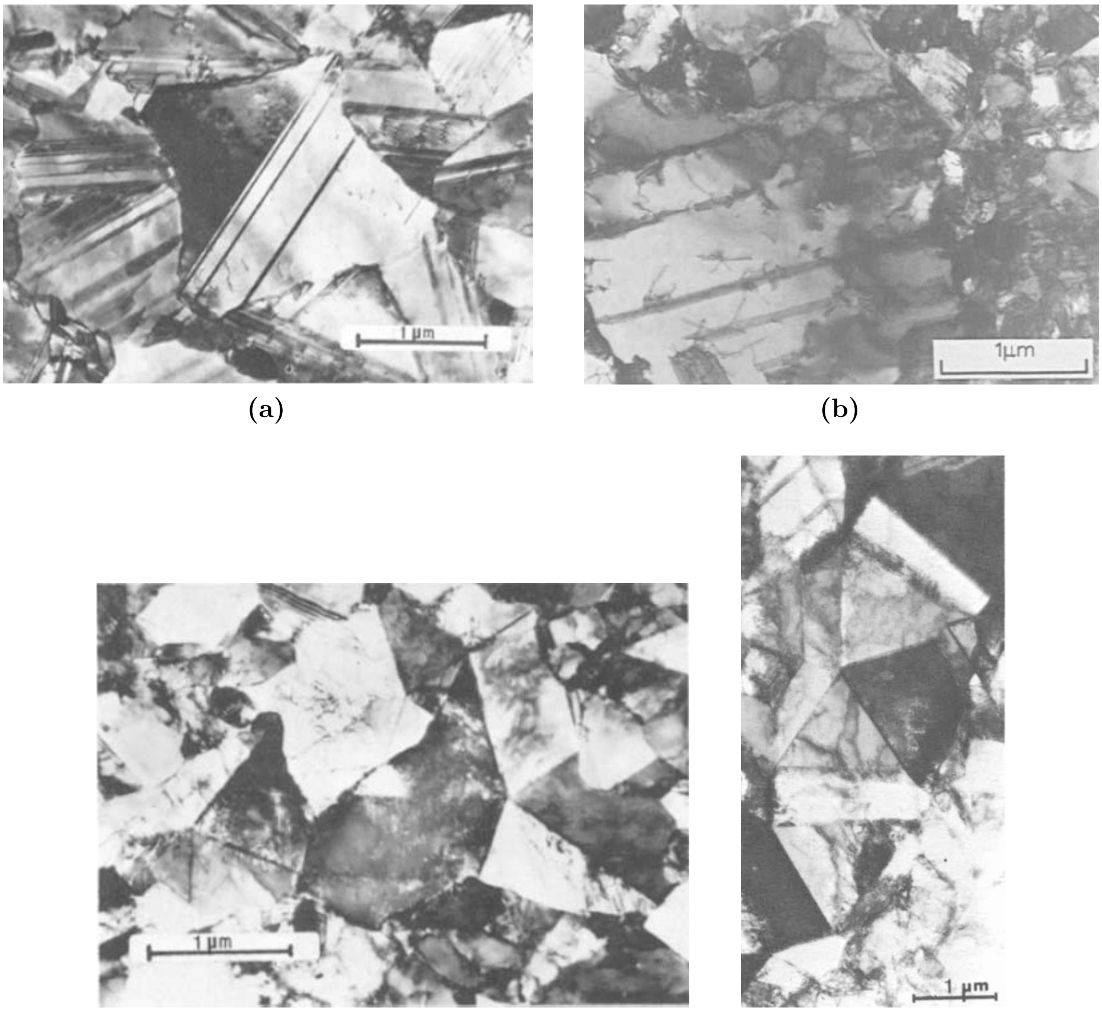

(a) **(b)**

(c) **(d)**

Figure 2.5: Microstructure of nickel deposits from Watts electrolyte with different texture: (a) <211> [75], (b) <100> [79], (c) <110> [75], and (d) <210> [81]. Note that (d) is a cross-section.

2.4.3 Additives to Watts Electrolyte

Additives in the Watts electrolyte, have the most significant influence on deposit properties and microstructural characteristics [56, 73, 75]. Hence, there are numerous additives used for modification of the electrodeposition of nickel in Watts electrolyte [44]. The key in successful modern bright nickel electrodeposition of nickel is simultaneous use of class(I) and class(II) brighteners [44]. The class(I) brighteners in Watts electrolyte, such as: benzene sulfonates, naphthalene sulfonates, saccharin, and p-toluenesulfonylamide, are relatively ineffective in increasing the cathode potential [89]. The class(II) brighteners which are characterized by the presence of an unsaturated group such as C=O, C=C, C≡C, C=N, C≡N, etc. [65] effectively increase the cathode potential [89]. In an extensive investigation, 76 organic additive agents were studied and categorized by change of cathode potential during the electrodeposition of nickel in Watts electrolyte [89]. In addition, the effect of many other chemical compounds on the nickel deposit from a Watts electrolyte were studied [44, 90–93]. The most commercially used additives in Watts type electrolyte for producing bright and leveling nickel deposits are saccharin representing class(I) and 2-butyne-1,4-diol, representative of class(II) [94, 95].

The effect of the presence of 2-butyne-1,4-diol, hereafter BDO, in Watts electrolyte on different aspects of electrodeposition process and properties of deposit is well documented in the literature [49, 94–98]. It has been reported that its presence in the electrolyte highly inhibits the nickel reduction [90], thus, the current efficiency decreases [96][6]. This is due to the unsaturated C≡C in the chemical structure of BDO, which hydrogenation reaction is catalyzed on the nickel surface [94, 95]. BDO is adsorbed at the surface of the cathode, the hydrogenation reaction occurs and afterwards the desorption of the chemical species takes place [49, 94]. The hydrogenation reaction requires H^+_{ads}, and it has been postulated that the rate of desorption is limited by the rate of hydrogen supply [49]. Due to hydrogenation of BDO, the concentration of H^+ in the vicinity of the cathode decreases, local pH increases and formation of hydroxides such as $Ni(OH)_2$ becomes favorable. This is the direct effect of BDO on increasing local pH. In addition, it has been argued that the presence of BDO, favors the discharge of hydrogen cations instead of the nickel [94]. Hence, BDO also enhances the local pH indirectly. As a result, highly inhibited modes of growth <211> and <111> which are associated with presence of colloidal $Ni(OH)_2$ at the cathode are forming in Watts electrolytes comprising BDO, Figure 2.6 [75]. It has been postulated that the hydroxyl group may establish weak interactions with chemical species and perturb their adsorption/desorption [49]. The activity of hydroxyl group at high pH is expected to be negligible [96].

In short, the presence of BDO in Watts electrolyte brings about grain refinmenet and formation of inhibited modes of growth i.e. <211> and <111>.

---

[6] BDO has a strong inhibitory effect in comparison with other common additives such as saccharin and sodium benzene sulfonate [95].

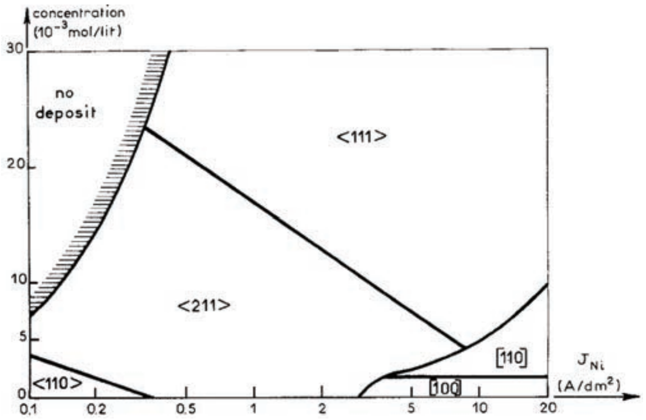

Figure 2.6: Stability of various fiber textures of nickel electrodeposits versus nickel current density and concentration of BDO. $pH_{sol} = 4.5$ and electrolyte temperature =50°C [75].

Chapter 3

Grain Boundaries and Grain Boundary Engineering

3.1 Grain Boundaries

A grain boundary in a solid crystalline material is a region separating two neighboring grains of the same phase. The two grains differ in orientation and, hence, the grain boundary is a transition region, where the atoms are shifted from their regular positions as compared to the crystal interior [99]. A grain boundary has eight degrees of freedom [100]. Three degrees of freedom describe misorientation between the two grains which is most often characterized by axis(o) - angle(θ) pair; two degrees of freedom describe the grain boundary plane orientation which is characterized by its normal ($\vec{n}$) [100]. These five degrees of freedom are described as 'macroscopic degrees of freedom'. Grain boundaries are classified into tilt (when $o \perp \vec{n}$), twist (when $o || \vec{n}$), and mixed (when $0 < \widehat{o\vec{n}} < 90$), see Figure 3.1.

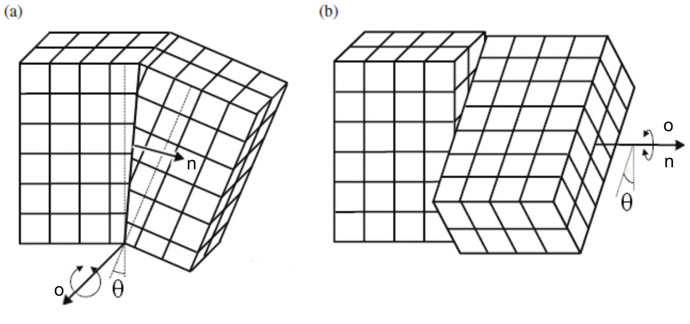

Figure 3.1: (a) Schematic representation of tilt boundary $o \perp \vec{n}$; (b) Schematic representation of twist boundary $o || \vec{n}$ [101]

The remaining three degrees of freedom, are 'microscopic degrees of freedom'. These characterize a rigid body translation of both grains relative to one another, parallel and perpendicular to the grain boundary plane [99, 102]. In materials science the 'microscopic degrees of freedom' for characterization of a boundary can usually be neglected. Thus, complete characterization of a grain boundary requires 5 independent parameters [102, 103]. From an atomic point of view, grain boundaries are classified as low-angle grain boundaries and high-angle grain boundaries.

3.1.1 Low Angle Grain Boundaries

When θ (the misorientation angle in axis-angle definition) is smaller than certain value, the misorientation is accommodated by an array of dislocations. Equilibrium arrangement of the 'primary grain boundary dislocations' in a periodic row to form a boundary is shown in Figure 3.2. Edge dislocations accommodate the misorientation in tilt grain boundaries, whilst screw dislocations apply for twist boundaries [99]. As the misorientation increases the dislocation density in the primary grain boundary dislocations increases and for $\theta \approx 13° - 15°$ the dislocation density increases such that they must overlap, and thus, the dislocation model is no longer applies [99]. Thus, for low angle grain boundaries θ is smaller than $13° - 15°$.

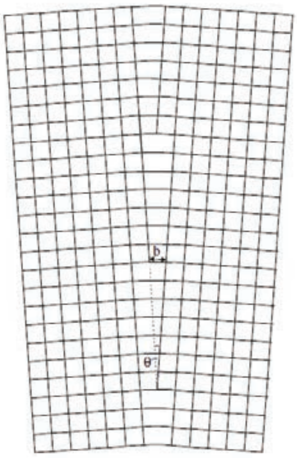

Figure 3.2: Schematic representation of a low-angle tilt boundary by a regular, vertical arrangement of edge dislocations along the boundary [101].

3.1.2 High Angle Grain Boundaries

A boundary with θ larger than $13° - 15°$, is classified as high angle grain boundary [99]. A 'Structural unit model' was developed to describe the arrangement of the atoms in high-angle grain boundaries. According to this model, a high-angle grain boundary is composed of repeated convex polyhedra (the structural units) that represent particular arrangements of a limited number of atoms [99].

Since the atomic arrangement of the grain boundary differs from that of the crystal interior, there is an energy associated with the grain boundary. If the arrangement of the atoms at the high angle grain boundary is close to that of crystal interior, then energy associated with the boundary decreases. This is normally the case when a single structure unit is sufficient for description of the arrangement of the atoms at the boundary (*singular grain boundary*). A high angle grain boundary which is described by two or more structural units is called a *general grain boundary.* Based on structural unit model, the complete set of grain boundaries has not been unambiguously established yet [99], thus, a different geometrical classification of grain boundaries are used. The first and most widely used model used for identification of high angle grain boundaries, is the coincidence site lattice (CSL) model.

3.1.2.1 CSL Model

Based on the assumption that energy of a boundary may be related to the number of broken bonds across the boundary, it concludes that, high coincidence of atomic positions in both neighboring grains has an inverse relation with the energy of the boundary [104]. Superimposing the lattice of two neighboring grains and forming a super-lattice, some of the sites are occupied by atoms from both grains (coincidence sites). The number of 'coincidence sites' indicates how many atoms are in perfect lattice position of both grains. Thus the density of coincidence sites is the most important parameter in this model, however, for ease of use its inverse value (Σ) is used. Mathematical description of Σ is as follows [99]:

$$\Sigma = \frac{\text{total number of all lattice sites in an elementary cell}}{\text{number of coincidence sites in an elementary cell}} \tag{3.1}$$

For instance two neighboring grains are shown in blue and red in Figure 3.3a. The super-lattice forming by superimposition of their lattices is shown in Figure 3.3b. The coincidence sites are shown in purple in Figure 3.3b. The supposed unit cell of CSL is shown in Figure 3.3c. In the cell of the blue lattice, 3 positions are enclosed by the yellow rectangle (2 sites inside the yellow rectangle and 4 corner sites ($\Rightarrow 4 \times \frac{1}{4} = 1$). 1 out of 3 of the elementary cell sites are coincidence sites, thus, $\Sigma = \frac{3}{1} = 3$. For geometrical reasons, Σ is very sensitive to change in misorientation, however, slight variation of θ does not change the character of the boundary significantly since the change in atomic positions is compensated by secondary grain boundary dislocations [99, 105]. Hence, it is

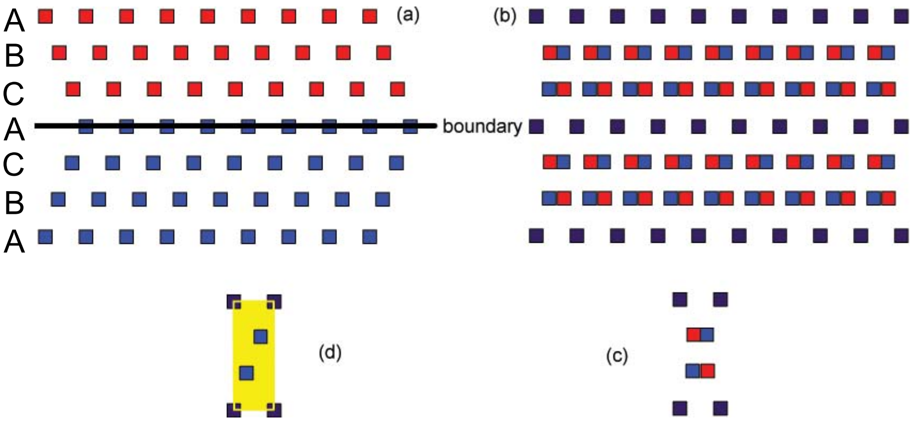

Figure 3.3: (a) Two neighboring grains in blue and red. (b) Superimposed lattice. (c) The unit cell of superimposed lattice. (d) Elementary cell, coincidence sites in purple and non-coincidence sites in blue

reasonable to define a range of misorientations for which the character of the boundaries is practically identical, and describe this range by the lowest value of Σ [99]. Maximum deviation allowed (ν_{max}) for any value of Σ, can be calculated from the following empirical equation [99]:

$$\nu_{max} = \frac{\nu_0}{\Sigma^{\xi}} \tag{3.2}$$

Where ν_0 is angular limit for low angle grain boundary (15°) and ξ has been suggested to have a value below one. $\xi = 0.5$ and $\xi = 0.83$ were proposed by Brandon [106] and Palumbo et al. [107] respectively.

The CSL model has some shortcomings: it is indifferent towards grain boundary plane, i.e. the grain boundary plane changes its orientation while the value of Σ remains constant. Hence, the model may fail to characterize the grain boundaries unambiguously [99]. Accordingly, characterization of boundary by all 5 macroscopic parameters is becoming more commonly used [12].

3.1.2.2 Twin Boundary

A coherent twin boundary is a high-angle grain boundary with a peculiarly low energy in comparison with general high angle grain boundaries [108] (see Figure 3.4). Twinning has occurred when the lattices of two neighboring grains are each others mirror image, see Figure 3.3a, and the mirror plane is the twin boundary plane [101]. In low stacking fault energy FCC materials twins are commonly observed [101]. In the case of crystals with a FCC lattice, twinning take place on the {111} planes [110]. In a perfect FCC metal the sequence of the most densely packed planes is ABCABCA. A twin in FCC metal has a sequence like ABC$\underline{\text{ACBA}}$ which the underlined part is a perfect FCC crystal but it is mirror of ABC sequence part [101, 110]. The stacking CAC containing the twin boundary

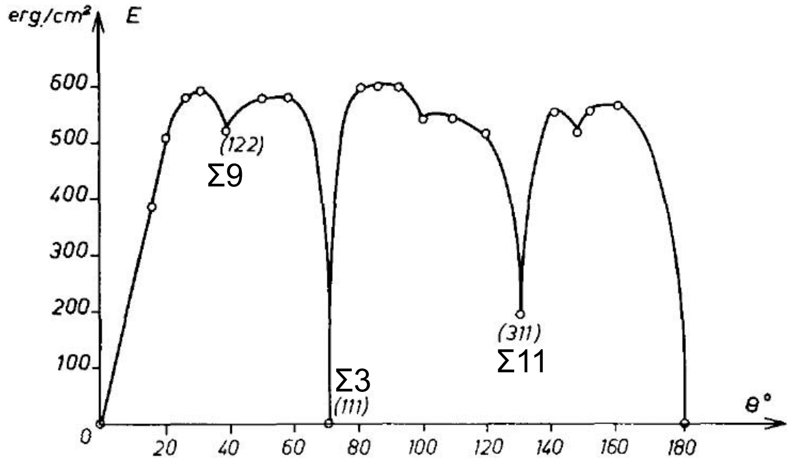

Figure 3.4: Energy of symmetrical tilt boundaries about [011] in aluminum [109]. Low energy CSL boundaries are marked on the figure.

is consistent with an HCP stacking.

At a coherent twin boundary, lattice sites at the boundary are coincidence sites between the two neighboring grains [101] and in the CSL model a coherent twin boundary is characterized by $\Sigma3$. It is worth mentioning that, not all $\Sigma3$ boundaries are coherent twin, since the plane of the boundary can be inclined with respect to the close-packed planes.

3.1.3 Grain Boundary Characterization

In order to characterize the boundaries, Orientation Imaging Microscopy(OIM) in scanning electron microscope (SEM) OIM-in-SEM is most often applied [111, 112]. OIM is a very powerful technique for microstructure characterization which is based on determination of crystallite orientation by analysis of Kikuchi bands in electron backscattered pattern (EBSP). Kikuchi bands form in a two step process: (i) incoherent scattering of the primary beam electrons (ii) elastic and coherent scattering of incoherently scattered electrons [113]. By detection and analysis of Kikuchi bands, orientation of diffracting crystallite can be determined and by scanning an area, the internal structure (grain size, grain orientation, grain boundary character, phase distribution, etc.) and microtexture can be obtained [111, 112]. More than orientation, the perfection of crystal lattices in diffracting volume can be assessed by analysis of image quality (IQ), a parameter describing the quality of a diffraction pattern [114]. When diffracting volume contains two or more adjacent crystallites, the resulting EBSP is a superposition of the patterns associated with each of crystallites. Thus, IQ is lower at the vicinity of crystallites boundaries in comparison with interior of each crystallite [114]. One of the limiting factors on the proper characterization of the boundaries, is the resolution of OIM-in-SEM. The resolution of OIM-in-SEM has been continuously improved in the past years, and it is dependent on the microscope, material, accelerating voltage, etc. [115–117]. OIM-in-SEM resolution is asymmetrical due to 70° tilt which is commonly applied for the measurement [118]. Parallel to tilt axis, resolution is the best and in direction perpendicular to tilt axis is the worst [118]. The effective resolution[1] of OIM for iron using 15 kV accelerating voltage was reported 30 nm and 90 nm in the mentioned directions, respectively [113]. Effective resolution of OIM-in-SEM has been successfully improved by lowering the accelerating voltage to 7.5 kV [117]. However, for operation the SEM in such a low accelerating voltage, rather special sample preparation, extremely stable microscope, enhanced detectors, etc. are required. When resolution of OIM-in-SEM is inadequate, orientation mapping in TEM (OIM-inTEM) can be applied [119, 120] However, that requires cumbersome sample preparation and special equipments in TEM. More importantly, irregular buckling of the thin foil [119] and number of grains in the width of the sample influence the reliability of the obtaining results. Hence, despite some successful reports on application of orientation mapping in TEM [121, 122], it is still not a common practice. Accordingly, full characterization of the grain boundaries of nano-crystalline materials, is still not readily attainable.

If full characterization of the grain boundaries intended (5 parameter analysis), grain boundary plane must be obtained. Serial sectioning is one the methods to obtain 3-dimensional characterization, hence, grain boundary plane [123]. In a simple view, serial sectioning is based on repeated loop of (i) 2-dimensional characterization and (ii) removal of certain thickness of the sample. Focused ion beam (FIB) is one the most often used tool, for removal of certain thickness even as small as 5 nm [123]. FIB is based on the interaction of accelerated ions and the atoms of a material [124]. On an elastic ion-atom collision, ions knock off the surface atoms [124]. This capability has been used extensively in materials science for sample preparation and micro-machining [124].

In a dual beam microscope which has the combined capabilities of a SEM and a FIB, it is possible to automatically apply the serial sectioning by FIB and 2-dimensional characterization by OIM-in-SEM. This technique is known as 3D-EBSD and successfully applied for characterization of grain boundaries misorientation and their plane [103, 125]

---

[1] The physical resolution is a parameter describing how far away from a large angle grain boundary, diffracted intensities stems from both crystals [113]. The effective resolution, depends on the physical resolution and indicates how accurately an orientation microscopy system can resolve a large angle grain boundary using software algorithms to deconvolute the overlapping patterns of the neighboring grains [113].

3.2 Grain Boundary Migration

The thermodynamically stable state of a pure metal, is a single crystal with definite number of vacancies (the number is a function of absolute temperature) [126]. Accordingly, polycrystalline materials, possessing other defects such as grain boundaries, triple lines, dislocations, etc., are thermodynamically less stable and at best meta-stable. However the kinetics of transformation is very often so slow that in practice polycrystalline pure metals are meta-stable at certain size. At sufficiently elevated temperatures when grain boundary migration is possible, grain growth occurs by migration in a direction to annihilate the grains with higher free energy [126]. A gradient of any thermodynamic variable, e.g. temperature, pressure, density of defects, density of energy, contents of impurity, etc., provides a driving force for grain boundary migration [104]. The driving force for grain boundary migration (P) has the dimension of energy per unit volume, which can be interpreted as pressure or equally a force acting per unit area on a grain boundary [104]. If the Gibbs energy of two neighboring grains per unit volume is different, the driving force for grain boundary migration is as follows [104]:

$$P = -\frac{dG}{dV} \tag{3.3}$$

Where, P is driving force for grain boundary migration; G, Gibbs energy; V, volume. In a simplistic model of migration which is based on the jumping of atoms across the grain boundary, the velocity of the grain boundary migration at $T \geq 0.3T_m$ is a linear function of the driving force [104]:

$$v = m.P \tag{3.4}$$

Where, v is velocity (migration rate) and m is mobility.

Three of the driving forces to study grain boundary migration are listed below [104]:

(i) An excess density of defects such as dislocations in one of the two neighboring grains. This can be seen in correspondence with recrystallization.

(ii) Pressure difference Δp on two sides of the grain boundary. The pressure difference stems from capillary forces on the two sides of a curved grain boundary (curvature driven migration).

$$\Delta p = \gamma \left(\frac{1}{R_1} + \frac{1}{R_2} \right) \tag{3.5}$$

where, γ is surface tension; R_1 and R_2 are the main radii of curvature of the neighboring grains.

(iii) Grain boundary in itself has an energy which enhances the total Gibbs energy of the system [126], thus, annihilation of the boundaries of higher energy is thermodynamically

favored.
In nano-crystalline materials, large portions of the poly-crystal are composed of grain boundaries, hence, there is a large driving force for annihilation of the grain boundaries by grain growth. Grain growth and thermal stability of nano-crystalline materials is discussed in further details below.

3.2.1 Thermal Stability of Nano-Crystalline Materials

In nano-crystalline materials a large fraction of atoms are at the inter-crystalline regions, i.e. grain boundaries, triple lines, and quadruple nodes. The inter-crystalline volume fraction of nano-crystalline materials is comparable to their crystalline volume fraction. This peculiarity is the main differentiates nano-crystalline materials and conventional polycrystalline or amorphous materials [127]. In nano-crystalline materials there is a large excess free energy associated with inter-crystalline component which make the material unstable [128]. Minimization of the Gibbs energy is the driving force for various transformations in such materials [31]. One of the most common transformations which takes place to reduce the inter-crystalline volume is grain growth. The driving force for grain growth (P) is given by the following equation [104]

$$P = \frac{2\gamma}{R} \tag{3.6}$$

where γ is grain boundary energy ($\approx 0.5 J/m^2$); R, is the grain boundary radius of curvature. When the average grain size is 10 nm (R=5 nm), the driving force is staggeringly large ($\approx 1 J/m^3$). Hence, there is a huge tendency for grain growth which may take place even at room temperature (self annealing) [30, 129]. Grain growth diminishes some of the desirable properties of nano-crystalline materials. Hence, thermal stability is of interest for industrial application of this type of materials and a prediction of the grain size over service time is necessary. The grain size at given time (t) can be calculated using the following equation [130]:

$$D^2 = D_0^2 + A\gamma t \tag{3.7}$$

where D is the mean grain size at time t; D_0 is the mean grain size at t=0; A is a constant. If grain growth occurs, it is acceptable to neglect the initial grain size, hence a simplified equation is obtained in which grain size would be a function of $\sqrt{t}$. In reality, ($D \propto t^{0.5}$), even for ultra-high purity metals is not valid and grain size is a function of t^n, in which $0.1 < n < 0.5$ [130].
Eq. 3.6 and Eq. 3.7 are simplistically describing the thermodynamics and the kinetics of

grain growth, respectively. Following those, stabilization of microstructure can be achieved by either (i) reducing the grain growth kinetics by decreasing the grain boundary mobility, or by (ii) reducing the thermodynamical tendency of grain growth by introducing certain metastable or stable compounds at the grain boundaries [17]. There are several mechanisms which affect grain growth like solute drag, pore/vacancy drag, second phase particle (Zener) drag, triple-line drag, and chemical ordering [131–134]. For pure nano-crystalline metals the effect of vacancy drag and triple-line drag on stabilization of the microstructure despite the large driving force for grain growth, has been discussed in [104, 132, 134]. In addition, impurities introduce solute drag on grain boundary migration, e.g. sulfur in nickel [135]. Alloying nickel with other elements very often increases the thermal stability of the material [31, 136, 137].

For instance, studies on Ni-P have shown that at lower temperatures solute drag is the dominant controlling factor to reduce the migration of grain boundaries while at higher temperatures, after formation of Ni_3P, Zener drag is the active controlling mechanism [138].

Grain boundary migration can also be inhibited by a decrease in grain boundary mobility and energy. The classic example of difference in grain boundary mobility is that: coherent $\Sigma3$ has very low mobility whereas incoherent $\Sigma3$ is very mobile boundary [139]. Thus, a material with high fraction of coherent $\Sigma3$ boundaries is expected to exhibit high thermal stability in comparison with a counterpart material in which most of the grain boundaries are general high angle boundaries. Segregation, especially in supersaturated nano-crystalline materials can influence the thermal stability as it influences the energy of the grain boundaries [140]. In nano-crystalline alloys, diffusion of particular solutes to grain boundaries may reduce the driving force for grain growth by reducing the grain boundary energy [141].

Studies of grain size, grain size distribution, grain boundary energy, and grain boundary mobility, all of are crucial in respect to grain growth investigations. More than that, careful study on texture evolution which may accompany grain growth provides better understanding about the growth mechanisms [142].

3.3 Grain Boundary Engineering

It is well-established that the properties of grain boundaries are not alike [107, 143]. Thus, increasing the fraction of grain boundaries which brings about improved properties at the expense of other boundaries, i.e. general high angle grain boundaries, is of high interest [144]. Accordingly, grain boundary engineering aims at deliberate manipulation of internal structure of polycrystalline materials to improve grain-boundary-controlled properties of poly-crystals [4, 5, 144, 145]. Some industrial applications have been emerged in 1990s showing that material properties (more precisely grain-boundary-controlled properties) such as corrosion, stress-corrosion cracking, creep, etc. were improved by increasing the fraction of 'special grain boundaries' [6].

A special boundary has been interpreted as a boundary with better properties than an average boundary, and very often low CSLs ($\Sigma \leq 29$) boundaries are referred to as special boundaries [107, 146]. In this definition only misorientation between the two neighboring grains is considered (3 parameters are needed to characterize a misorientation). The development of the OIM, equally known as electron backscattered diffraction (EBSD), provided the opportunity of easy characterization of the misorientation between the neighboring grains and defining special boundaries [147]. As grain boundary engineering has developed over time, it has been argued [12] that not all low CSLs have special properties, but coherent $\Sigma 3$ is the boundary with special properties. Coherency in its definition specifies the plane of the grain boundary, in addition to the misorientation between the two grains (5 parameters are needed to characterize a misorientation and the plane of a boundary). It is also shown [148] that the plane of the grain boundary plays a significant role in the properties of the boundary. Based on that, it has been proposed that special [149] grain boundary is defined as one that is terminated by at least one low-index plane. Using the 3-dimensional characterization techniques such as 3D-EBSD [125, 149] and diffraction contrast tomography (DCT) [150] it is possible to fully characterize the grain boundaries (5 parameter) [111]. However, technical difficulties that are associated with the 3D techniques have hindered wide application, consequently, 5 parameter characterization is still in its infancy. Accordingly, misorientation based definition of a special boundary is still the most common practice, but more emphasis has been put on $\Sigma 3^n$ boundaries rather than all low CSLs, in recent years [12].

Grain boundary engineered materials are not only those with high fraction of a $\Sigma 3^n$ boundaries but also with a broken networks (clusters) of general high angle grain boundaries. Grain boundary networks and the spatial arrangement of grain boundaries actually control boundary specific material behavior [144, 151]. In this respect, twinning has different roles in the processes to achieve such a grain boundary engineered microstructures, namely, to retain strain[2], generate $\Sigma 3$ boundaries, and finally to break up the general boundary network [12].

---

[2] in presumably strained material in thermo-mechanical treatment.

Hence, understanding the mechanism of (i) formation of twins and (ii) break up of network of general grain boundaries is of high importance in the the context of grain boundary engineering [144].

Formation of twins is discussed more, below.

3.3.1 Formation of Twins

Twins may form due to annealing [152–155], growth [21, 156, 157], and deformation [158–161]. While deformation twinning is beyond the scope of this dissertation, annealing twins and growth twins are discussed here.

3.3.1.1 Annealing Twins

Twining may occur during the grain growth [162] and it may be crucial on the microstructure evolution duo to grain growth. For instance, it is shown that by multiple twining the change of texture takes place [32, 163]. Furthermore, by formation of annealing twins, special boundaries fraction enhances [12]. Hence it is of high importance to study the formation of annealing twins.

Different mechanisms have been proposed to explain this process. Fullman and Fisher have related the formation of annealing twins to a decrease in the total Gibbs energy of the system [152]. They have proposed that the presence of annealing twins corresponds to a lower total interfacial free energy than would apply in absence of the twins [152]. In other words, they have concluded that due to migration of grain boundaries the annealing twin boundaries form whenever a decrease in the over-all interfacial free energy would result [152]. Gleiter proposed an atomic scale model, in which the movement of atoms across the boundary during grain boundary migration occurs in a faulty manner in terms of atomic packing [153, 164]. Faulty adherence of atoms from a shrinking grain, which often starts at a triple junction, brings about nucleation of an annealing twin which grows out over the entire grain [164]. Accordingly, a migrating general high-angle boundary divides into a $\Sigma3$ boundary and another general high-angle boundary of a different character [153, 164]. The models proposed by Fullman and Fisher, and Gleiter belong to the so-called 'growth accident' mechanisms [155]. Meyers and Murr proposed a 'pop-out' mechanism for twin formation, which contrary to the previous models, does not require any grain boundary migration for the initiation (nucleation) of the annealing twins [154]. Their model was based on a two stage process: initiation and propagation. They argued that initiation is due to one of the following circumstances: (i) two adjacent grains are at twin orientation, but the boundary plane is not closed-packed; in that case the boundary decomposes to a coherent and an incoherent boundary. (ii) two adjacent grains can form a lower energy boundary (lower than a general boundary); propagation of the twin nucleus is accomplished by the migration of the non-coherent boundary into the grain. They suggested that initiation sites for annealing twins are grain-boundary ledges and the annealing twin density increases with ledge density [154]. Later, Mahajan et al. proposed a unified mechanism which included different aspects of 'pop-out' and 'growth accident' mechanisms [155]. In this model, it is suggested that migrating grain boundaries possess $\{111\}$ steps and due to their migration, Shockley partial loops nucleate on consecutive $\{111\}$ planes by growth accidents. The higher velocity of the migrating grain boundary increases the probability of growth accidents [155]. Lateral growth of the faults occurs due to a repulsion between Shockley partials constituting the twin boundary [155]. It is argued that, high stacking fault energy materials do not form annealing twins because stacking fault, which separate the Shockley partials, are energetically unfavorable. The correlation between the deformation level and twin density has been attributed to the formation of additional $\{111\}$ steps on grain boundaries due to their interaction with slip dislocations [155].

It is argued that evolution of grain boundary distribution of all statically recrystallized FCC materials with low-medium stacking fault energy which is mainly consist of $\Sigma3^n$ boundaries, is due to multiple annealing twins [165]. It is also pointed out that $\Sigma3$ boundaries are the only energetically favorable boundaries, and all other $\Sigma3^n$ $(n \leq 2)$ are geometrically necessary for providing connections between $\Sigma3$ boundaries in the process of multiple twinning [12, 165].

Several parameters influence the annealing twin frequency during grain growth: grain size, temperature and time of annealing, velocity of grain boundary migration, grain boundary energy, twin boundary energy, texture, inclusions, etc. [166]. Thus, formation of annealing twins and multiple twinning influences $\Sigma3^n$ boundaries and grain boundary network, however, it is a very complex process.

3.3.1.2 Growth Twins

Growth twins form during the synthesis of materials in a bottom-up process such as electrodeposition and sputtering [25, 38]. Despite the enthusiasm on synthesis of materials possessing growth twins [21], the formation mechanisms of different types of growth twins are not strongly addressed yet and the existing information is scattered. Some of the factors influencing formation of growth twins especially during electrodeposition are pointed out in the following.

Twinned Nuclei

Twinning is a result of faults in the mono-layer arrangement of the crystal, and it can be seen in all stages of microstructure formation: nucleation, coalescence, crystal growth and grain growth [167]. Three different conditions can be imagined for a twinned nucleus: (i) Nucleus is twinned when it is formed; (ii) two perfect nuclei grow laterally and meet each other in twinned position; (iii) a perfect nuclei forms on a crystallographic plane, such that nucleus and the plane be in twin relation. All of the three proposed conditions have been argued to take place in electrodeposition. Type (i) and (ii) are suspected to be active in <211> oriented grains parallel to the deposition direction [157, 168] and type (iii) in <111> oriented grains [169].

Inclusion of Organic Molecules

On electrodeposition, organic molecules (additives) are routinely added to the electrolyte to influence the deposit properties [44]. Additives may entrap and, hence, be incorporated in the stacking sequence of {111} planes. This leads to a higher probability of growth twin formation [170, 171]. Wang studied the effect of very large additives in nickel electrodeposition and reported the formation of significant amounts of stacking faults and twins [171]. Since the twins were formed within the nickel matrix with a size comparable to additive size it was concluded that the additive molecule was embedded in the matrix and responsible for pronounced defect formation [171].

Stacking Fault Energy

Two-dimensional atom layers on certain crystal planes such as {111} of FCC metals are frequently nucleated in a twin orientation [172]. De Cusminsky studied electrodeposition of silver, copper and nickel and correlated the starting current density of twin formation with stacking fault energy [173]. He showed that FCC metals of lower stacking fault energy, require a lower current density in order to exhibit a twinned microstructure [173]. Using a sputtering technique, it has been found that low stacking fault energy material such as copper and stainless-steel high density of extremely fine twins (10nm in width) can be synthesized, in contrast with high stacking fault energy materials such as aluminum [25]. It has been reported that the twin density in electrodeposited Ni-Mn and Ni-Co is much higher than their pure nickel counterparts [174, 175]. It was postulated that a decrease in stacking fault energy by addition of alloying elements promotes twin formation [174–176]. In conclusion, a lower stacking fault energy brings about less energy penalty on fault stacking of atoms thus lower stacking fault energy increase the chance of formation of growth twins. It is worth reminding that, since stacking fault energy (γ_{sf}) and twin boundary energy (γ_t) have approximately the same value [110] they are often used, though incorrectly, interchangeably.

Stress Relaxation

Residual stress in electrodeposited materials and stress relaxation during and after electrodeposition are of significant importance. There are four classes of theories account for residual stresses in the electrodeposits [177, 178]: (a) plastic deformation during the deposition due to inclusions or differences in local temperature, (b) evolution of hydrogen entrapped during electrodeposition, (c) formation and occlusion of compounds and their subsequent reduction, (d) dislocations due to growth accidents. It has been argued that a strong inhibition brings about substantial hydrogen evolution reaction during electrodeposition which results in internal stress [77]. The correlation between stresses and twin formation has been addressed in different ways. For instance it has been argued that high internal stresses during electrodeposition may exceed the yield stress and some twins in electrodeposits can be of deformation-induced type rather than of growth type [170]. Hall and Fawzi studied <110> textured electrodeposited nickel and reported the presence of pairs of secondary twins at the boundaries and suggested that this has to be caused by stresses at the boundaries [179]. Tomov et al. postulated that the stress field generated by dislocations and foreign atoms may be relieved by the formation of twins [167]. Similarly, Liu and Wang suggested that the twin formation is energetically favorable since redistribution of stress occurs such that the whole system energy decreases [180].
Pulsed electrodeposition is known to be a method to increase twin density in electrodeposited materials [21, 181] and is also known as a method to decrease internal stresses [182]. It is postulated that during off-time of electrodeposition, stress relief and recrystallization may occur [183]. Xu et al. used computer modeling to study pulse-electrodeposited nanotwinned copper and argued that by applying a high current density at the peak of on-time, many nuclei form and the surface energy of the boundaries is reduced by coalescence of nuclei but it builds up stresses [184]. When the stress is higher than a certain value for a particular type of planes, a twinned structure becomes more energetically favorable than strained one [184].

Orientation Change

It has been shown that there is a correlation between the change in preferred orientation and the twinning process in the electrodeposited material, when then substrate influenced orientation is different from what electrodeposition conditions govern [82]. Setty and Wilman studied electrodeposition of silver and proposed formation of 4 possible layers, across an electrodeposited coat as follows (i) the initial deposition follows the orientation of the substrate (epitaxy) (ii) a layer twinned (iii) a layer of randomly orientated crystals (iv) a layer of crystals develops having a preferred orientation characteristic of the bath conditions [185]. For instance, in case of electrodeposition of nickel when a <211> fiber texture is favored on a (100) oriented copper single crystal, repeated twinning facilitates the achievement of a new orientation axis which has indices close to the <211> indices [82]. The change of texture might be as follows $<100> \rightarrow <221>_{T1} \rightarrow <744>_{T2} \approx <211>$.

Phase Transformation

Nakahara and Mahajan studied electrodeposition of cobalt at low pH (1.6) and reported highly faulted FCC cobalt with some regions of HCP cobalt [186]. They suggested that during the cobalt electrodeposition at low pH, metastable FCC cobalt hydride forms due to codeposition of atomic hydrogen. During and after the electrodeposition, the rapid diffusion of atomic hydrogen causes the FCC hydride phase to decompose and partially transform to HCP cobalt. This transformation involves the formation of faults on {111} planes [186].

Multiple Twinning & Five-fold Symmetry

There are several reports on a special kind of twinning of electrodeposited material showing a five-fold symmetry [75, 179, 187]. Five twins which occur on {111} planes make the five-fold symmetry, and very often there are secondary twins in addition to this five primary twins [179, 187], Figure 3.5. Hall and Fawzi reported that the density of these twins is altering with thickness such that there is maximum density at certain thickness [179]. This eliminates the idea that these twins originate from five-fold symmetry nuclei. In addition, accepting nucleation-originated mechanism imposes presence of all five {111} planes at the same time; this is contrary to what has been observed experimentally, where in many occasions not all five twins are present. Accordingly repeated twinning is suggested as the mechanism of formation of this type of twins [179]. This mechanism is shown schematically in Figure 3.6, in which simple five-fold symmetry develops.

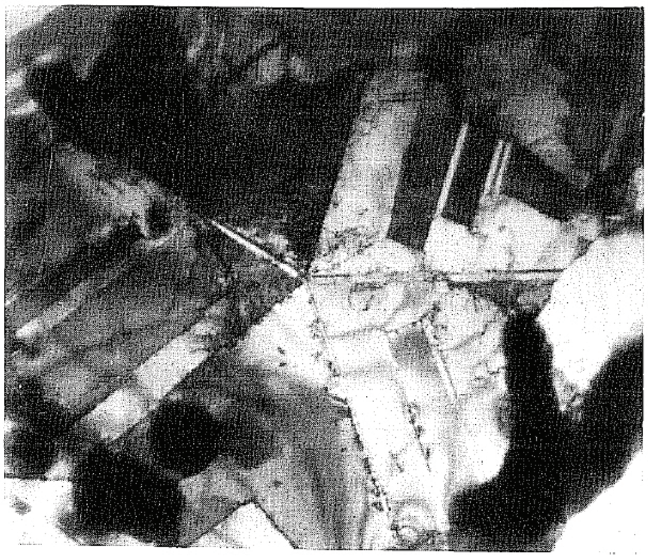

Figure 3.5: Five-fold symmetry in electrodeposited nickel.[179]).

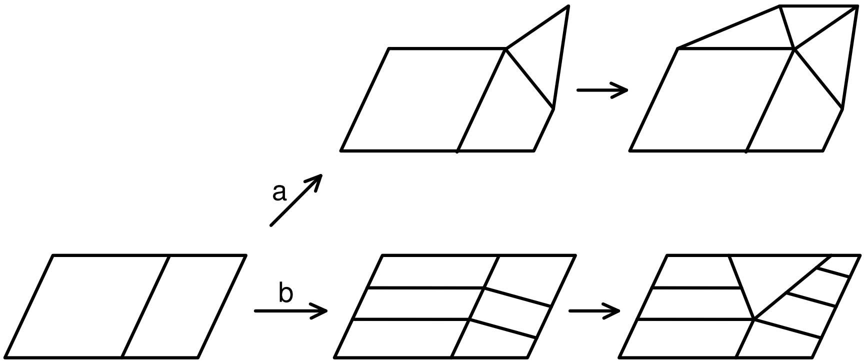

Figure 3.6: (a) Simple mechanism for formation of five-fold symmetry by repeated twinning. (b) Formation of multiple twinned cluster possessing five-fold symmetry [179]).

3.3.2 Grain Boundary Network

The importance of connectivity of general high-angle grain boundaries has been pointed out by different authors [5, 144, 188, 189] owing to the fact that propagating inter-granular cracks arrest at triple junctions coordinated by two special boundaries [190]. Thus, breaking the network of general grain boundaries to separated clusters, provides microstructural improvement in grain-boundary-controlled properties. Analysis of commercial grain boundary engineered materials has shown that there is a significant decrease (at least an order of magnitude) in the size of general grain boundary clusters [144].

It is already mentioned that $\Sigma3$ boundaries are actually the boundaries which very often have more desirable properties than all other CSLs and general high angle grain boundaries [12, 165]. Experimentally different spatial arrangements of the $\Sigma3$ boundaries have been reported [111]. In Figure 3.7, the topology of $\Sigma3$ in two microstructures formed due to simple twinning and multiple twinning is shown [111]. In simple twinning, there is back-and-forth twinning on parallel $\{111\}$ planes, hence, there is no intersection of the $\Sigma3$ boundaries, thus, all the triple junctions are general-general-$\Sigma3$. In this case, $\Sigma3$ has negligible effect on breaking the grain boundary network connectivity [111]. In contrast, in multiple twinning, twinning does not take place on parallel $\{111\}$ planes, but on different $\{111\}$ planes, e.g. $(\bar{1}11)$ $(\bar{1}\bar{1}1)$. This type of twinning plays a decisive role in breaking up the larger scale general boundary clusters [111]. Formation of triple junctions $\Sigma3$-$\Sigma3$-$\Sigma9$ and $\Sigma3$-$\Sigma9$-$\Sigma27$ is evident in multiple twining in Figure 3.7. Formation of the former is more probable than the latter and the importance of increase of the $\Sigma3$-$\Sigma3$-$\Sigma9$ triple junction to achieve so-called ‘twin-limited microstructure’[3] and hence, improved grain-boundary-controlled properties have been addressed in the literature [11, 191–193].

It has been pointed out that multiple twining is the mechanism that brings about such

---

[3] If every triple junction in the microstructure is composed of two $\Sigma3$ and a $\Sigma9$ the microstructure is called twin-limited microstructure [12].

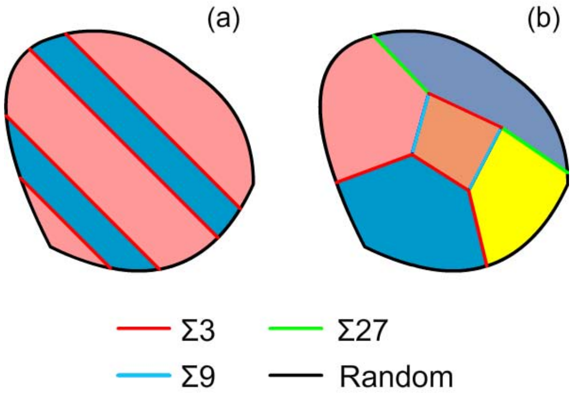

Figure 3.7: (a) Simple twinning, back-and-forth twinning on parallel {111} planes. (b) multiple twinning twinning on different {111} planes (depicted from [144]).

a connectivity between the $\Sigma3$ boundaries [189]. One of the mechanisms proposed for explanation of multiple twining is so-called '$\Sigma3$ regeneration model'. This mechanism is governed by interaction of $\Sigma3$ boundaries, following the rule for the joining or dissociation of CSL boundaries [193]:

$$\Sigma A + \Sigma B \longleftrightarrow \Sigma(A \times B) \qquad \text{or} \qquad \Sigma A + \Sigma B \longleftrightarrow \Sigma(A/B) \tag{3.8}$$

where A/B is an integer.

Thus, when two $\Sigma3$ boundaries interact, a $\Sigma1$ or $\Sigma9$ boundary forms. And similarly interaction of a $\Sigma3$ and $\Sigma9$ boundary bring about formation of a $\Sigma3$ or a $\Sigma27$ boundary. Experimentally, it has been shown that formation of $\Sigma3$ is more probable than the $\Sigma27$ [193]. Following similar argument interaction of a $\Sigma9$ and a $\Sigma27$ results in formation of a $\Sigma3$ boundary. It is shown [12] that, due to migration of the boundaries and interaction between those, $\Sigma3$-$\Sigma3$-$\Sigma9$ triple junction forms and connectivity of general high-angle grain boundaries is broken . Of significant importance, by interaction of $\Sigma3_{coherent}$, $\Sigma3_{incoherent}$ forms, which is a highly mobile boundary [139]. This assures further migration, interaction, and fragmentation of general high angle grain boundaries network.

3.3.3 Less-Explored Potentials of Grain Boundary Engineering

Thermo-mechanical treatment of low-medium stacking fault energy FCC materials is the main method to produce grain boundary engineered materials [8, 12, 145, 194–196]. However, "In our understanding GBE comprises all aspects which determine the choice of physical, chemical, thermal and mechanical treatments of a material to obtain a polycrystal with a desired distribution of interfacial characteristics, i.e., grain boundaries and their junctions with specific properties" [197]. Accordingly, in recent years,two different aspects

beyond that tradition of thermo-mechanical treatment of FCC metals has been explored:
(i) processes other than thermo-mechanical treatment , e.g. grain growth of nano-crystalline materials [30].
(ii) focusing on microstructural features other than grain boundary such as triple junctions [198].
In the previous sections of this chapter, triple junction importance is partly mentioned in thermal stability of nano-crystalline materials and fragmentation of general high angle grain boundary networks. It is noteworthy that even the term ‘grain boundary junction engineering’ is started to be used which shows the emphasis on the importance of triple junctions on some materials properties [198].

Chapter 4

Materials and Methods

This chapter is composed of three sections. In the first section, material synthesis by electrodeposition and thermal treatment of some of the selected materials are described. The second section is dedicated to sample preparation for microscopic techniques. And the last section, provides the details of different microstructural characterization methods.

4.1 Material Synthesis

4.1.1 Electrodeposition Procedure

Substrate Preparation

Pure copper sheet with a thickness of 1 mm was used to prepare the substrates for electrodeposition. Copper sheet was cut to pieces of 5×6 cm^2 in size and each was cleaned with acetone. In order to assure removal of all organic residues from the surface, the copper pieces were cathodically electrocleaned in an electrolyte of the following composition: 16.25 g/dm^3 NaCN, 16.25 g/dm^3 Na_2CO_3, and 54.16 g/dm^3 NaOH. The electrocleaning was applied potentiostatically at 5 V for 5 min using a stainless steel sheet as anode. After electrocleaning, the copper pieces were dried with cold air blow. Then the back side and the top of it were covered with a tape which was resistant to the chemicals in the used electrolytes. The non-covered area of the copper piece was measured and the current needed to achieve intended current density was calculated accordingly. The copper pieces were electrocleaned again for 30 sec, rinsed with distilled water and activated in an acidic solution. The composition of the solution was 50 g/dm^3 $NaHF_2$ and 50 g/dm^3 $NaHSO_4$. Then the copper pieces were coated with an extremely thin layer of palladium[1] by few seconds immersion in the following solution: 10 wt% NaCl, 4 wt% HCl,

---

[1] Palladium layer is required to facilitate the electroless deposition of Ni-P.

and 0.154 wt% $PdCl_2$. An X-ray amorphous Ni-P layer was coated afterwards from a commercially available electrolyte 'NIPOSIT™ 65R' for 80 min ($\approx 10\ \mu m$ in thickness). Ni-P auto-catalytic deposition was achieved at $\approx 92°C$. Finally the copper pieces coated with Ni-P layer (substrate) were cleaned with distilled water and immediately immersed in the nickel electrodeposition electrolyte.

Electrolyte Preparation and Electrodeposition Set-Up
Watts electrolytes with or without additive were utilized for synthesis of all samples. Thus, all the electrolytes had the following base composition in common: 300 g/dm^3 $NiSO_4 \cdot 7\,H_2O$ and 35 g/dm^3 $NiCl_2 \cdot 6\,H_2O$, and H_3BO_3. The concentration of H_3BO_3 was different for different series of experiments (see the details in section 4.1.3).
A 2 dm^3 glass beaker was served as the container for the 1.5 dm^3 electrolyte. In order to avoid evaporation of the electrolyte, a lid was placed on top of the beaker.
Before starting electrodeposition, the electrolyte's temperature was increased to $50°C$ and kept constant during the process. The electrolyte was agitated by a magnetic stirrer before and during the electrodeposition. The pH of the electrolyte was adjusted to the intended value,ranging from 2.0 to 5.5 (see the details in section 4.1.3), by addition of sulfuric acid or ammonia. All the samples were electrodeposited at constant current density using a rectifier. Nickel rounds in a titanium basket were used as anode. The intended current was checked before the actual electrodeposition on a dummy nickel piece for 2 min to assure stability of the process. For all series of experiments, the time for electrodeposition was chosen in relation with current density, such that equal charge transfer was achieved for all samples (current density×time = constant).

4.1.2 Thermal Treatment

As-deposited samples were cut into small pieces of 1× 0.5 cm in size and subjected to thermal treatment for 30 min at 4 different temperatures in the range $150 - 600°C$. At 150 and $200°C$ a furnace operating with air was used and at 400 and $600°C$ the furnace chamber was filled with argon. The thermally treated samples are named with a postfix of temperature to the as-deposited sample name. For instance, Y-150 is referring to the sample Y which is thermally treated at $150°C$.

4.1.3 Detailed Sample Synthesis Description

4.1.3.1 F-Series Samples

Electrodeposition of F-series samples were carried out in an electrolytes with 40 g/dm^3 H_3BO_3 and pH of 4.5. The electrolyte was used either without any organic additive or after addition of 5 $mMol/dm^3$ and 10 $mMol/dm^3$ 2-butyne-1,4-diol (hereafter BDO) to the electrolyte. For each of the mentioned electrolytes, samples were electrodeposited at three different levels of current density: $2A/dm^2$, $5A/dm^2$ and $10A/dm^2$. Thus 9 different samples were synthesized. F-series as-deposited sample names are listed in Table 4.1.
These 9 samples were thermally treated at 4 different temperatures, as explained in section 4.1.2, thus, 45 samples all together belong to this series of experiments.

Table 4.1: F-series as-deposited samples names in relation with applied current density (i) [A/dm^2] and concentration of 2-butyne-1,4-diol (BDO) [$mMol/dm^3$] in the electrolyte.

	$i = 2$	$i = 5$	$i = 10$
$BDO = 10$	F9	F8	F7
$BDO = 5$	F4	F5	F6
$BDO = 0$	F1	F2	F3

4.1.3.2 BipH-Series Samples

Eleven samples with different levels of H_3BO_3 (40, 50 and 60 g/dm^3) added to the base composition mentioned in section 4.1.1, current density (1 and 2 A/dm^2), and pH (4.5, 5 and 5.5) were synthesized in BipH-series samples ('B' is for Boric acid, 'i' is for current density and 'pH' is for pH). Sample names are 5 digit numbers in which the first two reflect H_3BO_3 concentration in [g/dm^3], 3^{rd} digit is current density, and the last two are pH×10. Synthesized sample names are listed in Table 4.2.
Note that the sample 40245 is identical to sample F1 in F-series samples.

Table 4.2: BipH-series as-deposited sample name in relation with concentration of H_3BO_3, applied current density (i), and pH of the electrolyte.

	$C_{H_3BO_3}$: 40 g/dm^3	$C_{H_3BO_3}$: 50 g/dm^3		$C_{H_3BO_3}$: 60 g/dm^3
	i=2 A/dm^2	i=1 A/dm^2	i=2 A/dm^2	i=2 A/dm^2
pH=4.5	40245	50145	50245	–
pH=5.0	40250	50150	50250	60250
pH=5.5	40255	50155	50255	60255

4.1.3.3 Co-Series Samples

Electrodeposition of Co-series samples was carried out in an electrolyte with 40 g/dm^3 H_3BO_3 added to the base composition mentioned in section 4.1.1 and pH of 4.5. Current density of $2A/dm^2$ was applied for electrodeposition. In two different electrolytes, Co^{2+} in concentration of 20 and 40 $mMol/dm^3$ was added, and the samples were named Co20 and Co40, respectively. In order to avoid alteration of electrolyte chemistry $CoSO_4 \cdot 7\,H_2O$ was used as the source of Co^{2+}.

4.1.3.4 Sample 8C10

Electrodeposition of sample 8C10 was carried out in an electrolyte with 40 g/dm^3 H_3BO_3 added to the base composition mentioned in section 4.1.1 and pH of 2.0. Current density of $10A/dm^2$ was applied for electrodeposition of this sample. Four more samples were obtained after thermal treatment of sample 8C10 at 150, 200, 400, and $600°C$, as explain in section 4.1.2.

4.2 Sample Preparation for Microscopic Analysis

In order to investigate the samples by electron/ion microscopy either on the film cross-section or as top view, samples were prepared by means of mechanical grinding and polishing and subsequent FIB milling.
The details of sample preparation procedure are provided below.

4.2.1 Preparation of Cross-Sections

4.2.1.1 Mechanical Grinding and Polishing

Cross-sectional sample preparation was started with sampling of a small piece (1×0.5 cm) via abrasive cutting (thermally treated samples had been cut earlier). Samples were clamped between two brass plates with an aluminum foil protecting the film surface as schematically shown in Figure A.1. The sample and its holder were subjected to preparation by means of manual grinding on SiC papers up to grade 4000. Mechanical polishing was performed afterwards, for several minutes on a soft synthetic fiber polishing cloth (NAP, Struers) with diamond paste of 1 μm and lubricant Blue (Struers). Final mechanical/chemical polishing was conducted with 0.04 μm colloidal silica (OP-S, Struers) on a chemically resistant synthetic fiber polishing cloth (OP-Chem, Struers) to achieve a scratch free area. Then the sample was taken out of the holder, ultrasonically cleaned in ethanol for 5 min, and dried in pressurized air.

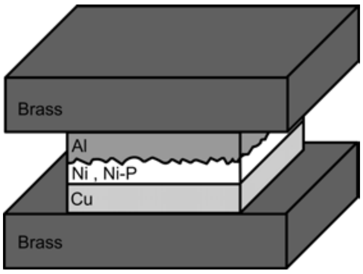

Figure 4.1: Schematic sample and sample holder configuration for cross-sectional sample preparation by mechanical grinding and polishing. 'Al' represents aluminum foil which was used for protection of film surface.

4.2.1.2 FIB Milling

The sample was mounted on a 36° pre-tilt SEM sample holder, Figure 4.2, and then put for further preparation in a dual beam FIB-SEM, Helios Nanolab™ 600 from FEI. In this microscope there is a 52° angle between electron beam (E-beam) and ion beam (I-beam) and the eucentric point is ≈ 4 mm below the electron column pole piece. Thus, in order to make the ion beam parallel to the sample cross section, 16° tilt of the stage was applied; and a working distance of 4 mm was used to benefit from simultaneous SEM imaging and FIB milling. This is shown in Figure 4.3a. A protective platinum layer (≈ 1 μm thick) was deposited on top of the site of interest to avoid curtaining. Then FIB milling was applied by Ga^+ ions of energy of 30 keV in a two step process: First, ≈ 750 nm was removed at a current of 2.8 nA (rough milling); Second ≈ 50 nm or more was removed at a current of 0.46 nA (gentle milling). It is noteworthy that the damaged layer for silicon after FIB milling by 30 keV Ga^+ ions with incident angle close to 90°, is below $10 - -30$ nm [199]. Since silicon has thicker damaged layer in comparison with FCC metals such as copper [199], 50 nm gentle milling secures the removal of the damaged layer

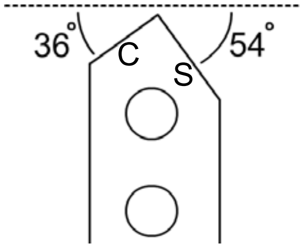

Figure 4.2: Schematic representation of pre-tilt SEM sample holder. 'C' and 'S' depict where samples were placed for cross-sectional and surface analysis, respectively.

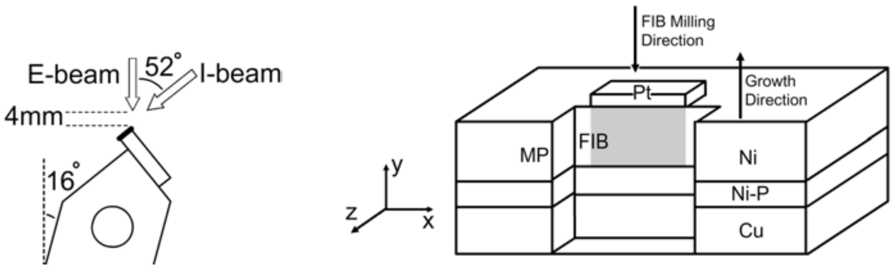

(a) (b)

Figure 4.3: (a) Schematic representation of the geometry for FIB milling. At 16° stage tilt, cross-section depicted by thicker black line is parallel to ion-beam. (b) Schematic representation of geometry of fully prepared cross-section; Site of interest is shown in gray. The location subjected to FIB milling is shown by 'FIB' and the rest of area which was treated to the end of mechanical polishing is marked by 'MP'.

induced by rough milling. As mentioned, FIB milling potentially alters the microstructure and it is of high importance to assure alteration of microstructure does not occur due to sample preparation. To assure the authenticity of the results, different sample preparation routines i.e. mechanical polishing, electropolishing and various FIB milling were examined and compared (see Appendix A). This is clearly documented in Appendix A that using the described procedure above, the alteration of microstructure is minimal, hence, smooth and artifact free area was prepared in this way.
The geometry of q fully prepared sample is schematically shown in Figure 4.3b.

4.2.2 Top View Preparation

As the small pieces of samples were obtained by abrasive cutting, there was a large deformed area at the edge of the pieces. Since FIB milling is only applicable to the vicinity of the samples edges, this fairly large deformed layer must be removed first. To achieve it, a cross section was prepared to the end of mechanical polishing as explained in section 4.2.1.2. This ensures removal of the deformed layer introduced by abrasive cutting. Then the sample was placed on a 54° pre-tilt SEM sample holder, and put in the microscope. By a 16° stage tilt, the film surface was brought parallel to the ion beam, Figure 4.4a. A protective platinum layer was deposited on to the cross section and the surface topography of the sample was removed by FIB milling (Ga^+ ions of energy of 30 keV and current of 0.46 nA) in the -z direction of the sample, Figure 4.4b. In this manner, a smooth and artifact free area for analysis of the film surface (top view) was prepared.

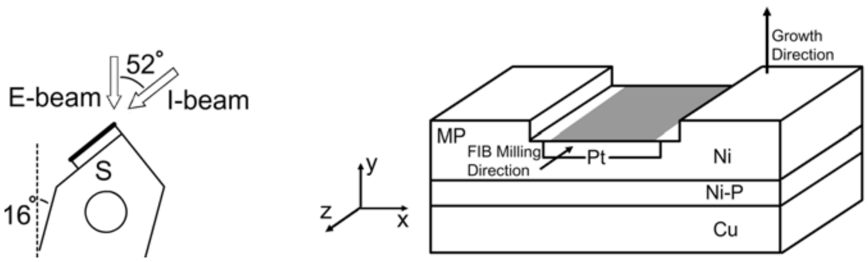

(a) (b)

Figure 4.4: (a) Schematic representation of the geometry for FIB milling. At 16° stage tilt, the surface is depicted by thicker black line is parallel to ion-beam. (b) Schematic representation of geometry of fully prepared film surface; Site of interest is shown in gray.

4.3 Microstructure Characterization

4.3.1 XRD Measurements and Data Processing

Samples were characterized by means of XRD by a Bruker AXS - D8 Discover X-ray diffractometer, using $Cu-K_\alpha$ radiation. The diffractometer was equipped with an Eulerian cradle.

4.3.1.1 Quantitative Texture Analysis

For quantitative texture analysis pole figures of 111, 200 and 220 reflections were measured using the following optics: The primary beam was collimated by a circular collimator of opening 1 mm and a vertical 6.0 mm receiving slit was used for the diffracted beam. Pole figure measurement was conducted by recording diffracted intensities at continuous rotation around the sample normal direction (ND), $0^\circ \leq \phi \leq 360^\circ$, for sample tilts, $0^\circ \leq \chi \leq 75^\circ$ (at an interval of 5°). By integrating intensity over each 5° interval of ϕ, pole figures on a $5^\circ \times 5^\circ$ grid were obtained. Pole figures were also measured for standard nickel powder in an identical set-up and used for defocusing correction [200]. For background correction, intensities at both sides of the Bragg angle of the investigating were measured too.
TexEval software (Bruker AXS) which accompanies the diffractometer system was used for data analysis. The orientation distribution function (ODF) was calculated for cubic crystal symmetry and triclinic sample symmetry. Based on the ODF inverse pole figures in ND and two arbitrary directions perpendicular to that (RD and TD) were obtained [200]. All the studied samples had a rotational symmetry with respect to ND. This means that samples had a fiber texture with the fiber axis <uvw> parallel to the sample's normal direction. Full texture representation of fiber textured samples requires only one inverse pole figure in the direction of the fiber axis. Accordingly maximum orientation density in

fiber axis direction (ND) is used as for identification of the fiber axis and a measure for the texture strength.

4.3.1.2 Line Profile Analysis

XRD line profile analysis was applied for microstructural characterization. It is based on the fact that broadening of diffraction peaks is caused by instrumental effectsand more importantly, physical effects due to structural imperfections in the material [201]. Two major contributors to physical contribution of peak broadening are finite crystallite size and micro-strain [201]. It is worth clarifying that crystallite size (or grain size used in later chapters) is referring to the domains coherently diffracting the incident X-rays. Eight line profiles (111, 200, 220, 311, 222, 400, 331 and 420) applying a step size of 0.02° in 2θ were measured. The following optics was used for the primary beam: 0.2 mm vertical slit, and a horizontal Soller slit and for the diffracted beam: vertical scatter slit of 0.6 mm, horizontal Soller slit, and vertical receiving slit of 0.1 mm. Standard Si powder was also measured in the same set-up and used for obtaining the instrumental contribution of peak broadening.

After the measurements, data processing was applied by home written MATLAB® scripts. First, to eliminate $Cu-K_{\alpha2}$ of the measured $Cu-K_{\alpha}$ doublet, two pseudo-Voigt functions were fitted to the measured line profile. Pseudo-Voigt function, which combines Gaussian and Lorentzian functions linearly, fits line profiles very well and its mathematical definition is as follows:

$$pV(2\theta) = I_0\big[\eta L(2\theta) + (1-\eta)G(2\theta)\big] \tag{4.1}$$

where η is the mixing term (Lorentz factor); and L, G and pV represent Lorentz, Gaussian and pseudo-Voigt functions respectively. Of two fitted pseudo-Voigt functions, the function corresponding to $Cu - K_{\alpha1}(\lambda = 0.1540562$ nm) was studied further. Position ($2\theta_P$), maximum peak intensity (I_0), integrated intensity (I), Lorentz coefficient (η), and full width at half maximum intensity (2H) of all reflections were obtained. Integral breadth, β[2], was calculated based on the obtained results. Using only well-fitted reflections (see Figure 4.5) and either applying single line analysis [202], or the Williamson-Hall method [203]; physical broadening was evaluated in terms of crystallite size and micro-strain. The details of these methods is provided below:

Single Line Analysis:

The integral breadths of Gaussian and Lorentzian components (β_G^h and β_C^h) of the fitted

---

[2] β is the width of a rectangle having the same area, A, and height as the studied line profile, ($\beta = I_0/A$).

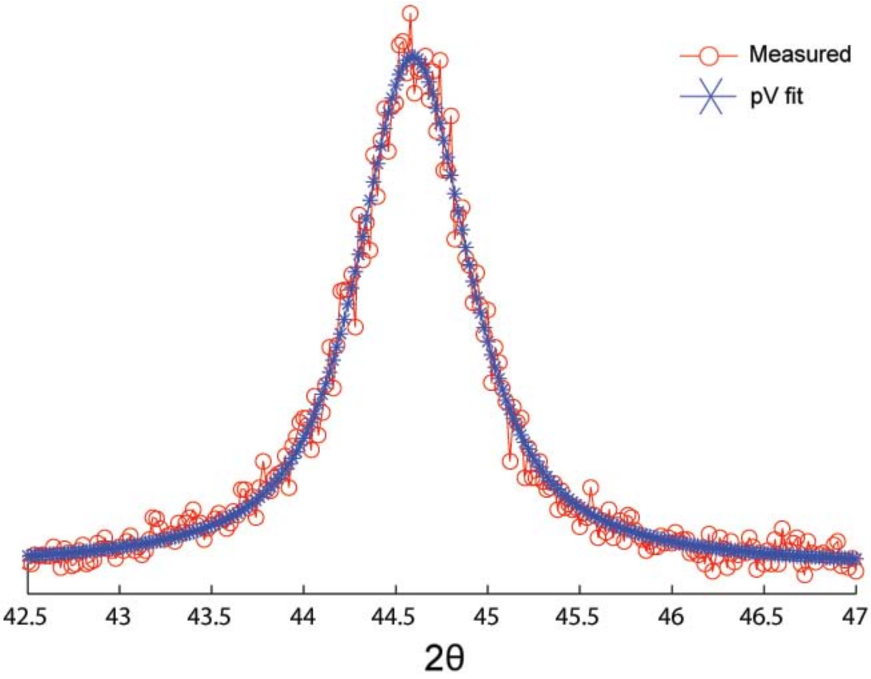

(a)

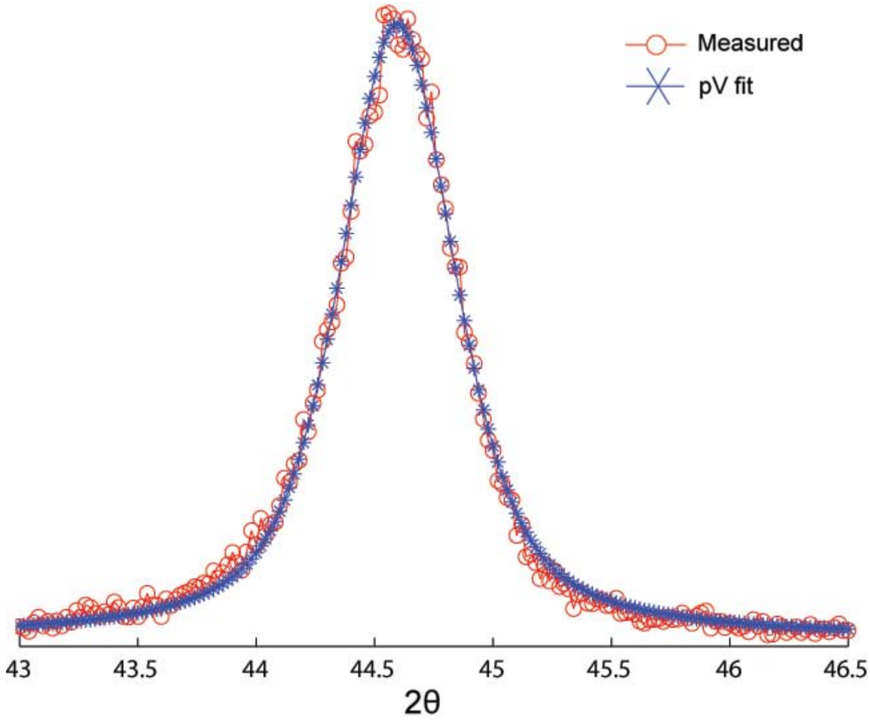

(b)

Figure 4.5: The measured 111 peak profile and the fitted pseudo-Voigt function to the measured data for (a) sample F9-150 and (b) F9-200.

pseudo-Voigt function were obtained from following equations:

$$\beta_C^h/\beta = a_0 + a_1\phi + a_2\phi^2 \tag{4.2}$$

$$\beta_G^h/\beta = b_0 + b_{12}\big(\phi - \frac{2}{\pi}\big)^{1/2} + b_1\phi + b_2\phi^2 \tag{4.3}$$

Where $\phi = 2H/\beta$, $a_0 = 2.0207$, $a_1 = -0.4803$, $a_2 = -1.7756$, $b_0 = 0.6420$, $b_{12} = 1.4187$, $b_1 = -2.2043$ and $b_2 = 1.8706$ [202].
Similarly, integral breadth of Gaussian and Lorentzian components of instrumental broadening were calculated based on a standard Si powder measurement (β_G^g and β_C^g). For nickel $2\theta_{111} = 44.5°$ and $2\theta_{200} = 51.85°$, and 220 reflection of Si standard powder ($2\theta = 47.3°$) was used for calculation of instrumental broadening. Accordingly integral breadth of Lorentzian and Gaussian constituents of the physical broadening (β_C^f and β_G^f) were obtained by the following equations:

$$\beta_C^f = \beta_C^h - \beta_C^g \text{ and } (\beta_G^f)^2 = (\beta_G^h)^2 - (\beta_G^g)^2 \tag{4.4}$$

In single line analysis it is assumed that the Lorentzian component of physical broadening is solely due to finite crystallite size and Gaussian component originates from micro-strain [202]. Accordingly, the crystallite size and micro-strain were estimated using Equ. 4.5 and 4.6.

$$D = K\lambda/\beta_C^f \cos(\theta_p) \tag{4.5}$$

Where D is volume averaged size in the diffraction vector direction.

$$\tilde{e} = \beta_G^f/4\tan(\theta_p) \tag{4.6}$$

Where $\tilde{e}$ is a measure for micro-strain [202].

Williamson-Hall method:
The breadth of reciprocal lattice points $\beta^*(= \beta\cos(\theta_p)/\lambda)$ against their distance from the origin $d^*(= 1/d = 2\sin(\theta_p)/\lambda)$ were plotted for all the reflections [203]. Linear regression of all the points in the plot was applied and the y-axis intercept and the slope of the linear model was obtained (Figure 4.6). The mean apparent volume-weighted size ($<\text{D}>_v$) and micro-strain (ϵ) was calculated, according to Equ. 4.7 [203].

$$\beta_f^* = 1/ < D >_v +2 < \epsilon > d^* \tag{4.7}$$

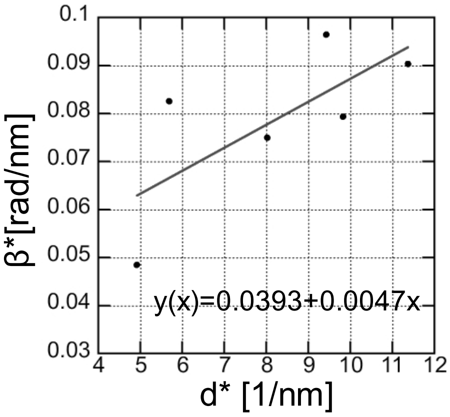

Figure 4.6: A typical Williamson-Hall plot for the 6 first line profiles; The linear model is also shown on the plot.

4.3.2 Orientation Imaging Microscopy

Data Acquisition

OIM-in-SEM (2D-EBSD) data acquisition was conducted with a field emission gun scanning electron microscope (FEG-SEM) of a dual beam FIB-SEM, Helios Nanolab™ 600 from FEI. The microscope was equipped with an EBSD system from EDAX-TSL and a Hikari camera. OIM-in-SEM (2D-EBSD) measurements were performed by an electron probe current in the range of 1.4 to 5.5 nA, and an acceleration voltage in the range of 12 to 20 kV. The measurements were conducted in a hexagonal grid of a step size in the range of 20 - 75 nm (the details of obtaining the optimal acquisition settings are provided in detail in Appendix B). The data acquisition was conducted in a working distance of 8 mm and tilting angle of 70° which was achieved by 16° stage tilt with the pre-tilted sample holder. This is schematically shown in Figure 4.7.

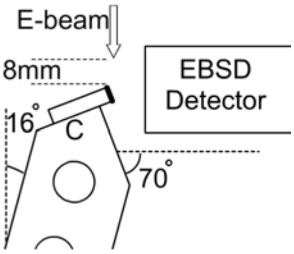

Figure 4.7: Schematic representation of the geometry for cross-sectional OIM measurement. After 16° stage tilt, cross-section depicted by thicker black line makes 70° with horizontal line.

4.3.2.1 Data Cleaning

As-measured OIM data was cleaned by routines available in OIM™ 5 software as follows: First, confidence index[3] (hereafter CI) of every point in the map within a recognized grain was assigned to the highest CI value found in that grain (a grain was defined as a region consisting of at least four connected points with misorientations of less than 5°). This clean-up process is called grain CI standardization. Secondly, orientation of a point which did not belong to any grain was changed to the orientation of the majority of neighboring points belonging to the same grain. This clean-up process is called grain dilation. The definition of a grain used in this clean-up process was similar to what is described for grain CI standardization. After grain dilation the number of altered data points was checked and if that exceeded 6% of the total number of data points, then this clean-up was disregarded and only grain CI standardization was applied.

Note that described cleaning procedure is chosen based on experimenting with different routines; the details of that is provided in Appendix C.

4.3.2.2 Data Analysis

OIM™ 5 software was used for quantification and analysis of the orientation image microscopy data in terms of grain size, CSL boundaries fraction, texture, etc. Only data points with CI>0.1 were studied, and misorientation less than 2° was disregarded.

For the measurements applied on the cross section, it was essential to define the substrate/film interface. To achieve this, the CI value of the as-measured data (without cleaning) was averaged for all the points with the same distance from the bottom of the map (points with equal y); and the *practical interface* was defined as where average CI exceeds 0.1. Similarly, the *practical film surface* was defined as where average CI reaches to a value below 0.1. A typical example is provided in Figure 4.8 on which practical interface and film surface are indicated. Note that practical interface does not coincide with the *actual interface* where CI starts to exceed 0.

For the microstructures evolving with the film thickness, sub-maps with intervals of $2\mu m$ in the y direction of the map (i.e. film growth direction) were produced using home written MATLAB® scripts (the scripts are provided in Appendix D). The practical interface

---

[3] For the detected bands of an electron backscattered pattern (EBSP), there might be several solutions. Confidence index is a parameter which ranks these different possible solutions based on a voting scheme. It is calculated during the data acquisition by following formula $CI = (V_1 - V_2)/V_{ideal}$ where V_1 and V_2 are the number of votes for most voted and second most voted solutions respectively. V_{ideal} is total number of votes for the detected bands, thus, CI is in the range of 0 - 1 [204].
For FCC materials by detecting 6 bands in EBSP, if CI>0.1 then highest voted solution is the correct solution 95% of the time [204].

was used as the start of the first sub-map and each sub-map was studied individually in OIM™ 5 software. Average horizontal intercept[4] length in the middle of each sub-map was calculated to characterize the size evolution with thickness. In case of equiaxed grains the average horizontal intercept length (AHIL) represents the average grain diameter and in case of columnar or elongated grains it is a parameter to quantify the width of the grain. The average horizontal intercept length is one the few available parameters to characterize the evolution of a microstructure consisting of columnar grains. In order to characterize the preferred orientation in each sub-map, percentage of the points in the sub-map with 10° deviation from certain direction was calculated.

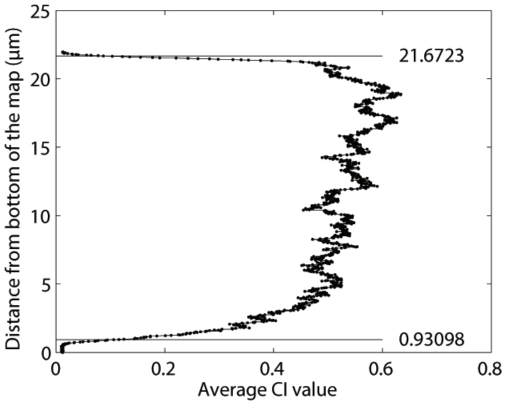

Figure 4.8: A typical plot of average CI value vs distance from bottom of the map. *practical interface* and *practical film surface* are 0.93 and 21.67 μm from the bottom of the map in this case.

4.3.3 Ion Channeling Imaging

Microstructural characterization by ion channeling imaging[5] was applied in the same dual-beam microscope mentioned earlier, using 30 keV Ga$^+$ ions. The imaging was conducted such that the ion beam was perpendicular to the analyzed area. For a cross-section, this was achieved by $-2°$ stage tilt, as shown in Figure 4.9.

Charge density (hereafter CD) for imaging was in the range of 1 - 8 C/m^2. It was calculated by the following equation:

$$CD = \frac{I.t}{A} \tag{4.8}$$

---

[4] An intercept is a high angle boundary, i.e. misorientation between two neighboring points is larger than 15°.

[5] A micro-graph made by detection of secondary electrons induced by Ga^+/matter interaction in which the contrast is solely based on difference in secondary electron yield of different crystallographic directions, is called ion channeling image.

where I is the ion beam current in A; t, the time for scanning the whole area of interest in seconds; A, the size of area of interest in m^2. It is noted that ion channeling imaging is a destructive technique and imaging can be associated with alteration of the microstructure. The details is discussed in Appendix E.

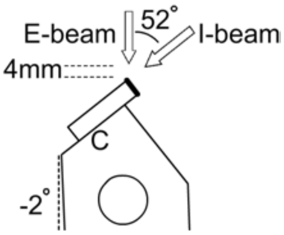

Figure 4.9: Schematic representation of the geometry for cross-sectional ion channeling imaging. By 2° stage tilt, cross-section depicted by thicker black line becomes perpendicular to ion beam.

4.3.4 3D Characterization

In order to characterize the samples in 3 dimensions serial sectioning in -z direction (by FIB milling) was applied and for each section 2D characterization was conducted by scanning in x and y direction (Figure 4.3b). Sequential 2D-EBSD, results in 3D-EBSD characterization. For a particular sample, F2, channeling ion imaging was applied in addition to 2D-EBSD measurement, this technique can be abbreviated as 3D-ICI-EBSD.

4.3.4.1 3D-EBSD Data Acquisition

Samples were prepared in the same routine explained for cross sectional sample preparation in section 4.2.1 to the end of FIB milling. A fully automated 3D-EBSD measurement was conducted using the scripts provided by microscope producer (FEI). It is worth clarifying that FIB milling for each section was conducted in -y direction and ion beam was deflected according to a pre-defined value in -z direction for the next sectioning. The cycle of measurement is expressed in the steps provided below, and more details of the processes are given, afterwards:
(i) FIB milling, (ii) stage rotation and changing the working distance, (iii) finding and positioning fiduciary marker, (iv) 2D-EBSD data acquisition, (v) stage rotation and and changing the working distance and (vi) finding and positioning fiduciary marker.
The fiduciary marker was an ‘X’ which had been made prior to actual measurement close to the site of interest. The marker was used as reference, in order to bring the sample to the exact intended position after each stage movement. The geometry of 2D-EBSD measurement, Figure 4.7, and FIB milling, Figure 4.3a, is such that both require 16° stage

tilt. As a result, no change in stage tilting angle was needed for 3D-EBSD measurement in this set-up. However, working distance for 2D-EBSD measurement was 8 mm and that for FIB milling was 4 mm (in relation with electron column pole piece). Thus, in order to change the position between FIB milling and 2D-EBSD measurement, other than 180° rotation, a working distance change was applied.

4.3.4.2 Grain Boundary Character Distribution Analysis

The sequential 2D-EBSD maps were aligned in OIM™ 5 software (primary alignment) to construct the 3-dimensional microstructure. The Primary alignment was based on minimization of the average offsets calculated from the red, green and blue channels of the inverse pole figure color coded maps [205]. Since parts of the substrate and platinum layer were measured with electrodeposited layer (see Figure 4.3b - page 44), the maps were cropped and cleaned as explained earlier (section 4.3.2). Using another cleaning procedure in OIM™, the average orientation of a recognized grain was assigned to all of the points in that grain (single grain orientation). In the same software 'grain boundary reconstruction' was applied and the skeleton of the microstructure was obtained accordingly [205]. The following steps were done using different computer codes that have been developed at Carnegie Mellon University (CMU) [103, 149].

To achieve grain boundary character distribution, as the first step, triple junctions[6] were found in each 2D map. In the second step triple junctions of neighboring sections were subjected to matching process. Triple junctions were matched if the misorientations between the three grains in the first section and three grains of one of a junctions in the second next section, was less than 5°. The matched triple junctions assumed to belong to a triple line [111]. In order to confine the computation time of the matching process, each triple junction was compared with the five closest triple junctions on the neighboring section. Accordingly, triple lines of the microstructure were obtained. Based on the assumption that a large number of triple lines are randomly distributed about the sectioning direction, a secondary alignment were conducted (sections were shifted in sub-pixel level). Afterwards normal direction and the area of grain boundary planes were calculated based on the fact that the triple line and the trace of the grain boundary on each section are belonging to the same plane. This is schematically shown in Figure 4.10. Cross product of grain boundary trace vector ($\vec{t_1}$) and triple line ($\vec{TL}$) provides the grain boundary plane normal and the area of grain boundary plane ($\vec{n_1} = \vec{TL} \times \vec{t_1}$), Figure 4.10.

---

[6] Any three segments on the reconstructed map which had a common endpoint was assumed as a triple junction.

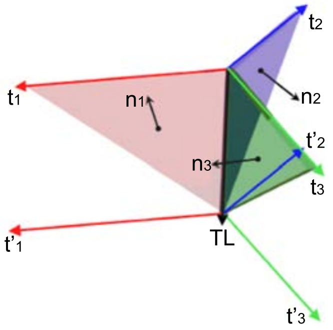

Figure 4.10: Schematic representation of calculation of grain boundary plane normal and area. $\vec{TL}$ represents triple line and traces of grain boundary planes are depicted by $\vec{t_x}$ [103].

Knowing the misorientation (Δg) across the boundaries and grain boundary planes' normal (n), the distribution of certain grain boundary, $\lambda(\Delta g, n)$, can be calculated accordingly. To achieve this, the 5 dimensional space was parametrized with three Eulerian angles (ϕ_1, Φ, ϕ_2) for misorientation space and θ, ϕ (surface of a unit sphere) for grain boundary plane normal [111]. Misorientation space was discretized with cells of equal volume and plane normal space was discretized with cells of equal area. The area of each boundary was put into its corresponding discretized space bin and all symmetrically equivalent bins. Normalization was applied to the accumulated grain boundary area in each bin by the average area per bin so that the distribution has units of multiples of a random distribution (MRD) [111].

4.3.4.3 3D-ICI-EBSD Data Acquisition

Since this technique is still not automated, the following cycle of 8 steps was conducted manually: (1) FIB milling, (3) high resolution secondary electron imaging, (5) 2D-EBSD, (7) ion channeling imaging. All even-numbered steps are stage movements to bring the sample to the appropriate position for its next step.

FIB milling for step (1) was conducted in -y direction as shown in Figure 4.11.

The configuration of the sample for high resolution secondary electron imaging in step(3) is shown in Figure 4.12. As indicated, a 36° stage tilt was applied on the 36° pre-tilted stage holder. In this configuration there is no angular distortion in secondary electron micrographs.

The distance between two consecutive sections was obtained by measuring the distance of the sections to the markers B and B', shown on the Figure 4.11.

Steps (5) and (7) were conducted in the configuration represented earlier in Figures 4.7 and 4.9, respectively. The red box indicated on the Figure 4.11 is a schematic location, where 2D-EBSD measurement and ion channeling imaging were conducted. After obtaining all

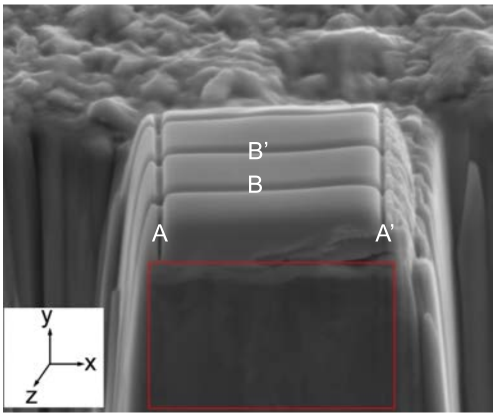

Figure 4.11: Configuration of 3D-ICI-EBSD data acquisition. serial sections where obtained by FIB milling in -z direction. 2D-EBSD and ion channeling imaging were conducted for each section as schematically shown by the red box. A and A' are markers used for alignment of ion channeling images; B and B' are markers used for measuring the distance between the sections.

the raw data, ion channeling images were aligned manually using the markers A and A'. Ion channeling images and EBSD data were comparison by eye and similar grains on the two images were located.

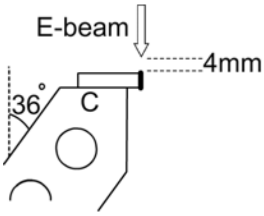

Figure 4.12: Schematic representation of the geometry for high resolution secondary electron imaging for 3D-ICI-EBSD. At 36° stage tilt, sample surface became parallel to horizontal line.

4.3.5 Energy-Dispersive X-ray Spectroscopy, EDS

An Apolo 10 silicon drift detector from EDAX attached to the dual beam FIB-SEM mentioned above was operated at 20 kV to characterize the chemical composition of alloys. Spectrum Genesis software from EADX was used for quantitative chemical analysis.

4.3.6 Microhardness Measurement

Microhardness measurement was conducted on cross sections. To achieve this, small pieces of sample were embedded in resin epoxy and prepared by mechanical grinding and polishing as explained earlier in section 4.2.1. Using Vickers geometry, microhardness was measured by a Future Tech Inc. FM 700 microhardness tester. Indentation was applied by 1 g load for 5 sec approximately half of the film thickness. The distance from the corners of the indentation mark to the film surface and substrate interface (d′) was measured and verified to exceed 2.5 times the indentation diameter (d), Figure 4.13. Indentation was applied such that distance between the corners of neighboring indents (D′) was larger than $2.5 \times d$, Figure 4.13. If $d' > 2.5 \times d$, then the effect of the surface and substrate interface on the measured microhardness, is expected to be negligible. The value of 2.5 is derived from ASTM standard for hardness measurement [206].

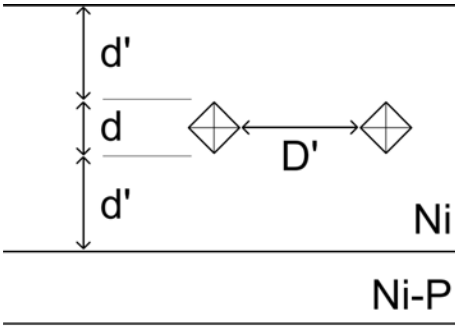

Figure 4.13: Schematic representation of the geometry microhardness measurement. (d′) did not exceed 2.5 times of the indentation diameter (d) and (D′) was chosen such to be larger than $2.5 \times d$.

Chapter 5

Results and Interpretation, As-Deposited State

In this chapter the results of different analysis methods that were applied to study the as-deposited state of the different series of experiments, i.e. F-series, BipH-series, Co-series and 8C10, are provided. Each series of experiments are discussed in separate section as follows.

5.1 F-Series Samples

In this series of experiments the current density and the concentration of additive were varied systematically (see section 4.1.3.1 for experimental details). The samples discussed in this section are indicated by a gray color in a 3 × 3 marker. For instance the marker shown below indicates that only samples F1, F2 and F3 are discussed.

F9	F8	F7
F4	F5	F6
F1	F2	F3

For the given markers, current density increases from left to right (2, 5 and 10 A/dm^2) and concentration of additive increases from bottom to top (0, 5 and 10 $mMol/dm^3$).

5.1.1 XRD Texture Analysis

▦ All the analyzed samples had a fiber texture in the normal direction (ND). For fiber texture a single inverse pole figure in ND fully characterizes the texture, and it is provided in Table 5.1. For clarification, the crystallographic direction of fiber axes <uvw>

Table 5.1: Inverse pole figures in normal direction for F-series as-deposited films obtained from XRD texture analysis. Orientation density maxima are indicated on the figures. Units are in MRD. The shown inverse pole figures are the standard triangle, (1/24) of stereographic projection circle. The crystallographic directions are shown for sample F1 and for the sake of brevity is not repeated for the rest of samples.

	i:2A/dm^2	i:5A/dm^2	i:10A/dm^2
C_{BDO} : 10	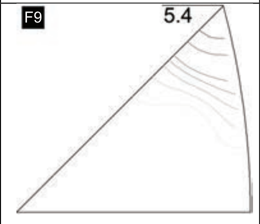	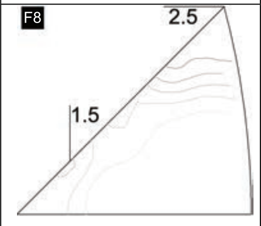	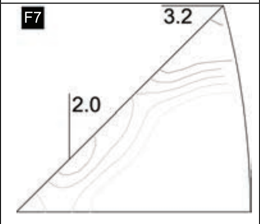
C_{BDO} : 5	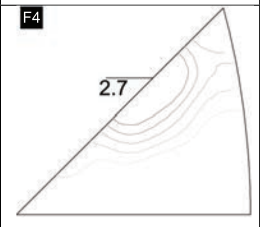	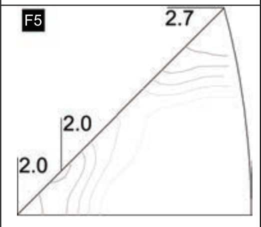	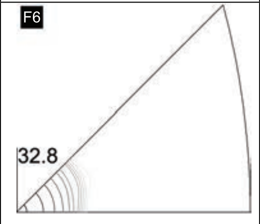
C_{BDO} : 0	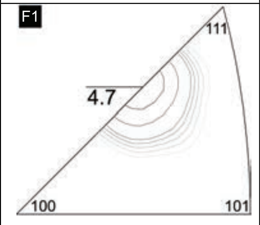	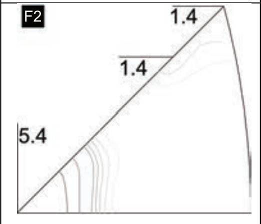	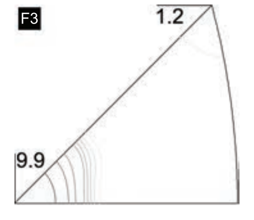

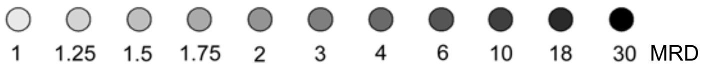

Table 5.2: Fiber axes and orientation densities in MRD of F-series as-deposited films, obtained from XRD texture analysis. C_{BDO} is in $[mMol/dm^3]$.

	i:2 A/dm^2	i:5 A/dm^2	i:10 A/dm^2
C_{BDO} : 10	<111> 5.4	<111> 2.5 <511> 1.5	<111> 3.2 <511> 2.0
C_{BDO} : 5	<211> 2.7	<111> 2.7 <511> 2.0 <100> 2.0	<100> 32.7
C_{BDO} : 0	<211> 4.7	<100> 5.4 <111> 1.4 <322> 1.4	<100> 9.9 <111> 1.2

and their orientation density in MRD are provided in Table 5.2.

Sample F6's texture (▦) is extremely strong (32.7 MRD). In order to assure the authenticity of the results, a second sample was electrodeposited under the same conditions and then subjected to XRD texture measurement. The obtained result of the second sample was identical to the first one.

Following Tables 5.1 and 5.2 it is evident that in an additive free electrolyte, at low current density (▦), a <211> fiber texture develops. Increasing the current density to $5A/dm^2$, the <100> oriented grains become dominant. Interestingly, rather weak texture component of <322> and <111> were revealed too. It is noted that <211> and <322> are separated by only 8°. Further increase of the current density to $10A/dm^2$ (▦) brings about stronger <100> fiber texture.

In the literature [75], it is shown that at lower current densities and relatively high pH, $Ni(OH)_2$ forms at the vicinity of the cathode surface, and acts as an inhibitor which promotes the formation of <211> fiber texture. And the <100> fiber texture in nickel electrodeposition forms when the metallic surface is dynamically cleaned from chemical species that adsorb on the surface (the so-called free mode of growth) [75].

At the current density of $i = 2A/dm^2$ (▦) , by addition of a medium level of the BDO, the <211> fiber texture becomes weaker and broader. Further addition of BDO in the bath, brings about a <111> fiber texture (▦). This is in accordance with the proposed mechanism of <111> fiber texture formation in which it is only expected to occur when all other modes of growth are severely inhibited [75].

At the current density of $i = 5A/dm^2$ (▦), in an additive free bath the main texture component is <100>. Addition of a medium level of BDO promotes formation of <111>. However, <100> is not fully suppressed by a medium concentration of BDO. The formation of <111> is accompanied with a weak <511> fiber texture, which is the first generation twin of <111> [207]. Further increase of the BDO concentration in the electrolyte, reduces <100> fiber texture strength. As a result, by increase of BDO concentration in the bath, formation of <100> is suppressed and in contrast, that of <111> is enhanced.

Note that, <111> and its first generation twin, <511>, are both present in samples F5 and F8 (▦). Comparing sample F3 and F7 (▦), the general trend at the current density of $i = 10A/dm^2$ is similar to what has explained for $i = 5A/dm^2$: formation of <111> and its twin orientation <511>, at the expense of <100> fiber texture. However at the medium level of additive, a very strong and sharp <100> fiber texture formed. This means that, introducing BDO to the electrolyte at the current density of $10A/dm^2$, results in the formation of a more pronounced <100> fiber texture (free mode of growth, see section 2.4.2). This observation is in contrast with the expectations that BDO suppresses the free mode of growth. Similar behavior has been reported in literature [95, 98].

5.1.2 Line Profile Analysis

5.1.2.1 Williamson-Hall Method

Due to the texture of the samples, from the 8 measured reflections, 331 and 420 reflections were virtually non-existing in several occasions . Similarly, the 400 reflection had a low intensity for samples with fiber texture other than fairly strong <100>, such that proper peak profile fitting was impossible. Hence, the Williamson-Hall method was applied using the peak profiles with acceptable intensity. The diffracted volume weighted average grain size and micro-strain were calculated and are listed in Table 5.3. The average grain size calculated for four of the samples were either negative or above the maximum experimental limit of the used set-up (300nm) and shown by 'N' in Table 5.3a. When size contribution of physical broadening is not quantified correctly the obtained values for micro-strain are not reliable either. This shows some shortcomings in using the Williamson-Hall method.

Table 5.3: Average grain size in nm (a), and micro-strain (b), of F-series samples in as-deposited state obtained by applying Williamson-Hall method. 'N' represents negative values for grain size or a calculated value above the upper determination limit of the used diffractometer. C_{BDO} is in $[mMol/dm^3]$.

(a)

	Average grain size $[nm]$		
	i:$2A/dm^2$	i:$5A/dm^2$	i:$10A/dm^2$
$C_{BDO}:10$	N	23	27
$C_{BDO}:5$	18	29	N
$C_{BDO}:0$	81	N	N

(b)

	Micro-strain		
	i:$2A/dm^2$	i:$5A/dm^2$	i:$10A/dm^2$
$C_{BDO}:10$	0.0100	0.0027	0.0027
$C_{BDO}:5$	0.0030	0.0027	0.0036
$C_{BDO}:0$	0.0003	0.0012	0.0015

Though the Williamson-Hall method is a well-established method for characterization of materials [203] and is extensively applied in the scientific literature, interpretation of the results obtained for electrodeposited samples should be done cautiously [208], specially when samples are textured. Strain anisotropy has not been taken into account in the classic Williamson-Hall method [209]. The modified Williamson-Hall method takes into account this effect and that improves the accuracy of the estimated size and micro-strain [210]. Apart from this, the grain shape is not necessarily spherical in the analyzed samples, which is an underlying assumption in the Willamson-Hall method [211]. This effect is more notable taking into account that, grain shape is often coupled with crystallographic preferred orientation in electrodeposited samples, thus there is a shape anisotropy. That means elongated grains in electrodeposition direction very often have specific orientations. This brings about notable scatter of the data points in the Williamson-Hall plot from linear model expected in this method ($\beta_f^* = \frac{1}{<D>_v} + 2 < \epsilon > d^*$) which consequently deteriorates the quantification based on this method.

Furthermore the 422 reflection cannot be measured using $Cu - K_\alpha$ radiation; Thus, for the samples with <211> fiber texture the majority of the grains are not included in the diffracted volume weighted averaging. This conditions lead to a deviation from the actual average grain size. Due to the described limitations of the Williamson-Hall method for the present samples, the results are supplemented by the single line analysis on those grains contributing the proffered orientation, i.e. <100> and <111> grains (<211> grains are not available by XRD profile analysis using Cu-K$_\alpha$ radiation).

5.1.2.2 Single Line Analysis

Table 5.4: Grain size in nm and micro-strain of certain orientation obtained by single line analysis for F-series samples in as-deposited state. (a) average size and (a) micro-strain of <111> oriented grains. C_{BDO} is in $[mMol/dm^3]$.

(a)

	grain size, 111 reflection		
	i:2A/dm^2	i:5A/dm^2	i:10A/dm^2
C_{BDO} : 10	19	18	21
C_{BDO} : 5	21	19	25
C_{BDO} : 0	89	91	98

(b)

	grain size, 200 reflection		
	i:2A/dm^2	i:5A/dm^2	i:10A/dm^2
C_{BDO} : 10	4	8	8
C_{BDO} : 5	9	11	41
C_{BDO} : 0	53	115	141

The estimated grain size and micro-strain for 111 and 200 refections are listed in Tables 5.4 and 5.5, respectively. In additive free electrolyte (▦), the average grain size is ≈ $90nm$. Addition of 5 (▦) or 10 $mMol/dm^3$ (▦) BDO into the electrolyte

Table 5.5: Grain size in nm and micro-strain of certain orientation obtained by single line analysis for F-series samples in as-deposited state. (a) average size and (a) micro-strain of <100> oriented grains. C_{BDO} is in $[mMol/dm^3]$.

(a)

	Micro-strain, 111 reflection		
	i:$2A/dm^2$	i:$5A/dm^2$	i:$10A/dm^2$
C_{BDO} : 10	0.0051	0.0014	0.0022
C_{BDO} : 5	0.0007	0.0019	0.0036
C_{BDO} : 0	0.0015	0.0015	0.0012

(b)

	Micro-strain, 200 reflection		
	i:$2A/dm^2$	i:$5A/dm^2$	i:$10A/dm^2$
C_{BDO} : 10	0.0009	0.0028	0.0023
C_{BDO} : 5	0.0029	0.0025	0.0030
C_{BDO} : 0	0.0013	0.0011	0.0010

reduces that size down to $\approx 20nm$. This clarifies that BDO grain refinement on <111> oriented grains is already achieved by addition of 5 $mMol/dm^3$ in the electrolyte and further increase in the concentration does not reduce that size any further.

For <100> oriented grains, in the additive free electrolytes (▦), there is an increase in grain size with increase of current density. Addition of 5 $mMol/dm^3$ BDO (▦) into the electrolyte reduces that size down to $\approx 10nm$ for samples F4 and F5. However the grain size of sample F6 (which has a very strong <100> fiber texture) is 4 fold larger than that of samples F4 and F5. Further increase of BDO (▦), decreases the grain size of <100> oriented grains down to 8nm. This shows that unlike <111> oriented grains, a higher concentration of BDO effectively refines <100> oriented grains, i.e. suppresses <100> oriented grain growth during the electrodeposition. Evidently for the lowest current density, sample F9 ▦, this effect is most pronounced. As a result, the addition of BDO into the electrolyte refines the grain size of <111> oriented grains down to $\approx 20nm$, and fully refines <100> oriented grains. Similar to what has been explained for Willamson-Hall method, samples F1 and F4, (▦) have a <211> fiber texture. Consequently the grain size and micro-strain of large volume fraction of these samples are unknown using single line analysis of 111 and 200 reflections.

5.1.3 Microscopy - Additive Free Electrolyte

5.1.3.1 Surface Topography

Surface topography was investigated by SEM, using secondary electron (SE) imaging. The surface topography of sample F1 (▦) synthesized with lowest current density is shown in Figure 5.1. It clearly shows that surface topography is rather uniform and is formed of protrusions with a 2-fold symmetry. This type of surface topography is typical for electrodeposited nickel films with <211> fiber texture [77, 87, 168]; and is therefore consistent with the texture analysis that yields a <211> fiber texture for sample F1 (see Table 5.2).

Removing the surface topography by FIB milling and investigating the microstructure of the film just below the surface, reveals that trenches on the surface are grain boundaries in the microstructure, Figure 5.2. Observing the change of contrast in Figure 5.2b, grains are halved by a dark and a light region. In addition, parallel twin lamellae are present in both halves, and are extended across the grains, Figure 5.2b. The twin lamellae in a grain are oriented parallel to the line of symmetry of that grain.

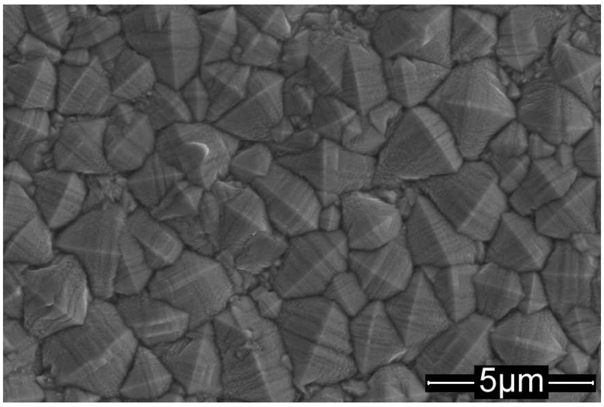

Figure 5.1: Surface topography of the sample synthesized in a additive free bath and current density of 2 A/dm^2 (sample F1). The protrusions on the surface have a 2-fold symmetry.

Increasing the current density to 5 A/dm^2, sample F2 ▦, the general surface topography is changed significantly, Figures 5.3a. The protrusions on the surface are rather irregular in shape and size. In some locations the protrusions are more developed and are as big as 1 μm, whereas in some other locations they are smaller than that. The protrusions are mostly irregular in shape (see Figures 5.3a), however, those which are larger in size occasionally show a 4-fold symmetry and rarely a 2-fold symmetry (Figures 5.3b and 5.3c respectively). The 4-fold symmetry protrusions are close to a square pyramid. The faces of the pyramids are not perfectly flat and they are composed of several ledges (see Figure 5.3b). It has been proposed [95] that the faces are composed of combination of

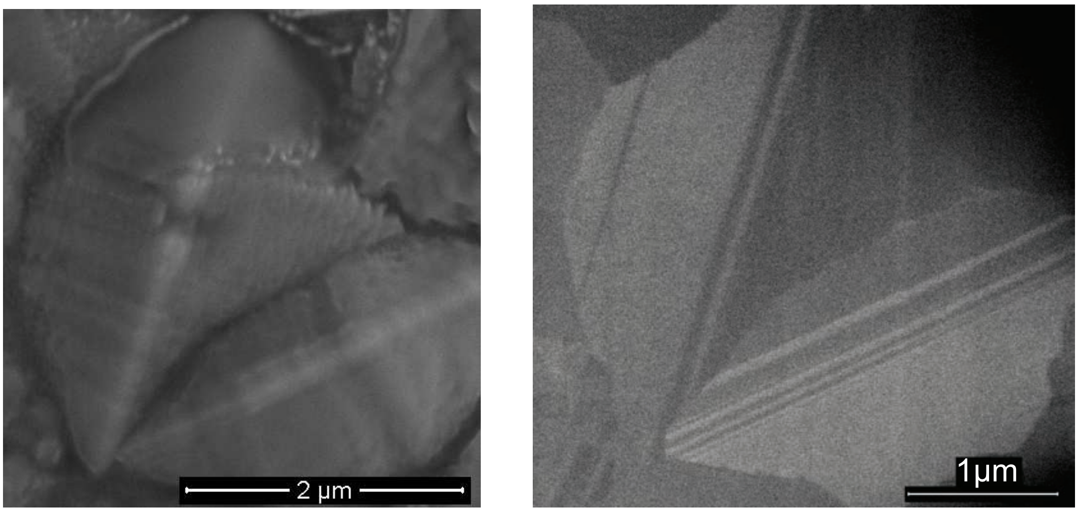

(a) (b)

Figure 5.2: (a) Secondary electron image of a selected location on the surface of sample F1. (b) The microstructure of the film right beneath the topography shown in Figure 5.28a; Fine twins lamellae are extended across the grains.

{111} and {100} planes . This is schematically shown in Figure 5.4. If the pyramid face is mostly composed of {111} planes then the protrusion looks like a sharp pyramid, Figure 5.3b; and if the contribution of {100} planes is higher then the protrusion will be fairly flat.

The 2-fold symmetry protrusions are very similar to the protrusions in surface topography of sample F1, as shown in Figure 5.1. This shows that an increase of current density from 2 to 5 A/dm^2 significantly changes the surface topography, and occasionally characteristic 2-fold symmetry protrusions can be found on the surface.

In order to study the orientation of those two examples of 2-fold and 4-fold symmetry protrusions, a flat surface of the the corresponding grains were prepared by site specific preparation with FIB milling, and the orientation is obtained by EBSD afterwards. The grain forming the 4-fold symmetry protrusion has a <920> orientation which slightly deviates from perfect <100>. And the grain with the 2-fold symmetry protrusion has a <532> orientation which is close to <211> and <322>.

Due to the lack of time for further experiments and also due to the sample geometry (the protrusions must be close to the edge of sample to be FIB milled and investigated) no further protrusion was investigated in this matter. Hence, no strong conclusion can be taken from the results; still one may speculate that 2-fold symmetry protrusions on the surface are corresponding to the <322> fiber texture component obtained by texture analysis, and they have characteristics similar to <211> oriented grains.

Further increase of current density from 5 to 10 A/dm^2 does not change the general surface

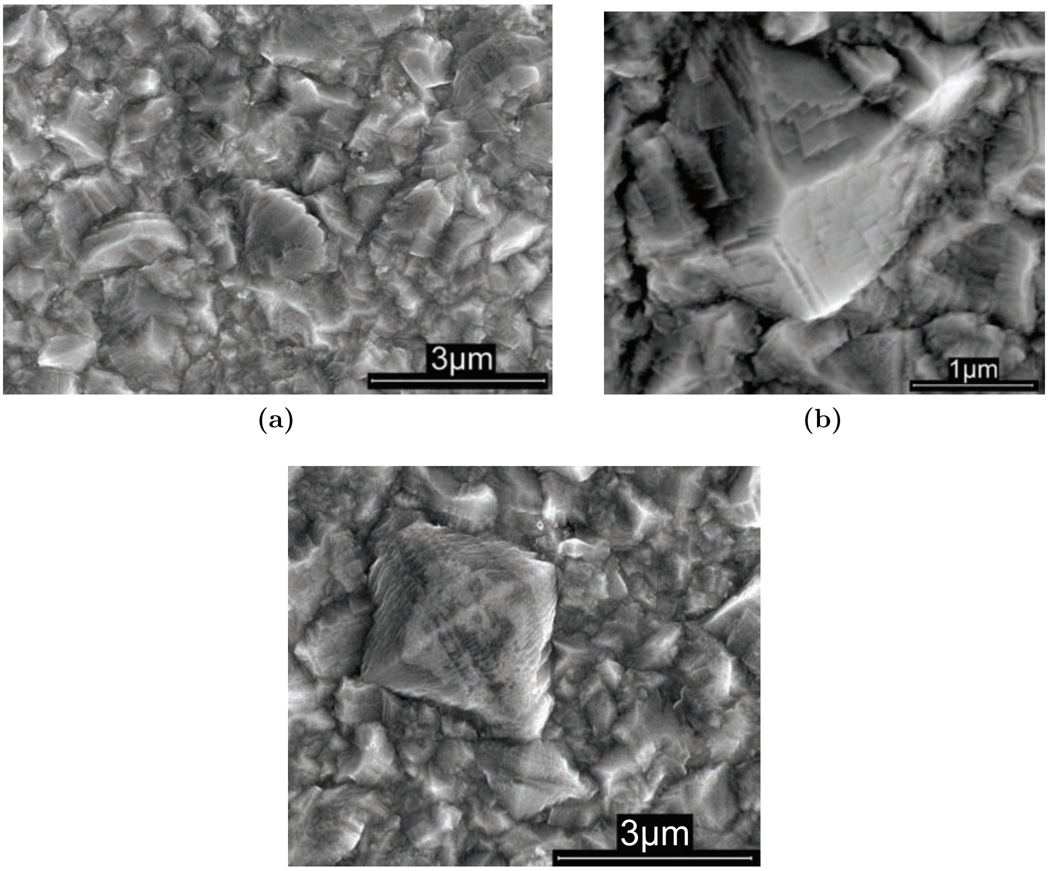

(a) (b)

(c)

Figure 5.3: (a) The general topography of sample F2. The protrusions are rather irregular in shape and size. (b) Relatively large 4-fold symmetry protrusion. (c) Relatively large 2-fold symmetry protrusion in sample F2 topography.

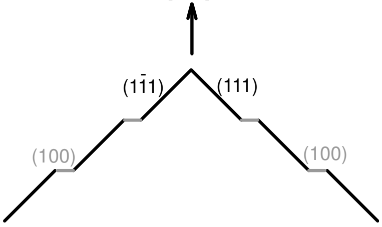

Figure 5.4: Schematic representation of pyramid face of protrusions in a [100] oriented grain. The faces are composed of {111} and {100} planes. The representation is inspired by [95].

topography notably, Figure 5.5. Pronounced 4-fold symmetry protrusion as indicated by red circles on the Figure 5.5 were observed and 2-fold symmetry protrusion were no longer found on the surface, which is consistent with disappearance of the <322> texture component (Table 5.2).

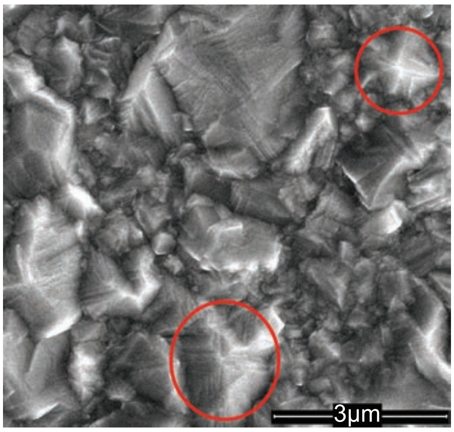

Figure 5.5: Surface topography of sample F3, two 4-fold symmetry protrusion are marked by red circles on the micrograph.

5.1.3.2 Microstructure evolution with thickness

Ion channeling imaging was applied on cross sections of the samples (▦), and due to its enhanced orientation contrast, the images revealed that all of them have columnar microstructure, Figure 5.6. Similar to typical columnar microstructures, the samples synthesized in additive free electrolyte are composed of very fine grains in the vicinity of the film/substrate interface and columnar grains away from the substrate. Twin lamellae can easily be recognized in the microstructure Figure 5.6. Numerous twin lamellae aligned parallel to the film growth direction for sample F1 (Figure 5.6a) and inclined to the film growth direction for samples F2 and F3 (Figure 5.6c and 5.6d). Occasionally, twin lamellae in samples F2 and F3 form 'L' shape features within the columnar grains as shown by red rectangle on Figure 5.6d.

Ion channeling images is used to characterize the size of grains in the plane parallel to the film/substrate interface. To achieve this, the black and white images were processed by edge detection algorithms. As a result, the points on the image where the difference between the two neighboring pixels exceeds a certain value were detected and called 'grain boundaries'. Note that, in the black and white ion channeling image it is impossible to determine the orientation difference between the two grains. Hence the term 'grain boundaries' used in this context is rather subjective. Nevertheless, horizontal line (parallel to the film/substrate interface) were drawn and the number of intercepts between that line

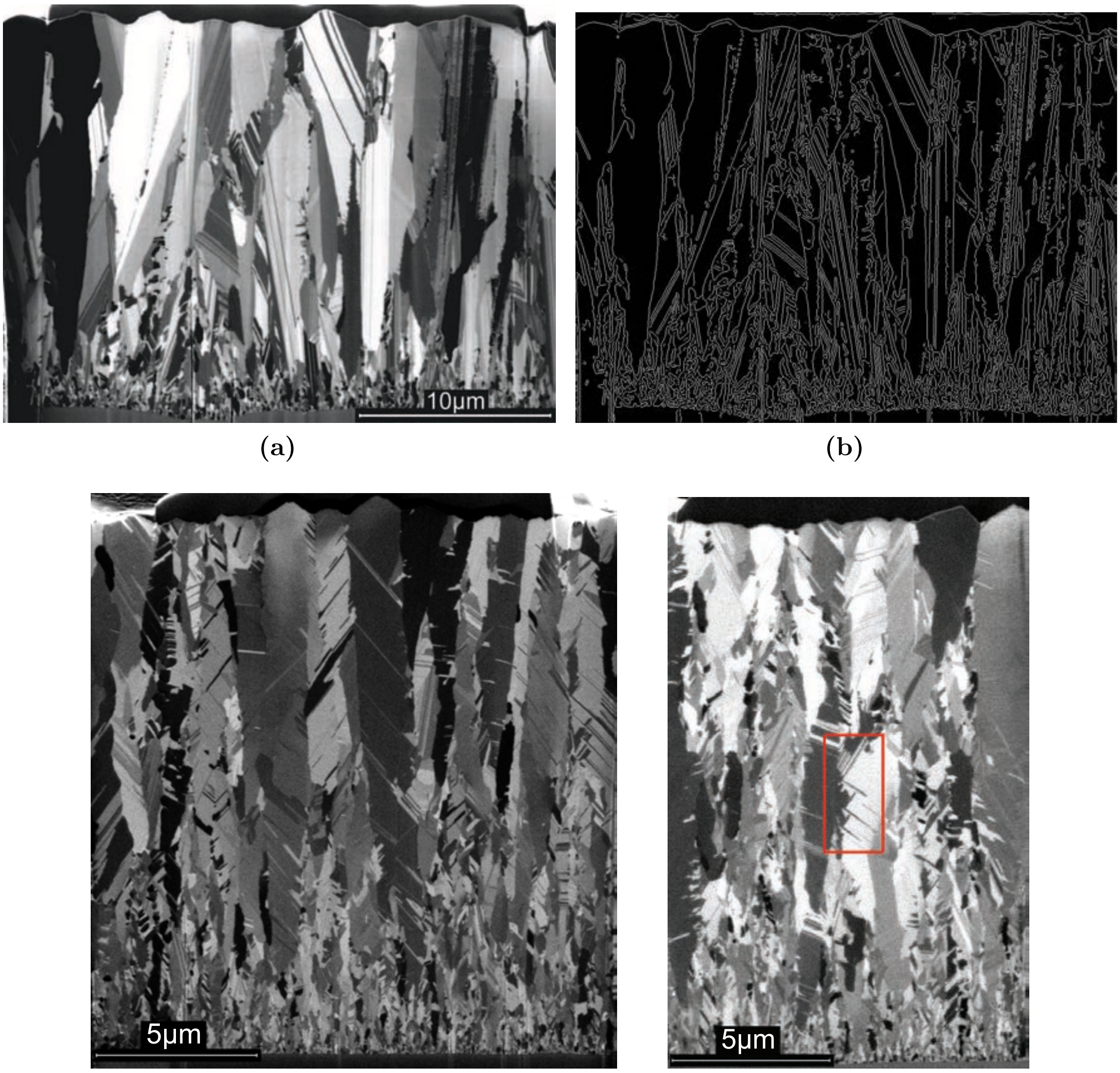

(a) (b)

(c) (d)

Figure 5.6: Ion channeling image of sample F1 (a), F2 (c), and F3 (d). (b) Detected grain boundaries including twins of the microstructure shown in (a), using canny edge detection

and the detected grain boundaries wear obtained. Based on the the length of horizontal line and the number of intercepts, the average horizontal intercept length[1] (AHIL) were calculated.

Figure 5.6a was processed with a MATLAB script using Canny edge detection algorithm [212] and the result is shown in Figure 5.6b. The processed image is not perfect and some noises are detected as boundaries while some boundaries are not fully detected. Nevertheless, it acceptably reflects the microstructure (compare Figure 5.6a and 5.6b). Using the processed image the evolution of AHIL with film thickness is quantified as shown in Figure 5.7. There is some evidence in the literature that that average horizontal intercept length, L, is related to the time of deposition, t. $L \propto t^P$ where P is ≈ 0.52 [213]. Hence, a square root function was fitted to the data points as well, shown in blue on the Figure 5.7. As can be seen, the square root function fits very well to the measured data.

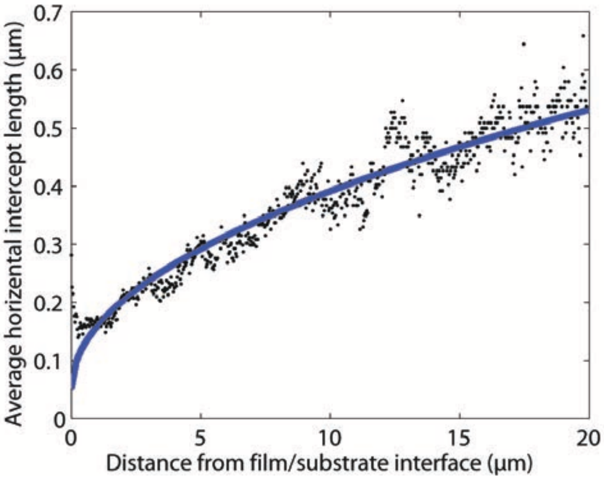

Figure 5.7: Average horizontal intercept length of sample F1, calculated based on edge detected image shown in Figure 5.6b.A square root function fitted to the measured data and is marked by blue line.

This is not the case for the first few micrometers, where the measured data is $\approx 150nm$ and the fitted function predicts $\approx 50nm$. To achieve a better estimate, a high magnification ion channeling contrast image was acquired which is shown in Figure 5.8a. Interestingly, the prediction of fitted function turns out to be very close to actual value of average horizontal length at film/substrate interface ($\approx 50nm$). This is shown in Figure 5.8b in which the first $1.5\mu m$ of the data corresponds to figure (a) and the data of 1.5-20 μm is similar to what is shown in Figure 5.7.

Similarly, micrographs of samples F2 and F3, shown in Figures 5.6c and 5.6d were processed, and the AHIL were fitted with a square root function; the results are shown in Figure 5.9.

---

[1] For each horizontal line on the image (y=constant), dividing the width of the image (in μm) to the number of grain boundaries provides average horizontal intercept length for that line.

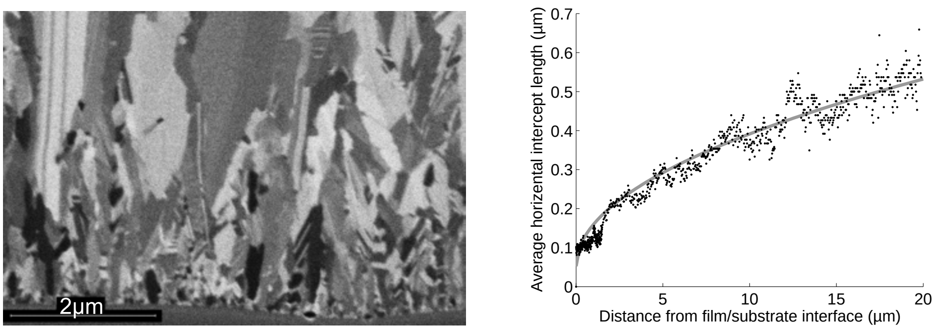

(a) (b)

Figure 5.8: (a) High resolution ion channeling image at the film/substrate interface. (b)Average horizontal intercept length vs distance. First 1.5μm of the data corresponds to figure (a) and the data 1.5-20 μm is similar to what is shown in Figure 5.7

It is evident that the AHIL of sample F1 is higher than that of samples F2 and F3.

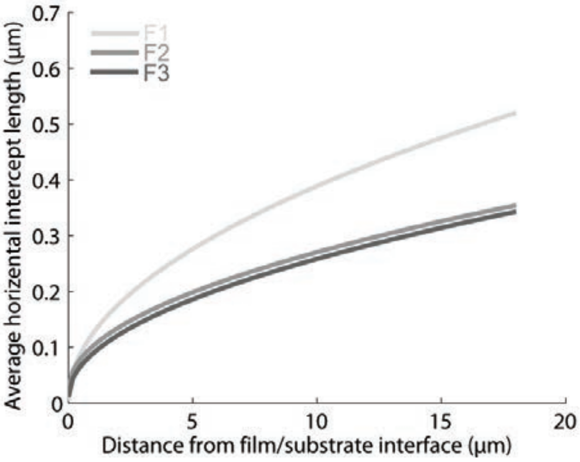

Figure 5.9: The square root functions, representing average horizontal intercept length of edge detected images shown in Figure 5.6.

In order to analyze grain boundary character and orientation relations of the samples, OIM was applied[2]. The columnar grains orientation is close to <211> in sample F1 and <100> in samples F2 and F3 in relation to the film growth direction, as shown in Figure 5.10. This is in good agreement with the results obtained by X-ray texture analysis in Table 5.2. For a characterization of the evolution of the grain boundaries with thickness, practical interface was defined and sub-maps were made as explained in section 4.3.2.2. Afterwards, length fraction of $\Sigma3/HAGB$ and $\Sigma9/HAGB$ were calculated for each sub-map. Close inspection of the orientation maps, reveals that $\Sigma3$ boundaries only occasionally separate

---

[2] Sample F3 was measured using accelerating voltage of 20kV, this has been applied in order to decrease the measurement time and consequently the problematic drift.

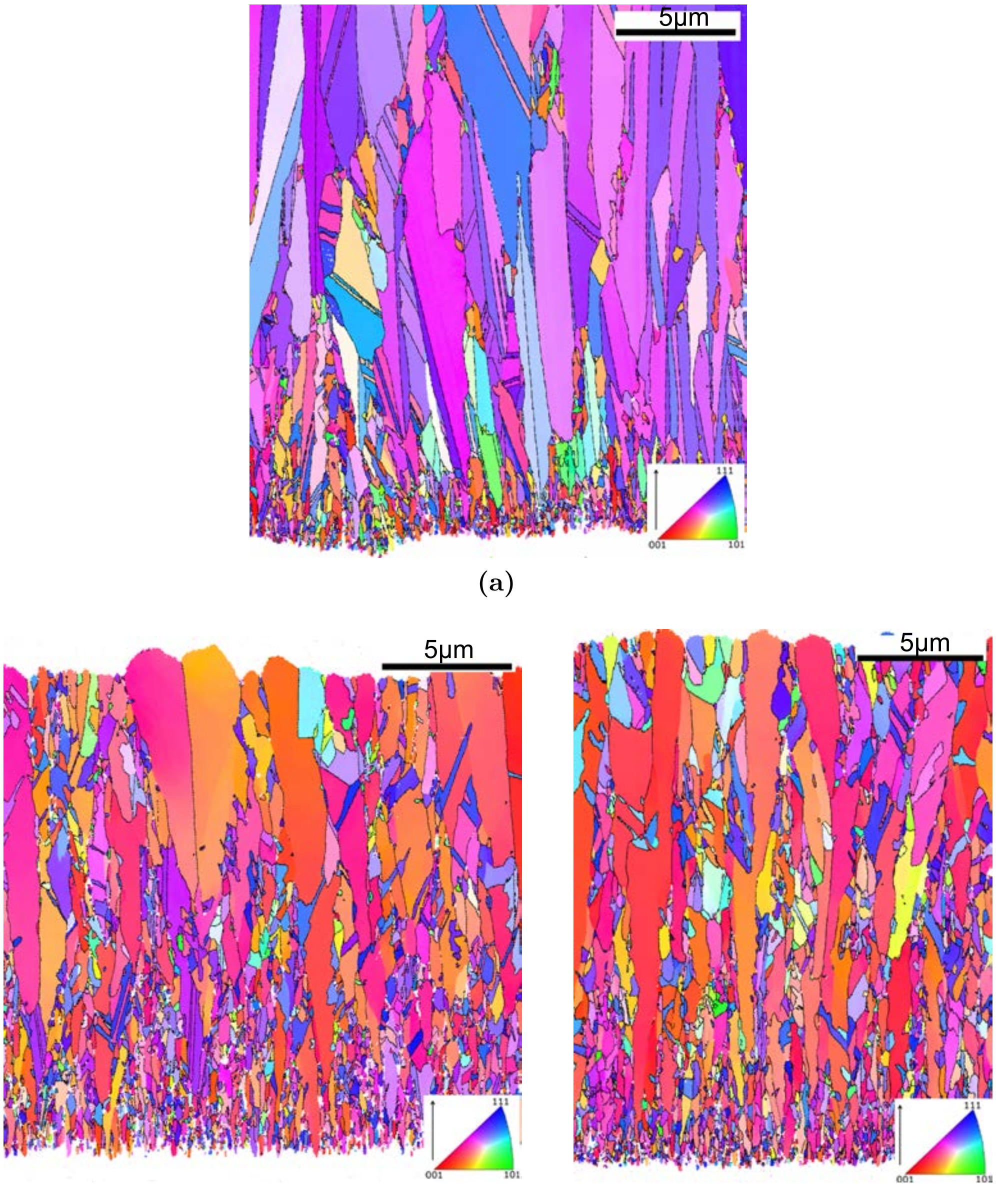

(a)

(b)

(c)

Figure 5.10: Orientation map color coded in relation with film growth direction shown by an arrow for samples synthesized in additive free electrolyte and current density of $2A/dm^2$ (a) , $5A/dm^2$ (b), and $10A/dm^2$ (c). High angle grain boundaries are indicated by black.

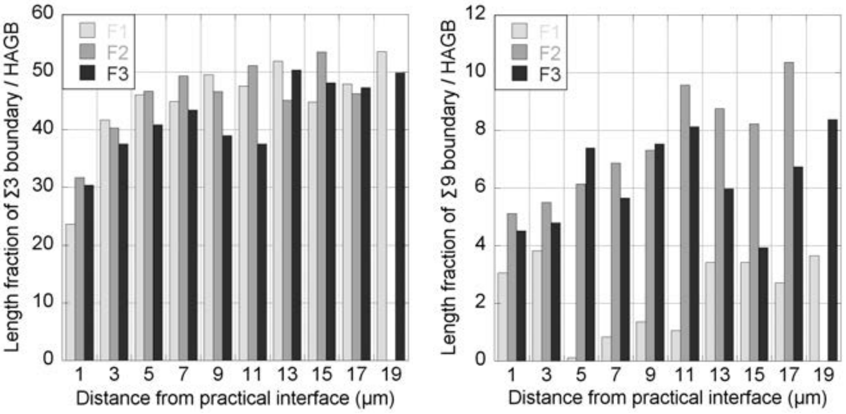

(a) (b)

Figure 5.11: (a) Length fraction of $\Sigma3/HAGB$, (b) Length fraction of $\Sigma9/HAGB$, for samples F1, F2, and F3. The analysis was done on the orientation maps shown in Figure 5.10.

two columns; most often they form the boundary between twin lamellae within columnar grains. $\Sigma3/HAGB$ for all three samples are comparable, however that of sample F3 is slightly lower than the other two, Figure 5.11a. It must be noted that, the first F1 and F2 were measured using accelerating voltage of 12 kV whilst sample F3 was measured at 20 kV. The similarity between the samples F2 and F3, see Figures 5.6 and 5.9, hints that use of higher accelerating voltage and associated lower resolution may influenced the $\Sigma3/HAGB$ value. $\Sigma9/HAGB$ of <100> oriented samples are notably larger than that of the <211> oriented sample (Figure 5.11b). Detailed observation of the microstructure of sample F2 revealed two types of Σ9 boundaries, Figure 5.12. (i) separating two neighboring columnar grains. (ii) separating two intersecting twin lamellae. In Figure 5.12a and 5.12b Σ9 boundaries are green and Σ3 boundaries are black. Type(i) of Σ9 boundaries can easily be seen in Figures 5.12a and 5.12b and type (ii) is the boundary separating twin lamellae 'A' and 'B' on Figure 5.12b. It is noteworthy that the length fraction of type(ii) is smaller than type (i).

One peculiarity of sample F1, with <211> columnar grains, is that close to the substrate, relatively high fraction of <100> oriented grains are present, Figure 5.10a. The fraction of each of these two orientations (allowing 10° deviation) in relation with distance from practical interface is quantified from the orientation map shown in Figure 5.10a and represented in Figure 5.13a. As the distance from the practical interface increases, there is a rapid increase and decrease in area fraction of <211> and <100> data points, respectively. In the first 2 μm, the area fraction of <211> oriented grains is almost double of that of <100>, however, analyzing the texture (for the first 2 μm), <100> is the dominant texture component, Figure 5.13b. Since, the statistics of the calculated texture is very

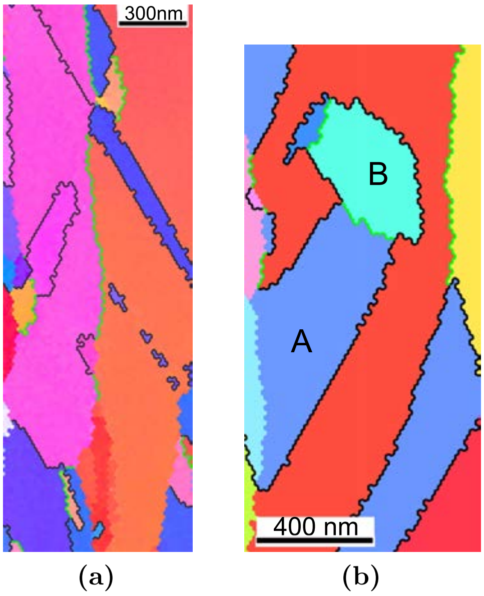

(a) (b)

Figure 5.12: (a) High resolution orientation map of sample F2. Σ3 and Σ9 boundaries are shown in black and green respectively. Σ3 boundaries are mostly within a column and Σ9 between the neighboring columnar grains.(b) Type (ii) of Σ9 boundaries which separate two twin lamellae; 'A' and 'B'in this case.

poor (total area of $2 \times 21\mu m^2$ is used) the values must be seen qualitatively; and only the importance of <100> oriented grains close to the film/substrate interface must be noted. Having mentioned that, presence of pronounced <100> oriented grains before dominance of <211> columnar grains in the microstructure is also observed in other samples studied (see Figure 5.32c in page 100). Thus, it does not likely to observe same phenomenon in two different samples accidentally.

5.1.3.3 Twin Lamellae Characterization

It was shown that Σ3 boundaries form a large fraction of the high angle grain boundaries in the internal structure of the films synthesized in the additive free electrolytes. Σ3 boundaries are most often separating twin lamellae from their encompassing columnar grain. Since the Σ3 boundary is in the core of grain boundary engineering, a detailed analysis was carried out to characterize twin lamellae in the studied microstructures.

<211> oriented grains

Analysis of ion channeling images, showed that in sample F1 with majority of <211> oriented grains, the number and the widths of twin lamellae within a columnar grain generally do not change in the growth direction, see Figure 5.14.

Counting the number of fine twin lamellae in ion channeling images, the average number of twins per grains is 3.5, thus there is ≈ 7 twin boundaries in each grain.

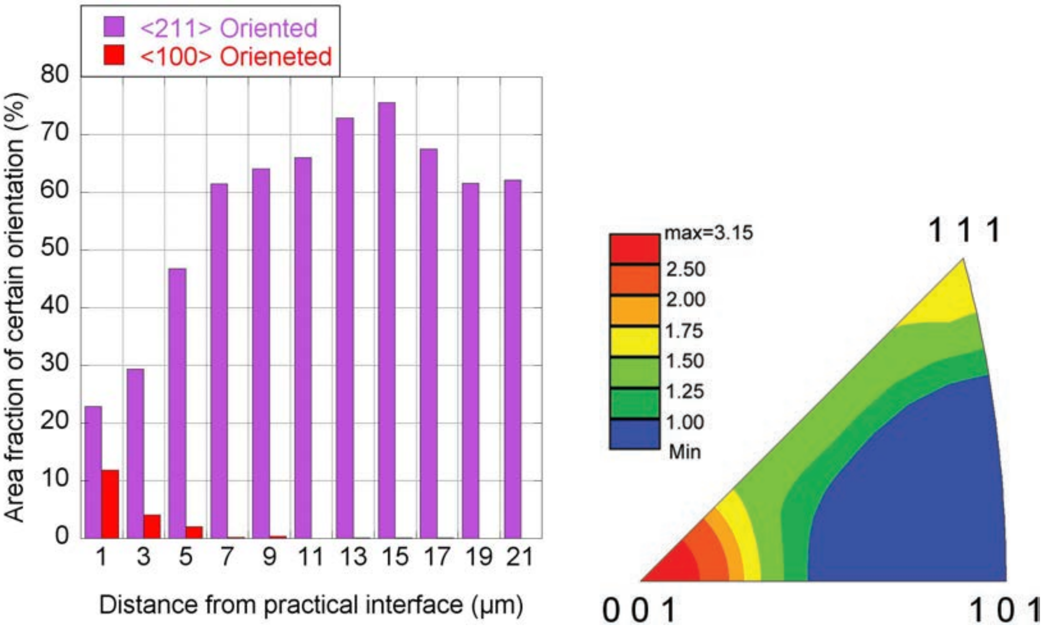

(a) (b)

Figure 5.13: (a) Area fraction of <211> and <100> oriented data points vs distance from the practical interface for sample F1. (b) Inverse pole figure of the first 2 μm from the practical interface of sample F1 obtained from OIM texture analysis.

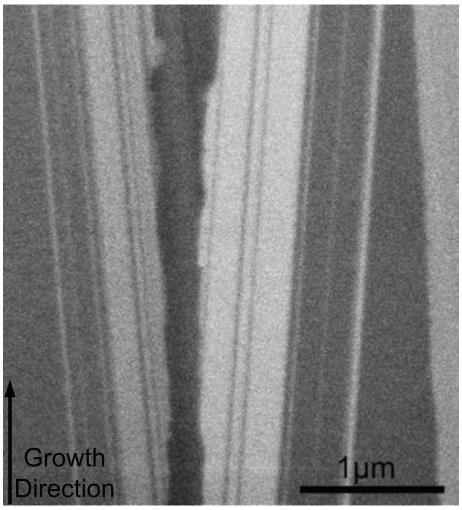

Figure 5.14: High resolution ion channeling image. Fine twins lamellae are mostly parallel to the film growth direction, their number and width do not change in film growth direction.

<100> oriented grains

Several 2D-EBSD measurements, ion channeling images and a 3D-ICI-EBSD were applied to characterize the twin lamellae in grains oriented close to the <100> orientation in sample F2. Using ion channeling images and counting the number of twins in columnar grains of sample F2, the average number of twin lamella is $\approx 1.5/\mu m$. Three configuration of twin lamellae in <100> oriented grains are: (i) Fault Formation at the Boundaries, (ii) Continuation of Twin Growth, and (iii) Neighboring Grains Interdependence Growth. It is noteworthy that these three configuration in formation of twin lamellae in <100> oriented grains are listed in the order of their frequency of observation, e.g. in the more than $250\mu m \times 20\mu m$ of the analyzed cross-section, fault formation at the boundaries is the most observed one whilst 'neighboring grains interdependence growth is observed only once.

(i) Fault Formation at the Boundaries:

Figure 5.15: High resolution ion channeling image. Fine twin lamellae are inclined to the film growth direction. At the columnar grain boundary relatively thick twin lamellae are present which terminate within the column, and relatively thin twin lamellae fully bridge across the width of the columnar grain in this 2D- representation.

Figure 5.15 shows a columnar grain which envelops several twin lamellae. Relatively thick twin lamellae are observed on the left hand side of the columnar grain; these terminate within the grain. This suggests that there is higher probability of formation of twin lamellae at the boundary of columnar grains.

The 3-dimensional configuration of these twin lamellae, is obtained by serial sectioning and ion channeling imaging. Figure 5.16 shows three consecutive sections a columnar grain. The distance between the sections No.1 and No.2 is 74 nm and that of No.2 and

No.3 is 64 nm. A particular twin lamella is marked by a red dot in all sections, which becomes thinner from section No.1 to No.3. In the next section (No.4 which is not shown here), 62 nm distant from section No.3, no sign of this particular twin lamella was found. Following the three ion channeling images, the complexity of the 3-dimensional character of the twin lamella is apparent. The upper twin boundary of the lamella is parallel in three consecutive sections. In contrast the lower boundary, in section No.2 has a $\approx 6°$ angle with that of section No.1 and consequently it has 6° angle with upper twin boundary. Assuming the upper boundary be a singular {111} plane, the lower boundary must be composed of more than one plane. This is very apparent in section No.3 where the lower twin boundary has a fairly large ledge (in comparison with atomic scales) on it. It is worth pointing out that the marked twin lamella in section No.1 and No.2 start at one boundary and terminates at the other boundary of the enveloping columnar grain, but in section No.3 it is terminated within the column. This shows that even twin lamella which fully bridge the width of a columnar grain in a 2D representation can terminate within the the column in the 3^{rd} dimension.

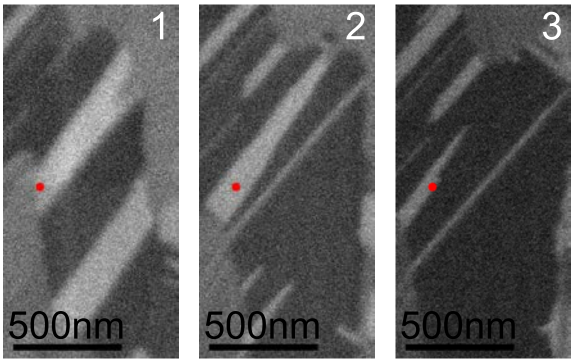

(a) (b) (c)

Figure 5.16: (a) – (c) A sequence of ion channeling image of a <100> oriented columnar grain. A particular twin lamella is indicated by red dot in all micrographs. The Distance between (a) and (b) is 74 nm and between (b) and (c) is 64 nm.

Another sequence of ion channeling images is shown in Figure 5.17. In the sequence of 6 micrographs, two twin lamellae are marked by green and red dots. Since the lamella marked by green is absent in the section No.6, and lamella marked by red is absent in section No.1, both these twins are evidently, terminated within the columnar grain. However they intersect and form an ‘L’ shaped feature which can be seen in sections No.3 to No.5. This is similar to what has been observed earlier in Figure 5.6d. The boundary between these two intersecting twin lamellae forming L is a $\Sigma 9$ boundaries as explained in Figure 5.12b.

Analyzing many <100> oriented columnar grains, no cross twinning were observed, i.e. two twin lamellae cross each other to make an 'X' shape feature.

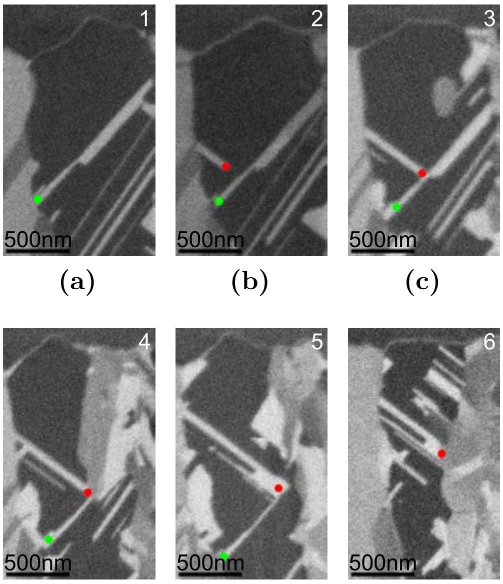

(a) **(b)** **(c)**

(d) **(e)** **(f)**

Figure 5.17: (a) – (f) A sequence of ion channeling image of a <100> oriented columnar grain. Two twin lamella are indicated by green and red dots on the micrographs. 'L' shaped feature can be seen in sections No.3 – No.5.

(ii) Continuation of Twin Growth:

In Figure 5.18a, two neighboring crystallites with relatively close orientation are shown. Apparently, a twin lamella in left hand side crystallite continued its growth into its neighboring grain. Analyzing the misorientation between the data points, there is sharp 10° point to origin misorientation change between the two crystallites along AB line, before the twin enters the right hand side grain, Figure 5.18c. The point to origin misorientation along CD line clearly shows that the twin reorients after entering the neighboring crystallite, Figure 5.18d. When the twin enters the neighboring crystallite, there is a $\approx 8°$ misorientation with respect to its origin (point 'C') shown in the Figure 5.18a. Point to origin misorientation along EF line, change over a relatively broad interval in contrast to line AB, Figure 5.18e. This clearly shows that the grain on the left hand side is reoriented after the twin entered into it; presumably dislocations compensated this reorientation. It is noteworthy that, from the orientation map it appears that the twin growth has stopped after $\approx 0.6\mu m$ beyond the low angle grain boundary. However from the image quality map, Figure 5.18b, it is evident that the twin width has reduced, but continues to the surface. This twin part cannot be resolved by OIM in terms of orientation. This concludes that the twin lamella on the right hand side grain is formed due to 'continuation of twin growth' present in the left hand side grain. High resolution channeling ion imaging has also shown that some fine

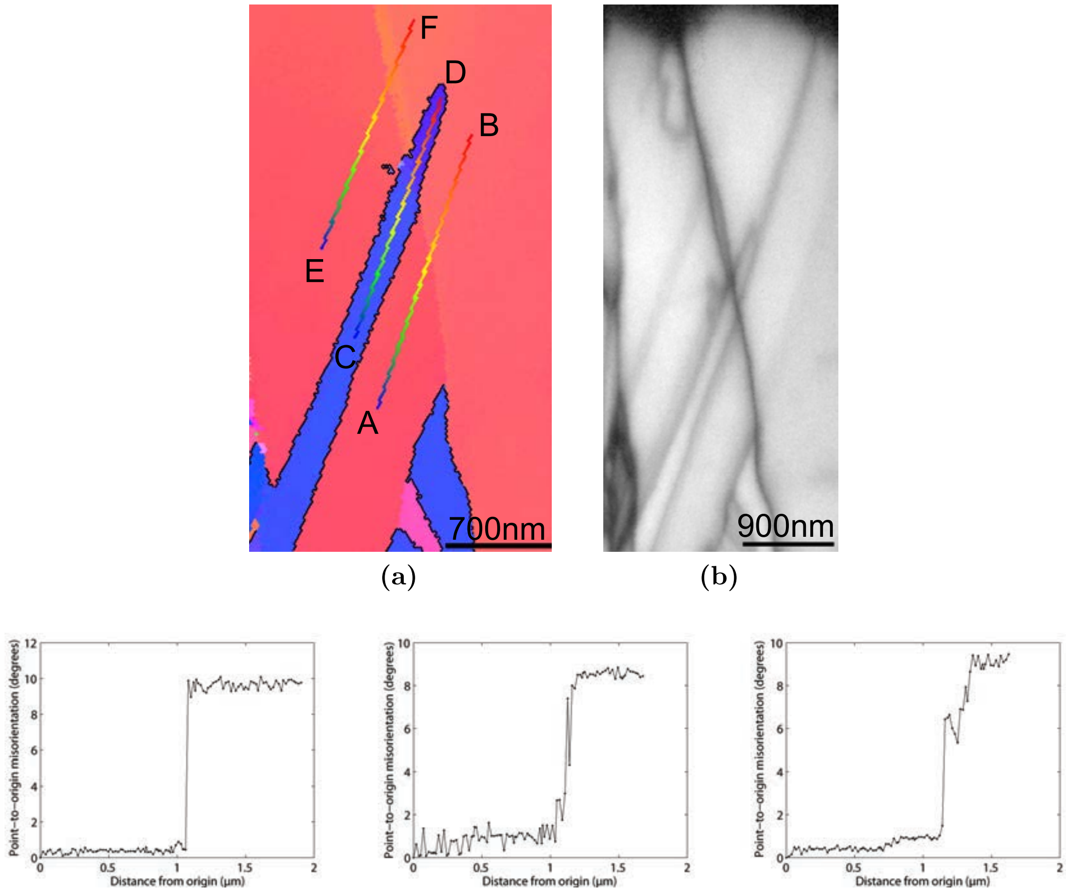

(a) (b)

(c) (d) (e)

Figure 5.18: (a) Orientation map of selected region of sample F2. A twin lamella in left hand side grain continues its growth into the neighboring grain. (b) Image Quality map of the same location. The twin gets thinner after $\approx 0.6\mu m$ growth in the neighboring grain.(c) Point to origin misorientation along AB shown in orientation map.(d) Point to origin misorientation along CD shown in orientation map.(e) Point to origin misorientation along EF shown in orientation map.

twin lamellae continue their growth into the neighboring grain. Figure 5.19 shows such an ion channeling image of a twin lamella that continues from grain ‘A’ via grain ‘B’ into grain ‘C’. There is a notable change in gray level of grain ‘B’ after the twin lamella enters it (this change is acknowledged by naming grain ‘D’ after the twin interence). The gray level of the twin lamella itself changes from 0.3125 to 0.375 (0 is black and 1 is white). This hints at a reorientation of both grain ‘B’ and the twin lamella. Furthermore, the twin lamella angle inclination angle changes when it continues its growth from grain ‘A’ into ‘B’. This change increases further when the twin lamella enters grain ‘C’ (altogether the direction of the lamella changes 28° from A to C). This illustrates the dynamic nature of continuation of twin growth in neighboring grains, which brings about a change in crystallographic orientation of neighboring grains and the twin.

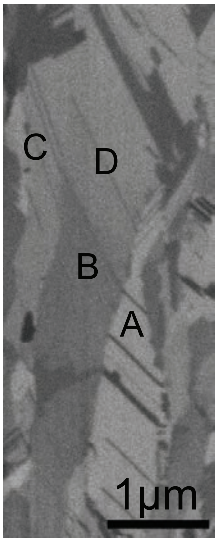

Figure 5.19: High resolution ion channeling image of sample F2. Twin lamella continues its growth from grain ‘A’ to ‘B’ and then ’C’. The orientation of grain ‘B’ and twin lamella changes due to this process.

(iii) Neighboring Grains Interdependence Growth

Figure 5.20a shows two neighboring grains, with numerous twin lamellae. It seems that, these two grains are crystallographically related to one another such that profoundly interacting. OIM, showed that there is a $\Sigma 33a$ boundary between these two grains. More importantly, an orientation variation along film growth direction was observed (Figure 5.20b). Studying the left hand side grain, point-to-origin misorientation along AB in Figure 5.20b, reveals that the average orientation gradient is $0.8°/\mu m$. The point-to-point misorientation, Figure 5.20c, shows that the orientation change is gradual. For a better comparison, higher magnification ion channeling image of the same location shown in orientation map (Figure 5.20b), is provided in Figure 5.20d. Note that there are many twin lamellae within the grain, Figure 5.20d, which are not resolved by orientation image microscopy (Figure 5.20b.

The twin lamella density, $\approx 5/\mu m$, is much higher than that of a typical <100> oriented columnar grains ($\approx 1.5/\mu m$) in this sample. It appears that due to ‘Neighboring Grains Interdependence Growth’, reorientation of both grains and formation of relatively high density of twin lamella occurs.

5.1.3.4 Grain Boundary Network

Grain boundary network is a core issue in grain boundary engineering. Figure 5.21 shows the high angle grain boundary network of the samples F1, F2, and F3, in which general high angle grain boundaries are in red and $\Sigma 3$, $\Sigma 9$, and $\Sigma 27$ are in green. Despite the high

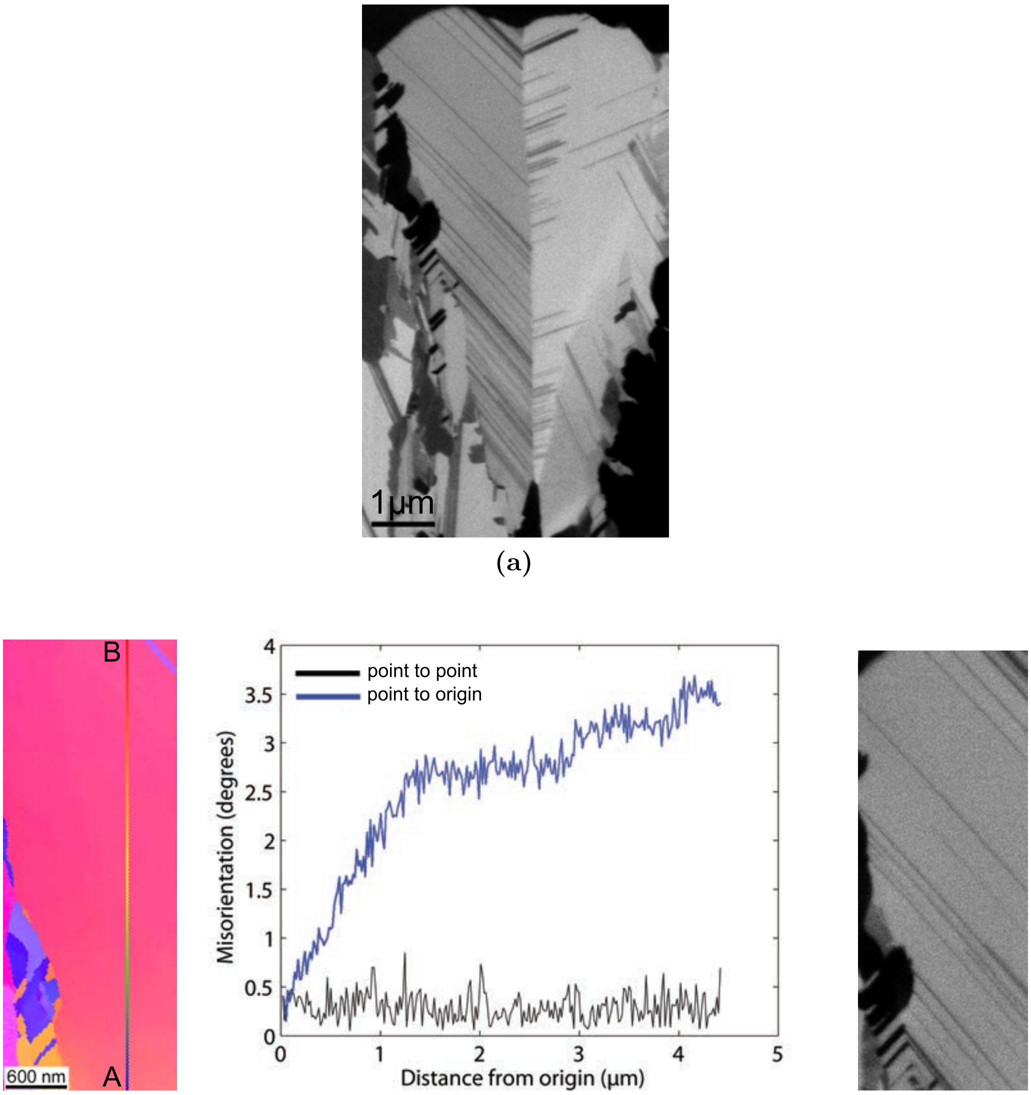

(a)

(b) (c) (d)

Figure 5.20: (a) Ion channeling image of two grains with interdependence growth with high density of twin lamellae. (b) Orientation map of selected region of the left hand side grain. (c) Point-to-origin and point-to-point misorientation along AB line. (d) Ion channeling image of the same location shown in (b). Fine twin lamella within the grain are not resolved orientation wise by OIMs.

fraction of $\Sigma 3^n, n = 1 - 3$ boundaries, especially away from the substrate interface, the network of general high angle grain boundaries is not fully broken in any of the samples; i.e. there is passage of general high angle grain boundaries from the surface to the substrate.

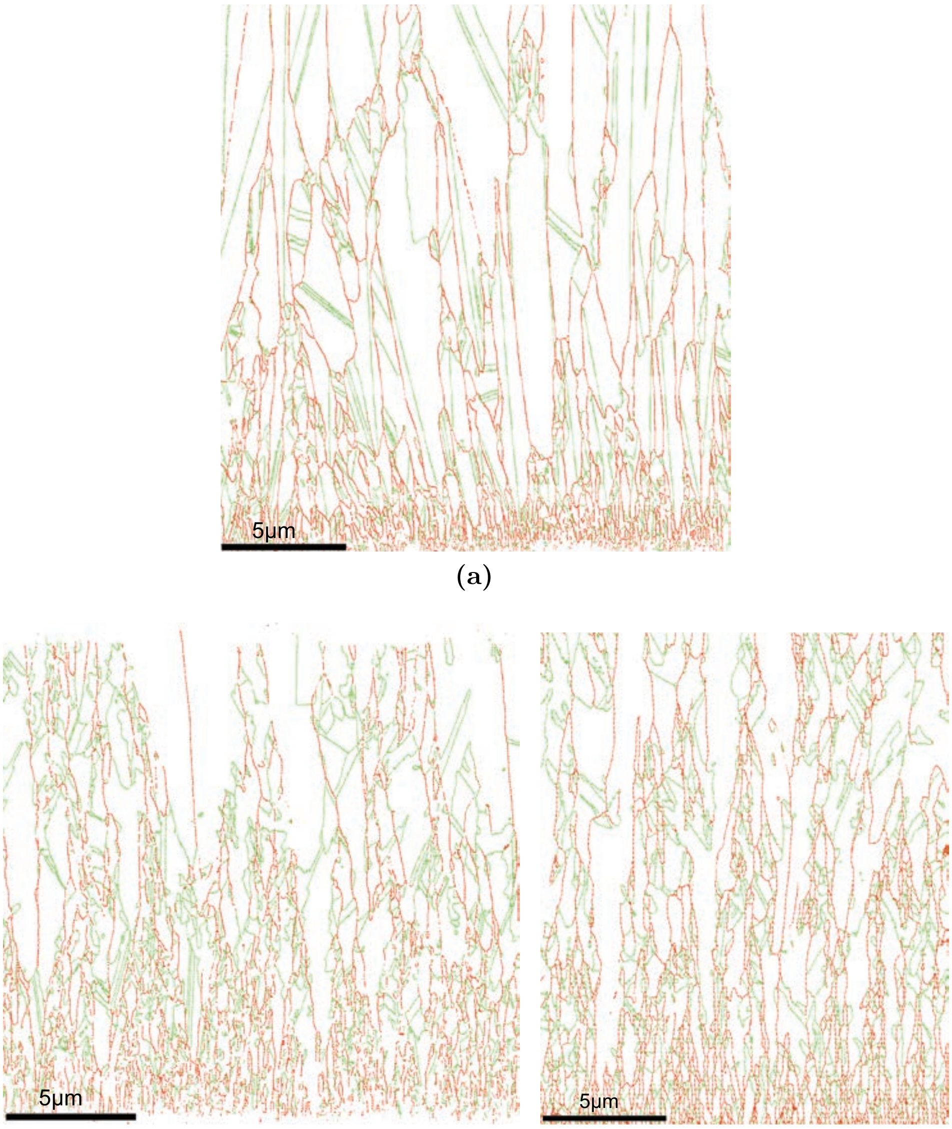

(a)

(b)

(c)

Figure 5.21: High angle grain boundary network of samples (a) F1, (b) F2, and (c) F3. $\Sigma 3$, $\Sigma 9$, and $\Sigma 27$ are shown in green and other high angle grain boundaries in red.

5.1.4 Microscopy - Medium Level of Additive

5.1.4.1 Surface Topography

The surface topography of samples synthesized in the presence of a medium level of BDO in the electrolyte, are shown in Figure 5.22. The surface topography of sample F4 is composed of both small and large protrusions. The relatively large protrusions are either elongated with a 2-fold symmetry (one is indicated by rectangle on Figure 5.22a), or have hemispherical shape (one is indicated by circle on the same figure). 2-fold symmetry protrusions seem like miniature of 2-fold symmetry protrusions shown for <211> oriented grains for sample F1 synthesized in an additive free electrolyte. Thus one may expect these protrusions are reflecting presence of <211> oriented grains in the microstructure, which is consistent with XRD texture analysis (Table 5.2). Increasing the current density from 2 to 5 A/dm^2 results in a fairly homogeneous surface topography in which some of the protrusions are slightly bigger than the rest (Figure 5.22b). A further increase of current density to 10 A/dm^2, sample F6, brings about relatively large blunt protrusions which are separated by a colony of relatively small protrusion, as shown in Figure 5.22c.

5.1.4.2 Microstructure

Ion Channeling Imaging

Ion channeling imaging was applied on the cross section of the samples, as shown in Figure 5.23. At a low level of applied current density the microstructure is composed of some notably elongated grains in the film's growth direction, and the rest of it is much smaller in size. Using applied current density to 5 A/dm^2, sample F5, the average grain size is reduced significantly, and the grain shape is less elongated in comparison with sample F4. A simple explanation is as follows: By increase of current density, nucleation rate increases and consequently, more grains are formed which are hindered to grow by the presence of BDO in the electrolyte; thus, the average grain size, decreases. Following the same argument, a further increase of current density to 10 A/dm^2, one may expect that further grain refinement occur. In contrast, the microstructure of sample F6 is composed of fine grains, mostly populated close to the film/substrate interface, and large columnar grains, mostly populated close to the film's surface.

A close observation of the columnar grains in sample F6 revealed the presence of very few twin lamellae, within the columnar grains. The twin lamellae are inclined with respect to the film's growth direction, similar to what has been shown for earlier for <100> oriented grains in samples F2 and F3. However, the twin lamella density is significantly smaller than what has been observed for <100> oriented grains synthesized in the additive free

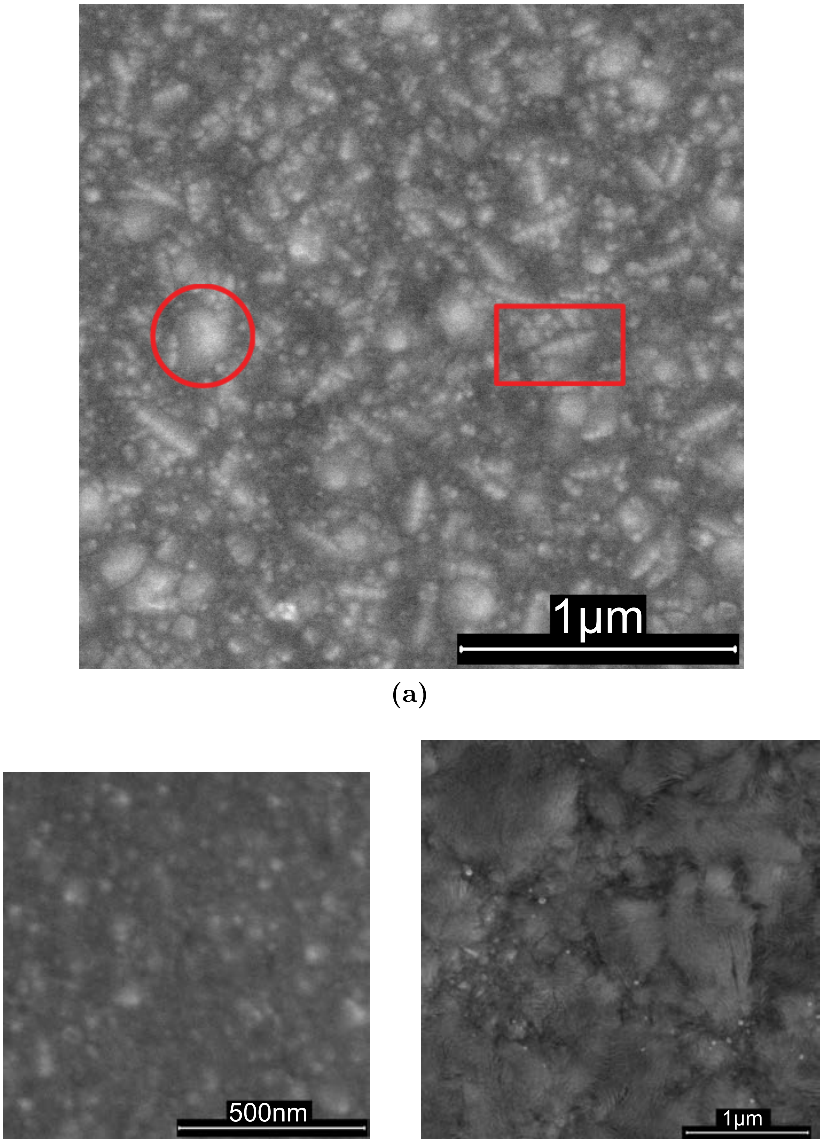

(a)

(b)

(c)

Figure 5.22: Surface topography of samples (a) F4, (b) F5, and (c) F6.

electrolyte. In addition, one can clearly see on the micrograph shown in Figure 5.23c that gray level value of most of the columnar grains is not constant and changes from one region of the column to another. This indicates that the columnar grains changing orientation.

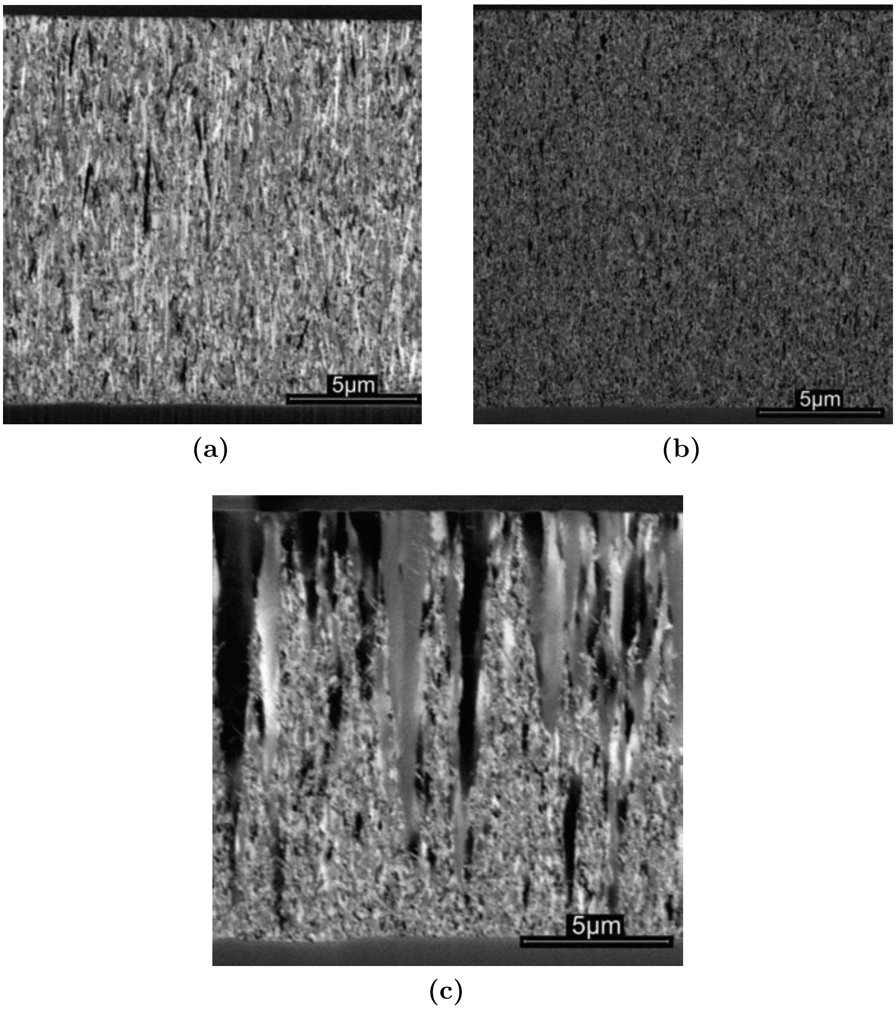

(a) **(b)**

(c)

Figure 5.23: Ion channeling image, applied on the cross section of sample (a) F4, (b) F5, and (c) F6. Applied current density increases from (a) to (c).

Orientation Image Microscopy

Though a portion of microstructure of sample F4 has such a fine grain size which is not possible to resolve with OIM, developed grains (mostly elongated) can be studied as shown in the orientation map (Figure 5.24). Most of the grains are <211> oriented (colored purple). About 60% of the data points with a confidence index[3] larger than 0.1 (38% of all data points) have an orientation that deviates less than 10° from a perfect <211> orientation.

---

[3] The definition of confidenece evidence has been provided in section 4.3.2.1

This is in good agreement with XRD texture measurement and surface topography analysis discussed earlier. $\Sigma 3$ boundaries are shown on the map by black lines which are mostly parallel to the film's growth direction, Figure 5.24b. Interestingly, most of the <211> oriented grains has a $\Sigma 3$ boundary which halves the elongated grains, similar to what has been observed for columnar grains in F1, Figure 5.24b. Since, elongated grains in Sample F4 all have the characteristics of columnar grains of sample F1 (topography, orientation, $\Sigma 3$ boundary) it is anticipated that nano-twins are present within the elongated grains but are not resolved with OIM. Since non-resolved grains are essentially very fine, and thus their boundaries contribute noticeably, quantification of the microstructure in terms of high angle grain boundaries length and $\Sigma 3/HAGB$ is not possible.

The orientation map of sample F6 is shown in Figure 5.25, the map is color coded in relation with film's growth direction. All the columnar grains shown in Figure 5.25, are approximately <100> oriented, which is in agreement with the very sharp $< 100 >$ texture obtained with XRD (Table 5.2). In the orientation map, the color of the columnar grains alters noticeably, confirming the previous conclusion from channeling imaging that there is a notable misorientation within the columnar grains. In addition, F6 has the highest value of micro-strain of <100> oriented grains in F-series samples (Table 5.5b), proving more evidence on the presence of lattice defects in this sample. However, in order to fully verify whether the large misorientations are an artifact of sample preparation, different samples were prepared with careful mechanical polishing. In the last step of preparation, even 7 μm from the prepared cross section was removed by gentle FIB milling. Regardless of the sample preparation routine, large misorientations were observed within the columnar grains. For the last check, a top view of sample F6 is also prepared, and that also showed the large misorientation. Thus, the results obtained by different methods for sample F6 are consistent.

For a columnar grain point-to-point and point-to-origin misorientations in the growth direction (marked by AB) and perpendicular to that (marked by CD) were calculated and are shown in Figure 5.25b and 5.25c. Along 'AB' line point-to-point misorientation is relatively small showing a gradual change in orientation. However this gradual change accumulates to close to 13° misorientation with respect to the origin ($\approx 1.3°/\mu m$). This shows a large change of crystal lattice orientation within the singular grain. Along 'CD' line point-to-point misorientation shows a peak showing that a low angle grain boundary is present within the columnar grain. This is also observed in other columnar grains, and it seems as columnar grains with fairly close orientations merge and form a larger grain. Point-to-origin misorientation in 'CD' direction shows very large misorientation across the column ($\approx 6.6°/\mu m$). Generally, misorientation per length in the film's growth direction

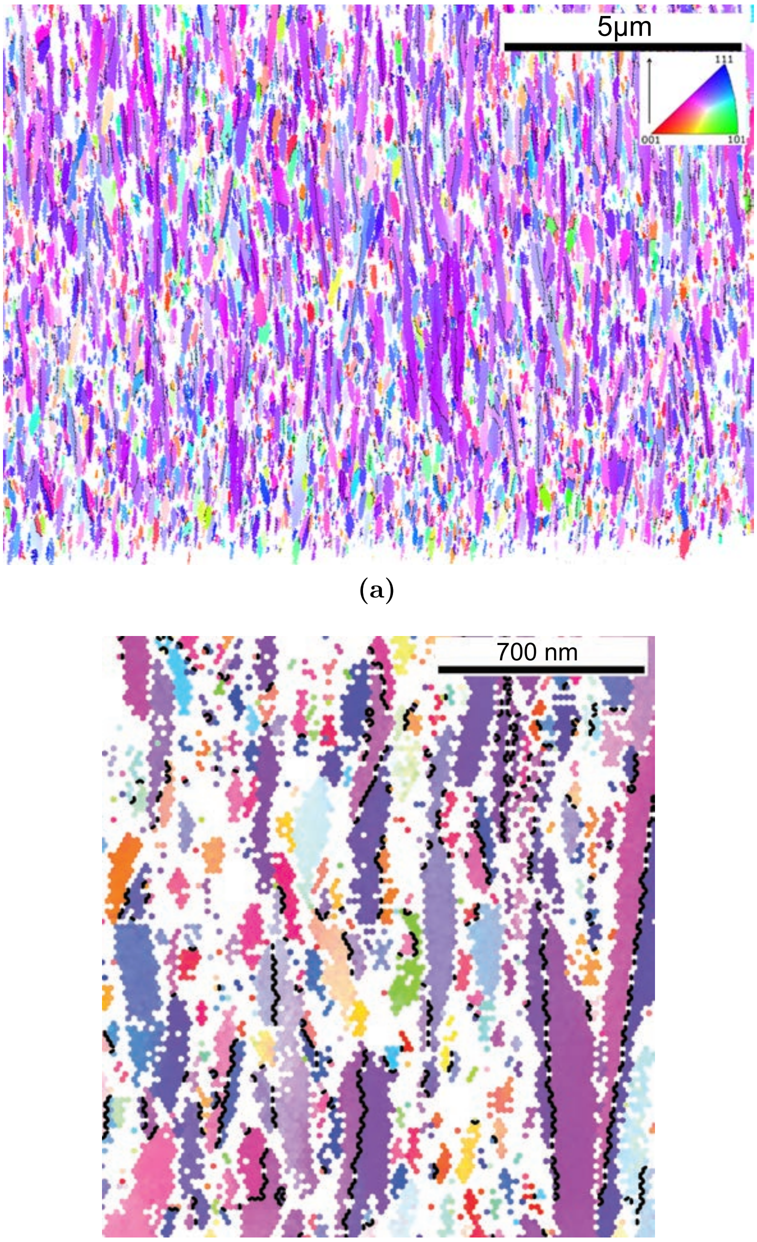

(a)

(b)

Figure 5.24: (a) Orientation map of sample F4. Σ3 boundaries are marked by black lines which are mostly parallel to the film's growth direction. The map does not cover whole cross section to the film's surface. (b) the same as (a) but in higher magnification to clarify the Σ3 boundaries.

is smaller than misorientation per length within the plane of the layer.

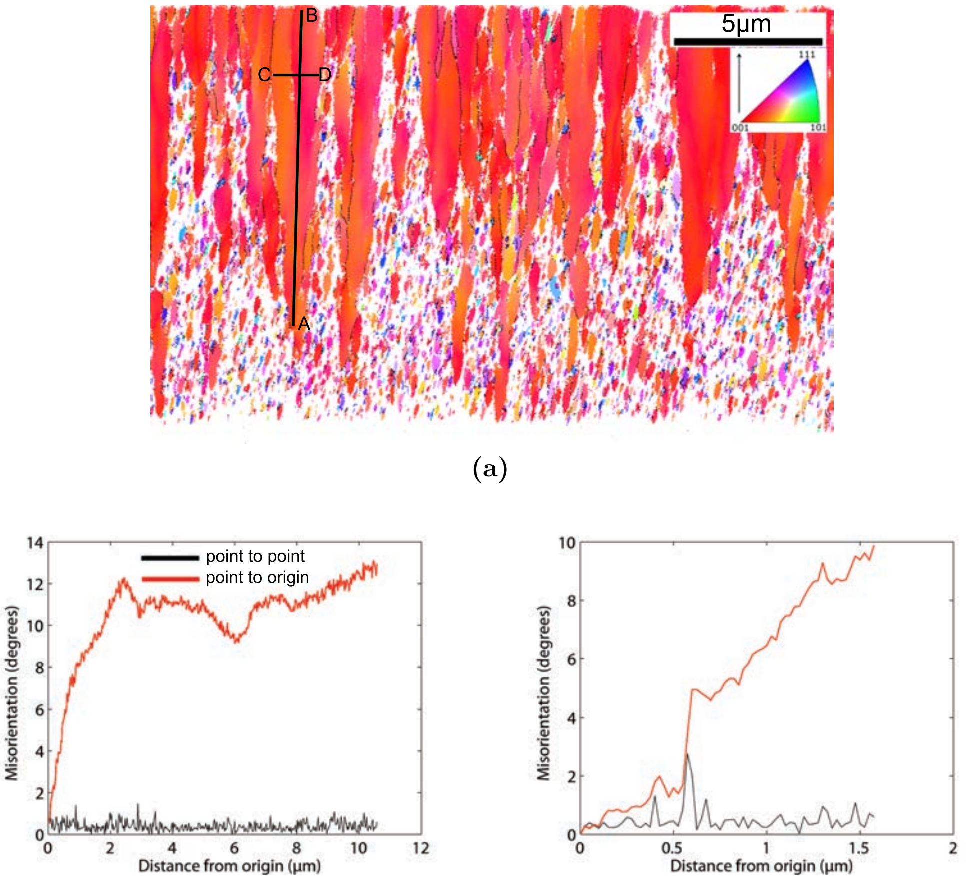

(a)

(b)

(c)

Figure 5.25: (a) Orientation map of sample F6. There is large misorientation between the points within large <100> oriented columnar grains. Point-to-point and point-to-origin misorientation in 'AB' (b) and 'CD' (c) directions.

These results show that by increase of the current density to $10 A/dm^2$, the inhibition intensity decreases such that grain refinement does not longer occur properly. Reduction of the inhibition intensity brings about formation of columnar grains.

5.1.5 Microscopy - High Level of Additive

5.1.5.1 Surface Topography

The surface topography of samples synthesized in the presence of a high level of BDO in the electrolyte, are shown in Figure 5.26. The surface topography of sample F9 (synthesized at low level of current density) has a cauliflower appearance in which relatively large protrusions ($\approx 200 nm$ in diameter) are composed of very small protrusions (fractal topography), Figure 5.26a. By increase of the applied current density to 5 and 10 A/dm^2, colonies do not form any longer and singular protrusions stick out of the surface, Figure 5.26b and 5.26c.

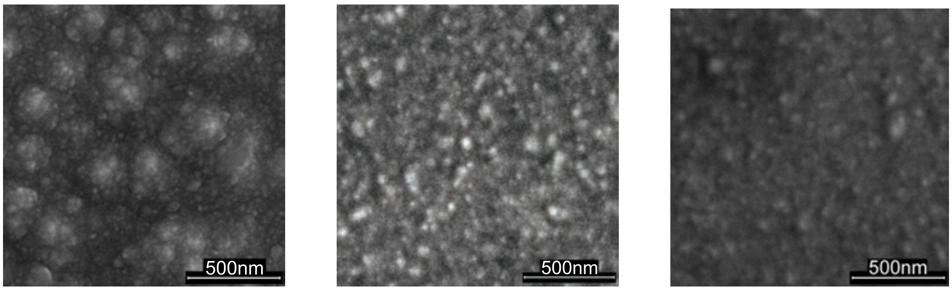

(a) (b) (c)

Figure 5.26: Surface topography of samples synthesized in high level of additive for direffent applied current density: (a) $2A/dm^2$: F9, (b) $5A/dm^2$: F8, and (c) $10A/dm^2$: F7.

5.1.5.2 Microstructure

Ion channeling imaging was applied on the cross section of the samples, as shown in Figure 5.27. At a low applied current density, sample F9, the microstructure is composed of some notably elongated grains in the growth direction. The width of these elongated grains is of the same magnitude as the diameter of cauliflowers shown in Figure 5.26a. Thus, it seems that elongated grains are actually the colony of fine grains which, however, cannot be resolved with ion channeling imaging. By increase of the applied current density to 10 A/dm^2, sample F7, the microstructure becomes more homogeneous in terms of grain size. Similar to what was argued for medium level of additive in the electrodeposition electrolyte, by increase of the current density, nucleation rate increases and hence fine grained microstructure forms.

5.1.6 Thickness

The thickness in the center of as-deposited films were measured at 10 different locations by light optical microscopy on cross-section. The average thicknesses of the films are listed in Table 5.6. In the absence of additive in electrolyte, there is no significant change in the film thickness by the increase of the current density. In contrast, at high additive concentration thicker films are synthesized with increasing current density.

Following Table 5.6, a general trend can be seen in which, as additive concentration increases in the electrolyte, the film thickness decreases.

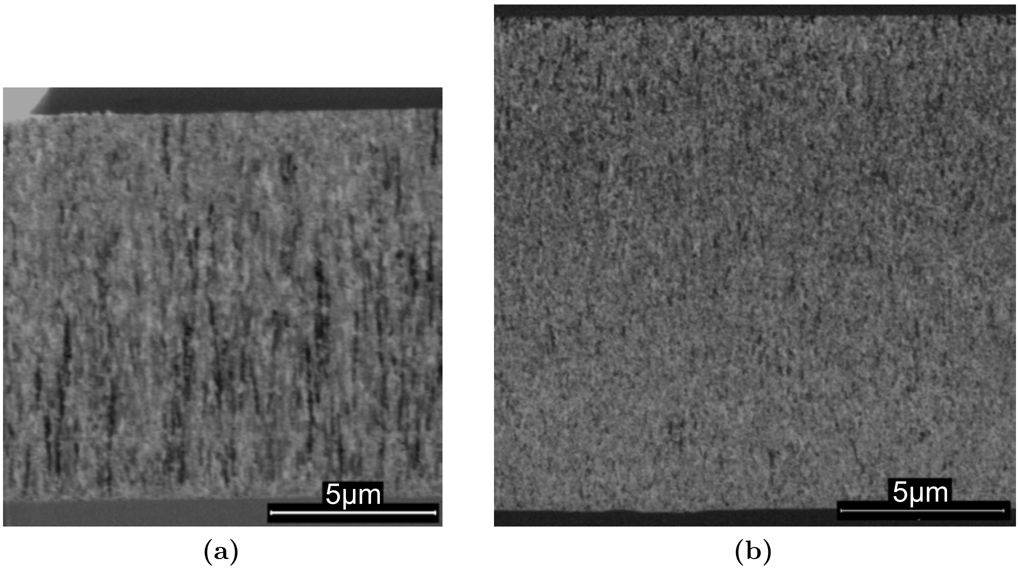

(a) (b)

Figure 5.27: Ion channeling image, applied on the cross section of sample (a) F9, and (b) F7. Applied current density increases from (a) to (b).

Table 5.6: Thickness of the F-series samples [μm], measured at the center of the electrode. C_{BDO} is in [$mMol/dm^3$].

	Thickness [μm]		
	i:2A/dm^2	i:5A/dm^2	i:10A/dm^2
C_{BDO} : 10	10.3±0.3	14.5±0.7	16.6±0.3
C_{BDO} : 5	14.9±0.5	18.1±0.5	15.3±0.4
C_{BDO} : 0	19.4 ±0.4	18±0.5	19.1±0.9

Current efficiency, is the ratio between the actual deposited mass (M$_{act}$) and the maximum theoretical mass (M$_{theo}$) calculated from Faraday's law [43]. Since the films were electrodeposited with equal charge (hence, equal M$_{theo}$) and on an equal area (A) and assuming all the films are fully dense; it concludes that film thickness is proportional to current efficiency (CE), as proved in Eq. 5.1.

$$\begin{cases} Th = M_{act}/(A \times D) \\ M_{act} = M_{theo} \times CE \end{cases} \Rightarrow Th \propto CE \tag{5.1}$$

Where D is density of electrodeposited material.

In case, the film thickness is equal all over the electrodeposited area, the current efficiency can be calculated quantitatively. In practice, it is rarely the case and most often the film thickness is varying ($Th_{corner} > Th_{edge} > Th_{center}$) [43]. Accordingly, quantitative estimation of current efficiency is not possible by thickness measurement only at the center of electrodeposited area; however that qualitatively can be used for comparison of the current efficiency. Based on that, the following trends are noted: (1) In general, the current efficiency decreases in the presence of a high concentration of BDO. (2) A lower current density is associated with a lower current efficiency at relatively high concentration of BDO.

Though the complex nature of electrodeposition impedes a universal explanation for a change of the current efficiency for all the samples, but still it can be explained partly by adsorption of BDO. BDO is dynamically adsorbed and desorbed on the cathode surface [50]. The adsorbed C≡C bond on the nickel surface undergoes a hydrogenation reaction, resulting in the formation the C=C and C−C bonds [94]. This reaction also promotes the reduction of the hydrogen cations [75, 94] which brings about more hydrogen evolution. This synergic effect of hydrogenation of BDO and hydrogen evolution, manifests itself in lower current efficiency. Thus, when the inhibition intensity of BDO is relatively high (BDO covers a higher portion of cathode surface [214]) a lower current efficiency is expected.

In this series of experiments, the concentration of BDO in the electrolyte is of the order of $mMol/dm^3$, thus based on [44], its transport to the cathode is diffusion controlled . By increasing the BDO in the bulk of electrolyte, higher coverage of additive at the cathode surface occurs. Similarly, a decrease of the current density brings about a slower formation of new surfaces, and an easy coverage of the cathode surface with BDO. Thus, the inhibition intensity of BDO is dependent on the diffusion rate to the surface and the rate of formation of new nickel surfaces.

5.1.7 Microhardness

▦ The average microhardness of the as-deposited films is tabulated in Table 5.7. Comparing the microhardness values of films synthesized with different levels of BDO in the electrolyte, it is evident that a higher concentration of the additive brings about higher microhardness. This behavior is most pronounced for the lowest current density(▦), where the microhardness is increased 2.6 and 3.5 fold due to the presence of medium and high level of BDO in the electrolyte.

It also notable that in the presence of BDO in the electrolyte, there is an inverse relation between film thickness and microhardness. The thinner the film, the higher is the microhardness. One may argue that, this originates from the effect of surface or interface with the substrate on the microhardness measurement. However, the distance from the corners of the indentation mark to the film surface and substrate was measured and it was larger than 2.5 times indentation diameter (see Figure 4.13), hence, the effect of nearby surface or interface can be ruled out.

When inhibition intensity is high, formation of new crystallites (grains) and crystallographic

Table 5.7: Microhardness of the F-series samples using Vickers method H_v, $[KgF/mm^2]$, measured in cross-section at the middle of film's thickness. C_{BDO} is in $[mMol/dm^3]$.

	Microhardness $[KgF/mm^2]$		
	i:$2A/dm^2$	i:$5A/dm^2$	i:$10A/dm^2$
C_{BDO} : 10	555±53	519±59	423±35
C_{BDO} : 5	409±33	381±26	256±13
C_{BDO} : 0	158 ±19	174±22	168±10

faults are more probable [214], accordingly the density of grain boundaries in the film and crystallographic faults increases (see Table 5.4 for grain size and micro-strain). Accordingly the change in hardness with increasing BDO concentration is due to grain refinement and increase of micro-strain.

5.2 BipH-Series Samples

It has been demonstrated [75]that, formation of a <211> fiber texture in nickel films electrodeposited in a Watts electrolyte is caused by the inhibition effect of $Ni(OH)_2$. Accordingly a higher pH of the electrolyte should result in the formation of more <211> oriented grains. To the contrary of this expectation, it was reported that an increase of pH deters formation of <211> oriented grains [75]. Hence, there must be an optimal concentration of $Ni(OH)_2$ at the surface, for which the highest strength of a <211> texture can be achieved. It is also argued that a buffer characteristic of NH_4^+ promotes dynamic formation and decomposition of $Ni(OH)_2$ which leads to a more pronounced <211> fiber texture [85]. Boric acid is used as the buffer agent in a standard Watts electrolyte. Accordingly a higher concentration of boric acid in an electrolyte with higher pH may promote the formation of a <211> texture. To study this, BipH-series of experiments were designed based on the results obtained in F-series experiments. In the Watts electrolyte used in the F-series experiments, sample F1 synthesized for a boric acid concentration of 40 g/dm^3, pH of 4.5 and applied current density of 2 A/dm^2 had the highest strength of <211> fiber texture (see section 5.1.1). This sample was used as the reference sample to study the effect pH and boric acid concentration on formation of a <211> fiber texture; For this purpose, 10 other samples were synthesized in this series of experiments. The samples have 5 digit names in which the boric acid concentration in g/dm^3 makes the first two digits -B-, the third digit is current density in A/dm^2 -i-, and the last two digits are pH×10 (see 4.1.3.2 for experimental details). The samples discussed in each are indicated by a gray color in a 3×4 marker. One should note that sample in BipH series is sample F1 in F-series samples. Thus,the data for sample 40245 is identical to what has been reported earlier in section 5.1.

5.2.1 XRD Texture Analysis

Since all the samples had a fiber texture in ND, inverse pole figures in ND fully characterize the texture (Table 5.8). Following the first column, an increase of pH from 4.5 to 5.0, weakens and broadens the <211> fiber texture. A further increase of pH to 5.5 in the electrolyte, leads to a weak texture away from <211>. The same trend is seen for boric acid concentrations of 50 g/dm^3 and 60 g/dm^3: samples synthesized at pH=4.5 have a relatively strong and sharp fiber texture and an increase of pH in the electrolyte brings about electrodeposits with broader and weaker texture away from the one for pH=4.5.

The general effect of an increase of the boric acid concentration in the electrolyte on the

Table 5.8: Inverse pole figures in normal direction for F-series as-deposited films obtained from XRD texture analysis. Orientation density maxima are indicated on the figures. Units are in MRD. The shown inverse pole figures are the standard triangle, (1/24) of stereographic projection circle. The crystallographic directions are shown for sample 40245 and for the sake of brevity is not repeated for the rest of samples. $C_{\mathrm{H_3BO_3}}$ in g/lit and i in A/dm^2.

	$C_{\mathrm{H_3BO_3}}$: 40	$C_{\mathrm{H_3BO_3}}$: 50		$C_{\mathrm{H_3BO_3}}$: 60
	i=2	i=1	i=2	i=2
pH=4.5	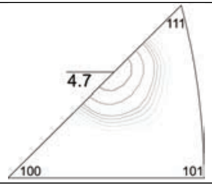	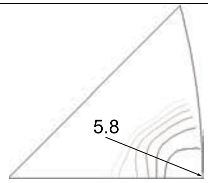	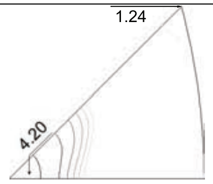	
pH=5.0	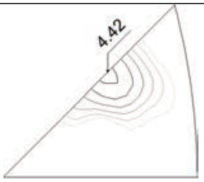	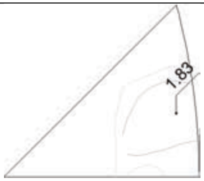	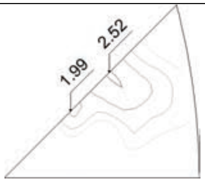	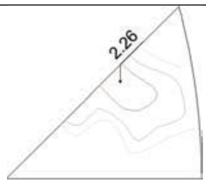
pH=5.5	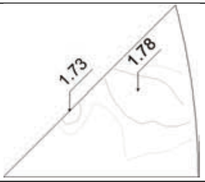	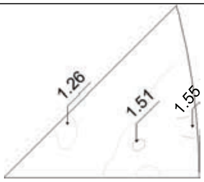	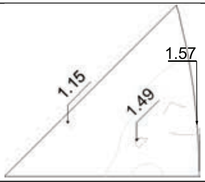	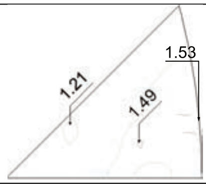

formation of a <211> fiber texture can be seen comparing samples 40250, 50250, and 60250 (▦). The maximum orientation density of the <211> fiber component in samples 40250, 50250, and 60250 is 4.42, 2.52, and 2.26 respectively. Hence, by increasing the boric concentration in the electrolyte (at $pH = 5.0$ and $i = 2\ A/dm^2$) the texture component becomes weaker and broader. The effect of boric acid is not limited to a reduction of texture strength. Comparing samples 40245 and 50245 (▦), clearly shows that an increase of the boric acid concentration in the electrolyte, influences the chemistry such that <100> becomes the preferred orientation. It means that formation of $Ni(OH)_2$ on the surface is significantly suppressed. Noting that boric acid acts as the buffer agent, its higher concentration hinders formation of hydroxides which requires an increase of pH [61].

The sample synthesized at a current density of 1 A/dm^2 (50145, ▦) under similar conditions as sample 50245, has a relatively strong <110> fiber texture. It is well known that for very low applied current density, <110> becomes the preferred orientation [75]. It has been shown that at pH=4.5 and boric acid concentration of 40 g/dm^3, the applied current density must be smaller than 0.3 A/dm^2, in order to obtain <110> fiber texture [75]. Hence, the current results show that for a higher concentration of boric acid, the maximum current density at which <110> oriented grains form, increases to a higher value. This concludes that at pH=4.5, an increase of the boric acid concentration from 40

to 50 g/dm^3, increases the range of current density at which <110> and <100> oriented grains form. And under these conditions (pH=4.5, $C_{\mathrm{H_3BO_3}} = 50\ g/dm^3$), formation of <211> is fully suppressed (or is limited to a very small range of current density).
In order to correlate XRD texture analysis to the samples microstructures and surface topographies, microscopy was conducted on some selected samples.

5.2.2 Microscopy

5.2.2.1 Effect of pH

The surface topographies of the samples synthesized at a boric acid concentration of 40 g/dm^3 (▦)are shown in Figure 5.28. The typical 2-fold symmetry protrusions of <211> oriented grains are visible in Figures 5.28a and 5.28b. However, in Figure 5.28c this type of protrusions is less populous. An increase of pH to 5.0 and 5.5, leads to the formation of cactus-like protrusions on the surface as can be seen on Figure 5.28b and 5.28c. These cactus-like features are colonies of grains formed by growth of branches to a main body (see protrusion marked by ‘C’ on Figure 5.29a). How these features form, can be realized by close observation of the surface topography shown in Figure 5.29a.

Looking at the location marked by ‘A’ on Figure 5.29a, it can clearly be seen that on a typical 2-fold symmetry protrusion new grains can nucleate. It shows that the inhibition was strong enough to impede further growth and instead nucleation of new grains occurs. As can be seen in Figure 5.29a in the location marked by ‘B’, nucleation of new grains takes place on either the faces of a 2-fold symmetry protrusion or on its tip. Those new grains which are formed on the faces grow untill they meet the neighboring grains. In contrast those which are formed on the tip of a 2-fold symmetry can grow freely into the electrolyte. This makes the body of cactus-like features and since it sticks out of the surface, on its sides, nucleation of new grains can occur. Growth of these nuclei forms the branches of the cactus-like feature, see location marked by ‘C’ on Figure 5.29a.
Ion channeling micrographs of the cross sections of samples 40250 and 40255 (▦) are shown in Figure 5.30. It is evident that there is a inverse relationship between the size of the cactus-like features at the surface and the distance from the substrate where the feature starts to form. At pH=5.0 the cactus-like feature starts to form relatively far away from the film/substrate interface, and by increase of pH to 5.5 these features can form much closer to the interface. The conical shape of the cross section of the cactus-like features confirms the conclusion drawn based on surface topography, in which the base of the feature sticks out of the surface and then branches nucleate on that base. Note that pronounced conical features in Figure 5.30 correspond to big cactus-like features in

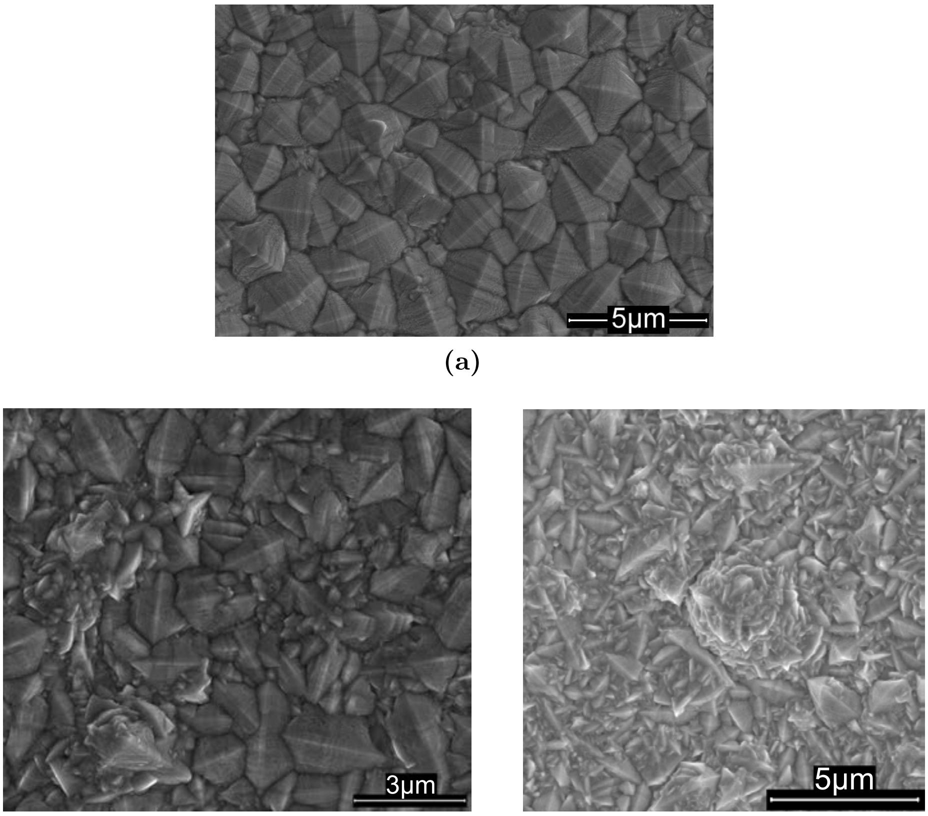

(a)

(b) (c)

Figure 5.28: Surface topography of samples (a) 40245, (b) 40250, and (c) 40255.

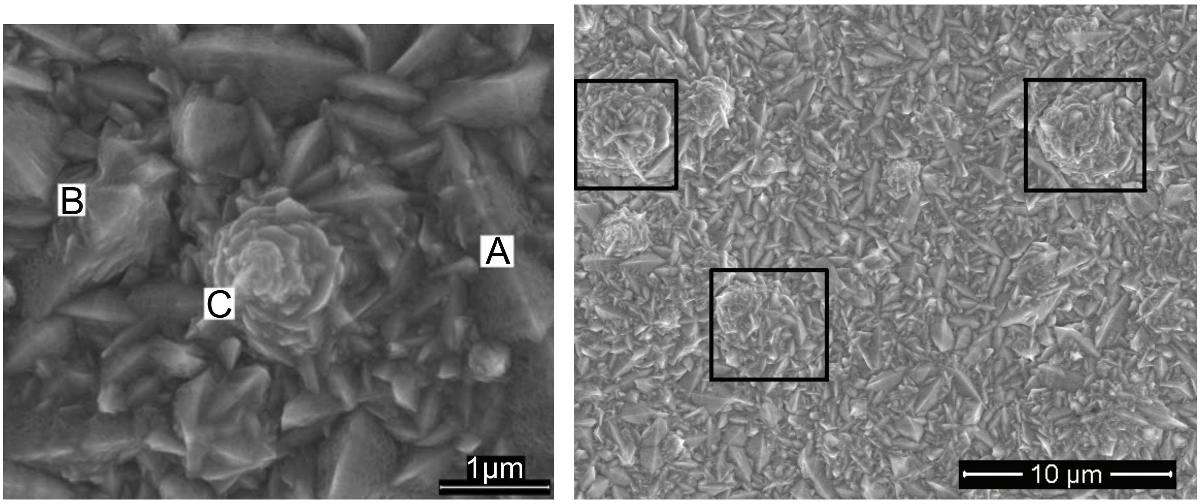

(a) (b)

Figure 5.29: (a) Surface topography (of sample 40255) of different stage of cactus-like features formation. ‘A’ shows very early stage; ‘B’ represents slightly developed stage; and ‘C’ indicates fully developed cactus-like feature. (b) Surface topography of sample 40255 showing different sizes of cactus-like features. Some (enclosed by rectangles) are as large as $5\mu m$ in width as .

Figure 5.29b and the small cactus at an early stage of formation is chosen to illustrate the mechanism of formation in Figure 5.29a.

XRD texture analysis and microstructure characteristics are correlated as follows: Formation of cactus-like features reduces the volume fraction of <211> oriented gains. When cactus-like features increase in the microstructure (see surface topography of sample 40255 in Figure 5.29b) the texture is not pronounced.

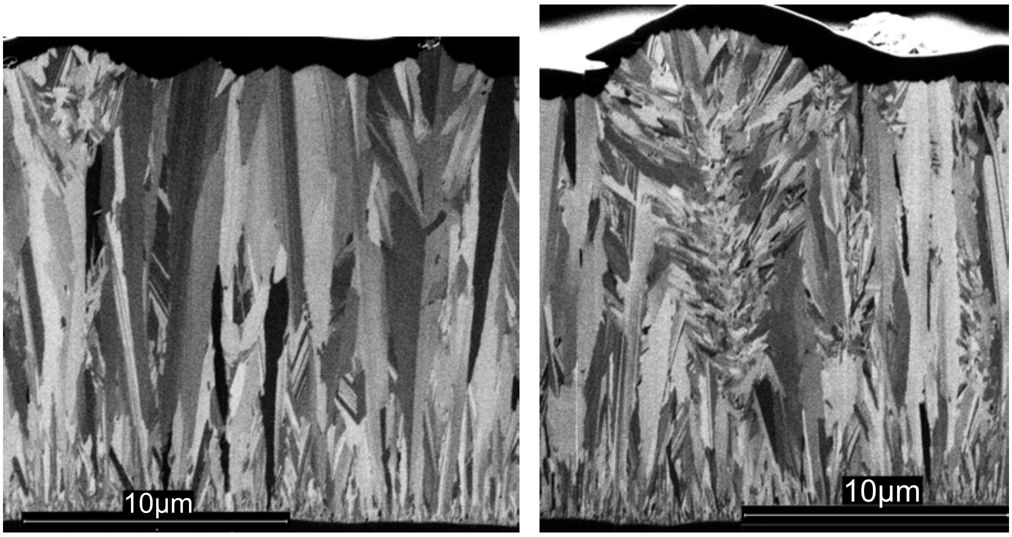

(a) (b)

Figure 5.30: Ion channeling images on the cross section of samples (a) 40250, and (b) 40255. Other than columnar grains with twin lamellae parallel to growth direction (typical of <211> oriented grains) the conical shape of cactus-like features with very many branches are clearly visible.

5.2.2.2 Effect of Boric Acid Concentration

The surface topography of sample 50250 (▦) is shown in Figure 5.31a. It is composed of fairly large typical 2-fold symmetry protrusions of <211> oriented grains and smaller protrusions some of which show 2-fold symmetry. Larger protrusions exceed 5 μm in diameter which is much larger than any other sample studied in this series of experiments. The microstructure of the sample was analyzed by ion channeling imaging on the cross section as shown in Figure 5.31b. Relatively wide columnar grains with twin lamellae approximately parallel to the film's growth direction, i.e. the signature of <211> oriented grains, [75, 168] are clearly visible in the microstructure. In addition, columnar grains are separated by relatively smaller grains. XRD texture analysis has revealed the presence of <211> and <311> oriented grains in this sample (see section 5.2.1). Thus most probably the smaller grains which do not show typical features of <211> oriented grains are <311> oriented grains.

Comparing the microstructure of samples 50250 (Figure 5.31b) with 40250 (Figure 5.30a), shows that a higher concentration of boric acid impedes the formation of cactus-like features. However, it promotes the formation of grains with orientations other than <211> in the electrolyte.

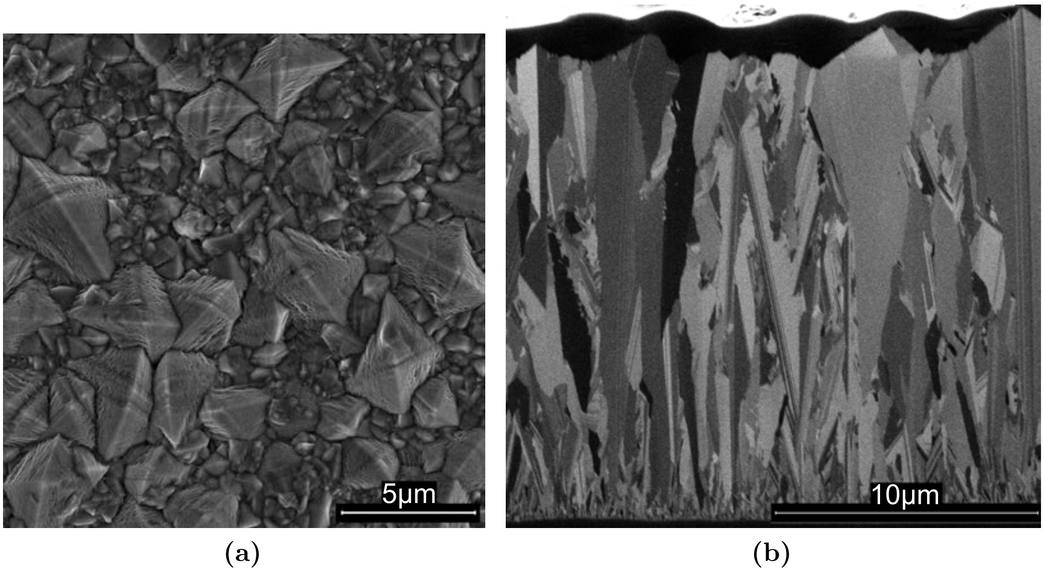

(a) (b)

Figure 5.31: (a) Surface topography of sample 50250, some pronounced 2-fold symmetry protrusions (typical of <211> oriented grains) are separated by relatively smaller protrusions. (b) Ion channeling images on the cross section of sample 50250.

In conclusion, sample 40245 (H_3BO_3 of 40 g/dm^3 and pH=4.5) brings about the most pronounced <211> fiber texture in the experimental conditions investigated. By increase of pH from 4.5 and boric acid concentration from 40 g/dm^3 the strength of the <211> fiber texture component is reduced and other texture components appear. Generally, the crystallite orientation approaches a random distribution.

5.3 Co-Series Samples

It has been shown in section 5.2 that in the experimental conditions examined in BipH series of experiments, the strongest <211> fiber texture was obtained in a Watts electrolyte as follows: boric acid concentration of 40 g/dm^3, applied current density of 2 A/dm^2, and pH=4.5. Based on that, the Co-series of experiments were conducted to study the effect of adding ^{27}Co into the electrolyte on the microstructure of the deposit. Since introducing chemical species in the electrolyte potentially influences the texture of electrodeposited film cobalt sulfate salt was added to the electrolyte. It is worth reminding that the two digits at the end of sample names indicates the concentration of Co^{+2} in $[mMol/dm^3]$, in the electrolyte (see section 4.1.3.3).
The texture of the samples was obtained by XRD texture analysis. The two samples had a fiber texture in ND and an inverse pole figure in ND is shown in Table 5.9.

Table 5.9: Inverse pole figures in normal direction for Co-series films obtained from XRD texture analysis. Orientation density maxima are indicated on the figures. Units are in MRD. The shown inverse pole figures are the standard triangle, (1/24) of stereographic projection circle. The crystallographic directions are shown for sample Co20 and for the sake of brevity is not repeated for the rest of samples. C_{ion} is in $[mMol/dm^3]$.

Co20	Co40
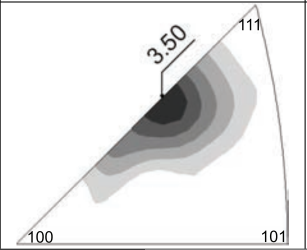	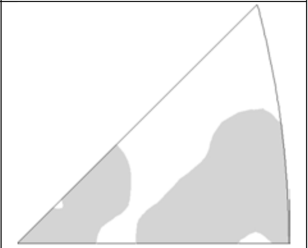

● ● ● ● ● ●
1.0 1.5 2.0 2.5 3.0 4.0MRD

Sample Co20 has a <211> fiber texture; however, the maximum orientation density of that(3.5 MRD) is smaller than 4.7 MRD which was obtained in an electrolyte with no Co^{2+} (see sample F1 in Table 5.2). This shows that formation of a <211> fiber texture is partially suppressed. Further increase of Co^{2+} in the electrolyte to 40 $mMol/dm^3$, bring about an almost texture free film (sample Co40).

Using the Williamson-Hall method on the first four reflections, the average grain size (coherently diffracting domain size) and micro-strain of Co-series samples were evaluated, and the results are provided in Table 5.10. It is evident that by increase of Co^{2+} from zero to 20 $[mMol/dm^3]$ in the electrolyte, the grain size and micro-strain do not change significantly (compare Co20 in Table 5.10 with F1 in Table 5.3a). However, increase of Co^{2+} concentration in the electrolyte from 20 to 40 $[mMol/dm^3]$ results in an increase of

Table 5.10: Co-series samples average grain size in $[nm]$ and micro-strain obtained by Williamson-Hall method for the first four reflections.

	Co20	Co40
grain size $[nm]$	88	100
Micro-strain	0.0001	0.0021

the average grain size and micro-strain.

Peak position ($2\theta^{\circ}_{p}$) of the samples are compared with pure nickel peak position $[JCPDS4-850]$ and the peak shift ($2\theta^{\circ}_{p}-2\theta^{\circ}_{standard}$) is calculated for the first two reflections (Table 5.11). It is evident that the peak positions are shifted to lower $2\theta^{\circ}$, proving the formation of Ni-Co alloy.

Table 5.11: The peak shift of 111 and 200 reflections for Co-series samples.

	Co20	Co40
111 peak shift $2\theta^{\circ}$	-0.06	-0.10
200 peak shift $2\theta^{\circ}$	-0.02	-0.03

In order to achieve alloy compositions quantitatively, EDS was applied on the samples. Samples Co20 and Co40 comprise 15.6 and 36.7 $wt.\%$ of cobalt respectively.

5.3.1 Microscopy

Ion channeling imaging was conducted on a cross section of the sample Co20, Figure 5.32a. Observing the microstructure in Figure 5.32a, clarifies that it is unlike typical columnar microstructure and there is a bi-modality in the columnar grains: Mode (i) the type columnar grains which form at certain distance from the film/substrate interface and continue their growth as electrodeposition continues. Mode (ii) is typified by relatively smaller columnar grains in comparison with grains of mode (i). Columnar grains of mode (ii) are evidently less favorable for growth, i.e. growth selection favors columns of mode (i). This is clearly shown in Figure 5.32a by enclosing a region by red rectangle.

OIM of the same location where ion channeling image was obtained, revealed that columnar grains of mode (ii) are mostly <100> oriented (see Figure 5.32b). Furthermore, columnar grains of mode (i) are mostly <211> oriented. The area fraction of <100> and <211> data points[4] of the map is evaluated for different distances from the practical interface, and the result is provided Figure 5.32c. It shows that up to 7 μm from the practical interface, <100> is the preferred orientation and afterwards <211> takes over. One singular <110> oriented grain (colored in green) is present close to the film surface, Figure 5.32b. In the orientation map which shows relatively few grains, it may seem significant. However,

---

[4] allowing 10° deviation

XRD texture analysis (Table 5.9) showed that <110> component is not a major texture component. Hence, the <110> area fraction is not shown in Figure 5.32c.
<211> oriented columnar grains in Figure 5.32b were located in Figure 5.32a to quantify the number of twin lamellae within these grains. The number of <211> oriented columnar grains are not large enough to assure reliable statistics, but it appears that the number of twin lamella is comparable with that of pure nickel films (see section 5.1.3.3). Hence, alloying nickel with cobalt did not result in higher twin lamellae formation in <211> oriented grains.

The EDS analysis was applied on the cross-section shown in Figure 5.32a. It was found that chemical composition is very homogeneous and the cobalt concentration is $\approx 15.6\ wt.\%$ all over the scanned area.

The average microhardness in the middle of the sample thickness was measured ($186 \pm 16\ H_v$). However since the criteria mentioned in section 4.3.6 did not prevail (distance from the corners of the indentation mark to the film surface and Ni-P interface was smaller than 2.5 × indentation diameter) the value is not authentic.

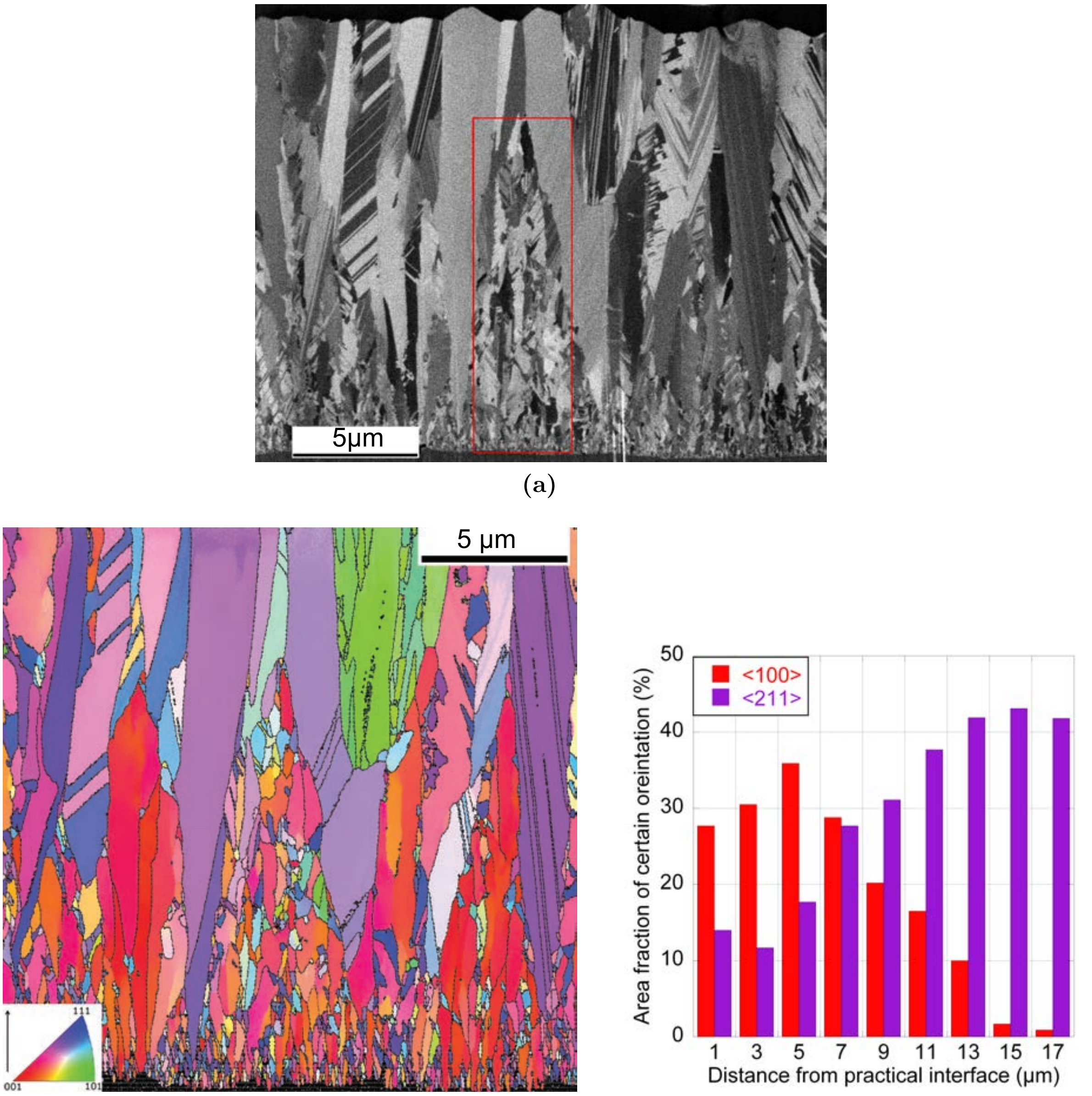

(a)

(b)

(c)

Figure 5.32: (a) Ion channeling image of sample Co20. Columnar grains are bi-modal. The region enclosed by red rectangle shows columnar grains of mode (ii). (b) Orientation map of sample Co20, color coded in respect with film growth direction shown by an arrow on the map's legend. High angle grain boundaries are in black^5. (c) Area fraction of <100> and <211> data points vs distance from the practical interface.

5.4 Sample 8C10

Sample 8C10 was synthesized in a electrolyte with 40 g/dm^3 H_3BO_3 and pH of 2.0, current density of $10A/dm^2$ (see section 4.1.3.4).

5.4.1 XRD Texture Analysis

Sample 8C10 was subjected to XRD texture analysis. Since the sample has a fiber texture in ND, an inverse pole figure in ND fully characterizes the texture, as shown in Figure 5.34. The major texture component of the sample is <210> fiber with orientation density of 3.8 MRD. There are also two minor components <542> and <711> fiber texture with orientation density of 1.4 and 1.2 MRD respectively.

Calculating the twin orientation in FCC nickel [207] shows that these three orientations are related to one another by a twining operation. The first generation twins of <210> is either <210> or <542>; The first generation twins of <542> are approximately <542>, <210> and <30 3 1> see Figure 5.33.

Since <711> and <30 3 1> are very close orientations (there is only 6.6° between the two), it concludes that <542> and <711> are first and second generation twins of major texture component, <210>, respectively. This strongly suggest that multiple twinning has occurred in this sample.

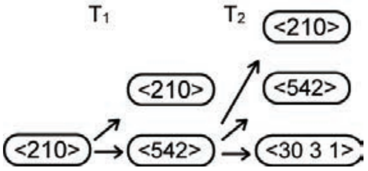

Figure 5.33: First generation and second generation twins of <210>.

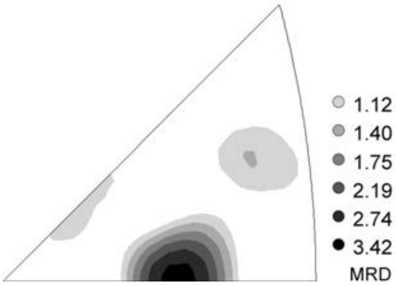

Figure 5.34: Inverse pole figure in ND for sample 8C10 obtained by XRD texture analysis. <210> is the major texture component (3.8 MRD). <542> and <711> are minor texture components (1.4 and 1.2 MRD respectively).

5.4.2 Microscopy

Ion channeling imaging was conducted on a cross section of the sample 8C10 such that the entire film from substrate interface to the surface is covered, Figure 5.35a. It shows that many of the grain boundaries are actually straight lines, suggesting that the majority of the grains are in twin relation with their neighboring grains. This puts more emphasis on the previous conclusion that multiple twinning has occurred in this sample. High magnification ion channeling image of the microstructure close to the film/substrate interface, Figure 5.35b, shows that in the first $\approx 1\ \mu m$, the microstructure is extremely fine. After that, relatively large grains with characteristic straight boundaries start to occur. As deposition continues, the grains become larger but still they have the same characteristic straight boundaries, as can be seen in Figure 5.35c, which shows the microstructure of the sample close to the surface.

It is noted that there is an inhomogeneity in the microstructure. The two rectangles in blue and red in Figure 5.35b, are at the same distance from the film/substrate interface ($\approx 7\ \mu m$), however, the microstructure enclosed by blue rectangle is finer than that enclosed by red rectangle. The very similar inhomogeneity can be seen at larger distance from the film/substrate interface, i.e. close the surface. In Figure 5.35c (ion channeling image close the surface) regions marked by blue and red rectangle ($\approx 15\ \mu m$ from film/substrate interface) have also different grain sizes.

Apart from the grain size, regions marked by blue in Figures 5.35b and 5.35c, have more non-straight boundaries (most probably general high angle grain boundaries) in comparison with the regions marked by red in the same figures.

Characterization of the boundaries and understanding the orientation relations between the grains was further investigated with OIM.

An orientation map covering the deposit in cross section of sample 8C10 is shown in Figure 5.36 ($\Sigma 3$ boundaries are marked in black). At the first glance, it becomes evident that the microstructure is composed of columns; most notably <210> oriented columns are sub-divided in several <210> oriented grains separated by $\Sigma 3$ boundaries. This can be more clearly seen in Figure 5.37a where data points with less than 10° deviation from <210> (the yellowish colored grains) form a column. It is evident that a <210> oriented grain, twinned to another grain which is <210> oriented, and that grain itself, later twinned to another <210> oriented grain, and this process was continued. Accordingly, these <210> oriented columns are the result of repeated twinning of <210> $\longrightarrow$ <210>. Figure 5.37b shows the same orientation map but only data points with less than 10° deviation from <210> or <542> are shown ($\Sigma 3$ boundaries are marked in black). Clearly

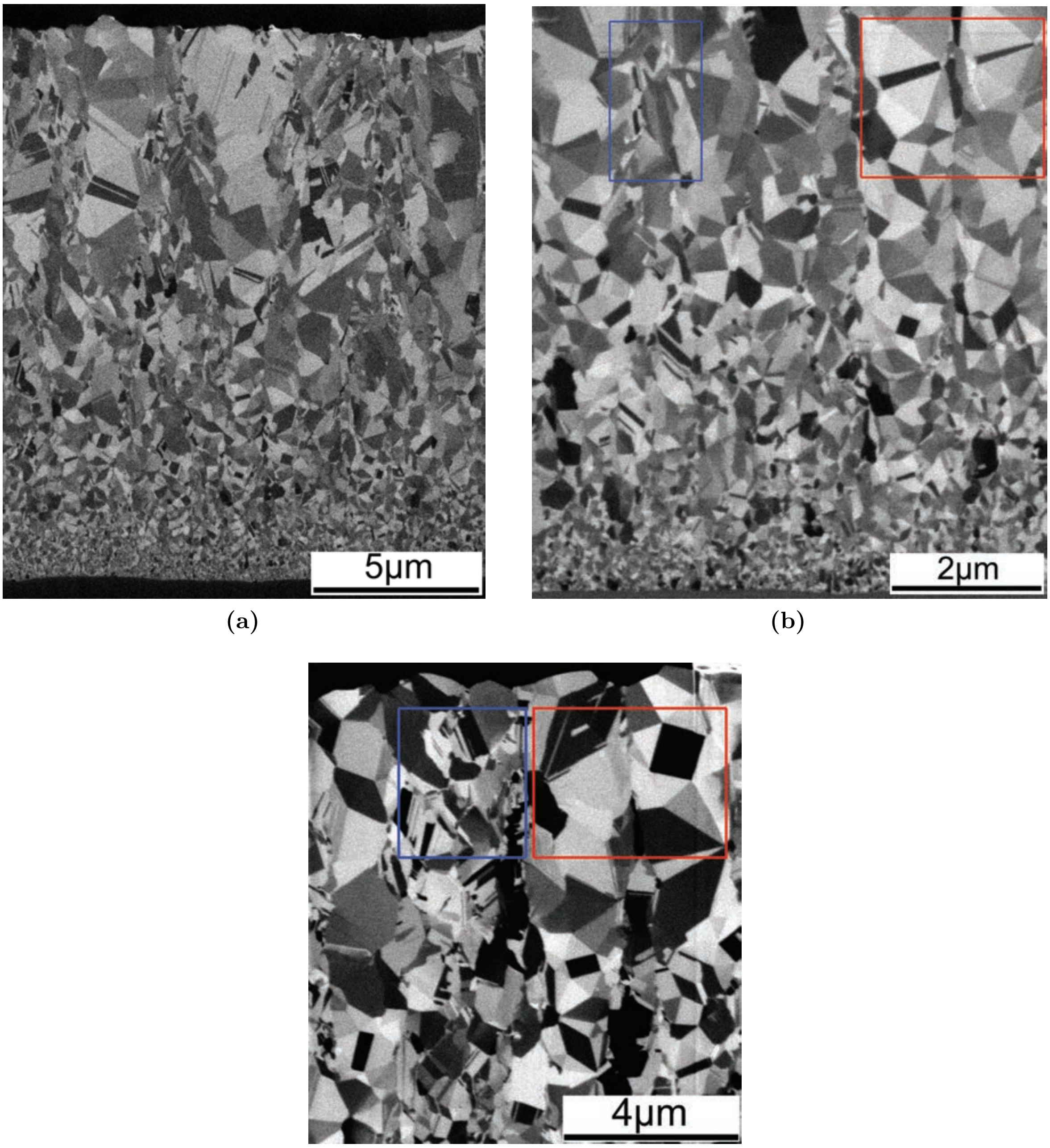

(a) (b)

(c)

Figure 5.35: Ion channeling images on the cross section of sample 8C10. (a) Whole cross section from the film/substrate interface to the film's surface. Note that many boundaries are straight lines. (b) Microstructure of the film close to the film/substrate interface. (c) Microstructure of the film close to the film's surface. Note the inhomogeneity of the microstructure by comparing regions marked in blue and red in each micrograph.

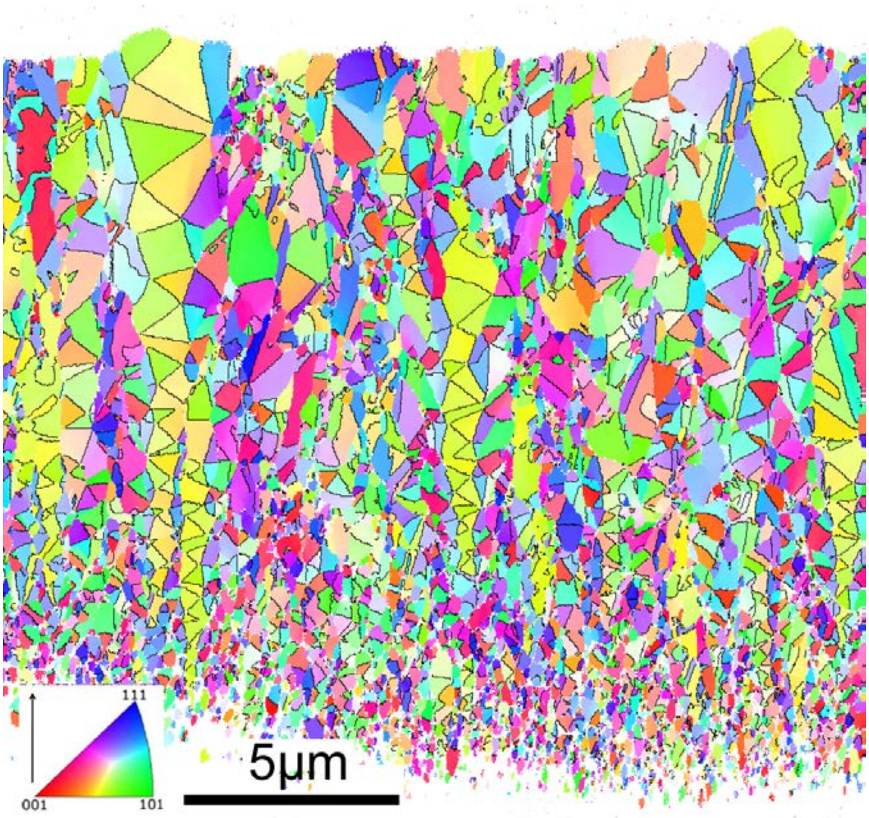

Figure 5.36: Orientation map of sample 8C10, color coded in relation with film's growth direction shown by an arrow; Σ3 boundaries are marked in black.

<542> oriented grains are formed to the side of the <210> oriented column in the shown orientation map. Furthermore, it can be seen on the map that <542> oriented grains have either a <210> or another <542> oriented grains as their neighbor. Unlike <210> oriented grains, <542> oriented grains are relatively dispersed in the 2D orientation map and they very rarely form a <542> column. Thus, <542> oriented grains do not form independently. Instead, they appear as a result of twinning of either a <210> or another <542> oriented grain (<210> ⟶ <542>⟶ <542>) and, <542>⟶ <542> does not occur repeatedly.

It is noted that average grain size of <210> oriented grains[6] is 0.36 μm^2 and average orientation spread weighted by area is 0.91°; and those of <542> oriented grains[7] are 0.31 μm^2 and 1.48° respectively. The larger orientation spread of the <542> oriented grains clearly shows that there is more orientation variation within these grains in comparison with <210> oriented grains.

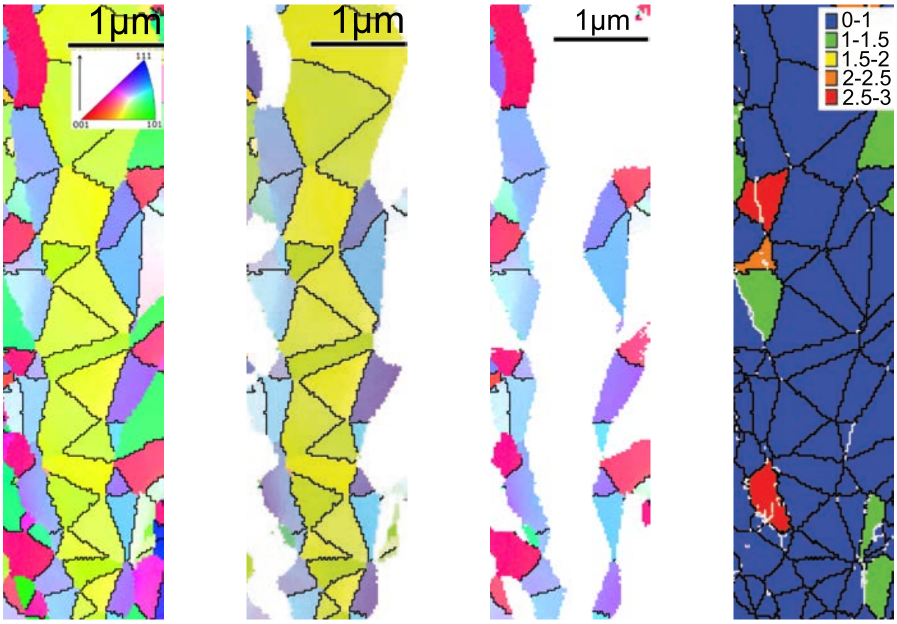

(a) (b) (c) (d)

Figure 5.37: Orientation map of sample 8C10, color coded in relation with film's growth direction shown by an arrow; Σ3 boundaries are marked in black. (a)all orientation; (b) <210> or <542> oriented grains; (c) <542> or <30 3 1> oriented grains. (d) The orientation spread (in degrees) of different grains; high angle grain boundaries are in black and low angle grain boundaries are in white.

Figure 5.37c shows an orientation map in which only data points with less than 10° deviation from <542> or <30 3 1> are shown (Σ3 boundaries are marked in black). It is evident that all <30 3 1> oriented grains (in reddish colors) shown in Figure 5.37c

---

[6] grains with less than 10° deviation from <210> orientation.

[7] grains with less than 10° deviation from <542> orientation.

have a <542> oriented grain as a neighbor, and a $\Sigma 3$ boundary separates the two grains. Following similar argument put forward earlier, <30 3 1> oriented grains are the result of twining of a <542> oriented grain and hence a second generation twin of <210> (<210> $\longrightarrow$ <542>$\longrightarrow$ <30 3 1>). Interestingly, one can see in Figure 5.37a that there are $\Sigma 3$ boundaries between <30 3 1> oriented grains (marked in reddish color) and <331> oriented grain (marked in dark green color). These two orientations are also in twin relation. This indicates that even third generation twins of <210> oriented grains are present in the microstructure.

For the characterization of the evolution of the type of boundary with thickness, a practical interface was defined and sub-maps were made as explained in section 4.3.2.2. Afterwards, length fractions of $\Sigma 3/HAGB$ and $\Sigma 9/HAGB$ were calculated for each sub-map; the results are provided in Figure 5.39a. As can be clearly seen in Figure 5.39a, there is an increase in $\Sigma 3/HAGB$ by increase of the distance. However, $\Sigma 9/HAGB$ is fairly constant or slightly decreasing by an increase of the distance. It is noted that in some regions, $\Sigma 3$ are in abundance and they form a pseudo 5-fold symmetry arrangement, Figure 5.38. In addition, $\Sigma 9$ boundaries are of different length in the map; and most of the $\Sigma 9$ boundaries are the third boundary of the triple junctions with two $\Sigma 3$ boundaries. Where $\Sigma 3$ boundaries are the dominant boundaries (e.g. the region shown in Figure 5.38b), $Sigma9$ are in the center of pseudo 5-fold symmetry arrangement of $\Sigma 3$ boundaries (two of the 5-fold symmetry arrangement are enclosed by small rectangles in the Figure 5.38b). In the same figure, a larger rectangle is used to enclose a center of pseudo 5-fold symmetry arrangement which includes multiple twins as well. In that case the arrangement is very complex, so pseudo 5-fold symmetry arrangement is not apparent in the first sight, nevertheless $\Sigma 9$ boundaries at the center is still visible.

The AHIL, once by including $\Sigma 3$ boundaries as high angle grain boundaries and once by its exclusion, was calculated and the result is shown in Figure 5.39b. Averaging over the film thickness, it is notable that the average horizontal intercept length is below 200 nm when $\Sigma 3$ boundaries are included for counting the intercepts.

In addition to the population of CSL boundaries, the topography and network of the high angle grain boundaries must be addressed in the context of grain boundary engineering. In Figure 5.40 the high angle grain boundary network of the sample 8C10 is shown; general high angle grain boundaries are in red and $\Sigma 3$, $\Sigma 9$, and $\Sigma 27$ are in green. Evidently for sample 8C10 (Figure 5.40) the network of general high angle grain boundaries is fully broken; i.e. there is no passage of general high angle grain boundaries from the surface to

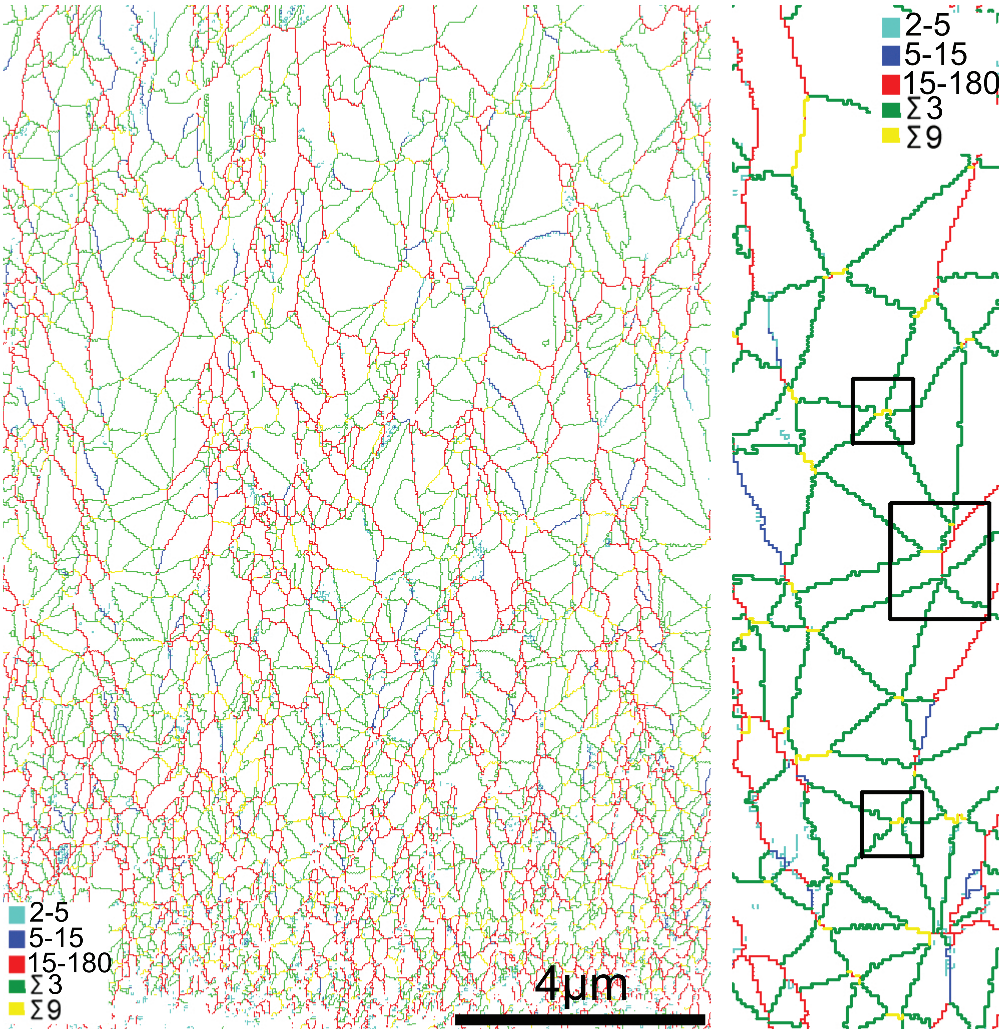

(a) (b)

Figure 5.38: (a) Grain boundaries network of sample 8C10. General high angle grain boundaries are in red, Σ3 in green, Σ9 in yellow, boundaries with misorientation 2-5° in light blue and 5-15 ° in dark blue. (b) A portion of (a) where Σ3 boundaries are the dominant boundaries. Small rectangles enclose simple pseudo 5-fold symmetry arrangement and large rectangle encloses a pseudo 5-fold symmetry arrangement with multiple twins.

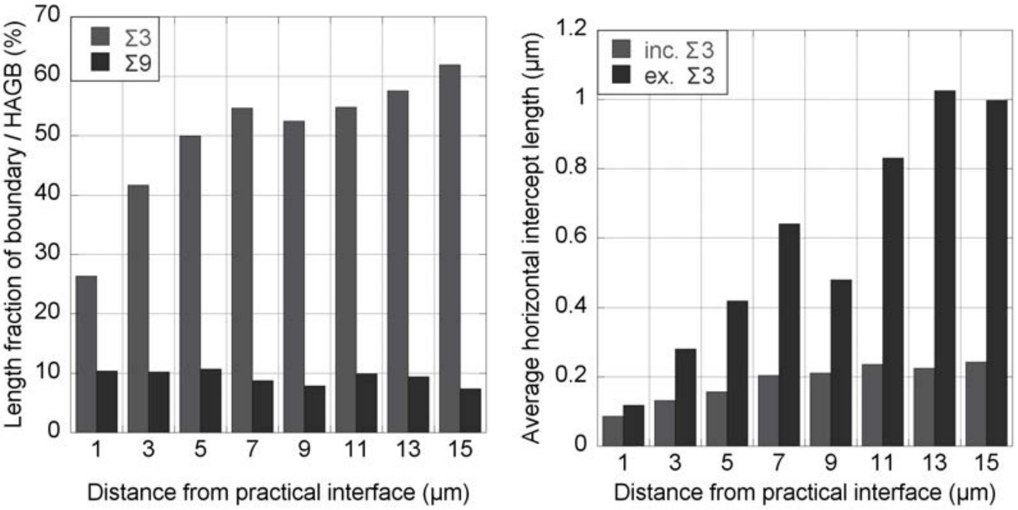

(a) (b)

Figure 5.39: (a) length fraction of Σ3 and Σ9 boundaries to total high angle grain boundaries vs distance from practical interface. (b) Average horizontal intercept length vs distance from practical interface. Intercepts were obtained either by including Σ3 in high angle grain boundaries or exclusion of that.

the substrate[8]. Hence, grain boundary specific properties are expected to be enhanced for this sample.

The average microhardness in the middle of the sample thickness was measured (186 ± 13 H_v). However since the criteria mentioned in section 4.3.6 did not prevail (distance from the corners of the indentation mark to the film surface and Ni-P interface was smaller than 2.5 × indentation diameter). Hence, the value could be influenced by presence of the surface or the substrate/film interface.

---

[8] Noting the 3-dimensionality of the microstructure, there might be some passages of high angle grain boundaries to the substrate that are not revealed by 2D analysis.

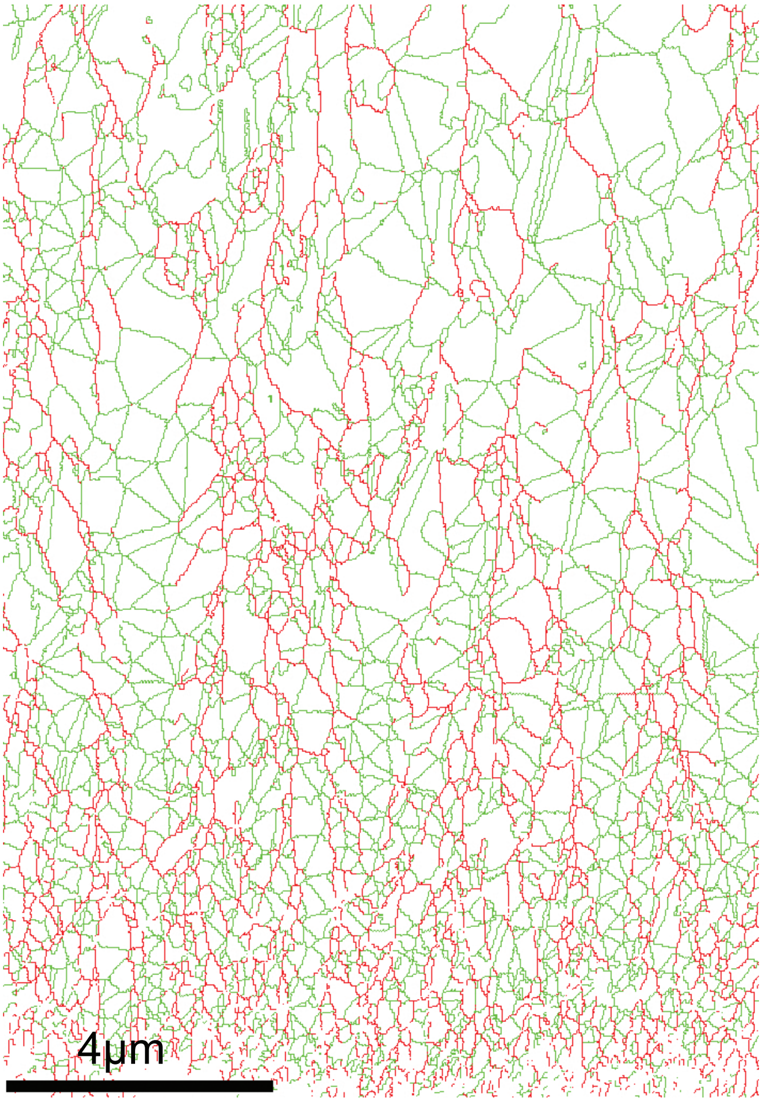

Figure 5.40: High angle grain boundary network of sample 8C10. Σ3, Σ9, and Σ27 are shown in green and other high angle grain boundaries in red.

Chapter 6

Results and Interpretation, Thermal Treatment

In this chapter the results of investigating the effect of thermal treatment on F-series and 8C10 samples are provided. The results are presented based on the microstructure of as-deposited state which are categorized into coarse-columnar and nano-crystalline microstructures. The evolution of texture, grain size and micro-strain are addressed in sections 6.1 and 6.2 respectively. In section 6.3 grain boundary character and thermal stability of samples is compared using the OIM data. Furthermore, in the same section the 5-parameter grain boundary character distribution (GBCD) analysis of three of the thermally treated samples are also provided.

6.1 Coarse-Columnar Microstructures

6.1.1 <211> Fiber Texture

Sample F1 in as-deposited state has a columnar structure with <211> fiber texture (see sections 5.1.3.2 and 5.1.1).

Upon thermal treatment of this sample up to $600°C$, a subtle texture evolution occurs. Quantitative XRD texture analysis revealed that the main texture component remains <211> fiber, however its strength increases, Table 6.1.

Table 6.1: Orientation density in MRD of sample F1 and its thermally treated counterparts. The results are obtained by XRD texture analysis.

	F1	F1-150	F1-200	F1-400	F1-600
<211>	4.7	5.0	5.3	6.5	5.7

Figure 6.1: Orientation map of sample F1-600, color coded in relation with film growth direction shown by an arrow. High angle grain boundaries are marked in black and $\Sigma3$ boundaries in yellow. Columnar grains are mostly <211> oriented and in the vicinity of film/substrate interface, grains are mostly <100> oriented.

An Orientation map of sample F1-600 is shown in Figure 6.1. It is evident that after thermal treatment at $600°C$ the microstructure is still columnar (Figure 6.1). In general, a large fraction of the microstructure is composed of <211> oriented grains (colored purple in the map). However, a fairly high population of <100> oriented grains (colored in red) is present close to the film/substrate interface(Figure 6.1). To characterize the preferred orientation versus distance from the practical interface, area fraction of <100> and <211> oriented data points for each 2 μm was calculated and is shown in Figure 6.2. It is evident that <100> oriented grains have a large area fraction in just the first 2 μm from the practical interface and beyond that <211> oriented grains take up the majority of the area fraction of the map. A similar analysis were applied for the as-deposited sample F1 (see Figure 5.13a, page 73). The comparison between the as-deposited state (F1) and after thermal treatment at $600°C$ (F1-600), shows that the area fraction of <211> and <100> oriented data points of sample F1-600 are both higher than that of sample F1. The area fraction of <211> oriented data points increases from 59.7% to 68.4%, and that of <100> oriented data points increases from 1.4% to 4.7% upon thermal treatment at $600°C$. Note that the three fold increase in area fraction of <100> oriented data point, is restricted to the first 2 μm from the practical interface. Unlike <100> oriented grains, the increase in area fraction of <211> oriented grains is rather homogeneous over the thickness except the first 2 μm where a very subtle decrease was observed (8% decrease).

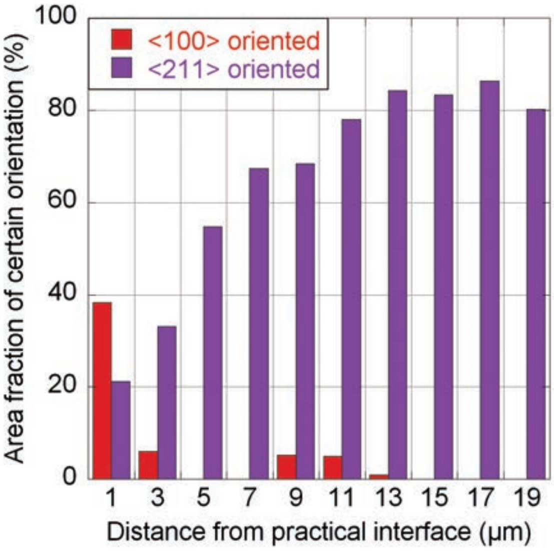

Figure 6.2: Area fraction of <100> and <211> oriented data points vs distance from the practical interface for sample F1-600 which is shown in Figure 6.1.

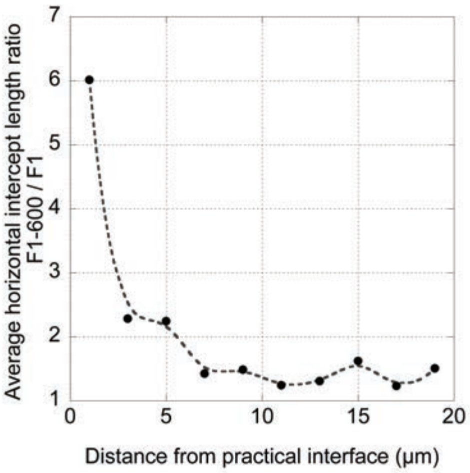

Figure 6.3: Average horizontal intercept length ratio F1-600/F1 ($\frac{AHIL_{F1-600}}{AHIL_{F1}}$) vs distance from the practical interface.

Comparing the average horizontal intercept length (AHIL) of samples F1 and F1-600 provides a quantitative measure of change in the width of the columnar grains. This comparison is conducted for different distances from the practical interface, by calculation of $\frac{AHIL_{F1-600}}{AHIL_{F1}}$ (Figure 6.3). Evidently, in the vicinity of the film/substrate interface dramatic grain growth took place whereas away from that, the grain growth due to thermal treatment is less pronounced.

It has been established, that in the as-deposited state the AHIL increases with distance from the film/substrate interface (see Figure 5.9 - page 69). In other words, the number and hence, the volume of grain boundaries decreases. Thus, more pronounced grain growth close to the film/substrate is expected due to a higher stored energy at the boundaries in that region. Evidently, this grain growth brings about equiaxed grains which are mostly <100> oriented (see Figure 6.1). Apart from that, a simultaneous increase of AHIL and area fraction of <211> oriented grains, shows that <211> columnar grains are widened due to thermal treatment.

Twin Lamella Thermal Stability

The typical twin lamellae in <211> oriented grains (parallel to the film growth direction) were observed in samples F1-400 (Figure 6.4a) and F1-600 (Figure 6.4b). This clarifies that twin lamellae in <211> oriented grains are fairly stable.

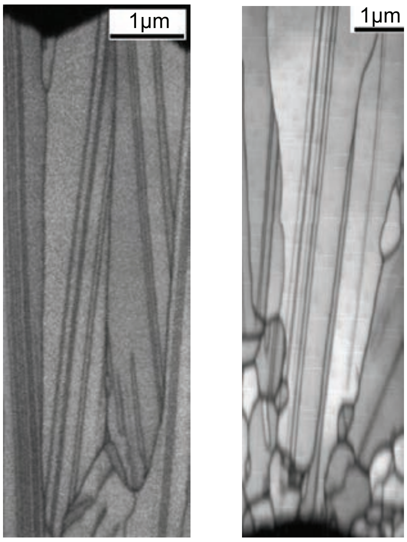

(a) (b)

Figure 6.4: Image quality maps of samples (a) F1-400, and (b) F1-600; Fine twin lamellae parallel to the film growth direction are visible

Analyzing ion channeling images of sample F1 showed that the twin lamella density is $\approx 3.5/grain$ and that of sample F1-600 $\approx 3.1/grain$ (a micrograph of $\approx 25\mu m \times 20\mu m$ is analyzed). Thus 11% of the twin lamellae are fully annihilated due to thermal treatment at 600°C.

6.1.2 <100> Fiber Texture

Samples F2, F3, and F6 have <100> fiber texture in as-deposited state (see section 5.1.1). Samples F2 and F3 show a typical columnar structure (Figure 5.6 - page 67), while in sample F6, columnar grains are separated by fine grains (Figure 5.23c - page 83). Regardless of the fact that sample F6 is not a coarse-columnar but a mixture of coarse-columnar and nano-crystalline, it is grouped with samples F2 and F3 for ease of comparison.
XRD quantitative texture analysis was conducted on all thermally treated samples, and it was found out that all of them have a fiber texture. The orientation density and fiber axes in ND of the samples are provided in Table 6.2.

Table 6.2: Orientation density in MRD for different fiber axes of samples F2, F3 and F6 and after thermal treatment for 30 min at 150, 200, 400, and 600 °C. The results are obtained by XRD texture analysis. AD stands for as-deposited state.

	Fiber axes	AD	150°C	200°C	400°C	600°C
F2	<100>	5.4	7.7	7.6	8.7	14.7
	<111>	1.4	–	–	–	–
	<322>	1.4	–	–	–	–
	<334>	–	1.3	1.3	–	–
F3	<100>	9.9	16.7	15.5	14.2	17.9
	<111>	1.2	–	–	–	–
F6	<100>	32.7	32.6	35.7	36.6	4.4
	<111>	–	–	–	–	4.3

Samples F2 and F3 both show an increase in strength of the <100> fiber texture component upon thermal treatment in the entire temperature range up to 600°C. In contrast, for sample F6 increase up to 400°C is observed and upon thermal treatment at 600°C, there is a dramatic decrease in the orientation density of <100> and an increase in the orientation density of <111>.
Since XRD texture analysis of samples F2, F3, F6, and all their thermally treated counterparts showed that the <100> fiber is the major texture component, single line analysis of the 200 peak profile was applied for these samples to characterize the average grain size and the micro-strain, Table 6.3.
Evidently, the grain size of samples F2 and F3 gradually increases due to thermal treatment up to 400°C and reaches values close to 300 nm which is the upper limit of the used diffractometer where instrumental broadening can be distinguished from the instrumental

Table 6.3: Average grain size [nm] and micro-strain for <100> oriented grain in samples F2, F3, F6, and their thermally treated counterparts (obtained by single line analysis of 200 peak profile). AD stands for as-deposited state. 'N' represents calculated values are beyond the determination limits of the used diffractometer; implying that only instrumental broadening is observed.

		AD	150°C	200°C	400°C	600°C
F2	Grain size	115 nm	156 nm	178 nm	300 nm	N
	Micro-strain	0.0011	0.0007	0.0007	0.0010	N
F3	Grain size	141 nm	195 nm	198 nm	296 nm	N
	Micro-strain	0.0010	0007	0008	0009	N
F6	Grain size	41 nm	53 nm	53 nm	64 nm	N
	Micro-strain	0.0030	0.0027	0.0028	0.0028	N

broadening. Apparently, due to the thermal treatment at 600°C, the average grain size exceeds 300 nm which corresponds to the detection limit for the applied XRD measurements. The average grain size of <100> oriented grains of sample F6 also exceeds 300 nm due to thermal treatment at 600°C, however, thermal treatment at 400°C, does not bring about grain growth as pronounced as observed for samples F2 and F3.

Further investigation of thermally treated samples was carried out by ion channeling imaging and OIM.

F2-400 and F2-600

Figures 6.5a and 6.5b show ion channeling images of samples F2-400 and F2-600 respectively. Sample F2-400 has a typical columnar microstructure with inclined twin lamellae. This resembles the microstructure of sample F2 (as-deposited state) as shown in Figure 5.6c - page 67. F2-600 also has some columnar grains, however in comparison with sample F2-400, notable growth has occurred (Figure 6.5b). To quantify the increase in width of the columns, Figures 6.5a and 6.5b were subjected to image analysis. Accordingly, the AHIL of samples F2-400 and F2-600 were obtained, and then described by a square root function[1] as shown in Figure 6.6. Due to thermal treatment at 400°C grain growth at the vicinity of the film/substrate interface is more pronounced than that close to the surface. However, thermal treatment at 600°C brings about a significant growth over the entire thickness. The growth close to the film/substrate interface results in formation of equiaxed grains, while away from the interface, the growth manifested as column widening. It is notable that most of the twin lamellae within the columnar grains are annihilated by thermal treatment at 600°C. The twin lamellae density of sample F2 is 1.5/μm and that of sample F2-600 is 0.3/μm, thus, 80% of the twin lamellae are annihiliated.

Figure 6.7 shows an orientation map of sample F2-600 in which most of the columnar

---

[1] See more details is section 5.1.3.2 - page 66.

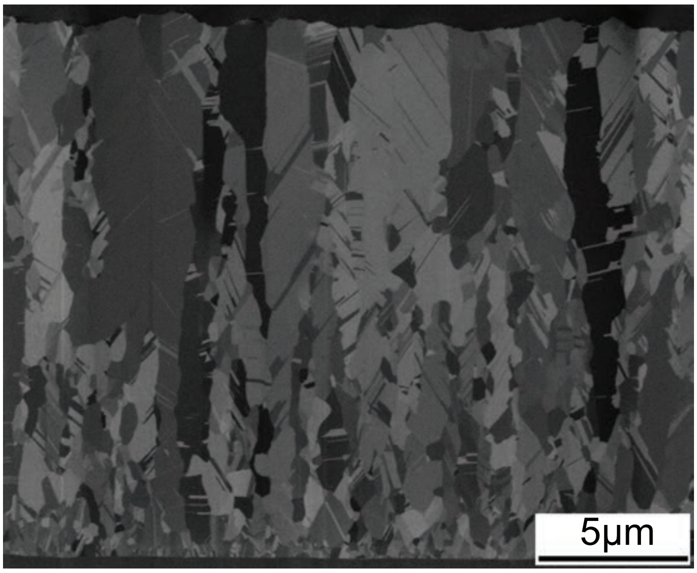

(a)

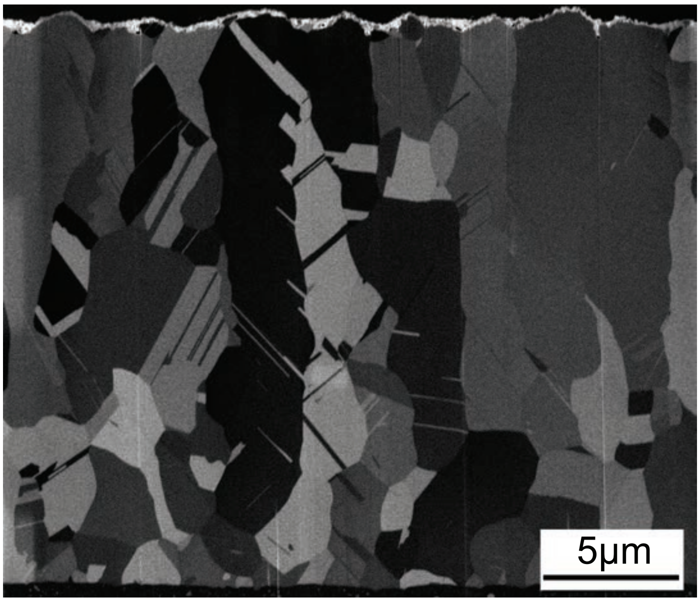

(b)

Figure 6.5: Ion channeling images of samples (a) F2-400, and (b) F2-600.

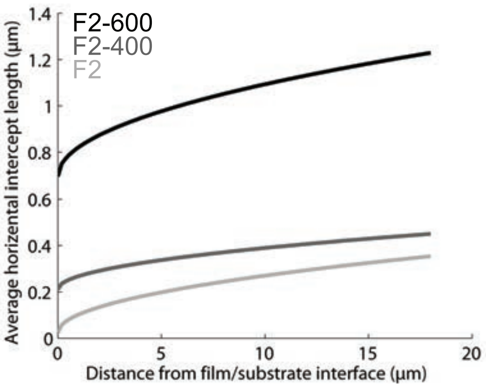

Figure 6.6: Average horizontal intercept length vs thickness of samples F2, F2-400, and F2-600, obtained by image analysis of channeling ion images in Figures 5.6a, 6.5a, and 6.5b, respectively.

grains are approximately <100> oriented (colored in red). This is in good agreement with XRD texture measurement. Analysis of the grain boundaries in F2-600 orientation map shows that $\Sigma 3/HAGB$ and $\Sigma 9/HAGB$ are 29.6% and below 1%, respectively whereas those of sample F2 were 45.6% and 7.5%, respectively. Thus, as a consequence of thermal treatment, the length fraction of $\Sigma 3^n$ boundaries decreases.

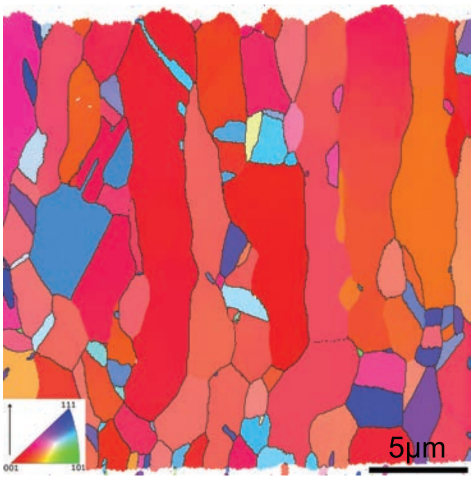

Figure 6.7: Orientation map of sample F2-600. High angle grain boundaries are marked in black. Most of grains are <100> oriented in relation with film growth direction.

F3-600

The microstructure of sample F3-600 is revealed by ion channeling imaging (Figure 6.8a). Evidently, the microstructure is rather inhomogeneous as indicated on Figure 6.8a, by two rectangles. The grains inside the red rectangle are equiaxed, in contrast to the grains enclosed by blue rectangle, which are still columnar. As shown in orientation map in Figure 6.8b, the orientation of columnar and equiaxed grains is similar.

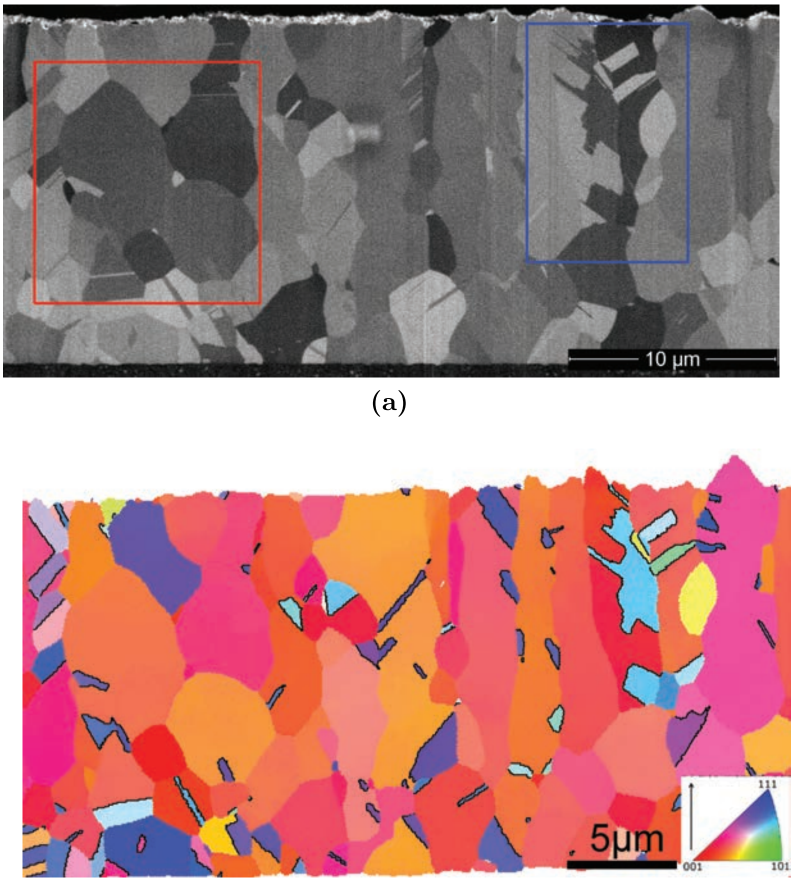

(a)

(b)

Figure 6.8: (a) Ion channeling image of sample F3-600. The microstructure is fairly inhomogeneous. The region enclosed by red rectangle is composed of equiaxed grains whereas, the region enclosed by blue rectangle is mostly composed of columnar grains. (b) Orientation map of sample F3-600. $\Sigma3$ boundaries are marked in black.

The average number of twin lamellae in columnar grains, outnumbers that of equiaxed grains ($\Sigma3$ boundaries are marked by black on Figure 6.8b). Note that the twin lamellae in columnar grains are growth twins whereas those in equiaxed grains are annealing twins. $\Sigma3/HAGB$ and $\Sigma9/HAGB$ are 35.8% and below 1% respectively for sample F3-600; Those for sample F3 are 40.9% and 6.1%, respectively). Thus, due to thermal treatment, the fraction of $\Sigma3^n$ boundaries, has decreased.

F6-400 and F6-600

The microstructure of samples F6-400 and F6-600 are shown in Figure 6.9. Comparing the microstructure of the thermally treated sample at $400°C$, Figure 6.9a, and as-deposited state (see Figure 5.23c - page 83), it is clear that some of the nano-crystalline grains which were mostly populated close to the film/substrate interface have grown to larger equiaxed grains. In addition, the <100> oriented columns are widened due to thermal treatment and they are less separated in comparison with the as-deposited state. This explains the increase of <100> orientation density measured by XRD texture analysis.

Even after thermal treatment there is a pronounced color variation within the <100> columnar grains in orientation map Figure 6.9a, which suggests large misorientation within the grains. This is in agreement with the results of micro-strain analysis which showed relatively large micro-strains, even after thermal treatment at $400°C$ of sample F6 (see Table 6.3).

One can see on Figure 6.9a that there are data points with confidence index smaller than 0.1 (shown in white). This suggests that fine grains are still present in the microstructure. Using channeling ion imaging, Figure 6.9b, it is evident that the microstructure of sample F6-400 possesses fine grains which are mostly located close to the film/substrate interface and some other are present between the columnar grains.

Increasing the thermal treatment temperature to $600°C$, the grains close to the film/-substrate interface grow more such that no fine grain can be recognized in that region, and the microstructure is fully equiaxed, Figure 6.9c. Interestingly, there is a significant grain growth close to the film surface such that no columnar grain is present in the microstructure any longer. The equiaxed grains which are present close to the substrate are mostly <100> oriented, and larger grains which are close to the surface are <111> and <100> oriented in sample F6-600 (see Figure 6.9c).

6.1.3 <210> Fiber Texture

The major texture component of sample 8C10 was <210> (see section 5.4.1) and it was shown that <210> oriented grains form columns (see Figure 5.37b in page 105). The

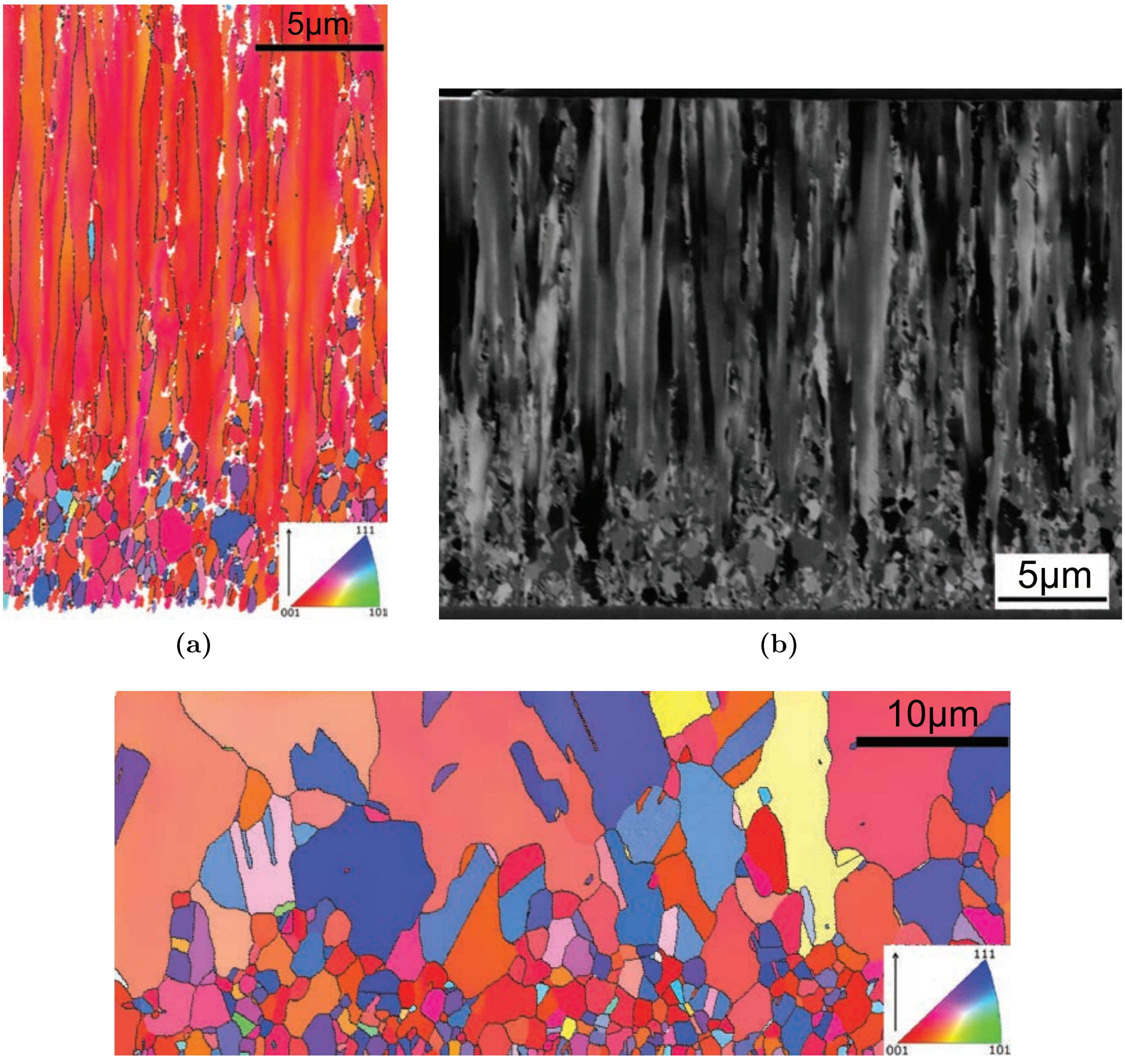

(a)

(b)

(c)

Figure 6.9: (a) Orientation map and (b) ion channeling image of sample F6-400. The microstructure is composed of columnar grains with orientation variation and equiaxed grains mostly populated close to the film/substrate. (c) Orientation map of sample F6-600. Orientation maps are color coded in relation with film growth direction shown by an arrow. High angle grain boundaries are marked by black.

thermally treated counterparts of sample 8C10 have also a fiber texture in ND. Thus, inverse pole figures in ND of these samples, shown in Table 6.4a, fully describe the texture. Following Table 6.4b, it is apparent that thermal treatment does not significantly influence the strength of minor texture components, i.e. <542> and <711>. And, the strength of the <210> fiber texture is roughly similar for thermally treated samples up to 8C10-400, however, there is a reduction in that for sample 8C10-600. Thus, major texture component weakens due to thermal treatment at 600°C.

Table 6.4: (a) Inverse pole figures of sample 8C10 and its thermally treated counterparts, obtained by XRD texture measurement. The legend (values in MRD) in right hand side of the table shows the orientation density levels. (b) Orientation density in MRD for different fiber axes.

(a)

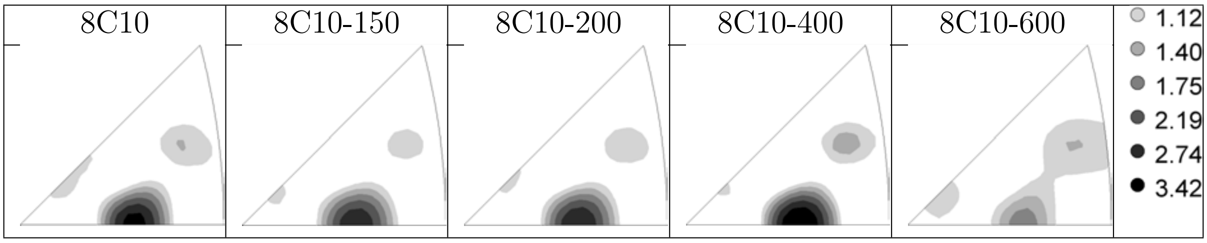

(b)

	8C10	8C10-150	8C10-200	8C10-400	8C10-600
<210>	3.8	3.3	3.4	4.4	2.0
<542>	1.4	1.3	1.4	1.6	1.4
<711>	1.2	1.2	1.1	1.2	1.2

Further investigation of the microstructure of thermally treated samples was conducted by electron and ion microscopy.

8C10-400 and 8C10-600

Figure 6.10a shows the microstructure of sample 8C10-400 obtained by ion channeling imaging. The figure is the result of combining 4 smaller micrographs together. That is why the contrast of a grain have abrupt change in the middle of the figure.

Thermal treatment at 400°C brought about significant grain growth; see the as-deposited state microstructure in Figure 5.35a - page 103). At $\approx 5\ \mu m$ away from the film/substrate interface the grain growth is most pronounced, and close to the surface, the microstructure is rather inhomogeneous. In some regions equiaxed grains are present, (grain growth has occurred) and in some other regions the, microstructure is very similar to the as-despited state, indicating that no significant grain growth took place. The microstructure of sample 8C10-600 is shown in Figure 6.10b, in an ion channeling image. Evidently dramatic grain growth has occurred due to thermal treatment at $600°C$, such that the microstructure does not show characteristic <210> multiple twinned structure and instead the annealing twins are visible.

In order to study the micro-texture of sample 8C10-400, OIM was conducted for this sample, Figure 6.11a. Some of the typical <210> oriented columns are still present in the microstructure (one of those is enclosed by a rectangle on the figure). In the other regions of the microstructure, there are evidence of growth of <210> oriented grains. As shown in Figure 6.11c, grain marked by 'A' has grown and only the reminiscence of typical multiple twinned <210> oriented grains is present in the microstructure (see the grain marked by 'B'). In the other regions of the microstructure, <210> oriented grains grew even more such that a <210> oriented column is not recognizable any longer, Figure 6.11d, which is rather equiaxed (e.g. the grain marked by 'D' in Figure 6.11d).

One of the <542> oriented grains indicated by 'C' divides the <210> oriented column into two pieces in Figure 6.11c. Since, in as-deposited state, <542> oriented grains were present to the sides of a <210> column (see Figure 5.37b, page 105) and a <542> oriented grain in middle of a <210> column was not observed, it appears that grain 'C' in Figure 6.11c has grown at the expense of its neighboring <210> oriented grain. It is not clear whether, the grain marked by 'C' in Figure 6.11c is a singular event or <542> oriented grains grow at the expense of the neighboring <210> oriented grain. However, XRD texture analysis has revealed that the relative volume fraction of <210> and <542> does not change due to thermal treatment at $400°C$ in comparison with the as-deposited state. This suggests that, there is a similar chance for growth of <210> and <542> grains at the expense each other. Similarly, some of the <711> oriented grains have grown, as can seen on Figure 6.11a in reddish colors. Thus, all the grains with different orientations have grown and there is no preferential orientation that outgrows the rest.

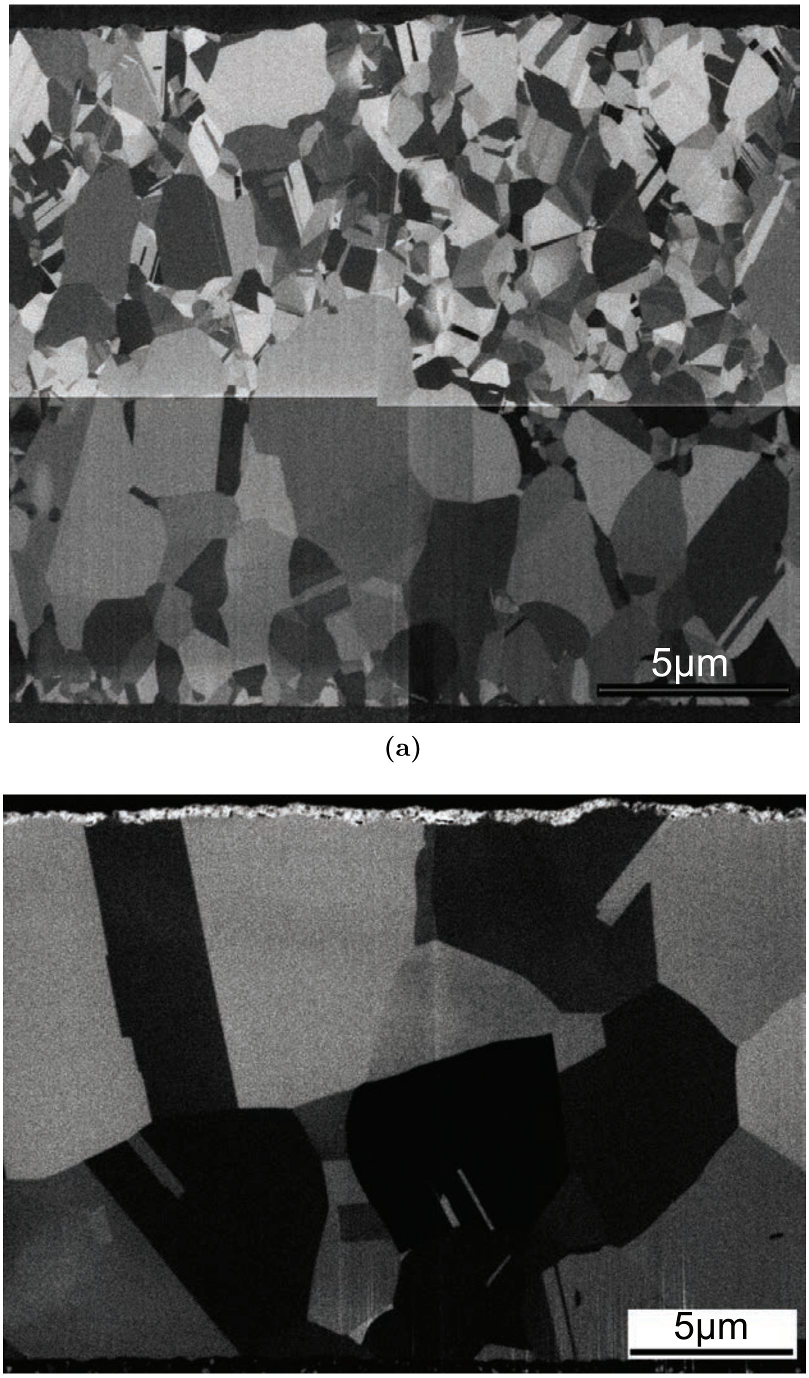

(a)

(b)

Figure 6.10: (a) Ion channeling image of sample 8C10-400. The largest grains are at $\approx 7\ \mu m$ from the film/substrate interface. The figure is the result of combining 4 smaller micrographs together. That is why the contrast of a grain have abrupt change in the middle of the figure.(b) The microstructure of sample 8C10-600 revealed by ion channeling imaging.

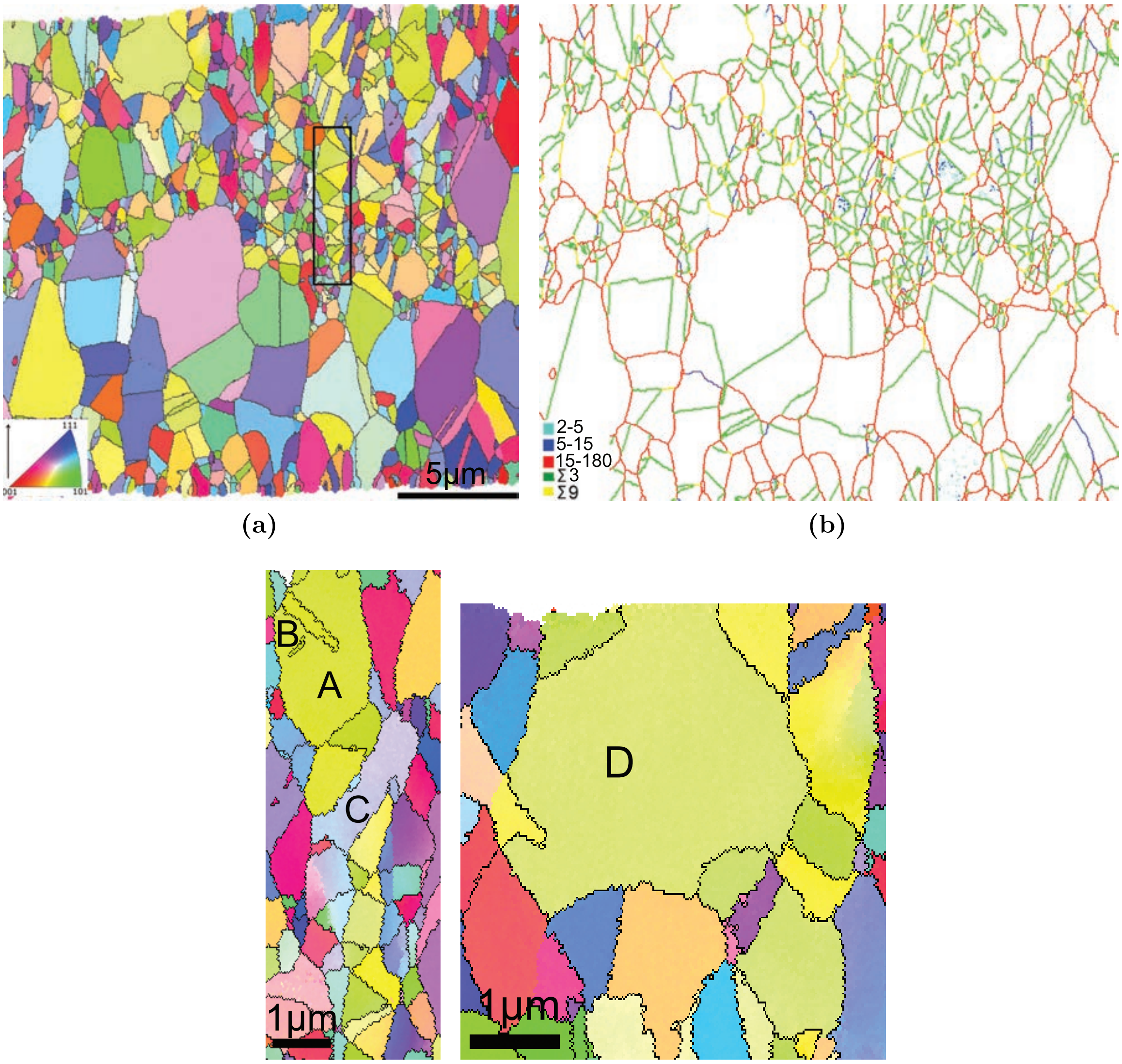

(a) (b)

(c) (d)

Figure 6.11: (a) Orientation maps of sample 8C10-400 color coded in relation with film growth direction shown by an arrow. High angle grain boundaries are marked by black. The black rectangle encloses a typical <210> column. (b) Grain boundary network; general high angle grain boundaries are in red, $\Sigma3$ in green, $\Sigma9$ in yellow, boundaries with misorientation 2-5° in light blue and 5-15 ° in dark blue. (c) grown grains A: <210> oriented and C: <542> oriented. (d) A grown equiaxed <210> oriented grain.

6.2 Nano-Crystalline Microstructure

Samples F4, F5, F7, F8, and F9 have a nano-crystalline microstructure with different fiber textures (see Table 5.2 - page 58). The evolution of the microstructure during thermal treatment of these samples was studied and the obtained results are discussed below. The samples were categorized according to their fiber axes. The first category comprises samples F4 and F9 which have a single component fiber texture in as-deposited state, <211¿*and*¡111 > respectively. And the second category comprises samples F5,F7, and F8 which have a multiple component fiber texture in as-deposited state.

6.2.1 Single Component Fiber Texture

6.2.1.1 <211> Fiber Texture

Quantitative texture analysis using XRD, was applied for thermally treated counterparts of sample F4. It was found that, all of the samples had fiber texture in ND. Accordingly, orientation density of different fiber axes in ND characterizes the texture and those are provided in Table 6.5.

Table 6.5: Orientation density in MRD for different fiber axes of samples F4 and its thermally treated counterparts. The results are obtained by XRD texture analysis.

Fiber axes	F4	F4-150	F4-200	F4-400	F4-600
<211>	2.7	–	–	–	–
<443>	–	2.1	2.1	–	–
<100>	–	3.8	3.6	–	–
<111>	–	–	–	3.7	7.5

Following Table 6.5, the <211> fiber texture evolves to a <100> <443> double fiber texture upon thermal treatment at relatively low temperatures (150 and 200°C). Thermal treatment at 400°C, brings about <111> fiber texture and upon further increase in temperature that texture strengthens. Hence, the volume fraction of <100> oriented grains is high at low thermal treatment temperatures while <111> oriented grains take up the majority of the volume of the sample after thermal treatment at high temperatures. Texture analysis revealed that <100> and <111> oriented grains are the main texture components of the samples. Hence, in order to characterize the grain size and micro-strain evolution due to thermal treatment, line profile analysis of 200 and 111 peak profiles was applied by single line analysis. The results are listed in Table 6.6. Comparing grain size of samples F4 and F4-200, there is a $\approx$ 1.4 fold increase in the average grain size of <100> and <111> oriented grains. Micro-strain also increases notably by thermal treatment at

Table 6.6: Grain size in nm and micro-strain of certain orientation obtained by single line analysis for sample F4 and its thermally treated counterparts. (a) Average size and micro-strain of <111> oriented grains. (b) Average size and micro-strain of <100> oriented grains. 'N' represents calculated value beyond determination limits of the used diffractometer.

(a)

111 peak	F4	F4-150	F4-200	F4-400	F4-600
Grain Size	21	24	28	242	N
Micro-Strain	0.0007	0.0020	0.0035	0.0004	N

(b)

200 peak	F4	F4-150	F4-200	F4-400	F4-600
Grain Size	9	11	13	75	N
Micro-Strain	0.0029	0.0041	0.0056	0.0009	N

200°C.

In sample F4-400 there is a significant increase in grain size of both <100> and <111> oriented grains, albeit most pronounced for <111> oriented grains. It is important to notice that micro-strain first increases and at F4-400 is lower than that in as-deposited state..

The microstructure of samples F4-200, F4-400, and F4-600 are studied by ion channeling imaging, Figure 6.12. F4-200 is formed of some elongated grains in film growth direction and the rest of microstructure is very fine, Figure 6.12a. Comparing the microstructure of sample F4-200, with that of sample F4 (see Figure 5.23a in page 83), it is obvious that elongated grains are more populous in the latter than the former. Since the elongated grains were <211>, it shows the <211> grains are transformed due to thermal treatment. This is in agreement with the XRD texture analysis (see Table 6.5).

Microstructure of sample F4-400, Figure 6.12b, clearly shows the growth of equiaxed grains, at the expense of elongated grains. Thermal treatment at 600 °C brings about fully equiaxed microstructure over the entire thickness, Figure 6.12c. However, it appears that larger and smaller grains have formed colonies, as indicated by red and blue rectangles on the Figure 6.12c and consequently, he microstructure is rather inhomogeneous.

6.2.1.2 <111> Fiber Texture

Sample F9 was the only nano-crystalline sample with a <111> fiber texture in as-deposited state. Quantitative XRD texture analysis was applied on the thermally treated counterparts of sample F9 and the orientation density of different fiber axes in film growth

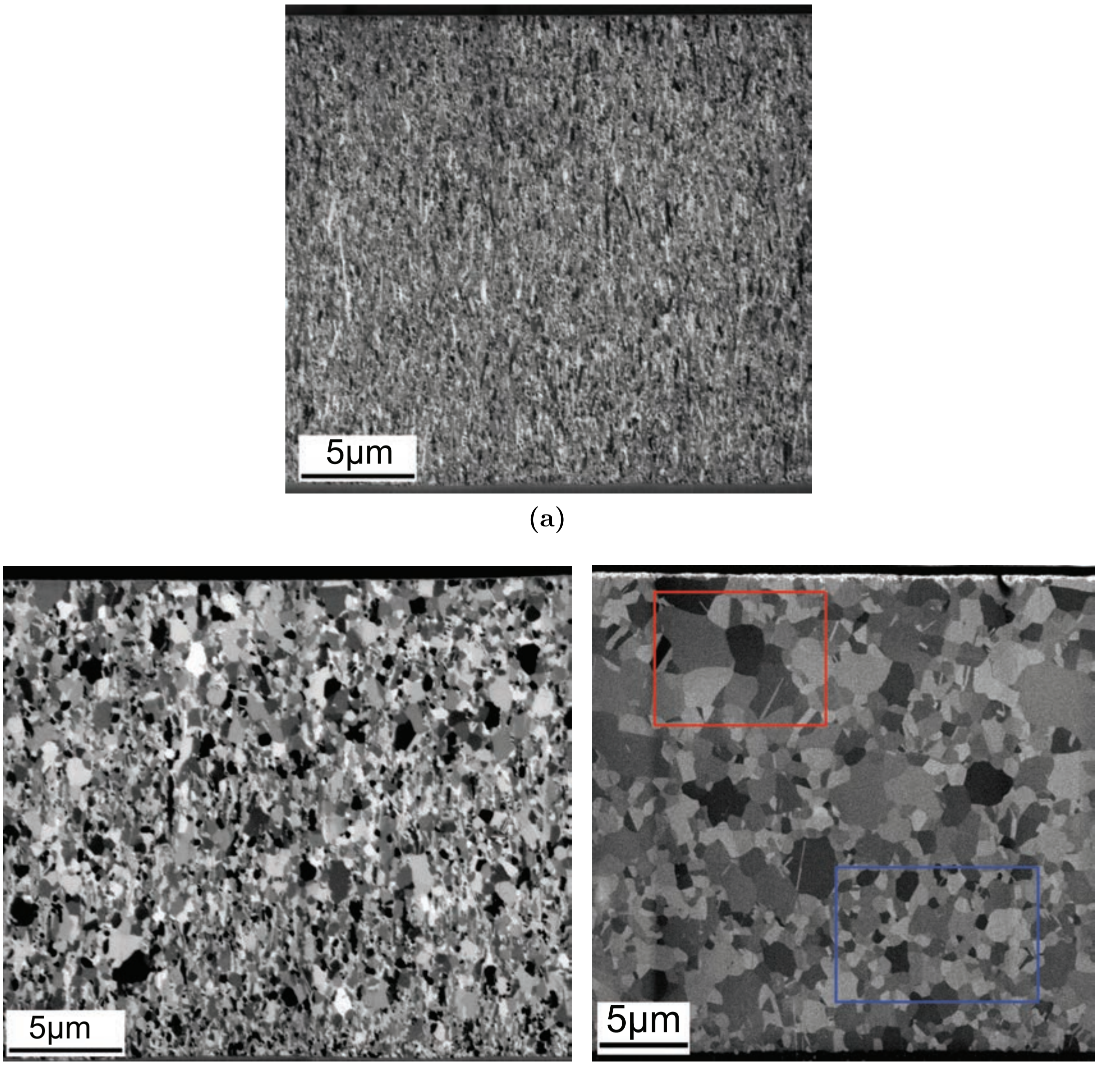

(a)

(b) (c)

Figure 6.12: Ion channeling images of sample (a) F4-200, (b) F4-400, and (c) F4-600. A colony of large grains is enclosed by red rectangle and a colony of small grains is enclosed by blue rectangle.

direction was calculated. The results are provided in Table 6.7.

It is evident that there is a significant decrease in orientation density of <111> due to thermal treatment at 150 and 200°C and no other preferred orientation forms at the expense of <111> oriented grains. However, thermal treatment at 400°C brings about an increase in <111> texture strength. Further increase in thermal treatment temperature to 600°C, brings about a pronounced <332> texture (5.7 MRD). The inverse pole figure of sample F9-600 in ND is shown in Figure 6.13.

Table 6.7: Orientation density in MRD for different fiber axes of samples F9 and its thermally treated counterparts. The results are obtained by XRD texture analysis.

Fiber axes	F9	F9-150	F9-200	F9-400	F9-600
<111>	5.4	1.8	2.2	5.6	–
<332>	–	–	–	–	5.7

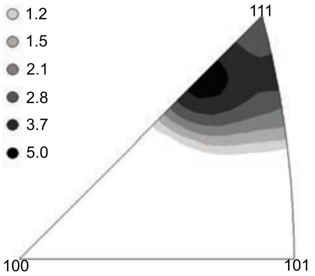

Figure 6.13: Inverse pole figures of sample F9-600 obtained by XRD texture measurement. The legend (values in MRD) in the left hand side shows the orientation density levels.

Since <111> oriented grains are the majority of the grains in the studied samples, 111 peak profile was subjected to XRD single line analysis to characterize the grain size (coherently diffracting domain size) and micro-strain. The results are listed in Table 6.8.

Following grain size evolution with thermal treatment temperature, it first decreases and then increases; i.e. grain refinement takes place due to thermal treatment. It is of high interest that even after thermal treatment at 400°C the average grain size of <111> oriented grains remains below 40 nm. Unlike the average grain size, there is a significant decrease in micro-strain upon thermal treatment at 400°C.

Figure 6.14 shows ion channeling image on a cross section of sample F9-400. The microstructure of this sample is comparable to the as-deposited state in the used magnification for imaging (see Figure 5.27a, page 88).

The orientation map of sample F9-600, Figure 6.15a, clearly shows that a drastic grain growth has occurred due to thermal treatment at 600°C. The microstructure of sample F9-600 is composed of very large grains which are elongated in film growth direction, and smaller grains which are mostly populated either in the vicinity of the film/substrate

Table 6.8: Grain size in nm and micro-strain of <111> oriented grains in relation with film growth direction, obtained by single line analysis for sample F9 and its thermally treated counterparts. 'N' represents calculated value above the upper determination limit of the used diffractometer (300 nm).

	F9	F9-150	F9-200	F9-400	F9-600
Grain Size	19	9	15	39	N
Micro-Strain	0.0051	0.0047	0.0063	0.0009	N

interface or in the vicinity of the surface.

The largest grain which is in the middle of the map is composed of four crystallites which are separated by low angle grain boundaries (low angle grain boundaries are not shown). Point-to-point and point-to-origin misorientation along the 'AB' line is shown in Figure 6.15c and clarifies the presence of three low angle grain boundaries between points 'A' and 'B'. In addition an oval shaped island is present in the same grain, all the boundaries of the island are Σ3 boundaries (shown by yellow). Following other Σ3 boundaries on the map, most of them appear to be curved. Grain boundary skeleton including low angle grain boundaries are shown in Figure 6.15b. It is notable that there is a large fraction of low angle grain boundaries (20.7%) with misorientation range of 2-5o. These boundaries are mostly accumulated relatively smaller grains located either close to the surface or film/substrate interface.

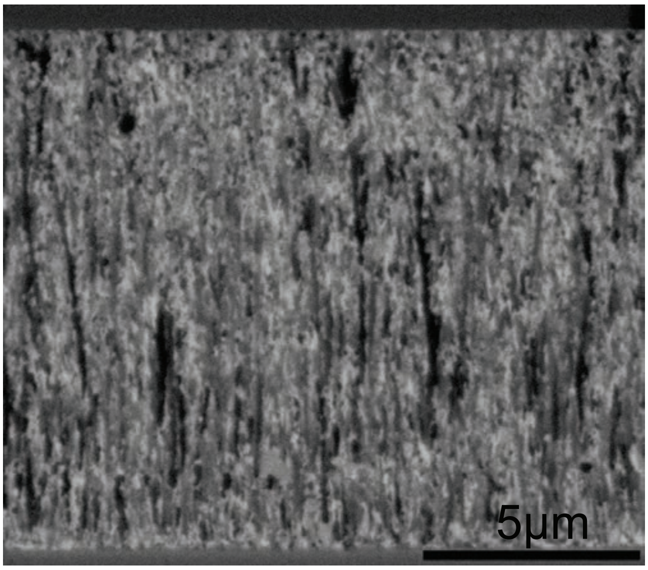

Figure 6.14: Microstructure of sample F9-400, obtained by ion channeling imaging.

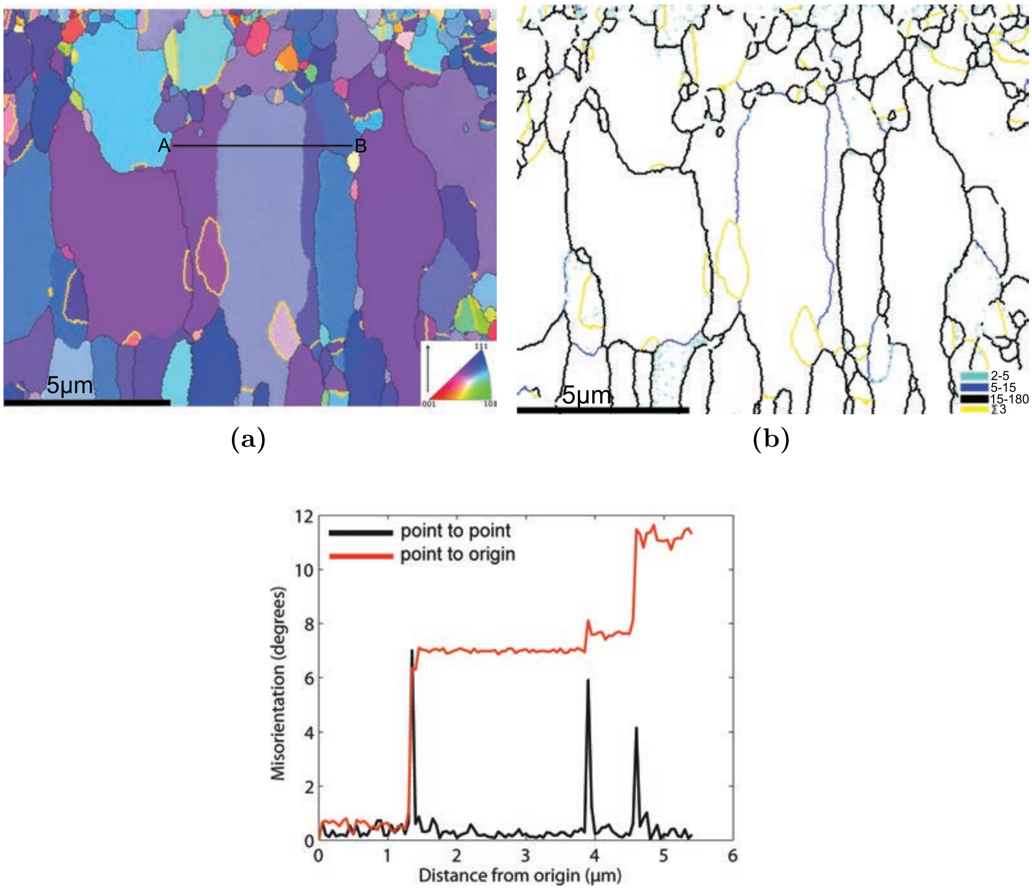

(a)

(b)

(c)

Figure 6.15: (a) Orientation map of sample F9-600 color coded in relation with film growth direction shown by an arrow. High angle grain boundaries are marked in black ans Σ3 boundaries are in yellow. (b) grain boundaries colored based on the misorientation. 2-5° : light blue, 5-15° : dark blue, 5-180° : black and Σ3 : yellow. (c) Point-to-point misorientation and point-to-origin misorientation along AB line shown in the orientation map (a); Three low angle boundaries are present between 'A' and 'B'.

6.2.2 Multiple-Component Fiber Texture

The thermal behavior of samples F5, F7, and F8 which have multi component fiber texture in as-deposited state (see Table 5.2 in page 58) are studied in this section.

All the studied samples in this section showed fiber texture in the film's growth direction. Accordingly, the texture evolution is studied by analysis of fiber axes and their orientation density in the film growth direction, Table 6.9.

Table 6.9: Orientation density in MRD for different fiber axes of samples F5, F7 and F8 and after thermal treatment for 30 min at 150, 200, 400, and 600°C. AD stands for as-deposited state. The results are obtained by XRD texture analysis.

	Fiber axes	AD	150°C	200°C	400°C	600°C
F5	<100>	2.0	3.9	3.2	4.7	4.8
	<111>	2.7	2.6	2.6	5.4	9.6
	<511>	2.0	–	–	–	–
F7	<100>	–	5.3	7.4	2.9	1.3
	<111>	3.2	3.1	2.9	5.1	9.2
	<511>	2.0	–	–	–	–
F8	<100>	–	–	–	–	–
	<111>	2.5	2.8	2.8	5.2	11.1
	<511>	1.5	1.6	1.6	–	–

Following Table 6.9, the orientation density of the <111> fiber has the same pattern for all the samples: Orientation density of the <111> fiber is below 3 MRD for thermally treated samples at 200°C, $\approx$ 5 MRD for thermally treated samples at 400°C, and $\approx$ 10 MRD for thermally treated samples at 600°C. The evolution of the <100> fiber is dissimilar for the different samples. For sample F5 there is a gradual increase in orientation density of <100> fiber such that in the final state, sample F5-600, it is relatively high (4.8 MRD). For sample F7, the <100> fiber texture strengthens and then reduces by an increase of thermal treatment temperature. Finally, for sample F8 the strength of the <100> fiber texture is insignificant regardless of the thermal treatment temperature.

Since texture analysis revealed that <100> and <111> oriented grains are the main texture components of the discussing samples, single line analysis of 200 and 111 peak profiles were applied to characterize the grain size (coherently diffracting domain size) and the micro-strain. The results are listed in Table 6.10.

The average grain size in the film growth direction of <111> oriented grains of samples (F5, F7, F8), (F5-150, F7-150, F8-150) and (F5-200, F7-200, F8-200) are comparable. However, there is a significant difference between the grain size of thermally treated samples at 400°C, such that F5-400 has the largest <111> grains and F8-400 has the smallest. A similar trend applies for <100> oriented grains.

Table 6.10: Grain size in nm and micro-strain of certain orientation obtained by single line analysis for samples F5, F7, F8 and their thermally treated counterparts. (a) Average size and micro-strain of <111> oriented grains. (b) Average size and micro-strain of <100> oriented grains. AD stands for as-deposited state. 'N' represents calculated value above the upper determination limit of the used diffractometer (300 nm).

(a)

111 peak		AD	150	200	400	600
F5	Grain size	19	23	28	N	N
	Micro-strain	0.0019	0.0023	0.0027	N	N
F7	Grain size	21	21	22	278	N
	Micro-strain	0.0022	0.0030	0.0026	0.0002	N
F8	Grain size	18	20	23	147	N
	Micro-strain	0.0014	0.0027	0.0029	0.0006	N

(b)

200 peak		AD	150	200	400	600
F5	Grain size	11	12	15	134	N
	Micro-strain	0.0025	0.0034	0.0048	0.0004	N
F7	Grain size	8	11	11	116	N
	Micro-strain	0.0023	0.0053	0.0027	0.0006	N
F8	Grain size	8	11	10	47	N
	Micro-strain	0.0028	0.0045	0.0027	0.0009	N

It is noted that there is a significant increase in grain size and decrease in micro-strain upon thermal treatment at 400°C.

Ion channeling images of the microstructure of samples F5-200, F7-200, F5-400 and F7-200 are shown in Figure 6.16. It can be clearly seen that microstructure of samples F5-200 (Figures 6.16a) and F7-200 (Figures 6.16c) are composed of relatively fine grains. By an increase of the thermal treatment temperature to 400°C, a significant increase in the average grain size occurs and equiaxed grains form, Figures 6.16b and 6.16d. Upon thermal treatment at 600°C further grain growth occurs and the microstructures are composed of only equiaxed grains, Figure 6.17. Note that some of the larger grains in the microstructure of sample F5-600 are <100> oriented whereas in samples F7-600 and F8-600 <100> oriented grains are relatively small in size. This is in good agreement with texture results provided in Table 6.9.

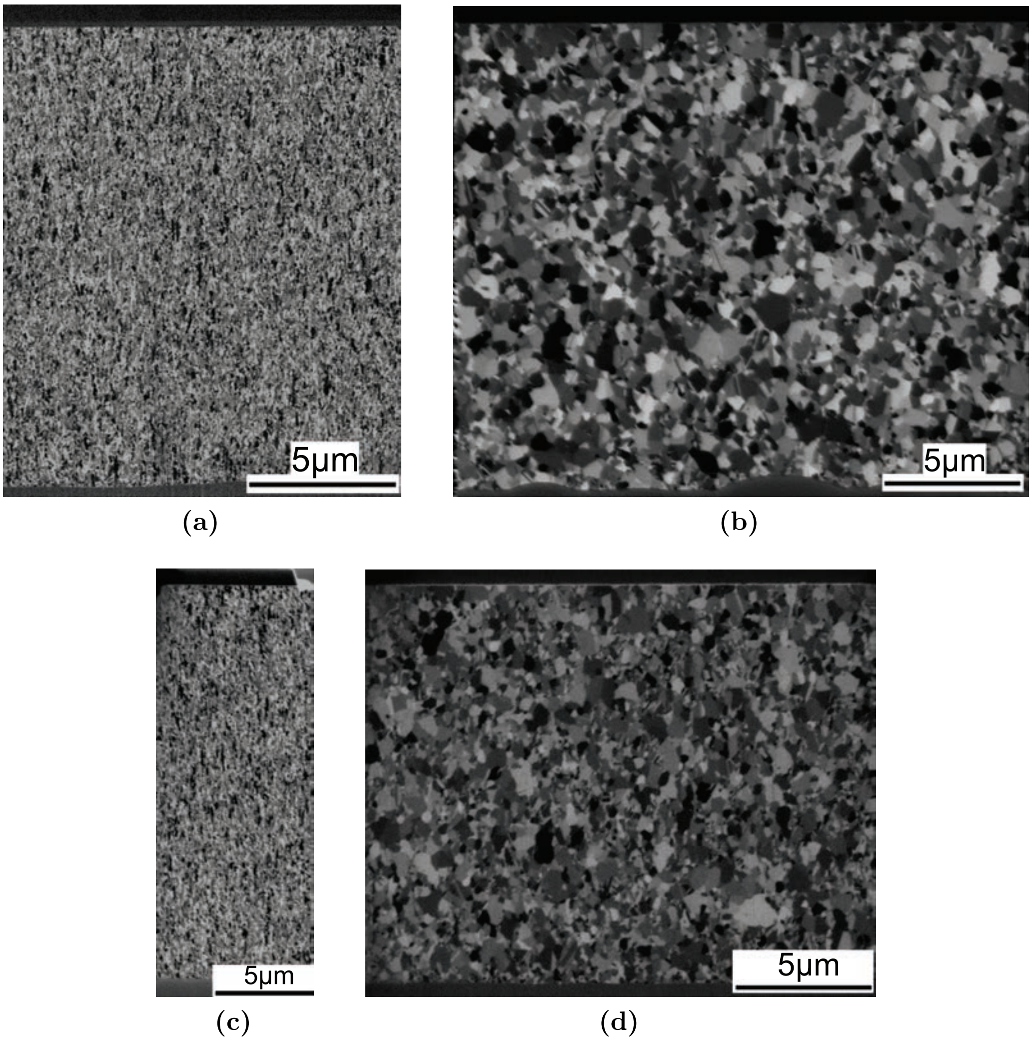

(a) **(b)**

(c) **(d)**

Figure 6.16: Ion channeling images of samples (a) F5-200, (b) F5-400, (c) F7-200, and (d) F7-400.

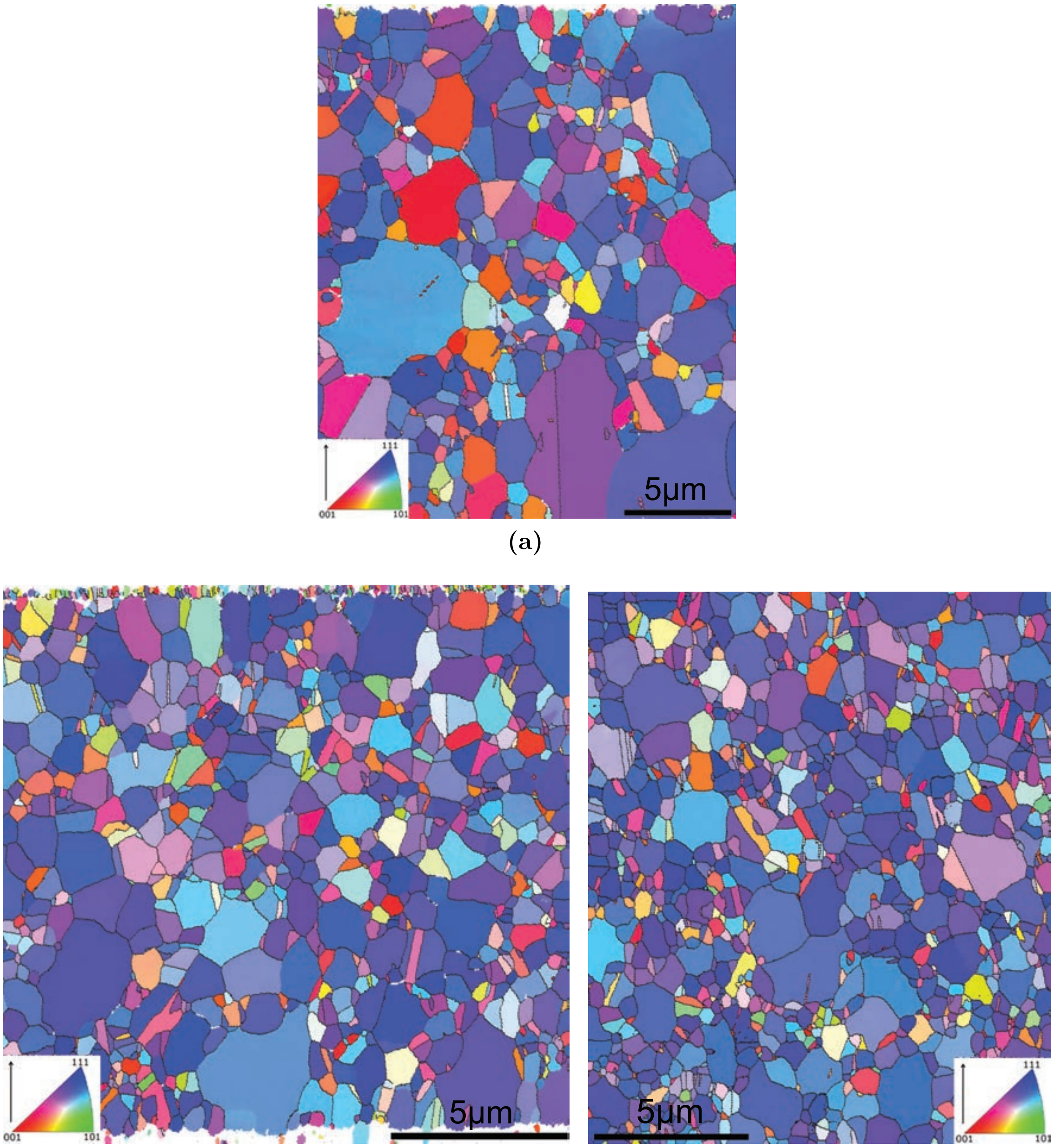

(a)

(b)

(c)

Figure 6.17: Orientation map of sample (a) F5-600, (b) F7-600 and (c) F8-600, color coded in relation with film's growth direction shown by an arrow. High angle grain boundaries are marked in black.

6.3 Grain Boundary Character and Thermal Stability

6.3.1 Length Fraction of the Boundaries

The evolution of texture, grain size, micro-strain and microstructure characteristics for some selected samples due to thermal treatment was presented in sections 6.1 and 6.2. In this section the grain boundary character of thermally treated samples is discussed in more detail.

In Table 6.11 five parameters are listed, characterizing the grain boundaries. The first two are: length fraction of high angle and low angle grain boundaries, respectively. Note that the sum of the these two is 100%. Length fraction of $\Sigma3/HAGB$ and $\Sigma9/HAGB$ are listed in the Table 6.11 too. In addition, AHIL was measured over whole film thickness and averaged, this is also provided for all samples in the Table 6.11. For columnar microstructures, AHIL represents the width of columns while in the microstructure composed of equi-axed grains, AHIL represents the diameter of the grain. Table 6.11a provides the results for those samples for which an acceptable orientation map was obtained in as-deposited state, whilst Table 6.11b provides that, only for thermally treated samples.

Based on the results provided in Table 6.11a, among samples with a columnar microstructure and nano-crystalline microstructure in the as-deposited state, sample F1 and F8 are the most thermally stable, respectively. Interestingly, sample 8C10 is the least thermally stable sample of all, and at the same time, this sample and its thermally treated counterparts have the highest length fraction of $\Sigma3/HAGB$.

Following Table 6.11b, thermally treated samples of F4,F5,F7, and F8 at $600°C$, have very similar grain boundary character, in terms of high angle grain boundary fraction ($\approx$ 87%) and $\Sigma3/HAGB$ ($\approx$ 25%). It is noteworthy that, all of these samples had a fairly strong <111> fiber texture after thermal treatment at $600°C$. Sample F9-600 has the lowest $\Sigma3/HAGB$ and highest fraction of low angle grain boundaries of all samples. 75% of low angle boundaries was of misorientation 2-5° and 25% of low angle boundaries was of misorientation 5-15°. This accumulation of low angle grain boundaries distribution towards misorientation of 2-5° was not observed in other samples.

6.3.2 5-parameter GBCD analysis

Observing the 2-dimensional microstructure of different samples shown in sections 6.1 and 6.2, it is apparent that not all of the boundaries are alike in terms of topography. Especially $\Sigma3$ boundaries which are of high importance in grain boundary engineering, are

Table 6.11: Length fraction high angle boundaries, low angle boundaries, $\Sigma 3/HAGB$, and $\Sigma 9/HAGB$ in (%) and average horizontal intercept length in μm for thermally treated samples. (a) Samples that the as-deposited state boundary analysis was obtained and (b), samples that as-deposited state boundary analysis could not be conducted.

(a)

Sample	HAGB(%)	LAGB(%)	$\frac{\Sigma 3}{HAGB}$(%)	$\frac{\Sigma 9}{HAGB}$(%)	AHIL(μm)
F1	75.4	24.6	43.5	2.5	0.28
F1-600	84.3	15.7	40.3	1.1	0.53
F2	72.8	27.2	44.5	7	0.17
F2-600	77.3	22.7	29.6	0.5	1.67
F3	71.8	28.2	41.0	6.1	0.23
F3-600	83	17	36.1	0.8	1.66
8C10	84.9	15.1	50.3	10.0	0.16
8C10-400	89.5	10.5	48.6	6.4	0.51
8C10-600	94.5	5.5	49.6	1.8	2.6

(b)

Sample	HAGB(%)	LAGB(%)	$\frac{\Sigma 3}{HAGB}$(%)	$\frac{\Sigma 9}{HAGB}$(%)	AHIL(μm)
F4-600	85.5	14.5	24.4	1.0	0.59
F5-400	85	15	20.4	1.3	0.21
F5-600	86.9	13.1	26.2	1.0	0.70
F6-600	83.2	16.8	33.4	0.6	1.61
F7-400	88.1	11.9	18.4	1.5	0.15
F7-600	90.5	9.5	23.5	0.9	0.44
F8-600	89.5	10.5	24.3	0.8	0.40
F9-600	72.4	27.6	18.1	1.9	0.82

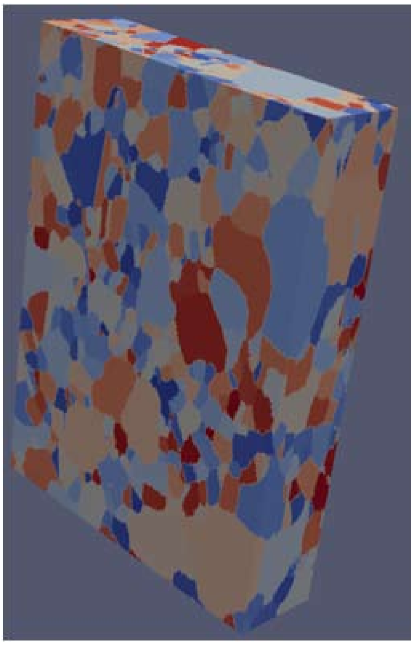

Figure 6.18: 3-dimensional microstructure of sample F5-600. the grain are colored randomly.

not the same in different samples. For instance, $\Sigma3$ boundaries in sample F1-600 are mostly straight (see Figure 6.1), while that of F9-600 are mostly curved (see Figure 6.15a). This, strongly suggests a difference in grain boundary plane of these boundaries. 3-dimensional characterization of the microstructure (that of sample F5-600 is shown in Figure 6.18) by 3D-EBSD and applying 5-parameter grain boundary character distribution (GBCD) analysis, provides the information necessary to study the difference between the plane of different boundaries [111] (see the details in section 4.3.4.2 - page 53). 5-parameter GBCD analysis has been applied on three of the thermally treated samples:

(i) F1-600, the microstructure is notably close to the as-deposited state after thermal treatment and the majority of the $\Sigma3$ boundaries are growth twin boundaries;

(ii) F5-600, the as-deposited microstructure is fully evolved due to thermal treatment and the $\Sigma3$ boundaries are mostly annealing twin boundaries; this sample is representative for samples F4-600, F7-600, and F8-600.

(iii) F9-600, the as-deposited microstructure is fully evolved, but $\Sigma3$ boundaries are not like typical annealing twins as seen in for F5-600.

The details of 3D-EBSD measurements on these samples are provided in Table 6.12.

Note that in the process of matching between the sections[2] to find the similar triple junctions and hence, obtain the triple lines, for sample F5-600 every second section (odd or even numbered) is matched. For samples F1-600 and F9-600 the matching process

---

[2] Since the 3D-EBSD is a serial sectioning process, each section is a surface on which a 2D-EBSD is conduced.

was applied for every section[3]. This owes to the fact that the distance in z direction (perpendicular to 2D-EBSD maps) was twice the step size in 2D-EBSD maps for F1-600 and F9-600, hence there was no need for matching every second sections.

The details of matching triple junctions of 2D-EBSD maps for different samples is provided in Table 6.13.

Observing the grain boundary plane distribution, $\lambda(n)$, there is a peak at $\{111\}$, for all three samples, Figure 6.19. Sample F1-600 has the strongest $\{111\}$ peak (3.67 MRD) and that of samples F5-600 and F9-600 are ≈ 1.9 MRD and ≈ 1.5 MRD respectively[4].

In order to study the coherency of $\Sigma 3$ boundaries, grain boundary plane distribution of 60°/[111] was studied and the results are provided in Figure 6.20. $\lambda(n) \mid 60°/[111] =$ 1364, 466, and 243 MRD for samples F1-600, F5-600[5] and F9-600 respectively. Thus, the fraction of coherent twin boundaries in sample F1-600 is three times and more than five times larger than that of F5-600 and F9-600, respectively.

The upper limit of the population measured in MRD is equal to the number of distinguishable cells of discretized 5 dimensional space [111]. The number of distinguishable cells for the applied analysis is 6561, accordingly at least $1364/6561 = 21\%$ of all grain boundary planes are coherent twin boundaries for sample F1-600. Using a similar calculation, at least ≈ 7% and 4% of all grain boudaries are coherent twin boundaries in sample F5-600 and F9-600, respectively.

The pronounced peak of $\{111\}$ planes in Figure 6.19a for sample F1-600 is due to the presence of a very large population of coherent twin boundaries. Following the same argument for samples F5-600 and F9-600 there is a direct relation between the population of $\{111\}$ planes in the sample and the population of coherent twin boundaries.

Table 6.12: 3D-EBSD measurement details for samples F1-600, F5-600, and F9-600: Step size in nm of 2D-EBSD maps, slice thickness in nm, number of slices, and total analyzed volume in μm^3.

	2D-EBSD Step Size (nm)	Slice Thickness (nm)	Number of Slices	Volume μm^3
F1-600	50	100	41	$10 \times 20 \times 4.1$
F5-600	60	60	74	$16 \times 20 \times 4.4$
F9-600	50	100	65	$15 \times 11 \times 6.5$

---

[3] More details of GBCD analysis is provided in section 4.3.4.2 - page 53

[4] 1.9 MRD for sample F5-600 is the average between 1.8 MRD for odd numbered and 2.0 MRD for even numbered sections.

[5] 466 MRD for sample F5-600 is provided as the average of 433 MRD for odd numbered and 500 MRD for even numbered sections.

Table 6.13: Average number of triple junctions in 2D-EBSD maps, average number of matched junctions between the sections, and fraction of matched junctions in percent which is obtained by dividing the second column to the first.

	No. triple junctions	No. matched junctions	fraction of matched junctions %
F1-600	395	171	43
F5-600	794	286	36
F9-600	372	100	27

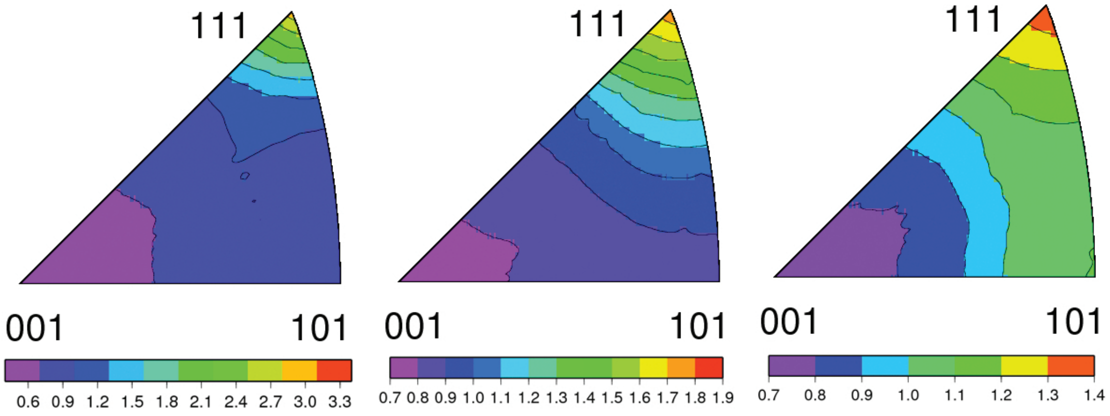

(a) (b) (c)

Figure 6.19: Grain boundary plane distribution $\lambda(n)$ of (a) sample F1-600, (b) sample F5-600 and (c) sample F9-600. The levels are in MRD. Note that the levels are different for different samples. (b) corresponds to sections with odd numbers. Even number sections are not shown here for the sake of brevity.

6.3.3 Grain Boundary Network

More than grain boundary population, grain boundary network must be addressed in the context of grain boundary engineering. To achieve this, high angle grain boundaries network of some of the thermally treated samples are shown in Figure 6.21 and Figure 6.22. It is notable that the network of general high angle grain boundaries (high angle boundaries, shown in red, other than $\Sigma3$, $\Sigma9$, and $\Sigma27$ which are shown in green) is not fully broken in any of the samples; i.e. there is passage of general high angle grain boundaries from the surface to the substrate.

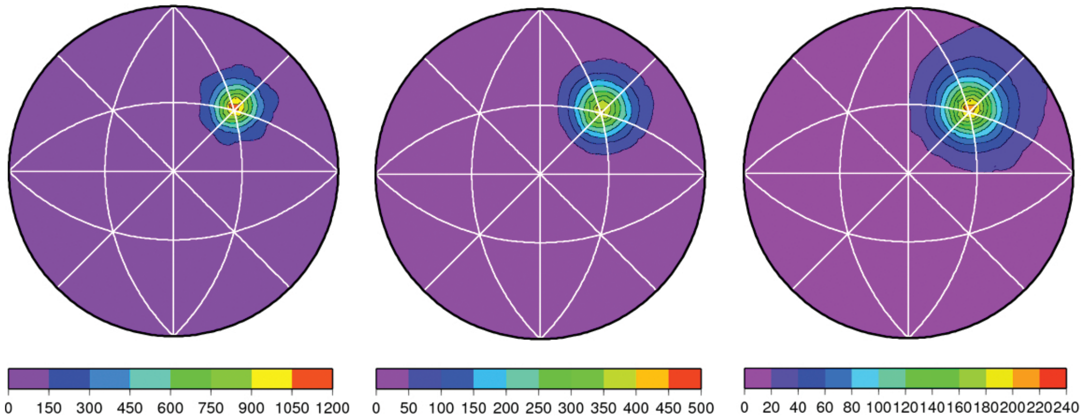

(a) (b) (c)

Figure 6.20: Grain boundary plane distribution of Σ3 misorientation, ($\lambda(n) \mid 60°/[111]$) of (a) sample F1-600, (b) sample F5-600 and (c) sample F9-600. The levels are in MRD. Note that the levels are different for different samples. (b) corresponds to sections with odd numbers. Even number sections are not shown here for the sake of brevity.

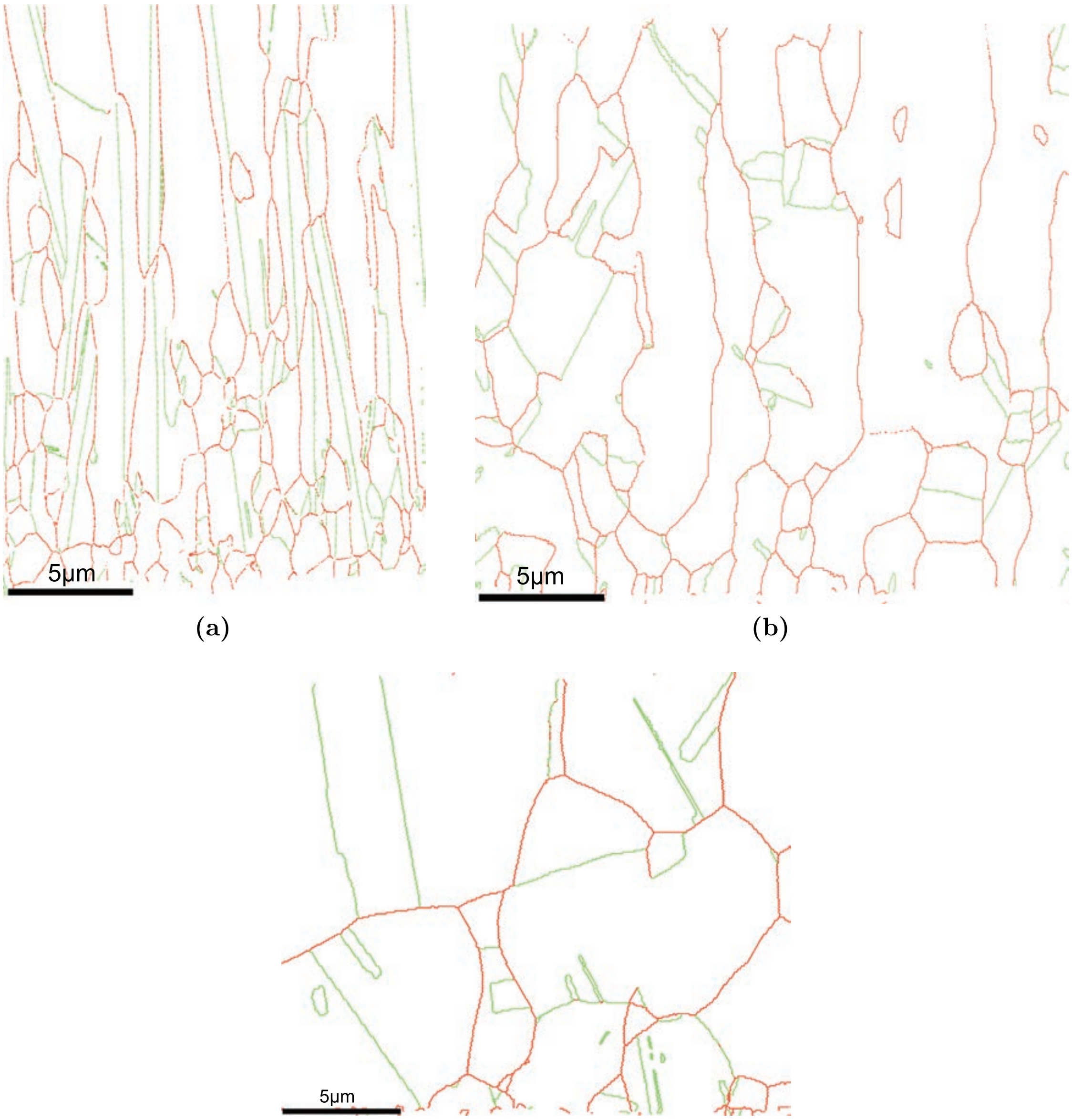

(a)

(b)

(c)

Figure 6.21: High angle grain boundary network of samples (a) F1-600, (b) F2-600, and (c) 8C10-600. Σ3, Σ9, and Σ27 are shown in green and other high angle grain boundaries in red.

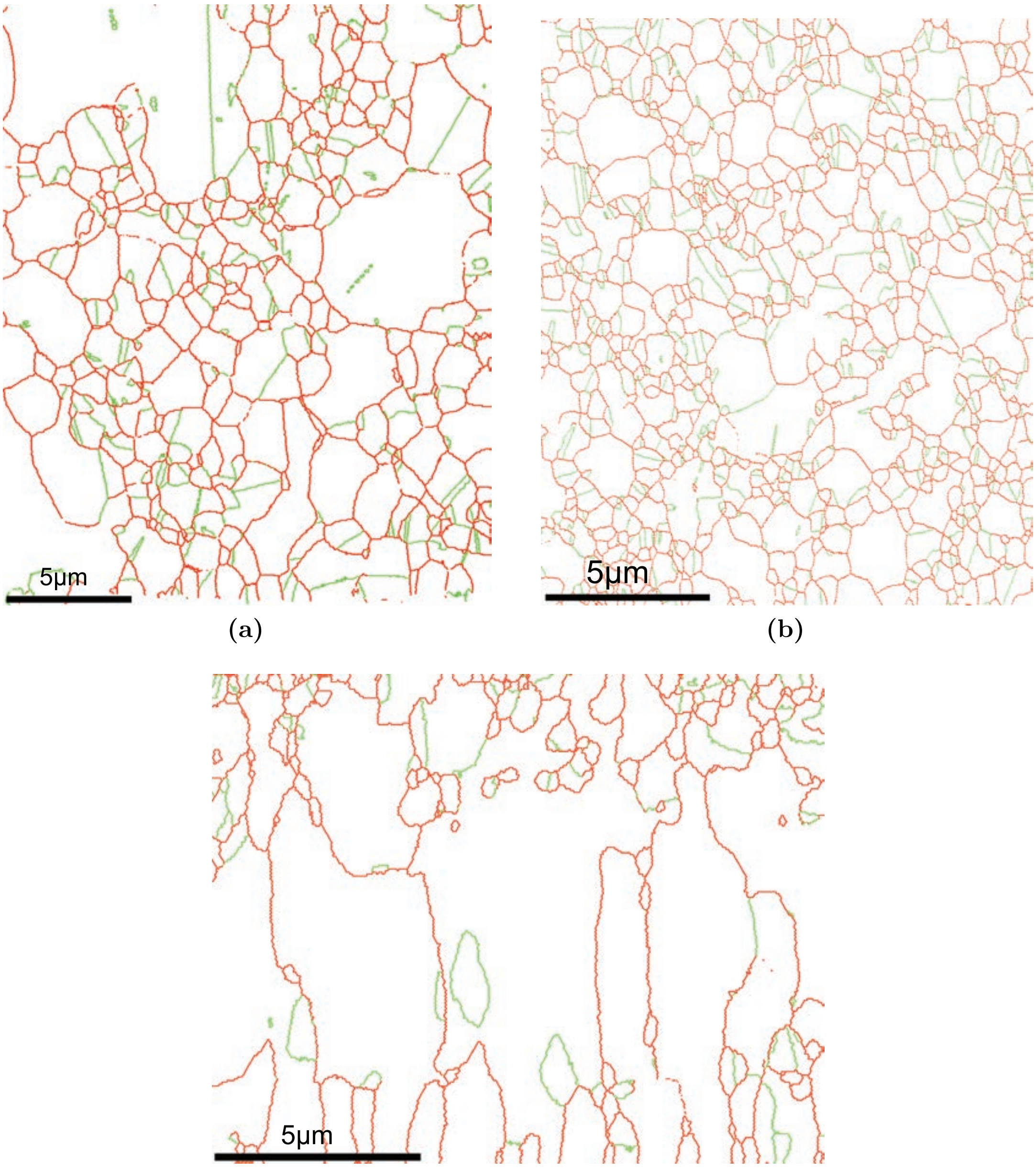

(a) (b)

(c)

Figure 6.22: High angle grain boundary network of samples (a) F5-600, (b) F8-600, and (c) F9-600. Σ3, Σ9, and Σ27 are shown in green and other high angle grain boundaries in red.

Chapter 7

Discussion

In this chapter, the results which were provided and briefly interpreted in chapters 5 and 6 are discussed in depth with a main emphasis on grain boundaries and grain boundary engineering. The studied samples in chapter 5, had either (i) a fully nano-crystalline microstructure or (ii) a coarse columnar microstructure. In the first case the grain boundary character in the as-deposited state is not assessed (due to experimental limitations to study nano-crystalline microstructure with OIM) and thermal treatment is applied to study the evolution of the microstructure, and how it can be used for deliberate manipulation of the microstructure. In the second case, the high fraction of special boundaries (due to formation of growth twins) in the as-deposited state is obtained, and the major focus is to study the stability of the special boundaries. Cases (i) and (ii) are discussed in sections 7.1 and 7.3, respectively. Furthermore for sample F6, the microstructure is a mixture of coarse columnar and nano-crystalline, hence, it is discussed in a separate section (7.2).

Note that, for characterization of the boundaries in nano-crystalline samples, lowering the accelerating voltage, changing the working distance, and increasing the acquisition time have been attempted for experimental investigations with OIM in SEM. Despite some promising results, stability of the microscope and carbon contamination hindered obtaining a proper and sufficiently large orientation map (see Appendix F). Furthermore, in relatively large grained samples, in which acceptable orientation maps were obtained, nano-structures such as nano-twins, occasionally could not be resolved fully by OIM-in-SEM. For instance, in Figure 5.20 (page 79) the presence of numerous fine twin lamellae were shown by ion channeling imaging whereas in the corresponding orientation map they were absent. This example shows inadequate resolution of OIM-in-SEM, but more importantly it reveals that ion channeling imaging supplements OIM-in-SEM very well. Hence, by applying these two techniques supplementary, a thorough microscopic characterization can be obtained.

Through chapters 5 and 6 the combination of OIM-in-SEM and ion channeling imaging on different samples was shown. The integration of the ion channeling image into the OIM data was also applied and that is shown in Appendix G.

7.1 Thermal Behavior of Nano-Crystalline Samples

In chapter 5 it was shown that samples F4 to F9 except F6 are fully nano-crystalline and thermal behavior of these 5 samples were studied in chapter 6. Sample F9 showed a peculiar behavior, unlike the rest:

- Grain refinement was observed for samples F9-150 and F9-200.
- Microstructure of F9-400 was still nano-crystalline.
- Microstructure of sample F9-600 had the lowest fraction of $\Sigma 3$ boundaries among all thermally treated samples and those boundaries were oddly curved.

Accordingly, thermal behavior of sample F9 will be discussed first and based on that, thermal behavior of other nano-crystalline samples will be addressed afterwards. For the sake of brevity samples F4, F5, F7, and F8 are referred as F-NC hereafter.

7.1.1 Thermal Behavior of Sample F9

In samples F9-150 and F9-200 grain refinement of <111> oriented grains and a reduction in the volume of <111> oriented grains were observed (reduction of orientation density from 5.4 MRD in as-deposited state down to 1.8 and 2.2 MRD for samples F9-150 and F9-200 respectively). Grain refinement upon thermal treatment is contrary to the expectations. Thus, possible errors in the measurement, peak profile fitting, inherent errors in the calculations, accuracy of the reported value, etc. all should be taken into account. The measured 111 peak profile and the fitted pseudo-Voigt function to the measured data for sample F9-150 and F9-200 are shown in Figure 4.5 - page 47, which seems to be acceptable. Assuming no systematic error has happened, three different explanations are put forward for grain refinement and the change in the volume of <111> oriented grains:

1. Grain growth of grains with orientations other than <111>, at the expense of <111> oriented grains has occurred. Thus, the grain size of <111> oriented grains was reduced, and hence, texture strength of <111> decreased. It is proposed in [215] that for FCC metals, when grain growth is driven by minimization of total strain energy, growth of <111> is not favored.

2. A rotation-coalescence mechanism was active for grain growth [216]. In rotation-coalescence, two neighboring grains separated by a grain boundary, rotate (reorient) and merge into a single grain (coalescence) [216, 217]. In this process, the shared boundary is annihilated, hence, the Gibbs energy of the system is reduced [216] (interface energy minimization [215]). It is argued in [216] that, this process is more likely to occur for grains with close orientations[1] than for grains with large misorientation. As a reminiscence of the annihilated grain boundary, dislocations (and/or vacancies) appear in the newly formed grain [216].

   The grain boundary characteristics of sample F9 (as-deposited state) are not assessed. However, from line profile analysis, it was concluded that the grain size of <111> oriented grains is 19 nm; and based on surface topography and ion channeling image it was speculated that these fine grains form colonies of fairly close orientation (see section 5.1.5 - page 86). Thus, it is highly probable that grain boundaries with relatively small misorientations are in abundance in the colonies. Assuming that relatively large <111> oriented grains in as-deposited state are more likely to reorient than the small ones; the diffracting volume of <111> oriented grains (hence, texture strength) and measured grain size of <111> oriented grains decreases. Furthermore, micro-strain due to formation of dislocations and vacancies increases. This in fact was observed: micro-strain for sample F9-200 and F9 are 0.0063 and 0.0051 respectively. But, micro-strain of sample F9-150 (0.0047) is smaller than F9 and F9-200.

   The explanation of this discrepancy (reduction of micro-strain in F9-150) is not straightforward. It is pointed out in [218], when the grain size in nano-meter range, “a large micro-strain values can be obtained even when there are no lattice defects besides grain boundaries”, i.e. micro-strain without strain field due to other imperfections of the lattice. Even though “the origin of this distortion is not understood” [218] it might stem from the triple lines. Triple line “embodies a core structure with atomic-level strain and/or bonding defects, and also may have a long-range strain field with both disclination and dislocation nature, it embodies a line energy in the same sense that any other line defect does” [100]. Thus, there is a strain field associated with the triple lines [100]. And the energy of a triple line is realized with its strain field (elastic stored energy) similar to the energy of a lattice dislocations are modeled [100, 219].

   The strain in triple lines depends on many parameters, especially configuration and relative crystallographic orientation of the neighboring grains [100]. A triple line is

---

[1] In the example provided in [216], two grains separated by a 18° undergo a rotation-coalescence.

very complex in nature and there are 11 macroscopic degrees of freedom associated with it [100]. Hence, minimization of the strain energy for the systems with elastic energy stored in the triple lines is not addressed in the literature.

In rotation-coalescence events, grain boundaries and consequently triple lines annihilate; this removes the interface energy of the boundaries, and strain energy of triple lines. And adds strain energy in terms of dislocations and vacancies. Hence, the development of micro-strain due to grain growth, especially when there is a notable strain in triple lines, is fairly complex and reduction in micro-strain of F9-150 can be attributed to that.

3. Another possible explanation for the observed thermal behavior of sample F9, includes vacancy generation and vacancy drag on the boundary migration. [104, 134]. It is well-known that the atomic density of a grain boundary is smaller than that of the interior of the grain [17, 104], i.e. grain boundaries have ‘excess free volume’. Thus, grain growth which is associated with annihilation of low atomic density regions (grain boundaries), brings about formation of vacancies in the interior of the grains [104, 134]. The annihilation of the faults reduces the Gibbs energy of the system in one hand, and on the other hand, the generated vacancies increases the Gibbs energy [220]. Thus, due to vacancy generation and supersaturation of the vacancies in the grains, further grain growth is hindered [104, 134]. After a certain amount of time the supersaturated vacancies diffuse to the available sinks and afterwards grain growth can continue. When grain growth starts again, boundary migration generates new vacancies, and vacancy supersaturation stops the migration again. This phenomenon predicts that the grain migration is a stop/start process [221]. A recent in-situ TEM study on grain growth, confirms start/stop boundary migration for nano-crystalline nickel thin film [222]. At low temperatures, the diffusion rate of vacancies is small and hence, the time needed for dissipation of the vacancies is noticeable. Thus, vacancies are generated due to boundary migration and vacancies impose drag on boundary migration at low temperatures. Higher micro-strain of sample F9-200 (0.0063) in comparison with that of as-deposited state (0.0051) can be, at least partially, attributed to the increase of vacancies in the interior of the grains due to boundary migration. In addition, it has been shown in [134] that, grain refinement can take place due to supersaturation of the vacancies. It is noted that, grain refinement due to supersaturation of the vacancies is orders of magnitude smaller than what was observed for sample F9, hence, it cannot be the sole reason of the grain refinement.

   Electrodeposited material may comprise very high concentration of vacancies already in as-deposited state, i.e. comparable with vacancies in a very quick quenched metal from a high temperature [26]. Thus it is probable that vacancies play a role in the evolution, upon thermal treatment.

The three hypotheses above are based on two grain growth mechanisms i.e. rotation-coalescence and grain boundary migration. It has been argued in [216] that, rotation-coalesce is coupled with grain boundary migration. And since there is no contradiction between the three explanations, all are likely to contribute.

After discussing thermal behavior of samples F9-150 and F9-200, it is natural to follow that of F9-400 and F9-600. For pure nano-crystalline nickel, at low temperatures, the average grain size increases gradually, while a rapid (major) grain growth takes place when the annealing temperature is increased beyond a transition temperature [223]. In a review of calorimetric studies, this transition temperature[2] is suggested to be in the range of ($\approx 250 - 350°C$) [33]. Hence, by thermal treatment at $400°C$, a major grain growth for nano-crystalline nickel is expected.

Thermal treatment of sample F9 at $400°C$ brings about a huge reduction in micro-strain (0.0009) in comparison with the as-deposited state (0.0051). However, interestingly, the average grain size of <111> oriented grains remains in tens-of-nanometer range (39 nm). At $400°C$, high diffusion rate brings about annihilation of vacancies and dislocations readily (this explains the reduction in micro-strain). Hence, vacancy generation and drag, is not an active mechanism at $400°C$ for nickel and cannot count as a reason for retardation of grain growth. Hence, another source of drag must be active .

The effect of triple lines on grain growth has been neglected in many occasions[3], but it has been shown in [132] that excess energy associated with triple lines can be as significant as excess energy associated with grain boundaries. It is known [132] that triple lines mobility can be lower than that of grain boundaries, hence, it can potentially slow down the predicted grain growth by grain boundary migration (triple line drag). Thus, triple lines may control the microstructure evolution of nano-crystalline materials depending on their mobility [132]. Due to the complex nature of a triple line, its characterization and study is extremely hard. Thus, despite the importance of triple lines in nano-crystalline materials, very little is known about their energy and mobility. Nevertheless, some models have been developed [219]. Based on a simplistic model it was shown that triple junction energy is largest when the boundary between the grains forming the junction are low

---

[2] Pronounced peak assigned to the major grain growth [20].

[3] based on the assumption that triple line role is to maintain the equilibrium angles at the points where boundaries meet [222].

angle grain boundaries [219] (see Fig. 13 in there). In addition, in that configuration, triple line mobility is low, and hence, the triple drag is high [219]. It is worth clarifying that, even though large stored energy provides larger driving force for grain growth in one hand, in the other, large line tension associated with triple lines brings about resistance to curvature, and consequently resistance to migration [219]. As a result, the relation between stored energy and mobility of triple lines is also complex which adds more to the complexity of studying triple line effect on grain growth.

Bringing back the discussion to thermal stability of sample F9, it is reminded that no TEM studies were conducted on this sample. Hence the triple junctions (and consequently triple lines) in as-deposited state are not characterized, however it was speculated that the LAGBs are in abundance within the colonies. Thus, triple lines' mobility might be low, i.e. triple line drag is high, hence, in the absence of vacancy drag, triple line drag is still effective and hinder the grain growth such that the microstructure remains nano-crystalline even at $400°C$.

So far in the discussion, a pure nano-crystalline material was assumed. However, electrodeposited films almost always contain various types of inclusions or impurities [50] such as entrapped additives, hydrogen, sulfur, etc. Presence of foreign atoms and molecules in fact influences grain boundary migration and micro-strain too. Most notable of all it is suggested that sulfur influences the grain growth of electrodeposited nano-crystalline nickel, by accumulation at the migrating boundaries [135, 224]. Thus, solute drag or Zener drag can also play a role in grain growth of electrodeposited nano-crystalline nickel. In the absence of TEM analysis the effects impurities cannot be ruled out, however, the source of sulfur in electrodeposited nickel is saccharine, thiourea, and other sulfur containing additives which are common additives for nickel plating [56]. Since BDO, a sulfur-free additive, was used in the present electrolyte it is expected that the sulfur concentration is low [56].

Thermal treatment at $600°C$ brought about drastic grain growth, such that microstructure of F9-600 was far from nano-crystalline (average horizontal intercept length of 0.82 μm). This is due to absence of any dragging effect.

As the grain growth (either by rotation-coalescence or migration) continues, the number of triple lines and, hence, the triple line drag decreases. Thus, grain growth is very subtle first by annihilation of triple lines, the drag reduces and further grain growth though gradual takes place. This causes faster reduction of triple line drag and when triple line drag is virtually absent, major grain growth occurs. Based on this, there must be a transition stage, before the major grain growth. This in fact is observed in calorimetric studies[4] of nano-crystalline Ni [33, 135], in which a broad low energy exotherm was observed before main heat release peak.

The curvature of the boundaries in sample F9-600 is worth discussion too. For nano-crystalline materials, the energy associated with triple lines and grain boundary planes is the driving force for grain growth (strain energy of dislocations, etc. neglected in here). Depending on grain size, energy associated with one of these two is higher [132]. It is estimated [132] that for copper, at grain size of 55 nm, the driving force stemming from triple lines is equal to that of grain boundaries . Hence in the case of copper, at a grain size below 55 nm triple line energy minimization is more pronounced than that for boundary planes. Thus annihilation of the triple lines is favored by the system. Rotation-coalescence is an effective mechanism for triple lines annihilation. This is due to the fact that two triple lines are eliminated from the system when a boundary is annihilated in a rotation-coalescence [216]. Accordingly, it is anticipated that for a system in which the triple line energy is high, below certain grain size, rotation-coalescence become particularly active. It is argued that rotation-coalescence also brings the about formation of curved grain boundaries (see Figure 13 in [216]). Thus, as these processes take place before major grain growth, the number of concave grains is high. Hence, when triple line drag effectively vanishes, there is large driving force for fast moving concave boundaries (curvature driven grain growth). This effect might had an influence on the topology of the grain boundaries of sample F9-600.

Another effect may stem from the change in mobility of low angle grain boundaries by temperature. For aluminum, it was shown [225] that the mobility of low angle grain boundaries is smaller than high angle grain boundaries at $300°C$, but at $600°C$ that is vice versa. The mobility of LAGBs vs temperature for nickel is not studied, at least to the best of author's knowledge, and that might have an influence on the observed topology of grain boundaries too. The LAGBs which are connected to oval-shaped grains (see Figure 6.15b - page 131) provides some evidence for this speculation.

It is suggested that, high velocity of the migrating boundaries brings about a higher density of annealing twins [155, 166]. Contrary to this, despite the higher velocity of grain boundary migration in sample F9-600, the $\Sigma3$ boundary fraction is smaller than any nickel sample studied (see Table 6.11 - Page 137). Peculiarly, $\Sigma3$ boundaries which are expected to be straight where formation of annealing twin boundaries is plausible, had an apparent curvature and even oval shapes (Figure 6.15 - page 131). This curvature manifested itself

---

[4] e.g. differential scanning calorimetry (DSC), modulated differential scanning calorimetry (MDSC), etc. [20]

in very low fraction of coherent $\Sigma3$ boundaries (only 4%) studied by 5 parameter GBCD analysis (see page 139).

In recent studies, it is argued that nucleation of annealing twins takes place preferentially at the triple lines [226]. And migration of triples line actually influences the density of annealing twins [226]. Thus, it seems that minor grain growth activities which took place before the major grain growth alters the triple line character, and that influences the formation and topography of the $\Sigma3$ boundaries too.

7.1.2 Thermal Behavior of Samples F-NC

It is worth reminding that samples F4, F5, F7, and F8 are called F-NC samples for the sake of brevity. Following micro-strain of <111> oriented grains, there is an increase in comparison with as-deposited state for F-NC samples due to thermal treatment at $200°C$ (see Tables 6.6 - page 127 and 6.10 - page 133). Thermal treatment at $400°C$ brings about significant decrease in micro-strain. This is in good agreement with the generation of dislocations due to rotation-coalescence during grain growth and vacancies due to boundary migration at low temperatures and annihilation of these sources of micro-strain at elevated temperatures. However no grain refinement is observed for these samples; and the grain size of <111> oriented grains of samples F-NC-400 is at least 8 fold larger than their as-deposited counterparts. Thus, the triple line drag is not very effective in these samples at $400°C$ and the major grain growth takes place in the temperature range of $200 - 400°C$ (in agreement with the literature [20, 33]). It is notable that for F-NC samples at $400°C$ <111> becomes the major texture component which is further strengthened by thermal treatment at $600°C$. This is in good agreement with the majority of the reports, showing <111> fiber texture is the major texture component of thermally treated electrodeposited nano-crystalline nickel [31, 142, 227]. However, at low temperatures ($150°C$ and $200°C$), <100> fiber texture is the major texture texture component of F-NC samples except F8. As briefly introduced earlier, upon thermal treatment of nano-crystalline materials minimization of the stored energy, either at the interfaces or as strain energy are the driving force for grain growth [215]. For FCC metals, strain-energy-driven grain growth brings about formation of <111> while that of interface-energy-driven results in <100> [215]. This very well describes the co-occurrence of a significant decrease in micro-strain and increase in grain size of <111> oriented grains, as well as strengthening of <111> fiber texture for F-NC-400 samples. In addition, at low temperatures there is general tendency of relatively high micro-strain and relatively high strength of <100>. Despite this general tendency, the <100> texture strength evolution is not exactly the same for all samples. For instance, <100> texture strength of samples F4 and F5 at 150 and 200 $°C$ is almost constant around

$\approx 3.5 MRD$[5] and in contrast <100> texture strength for sample F7-150 it is 5.3 MRD and increases to 7.4 MRD for sample F7-200. Most notably, in sample F8 with fairly close resemblance to sample F7 in terms of texture, micro-strain and size, the strength of <100> texture remains below random distribution for all the thermal treatment temperatures. The this clarifies that there are parameters which have not been characterized, but have an influence on the textural evolution. Triple line is at least one of the key parameters. Here again the strain field associated with the triple lines and the elastically stored energy [100], should be noticed. Unlike, the strain in dislocations which minimization is due to elastic anisotropy of different crystallographic directions [215], the strain in triple line is dependent on many parameters, especially the configuration and relative crystallographic orientation of the neighboring grains [100]. Unfortunately, minimization of strain energy for the systems with elastic energy stored in the triple lines is not fully addressed in the literature. Hence, the proposed [215] development of <100> texture for minimization of strain energy has some short comings as the triple line strain is neglected. Accordingly, the differences in the strength of <100> texture which develops at the low temperatures supposedly by strain-energy-driven grain growth might be attributed to the difference in the triple line strain field of different samples in as-deposited state.

7.1.3 Remarks on Grain Boundary Engineering

Observing the grain boundary network of F9-600 and F-NC-600 (see Figure 6.22 - page 143) the network of general high angle grain boundaries is not broken. And fractions of $\Sigma 3$ and $\Sigma 9$ boundaries are not especially high (see Table 6.11 - page 137). Thus, they do not have the two necessities which are held accountable for enhanced boundary specific properties in grain boundary engineered materials. However, it is emphasized that triple lines must be taken into account when nano-crystalline materials are discussed. For instance, it is suggested in the above that, (i) the outstanding thermal stability of sample F9, even at $400°C$ is due to *triple line drag.* (ii) The presence of curved grain boundaries in sample F9-600, at least partly is attributed to the *triple line* activity before the major grain growth. (iii) The texture evolution of the samples at low temperature depends on the strain field associated with the *triple lines.*

'Grain Boundary Junction Engineering' is a new branch of GBE in which the importance of triple lines is taken into account [104, 198], especially in relation with grain growth, both for engineering the desired microstructure and for stabilization of a microstructure with special properties [220]. Higher thermal stability of sample F9 in comparison with all

---

[5] Note that major texture of sample F4 in as-deposited state is a <211> and that of F5 is triple fiber texture of <100><111><511>.

other nano-crystalline samples in this study and majority of the literature reports and non-typical microstructure after thermal treatment of the same sample at $600°C$, provides two examples for the potential in 'Grain Boundary Junction Engineering'.

7.2 Mixed Coarse Columnar and Nano-crystalline Microstructure

7.2.1 As-deposited State

In F-series samples, sample F6 had a peculiar microstructure, composed of both nano-crystalline and relatively coarse <100> columnar grains. The formation of large grains shows that grain refinement additive in the electrolyte (BDO) did not inhibit the growth properly. Samples electrodeposited in the presence of the same concentration of BDO in a similar electrolyte, but at lower current densities were fully nano-crystalline (samples F4 and F5). A higher current density used for sample F6 (10 A/dm^3) implies that more Ni^{2+} cations are converted to Ni^0 per unit of time. Hence, a faster renewal of the surface takes place. It appears that this renewal is so fast that BDO can no longer compete with this, and cannot cover the newly created surface. This explains why large columnar grain form, however its does not address why a strong <100> fiber texture develop; Two possible answers are:

- Since sample F6 is electrodeposited after the deposition of samples F4 and F5, the concentration of BDO is lowered in the electrolyte such that inhibition intensity of the additive is reduced. Hence, <100> fiber texture (free mode of growth) has formed in practical absence of additive. In case of reduction of the BDO concentration by hydrogenation, it is expected that the products chemical compounds, Trans 2 butene-l,4 diol, Cis 2 butene-l,4 diol and Butane-l,4 diol become active [49]. BDO is extremely effective in grain refinement and depending on the electrodeposition conditions even ≈0.5 Mol/dm^3 of it can suppress formation of columnar microstructure [77]. Thus it is expected that a concentration, lower than ≈0.5 Mol/dm^3 of that be present in the electrolyte when a columnar microstructure is observed. Since 5 Mol/dm^3 BDO was present in the electrolyte, the products of hydrogenation reaction in total must be ≈ 4.5 Mol/dm^3. Trans 2 butene-l,4 diol, Cis 2 butene-l,4 diol promote formation of <110> and Butane-l,4 diol has no effect on preferred orientation [49]. Thus, formation of <100> is mostly due to reduction of BDO concentration in the electrolyte, and concentration of products is not in the range to exert an effect on the preferred orientation.

Having mentioned that, the electrodeposition is a very complex processes, and interdependence of the chemical compounds at different depositing conditions is different. Hence, the alteration of BDO concentration and formation of new chemical compounds might have an effect on the formation of strong <100> fiber texture.

- In absence of BDO in the electrodeposition electrolyte, <100> fiber texture forms, with protrusion comprising {100} and {111} planes. Adsorption of BDO molecules on {111} planes is more favorable than on {100} planes [95]. In addition, in chapter 5 is was shown that BDO does not refine the <111> oriented grain smaller than $\approx 20nm$ but it does for other orientations. Hence, BDO adsorbs on the {111} planes more favorably. Due to the catalytic effect of nickel hydrogenation occurs, and then the chemical products desorb. However on other planes like {100} it adsorbs less favorably, but it remains longer on the surface before desorption. As a result, when BDO is limited in concentration at the surface of the cathode in comparison with the rate of renewal of the surface, {111} planes are covered first by the additive while the {100} are partially covered. Thus {100} planes grow faster, both in the growth direction and in lateral direction, which brings about pronounced <100> oriented grain; this is schematically shown in Figure 7.1. This explanation is consistent with surface topography shown for sample F6 in Figure 5.22c (page 82) where the protrusions are flat.

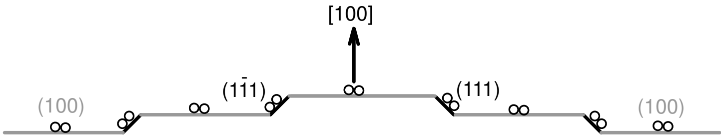

Figure 7.1: Schematic representation of adsorption of BDO molecules when the concentration on the surface is not sufficient to cover the entire exposed surface. {111} planes are fully and {100} planes are partially inhibited.

The last peculiarity that needs to be addressed is the presence of pronounced misorientation within the columns.

In absence of a conclusive TEM analysis only a few hypotheses can be put forward:

- The lateral growth of {100} planes necessitates growth on the neighboring grains. To accommodate the mismatch with the neighboring grains' lattice, geometrically necessary dislocations may form. Though this is valid for all columnar growth, for this sample, the neighboring grains' size is significantly smaller than that of the typical columnar grain. In other words, the number of neighboring grains is significantly larger than that in typical columnar grain growth (compare Figure 7.2a and 7.2c). Thus in this case the columnar grain must accommodate more dislocations. More than that, in normal columnar growth the orientation of neighboring grains does not change significantly as electrodeposition continues. In contrast, in this sample, there are always new grains with different orientations at the neighboring (compare Figure 7.2b and 7.2d). As a result the columnar grains in sample F6 have a higher dislocation density than the grains in regular columnar grains. This is manifested in large misorientations within the grains.

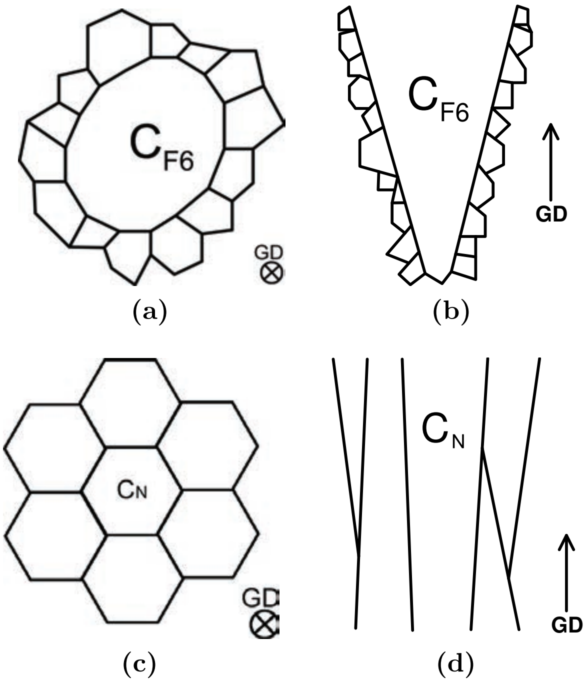

(a) (b)

(c) (d)

Figure 7.2: (a) and (b) Schematic representation of number of neighboring grains for sample F6. (c) and (d) that of an typical columnar microstructure. GD is the growth direction.

- The surface of {100} planes is not fully covered by BDO molecules, thus they don't grow freely but instead some islands grow independently from others (step 1 in Figure 7.3a). When the inhibited area is freed by desorption of additive molecules new nickel atoms lead to coalescence of these islands. Since the islands grow initially independently there could be a misorientation between the two. Thus the *coalescence part* contains dislocations (see Figure 7.3b) to accommodate the misorientation (step 2 in Figure 7.3a). As deposition continues, new surfaces are inhibited and new surfaces are freed for island grow. These new free surfaces are composed of previous *coalescence part* and islands. And since these new island, at least partially, follow the lattice that they grow upon, some dislocations lengthen into the new growing island. Coalescence of new islands adds more dislocations. Accordingly, as the electrodeposition continues, dislocations with different Burgers vector form, which are responsible for misorientation within columnar grains of sample F6.

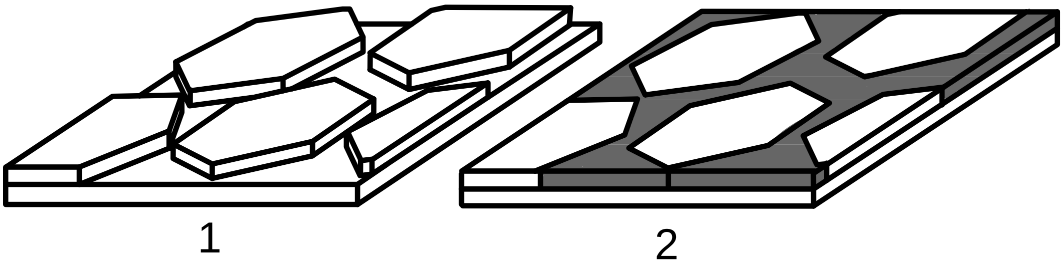

(a)

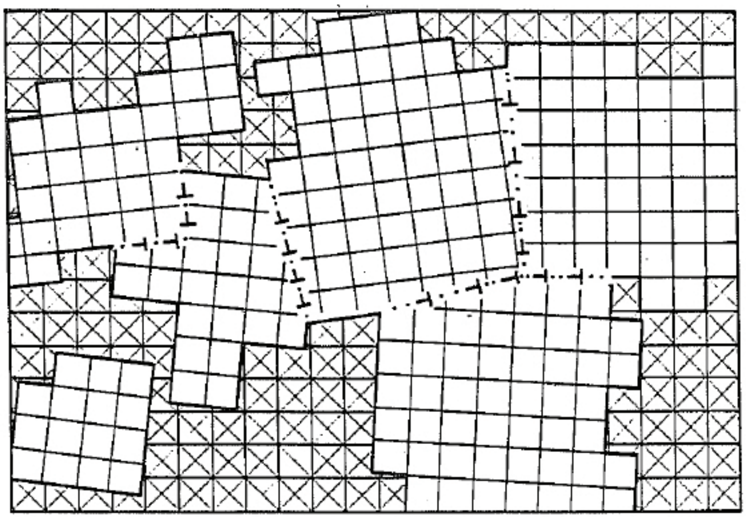

(b)

Figure 7.3: Island growth and merging of the islands, and continuation of this process. (1) some islands, depicted by hexagons, are growing independently, the surface between them in covered by additive. (2) additives are desorbed and coalescence takes place, this region has dislocations shown in gray. (b) Formation of dislocations to accommodate the misorientation between the the islands that meet (coalescence) [76].

7.2.2 Thermal Behavior

The thermal behavior of sample F6 was studied in section 6.1.2 (page 115). By OIM and ion channeling imaging it was shown that upon thermal treatment at 400°C the columnar grains were widened, but the pronounced misorientation within the columns were still present (see Figure 6.9 - page 121). The orientation distribution within the columns strongly suggests the presence of geometrically necessary dislocations. In addition, micro-strain of <100> oriented grains after thermal treatment at 400°C was at the same level as micro-strain in as-deposited state (see Table 6.3 - page 116). Since in this sample <100> oriented grains are fairly large, the micro-strain can be mostly attributed to the dislocations. Thus, at 400°C the columnar grains which are concave in as-deposited state (see Figure 7.2b) are widened in a curvature driven growth, but the dislocations were not annihilated. In the two mechanisms suggested (see section 7.2.1) for the formation of dislocations in the as-deposited state, it is expected that they form randomly, thus, they may have entanglements which inhibit their movement even at elevated temperature. At 600°C drastic grain growth was observed close to the films surface (see Figure 6.9c - page 121), where columnar grains were located in as-deposited state. The texture of these grains is double fiber of <111> and <100>. It is not clear whether formation of <111> oriented grains is due to nucleation of new grains or growth of existing <111> fine grains. In any case, the energy associated with the dislocations and general high angle grain boundaries, and large mobility of general high angle grain boundaries brought about the significant growth close to the film surface. In contrast, in the film/substrate side, the grain growth is less pronounced and the microstructure is similar to what has been reported for F-NC samples in terms of size and topology of the grains.

7.3 Coarse Columnar Microstructure

Samples with different textures, i.e. <211>, <100>, and <210>, were electrodeposited in additive free Watts electrolytes. The conditions at which these textures were obtained is in good agreement with the texture map (pH and current density are variables) provided in [75]. At a low current density (2 A/dm^2) and high pH (4.5) a <211> texture was obtained (sample F1). Formation of this texture is attributed [75] to the formation of colloidal $Ni(OH)_2$ in the mentioned conditions. A <210> texture for sample 8C10 was obtained under the conditions which favors formation H_2 [75], i.e. high current density (10 A/dm^2) and a low pH (2.0). Lastly, a <100> texture was obtained for samples F2 and F3. It is suggested [75] that, <100> forms in the absence of effective chemical species that exert inhibition, hence, <100> is known as free mode of growth [75].

The configuration and characteristics of twins were different for different textures; those are discussed in further details first, and afterwards the thermal stability of twins is addressed. Sample F2 is discussed further in this chapter only, hence, hereafter when <100> textured sample is used, sample F2 is meant.

7.3.1 Twin Configuration and Characteristics

7.3.1.1 <211> Texture

In <211> oriented grains, twin lamellae are elongated parallel to the growth direction and enveloped in the columnar grain. In addition, the width of twin lamellae does not change with the film thickness (see Figure 5.14 - page 73). Not only twin lamellae are parallel along the growth direction, but they are also parallel to one another in the plane parallel to the substrate (see Figure 5.28a - page 94). This observation is in accordance with the reports in the literature [75, 168, 228]. It has been proposed [157, 229] that, twin boundaries in <211> oriented grains, form due to (i) formation of defective nuclei containing {111} twinning planes and/or (ii) coalescence of clusters which meet and favor low-energy {111} boundaries. Defective nuclei and coalescence of clusters, address formation of twin boundaries due to lateral growth. In addition, it was shown that (see Figure 5.13 - page 73) at the very vicinity of the amorphous substrate a very fine microstructure forms first and as the deposition continues columnar microstructure develops. It is shown [54, 230] that on an amorphous substrate (actual film/substrate interface) a random texture develops first. The OIM analysis on a cross-section of sample F1 with <211> fiber texture, showed that[6] at the first $2\mu m$ from the practical film/substrate interface, the texture is a <100><111> double fiber[7]. It is obvious that the crystallography and topography of already deposited material influences the formation of columnar grains, similar to the way that an etched crystalline substrate does(see Fig.6 in [231]). Accordingly, formation of a <100><111> double fiber texture (the strength of <100> is twice more than <111>) prior to a <211> may have an influence on twin formation in <211> oriented grains as well. To elucidate more on this, further investigations are required.

7.3.1.2 <100> Texture

The majority of the twins in <100> oriented grains appeared as inclined lamellae with respect to the growth direction (see Figure 5.6c - page 67). This is in agreement with the reports in the literature [75, 83, 228]. By cross-sectional TEM studies in [228], the characteristics of twins in <100> oriented grains is described. However, a more detailed characterization of twin lamellae in <100> oriented grains was provided in section 5.1.3.3. Three different configurations of twin lamellae in <100> orientated grains are: (i) Fault Formation at the Boundaries, (ii) Continuation of Twin Growth, and (iii) Neighboring Grains Interdependence Growth. All these configurations, originate from the effect of

---

[6] most probably for the first time

[7] It is reminded that the orientation of the layer between the actual film/substrate and practical film/substrate is not analyzed but it is most probably close to random.

neighboring grains. To elaborate more on that, it is noted that after neutralization of nickel ions at the surface, they diffuse to the active growth sites [43]. In general at the grain boundaries, due to the difference in the crystallographic orientation of the neighboring grains, it is more probable for the atoms to occupy a fault position. This brings about 'Fault Formation at the Boundaries'. Accordingly, the probability of formation of twins in a grain is dependent on the crystallography of the neighboring grains. When the crystallography of a neighboring crystallite at the boundary changes, the probability of formation of twins changes too. In this regard, 'Continuation of Twin Growth', can also be interpreted as the change of the probability of formation of twins. This is schematically shown in Figure 7.4. Lets assume two neighboring grains A and B are positioned such that cannot cause formation of twin lamellae into one another, but C and B can. Hence, a twin lamella, T_1, forms due to 'Fault Formation at the Boundaries' in grain B. At certain conditions T_1 can continue its growth and reaches the neighboring grain A; and since the crystallography and topography of T_1 is different from grain B, those can be such to increase the chance of formation of twin lamellae in grain A. Hence, formation of twin lamellae T_2 is induced. Accordingly, 'Continuation of Twin Growth' can be seen as 'Fault Formation at the Boundaries'.

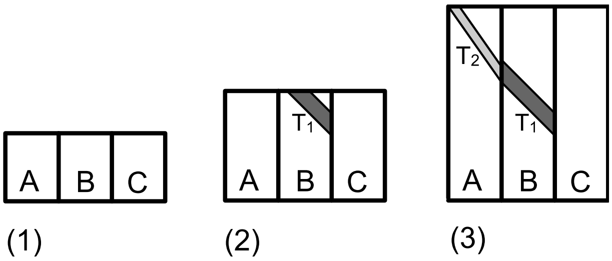

Figure 7.4: Twin lamellae, T_1, form due to 'Fault Formation at the Boundaries' in grain B. The crystallography and topography of T_1 is different from grain B, those can be such to increase the chance of formation of twin lamellae in grain A.

'Neighboring Grains Interdependence Growth' (see Figure 5.18 - page 77), seems to stem from a peculiar crystallography and configuration of neighboring grains is such that the probability of 'Fault Formation at the Boundaries' is high for both grains.

Thus, three configurations of twin lamellae in <100> oriented grains stem from higher chance of fault formation at the boundaries. This is valid for all electrodeposition processes in general. However, since in all other textures except <100> there is an effective chemical species at the surface, these faulty positioned atoms at the boundaries are less likely to be screened by the newly arrived atoms. Hence, the faults that are formed at the boundaries do not develop into the grains easily. In contrast, in case of <100>, (free mode of growth) at which there are no inhibitors at the surface and atoms can migrate more freely at the surface, the influence of faulty positioned atoms at the boundaries can develop more readily. Hence, combination of fault formation at the boundaries and absence of inhibitors at the surface results in the formation of twin lamellae.

The inclination of the twin lamellae is due to the geometry of the surface topography of <100> oriented grains. Since formation of square pyramid with faces composing of {111} planes and to lesser extent {100} planes is favored [95, 228] (see Figure 5.4 - page 65) , the twin lamellae which starts at the boundaries follow the underlying {111} planes.

7.3.1.3 <210> Texture

The twins in <210> nickel is least discussed in the literature. However, there is an interesting cross-sectional TEM study [81] showing that <210> oriented grains were composed of a complex helical pile-up of twinned tetrahedra. The result provided in section 5.4 - page 101, clearly confirmed that peculiar arrangement of the grains which are mostly separated by $\Sigma3$ boundaries which form 5-fold symmetry configuration (see Figure 5.38b - page 107). Though the origin of these twins is not well-understood yet, it is highly probable that the presence H_2 either at the cathode surface or in the deposit is a major influencing factor. This hypothesis owes to the fact that the applied deposition conditions favors hydrogen evolution. More importantly, in the mentioned configuration of the grains, there is a connected network of $\Sigma3^n$ boundaries, which successfully break the network of general high angle grain boundaries. Thus, in the as-deposited state sample with <210> texture possess the two requirements of grain boundary engineered material: (i) high fraction $\Sigma3^n$ boundaries and (ii) fragmented network of general high angle grain boundaries.

Note that, the network of grain boundaries for the films must be studied on a cross-section (see Figures 5.40 - page 109). This is the only way that a path of general high angle grain boundaries from the surface to the substrate can be assessed.

7.3.2 Twin's Thermal Stability

The thermal stability of coarse grained columnar microstructure and more importantly twins in <211>, <100>, and <210> fiber textured samples were studied in section 6.1. It was found that the fine twin lamellae in <211> oriented grains are most, and <210> twins are least thermally stable. In the stability of the growth twins at elevated temperature different points must be taken into account simultaneously. The annihilation of stored excess energy associated with the grain boundaries is a driving force for the grain growth [104]. Hence, annihilation of general high angle grain boundaries with higher stored energy than CSL boundaries [232, 233] is favored from a thermodynamical point of view. However, other than energy, the mobility of the grain boundaries must be taken into account[8]. The low mobility boundaries which are stationary are prone to be consumed due to migration of highly mobile boundaries. In general low energy boundaries are of low mobility [234], but this general statement must be used only as a general estimation. It is shown [225] that, the mobility is dependent on the character of the boundary and number of coincidence sites (Σ value) is not a proper indicator of the boundary mobility [225]. For instance, coherent $\Sigma 3$ boundaries, has an extremely low mobility [139], and in contrast $\Sigma 7$ boundaries were found being of high mobility in FCC metals [225] or $\Sigma 9$ boundaries are more mobile than general high angle grain boundaries in Fe-Si alloy [235] (follow the ref. there). Thus low Σ CSL boundaries, which have lower energy than general high angle grain boundaries [233] can have higher mobility than general high angle grain boundaries. In addition to the misorientation, the grain boundary plane influences the grain boundary mobility drastically [139]. As mentioned, high-coincidence coherent $\Sigma 3$ boundary is in fact of very low mobility however, for the same misorientation if the grain boundary plane is of mixed character (other than single {111} plane) then the boundary is of very high mobility [139]. Furthermore there is a dynamic in the grain boundary boundary character when subjected to thermal treatment. It is shown [12] that the plane and misorientation of the grain boundaries alter when interacting with each other. Accordingly, the evolution of the grain boundary character distribution (GBCD) due to thermal treatment is dependent on the as-deposited state GBCD in terms of energy, mobility and the configuration boundaries in the as-deposited state, and how they interact with one another as grain boundaries migrate. Hence, there is not general prediction of the stability of the twins in the as-deposited micro-structures, and every individual case should be addressed separately.

7.3.2.1 <211> Texture

Upon thermal treatment the fine equi-axed grains close to the film/substrate interface were grown notably (6 fold increase in the size of grains located at the first 2 μm from the practical interface). The width of columnar grains also increased (column widening) but to a much lesser extent (≈ 1.5 fold increase in size). Most notably the twin lamellae enveloped within the <211> columnar grain remained fairly stable at $600°C$. Micrographs obtained from the cross-section (Figure 5.6a - page 67) and the top view (Figure 5.28a - page 94) <211> oriented columns showed that twin boundaries are straight lines in both views. Thus, the twins are composed of single {111} plane and they are not of mixed character

---

[8] This is normally achieved by using reduced mobility, K', which is defined as gain boundary energy, γ, times grain boundary mobility, M ($K' = \gamma \times M$) [225].

(fully coherent twin boundaries). Accordingly these coherent twin boundaries are of low energy and low mobility. However, the boundaries between the columnar grains were of general high angle character, thus, of higher mobility and energy, in as-deposited state. After thermal treatment at $600°C$, the character of grain boundaries between the columns remained of general high angle. In addition, the orientation of columns did not change concluding that nucleation of new orientation did not happen. Thus, it seems that the grain growth (column widening), was curvature driven, and the major activity was at the columnar grain boundaries. Hence, the twin lamellae enveloped within the columnar grains were not prone to be consumed by other migrating boundaries, and remained stationary even at $600°C$.

7.3.2.2 <100> Texture

It was shown that the boundary plane of twin lamellae enveloped within <100> oriented grains were not always of a single {111} plane but instead some of the boundaries were mixture of different planes (Figure 5.16 - page 75). Thus, these twin boundaries are of high mobility.

Other than elimination of the boundaries, it is proposed [236, 237] that 'fine tuning' reduces the Gibbs free energy of the system. In this process, the grain boundary planes reorient to come to a lower energy configuration (in this case {111} planes). Thus how much the boundary deviates from the perfect {111} planes, controls its mobility, energy, and whether elimination of the boundary occurs or fine tuning. Upon thermal treatment at $600°C$, 80% of the twin lamellae were annihilated, showing the tendency to elimination of these twins in this system. After thermal treatment at $600°C$, most of the twins had widths notably larger than what was observed in as-deposited state, showing that the twin boundaries occasionally migrated into the enveloping columnar grain.

7.3.2.3 <210> Texture

Upon thermal treatment at $600°C$ all of the as-deposited twins were annihilated from the microstructure and all the twins were of annealing character. The grain growth was so pronounced that no resemblance to the as-deposited state remained. Hence, the microstructure of the sample thermally treated at $400°C$ is of more interest to study the evolution of microstructure. Even at $400°C$ substantial grain growth was observed. The grain growth was most pronounced in the first 7 μm from the film/substrate interface. That region in as-deposited state had higher length fraction of general high angle grain boundaries in comparison with the rest of the microstructure, and also the grain size was smaller. The higher mobility and higher energy of general high angle grain boundaries provides a larger tendency for grain boundary migration. In addition it was shown that (see Figure 5.38b - page 107) short $\Sigma 9$ boundaries are often presence in the $\Sigma 3 \Sigma 3 \Sigma 9$ triple junctions, in as-deposited state. It is shown [234] that in the microstructures where $\Sigma 3 \Sigma 3 \Sigma 9$ triple junctions are in abundance, $\Sigma 9$ boundaries tend to be in a high mobility configuration rather than the lowest energy configuration. Thus it seems that, $\Sigma 9$ boundaries are in high mobility configuration in the as-deposited state, and they tend to migrate readily at elevated temperatures.

Close to the film surface, where the length fraction of coherent $\Sigma 3$ boundaries was high, the effect of migration of general high angle and/or $\Sigma 9$ boundaries is less pronounced, hence, grain growth is less significant.

In addition, in the first 7 μm from the film/substrate interface, it appears that those $\Sigma 3$ boundaries which were connected to the migrating general high angle boundaries were lengthened as the migration of general high angle grain boundaries continued (see Figure 6.11b - page 125). Thus, most of the $\Sigma 3$ boundaries are consumed due to the interaction with general high angle grain boundaries, and the others which were connected to the migrating boundaries are lengthened. Hence, the number of $\Sigma 3$ boundaries decreased as grain growth occurs, however, the length fraction of $\Sigma 3$ boundaries remained constant.

Even though it appears that migration of general high angle and/or $\Sigma 9$ grain boundaries play the major role in grain growth, it is worth noting that the configuration of pseudo 5-fold symmetry may provide a driving force for the growth.

In a presumably perfect 5-fold symmetry junctions, the {111} planes make 70.53° to one another. Five grains with 70.53° angle between their boundaries cannot fill the space and there is[9] 7.36° left which should be filled with geometrically necessary dislocation or low angle grain boundaries. The orientation spread is a rough measure for the abundance of dislocations in the grains (the presence of dislocation also observed in cross-sectional TEM analysis [81]). Since the orientation spread is uneven among the neighboring grains (see Figure 5.37d - page 105), it is expected that some of the grains possess a higher density of dislocations. This potential difference in the faults in neighboring grains, provides a pressure on the boundary for the growth in the direction to annihilate the faults [126].

---

[9] $360^\circ - (5 \times 70.53^\circ) = 7.36^\circ$

7.3.3 <211> Textured Films Optimization

The twins in the sample F1 with <211> texture, had the highest thermal stability. Based on this information BipH and Co-series experiments were conducted.

Twin boundaries are planar defects and similar to general high angle grain boundaries hinder dislocation movement and improve mechanical properties in terms of strength [21, 25]. However, due to the low energy associated with this boundary, the activation energy for migration of twin boundaries in comparison with general high angle grain boundaries is higher; Thus twin boundaries has higher thermal stability [238]. It the shown that twins in <211> oriented grains, have the higher thermal stability in comparison with other material studied. Thus, it is expected that by increase of twin lamella density which are enveloped by <211> oriented grains, some of the mechanical properties to improve while the thermal stability remain intact. Hence, increase of <211> oriented grains and number of twin lamellae is favored for engineering a film with relatively high thermal stability and improved mechanical properties. To achieve this, two points are of high significance: (i) to find the electrodeposition condition at which <211> fiber is sharp and strong (ii) to increase the probability of twin lamella formation.

It was noted that in the conditions that sample F1 was deposited, most of the grains at the surface had a 2-fold symmetry, typical of the <211> oriented grains. In addition, OIM of a cross-section also showed that more than 60% of the grains are <211> oriented close to the film surface. Thus, in the BipH series of experiments, the electrodeposition conditions of sample F1 were slightly altered, to investigate the effect of boric acid concentration, current density, and pH. It was shown that, increase of pH and boric acid concentration, both deter the formation of <211> oriented grains. Higher boric acid concentration than 40 g/dm^3 promotes formation of <100> and <311>. Formation of <311> has been reported [230] in nickel electrodeposits, however, the formation of this texture is not assigned with any chemical species. The complexes that boric acid forms with nickel [61, 62] might have an influence on the formation of <311> texture.

Increase in pH above 4.5 was associated with formation of cactus like features in the films which reduced the strength of <211> texture in comparison with what was obtained at pH=4.5 and boric acid concentration of 40 g/dm^3.

Concluding that $C_{H_3BO_3}$=40 g/dm^3, pH=4.5, and i=2 A/dm^2, brings about highest strength of <211> texture, in the studied electrodeposition conditions; A method to increase the twin lamella density was studied.

Alloying is known to be a method of decreasing stacking fault energy, hence, increasing the probability of twin formation [176]. There are many of different nickel alloys e.g. as Ni-Co [36, 175], Ni-Pd [26], Ni-W [239, 240], Ni-Fe [31, 223], Ni-Mn [80, 174], etc. with different properties reported in the literature. Among these, Ni-Co is synthesized in the electrolytes similar to which is shown to be appropriate for electrodeposition of <211> nickel [26]. In addition, it is shown [175] that not only twin density of the Ni-Co alloy is higher than in pure nickel, but also twin density can deliberately be tailored. Hence, Ni-Co is a suitable case to study its effect on the twin density of <211> grains. Accordingly, relatively small concentration of cobalt ions were added into the Watts electrolyte. In section 5.3 (page 97), it was shown that addition of 20 and 40 $mMol/dm^3$ of Co^{2+} into the electrolyte resulted in the deposits containing 15.6 and 36.7 wt.% of cobalt respectively. The synthesized Ni-Co alloys comprised cobalt at a much higher concentration than in the electrolyte. This is due to well-known anomalous codeposition of binary iron-group alloys [241]. More than that, it was also shown that Ni-36.7 wt.% Co was almost texture free while, Ni-15.6 wt.% Co had a <211> texture. It is reported in [242]that the surface topography of Ni-Co alloys[10] comprising 7 and 27 wt.% Co, have typical 2-fold symmetry pertrusions of <211> texture.

While, Ni-49 wt.% Co has another type of surface topography. High magnification surface protrusions of samples with highest strength of <211> fiber texture (F1) and Ni-15.6 wt.% Co (sample Co20) are shown in Figure 7.5. These two are considerably different and the major differences are:

- In Ni-Co alloy the 2-fold symmetry protrusion has a peak, this is unlike pure nickel in which the highest points of protrusion form a line.
- In Ni-Co alloy the faces of 2-fold symmetry protrusion are composed of several distinguishable planes, whereas in pure nickel those faces very often are composed of numerous nano-sized hills.

These differences suggest that chemical species adsorbing on the surface are changed due to presence of Co^{2+} in the electrodeposition electrolyte. And it appears that increase of cobalt concentration in the electrolyte above a critical value, alters the chemical species on the cathode surface such that $Ni(OH)_2$ is not the most influencing species, hence, <211> fiber texture does not form. This is in good agreement with the argument that in anomalous codeposition of iron group metals, the less noble metal (in this case cobalt) inhibits deposition of more noble metal [241].

Despite the successful synthesis of <211> fiber textured Ni-Co alloy, cross-sectional analysis of Ni-15.6 wt.% Co (see Figure 5.32a - page 100) revealed that the effect of cobalt

---

[10] synthesized in fairly similar conditions to this study

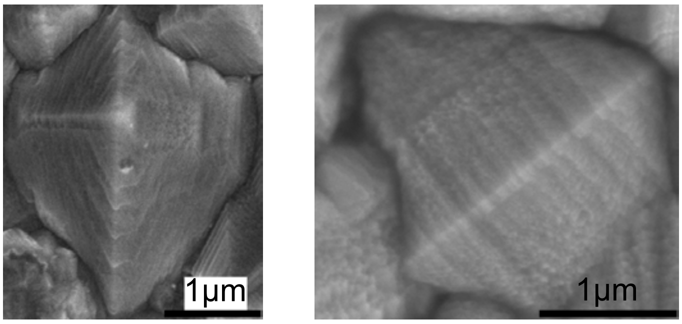

(a) **(b)**

Figure 7.5: High magnification micrograph of a protrusion with a 2-fold symmetry of sample Ni-Co alloy (a), F1 (b).

on formation of twins of <211> oriented grains is not significant. This might stem from the mechanism of formation of twin lamellae discussed earlier.

Chapter 8

Summary, Conclusions and Future Work

8.1 Summary

8.1.1 Characterization Techniques

There are advantages and disadvantages associated with all the techniques available for materials characterization. It is of high importance to follow a strategy of supplementing techniques to overcome the disadvantages (limitations) of one technique by advantages (strength) of another one. In this study, supplementation strategy had three different aspects: (1) Statistical, (2) Geometrical, and (3) Resolutional.

1. A very successful case of statistical supplementation was obtaining the macro-texture with XRD and the micro-texture with OIM-in-SEM. XRD techniques provide the average information of relatively large volume of the materials, ensuring that sufficiently large number of grains are included in the analysis. Hence, the results are statistically valid. Having statistically ensured result of macro-texture, it is trivial to decide whether the micro-texture investigated area is 'typical' or it is off the statistical average. For instance, in the studied Ni-Co alloy a <110> oriented grain was revealed which was confidently rejected of being of high importance since the macro-texture had shown that <110> texture is present in the sample less than the random distribution. In the absence of XRD macro-texture analysis, a large area should have been analyzed with OIM-in-SEM to obtain statistically relevant information required for texture analysis.
   In general, XRD techniques providing information of relatively large volume, supplement the local information of electron and ion microscopy techniques very well.

2. The chosen geometry for XRD characterization was such that the diffraction vector was parallel to the growth direction. Accordingly, the regions with larger distance from the surface contributed less to the diffracted beam. Cross-sectional analysis with the same techniques is impossible for the fairly thin films. However, by utilizing cross-sectional analysis of other techniques a more complete characterization was obtained. For instance, it was clearly demonstrated that samples with coarse columnar microstructure and <211> fiber texture, have a <100> texture in the vicinity of the film/substrate interface. This piece of information was totally missed in XRD characterization as a consequence of the limited information depth with XRD. Furthermore, information on the location of the different grain orientations within the film is not available by XRD, but due to the visibility of the microstructure by microscopic techniques (OIM) they essentially supplement the XRD data.

3. For investigating nano-crystalline samples, XRD line profile analysis was successfully applied for characterization of grain size, prior to the major grain growth. However this technique is not applicable after major grain growth (detection limits with the XRD). OIM and ion channeling imaging had the opposite condition, i.e. their resolution is insufficient for characterization of nano-crystalline microstructure, whereas they were suitable for characterization of microstructure after major growth. By use of the mentioned three techniques, the full spectrum of grain size in the studied samples was characterized.

   In addition to this, characterization of nano-twins was readily carried out with channeling ion imaging. However, utilizing IOM-in-SEM, such characterization of nano-sized grains is associated with significant technical limitations. The idea of implantation of ion channeling images data into the OIM maps is attempted for the first time in this study. The importance of this approach is its ease of application in FIB/SEM microscopes. 3-dimensional supplementation of OIM and ion channeling image is also attempted in this study to overcome the limitations in resolution of 3D-EBSD technique. However, this requires further development in terms of automatic data acquisition and data analysis.

8.1.2 Cross-Sectional Characterization

In this study, a particular emphasis was put on cross-sectional characterization i.e. all those samples which were studied by ion channeling imaging and OIM, characterization was applied on a cross-section, despite the particular challenges on cross-sectional sample preparation. This emphasis stemmed from the fact that the size and the orientation of the grains in a coarse columnar microstructure evolves with thickness and cross-sectional characterization is a proper approach to address this evolution. For OIM data, the necessary computer codes to automatically find the film/substrate interface, and make the sub-maps parallel to the interface were developed (see appendix D). Utilizing these codes, characterizing the evolution of microstructure with thickness, in terms of average horizontal intercept length, orientation, special boundaries population, etc. was significantly eased. Top view analysis was also applied, though occasionally, to obtain more information on the topography of the films. Sole top view analysis lacks the information on the evolution of microstructure and would mislead microstructure interpretation. However, the ease of sample preparation parallel to the film/substrate interface encourages the top view analysis and might be the reason why it still is widely used in literature.

Even though the cross-sectional sample preparation for OIM analysis was not discussed in depth in the main body of this thesis and instead is provided in the Appendix A, it is worth noting that cross-sectional sample preparation is challenging for the films.

8.1.3 Grain Boundary Engineering

Grain boundary engineering is a well-established concept, with some successful industrial applications. However, the mechanism(s) by which the boundary specific properties can be improved is not yet well-understood. This, at least partly, owes to the lack of robust characterization methods for the grain boundaries in the 1980s and the early 1990s. In the past decade, significant improvements in the 2-dimensional analysis of the grain boundaries has happened and OIM-in-SEM is readily available for this purpose. The 3-dimensional characterization (complete characterization) of the grain boundaries is developing too. These improvements in the techniques, provide the tools for characterization of the grain boundaries and based on a thorough characterization it is possible to engineer new materials.

The scientific literature is stupendously rich of the reports on Watts electrolyte. Nevertheless, there are very few, if any thorough, studies on the grain boundary character and its evolution with the temperature of nickel electrodeposits. In this study, the most widely used electrodeposition electrolytes was chosen for synthesis of nickel films and investigating the possibilities to enhance material properties. It was shown that it is possible to synthesize nickel deposits which have the requirements of the grain boundary engineered materials. Thus, even an ‘old-fashioned’ electrolyte, provides the possibilities of synthesis of materials with potentially enhanced properties, however to exploit that, a fresh insight and enhanced characterizations is required.

8.2 Conclusions

The major conclusions drawn in this study are as follows:

- Using additive free Watts electrolyte, coarse columnar microstructures are synthesized with different texture and fairly high fraction of $\Sigma 3^n$ boundaries.
- <211> oriented grains possess fully coherent twin boundaries (twin lamella width of few tens of nano-meter) with relatively high thermal stability.
- The conditions at which strong <211> fiber texture forms in Watts electrolyte are: deposition temperature = $50°C$, pH = 4.5, applied current density = 2 A/dm^2, and boric acid concentration = 40 g/dm^3.
- It is possible to synthesize Ni-Co alloy with <211> fiber texture, but the twin lamellae density does not change notably in comparison with that of pure nickel.
- Based on 3-dimensional characterization of twins in <100> textured film, some of the boundaries are incoherent; at elevated temperatures the twins tend to annihilate rather then grow or fine-tune.
- In <210> textured nickel film, multiple twinning occurs which brings about pseudo 5-fold symmetry arrangement of the twin boundaries; these boundaries annihilate at elevated temperatures.
- The arrangement of $\Sigma 3^n$ boundaries in <210> textured films is such that the network of general high angle grain boundaries is fragmented and there is no path of general high angle grain boundaries from surface to the substrate for sufficiently thick layer.
- <210> textured film has requirements of grain boundary engineered material and it is expected to have improved boundary specific properties.
- Grain boundary engineered material with average grain size of ≈200nm is produced; this is one of the few reports of sub-micron grain boundary engineering of nickel.
- The microstructure of thermally treated nano-crystalline nickel films, neither show high fraction of $\Sigma 3^n$ boundaries, nor fragmentation of network of general high angle grain boundaries.
- Generally, at elevated temperatures but below the major grain growth, <100> texture tends to strengthen and that is attributed to strain energy minimization.

- Generally at elevated temperatures above the major grain growth, <111> texture tends to strengthen due to interface energy minimization.
- The last two conclusions are general and there are interesting cases of exception from the general trend; it is proposed that by including the effect of energy of triple lines, a better understanding of evolution of microstructure can be obtained.
- For a nano-crystalline sample with <111> texture in as-deposited state, a higher thermal stability than what is reported in the literature is observed, and it is suggested that high triple line drag may be the cause.
- The microstructure of nano-crystalline samples after thermal treatment have different characters, and the activities prior to the major grain growth hold responsible for that.

8.3 Future Work

The following are points of interest suggested for future studies:

- Further studies on the <210> textured nickel films to elucidate more on the formation of twins, their spatial arrangement, and how the twin boundaries population and thermal stability can be increased.
- Characterization of mechanical strength and ductility as well as actual testing of boundary specific properties such as corrosion, stress corrosion cracking, etc. is required.
- TEM analysis of the nano-crystalline samples specially aiming to characterize the triple junctions.
- More detailed 3-dimensional analysis (even singular grains) that at present can be investigated; and thorough quantitative analysis of the 3D data.
- Developing routines for characterization of triple lines based on 3D-EBSD data.

References

[1] T. Watanabe. Grain boundary design and control for high temperature materials. *Materials Science and Engineering: A*, 166(1-2):11–28, 1993.

[2] U. Erb, AM El-Sherik, G. Palumbo, and KT Aust. Synthesis, structure and properties of electroplated nanocrystalline materials. *Nanostructured materials*, 2(4):383–390, 1993.

[3] G. Palumbo, U. Erb, and K. T. Aust. Triple line disclination effects on the mechanical behaviour of materials. *Scripta Metallurgica et Materialia*, 24:2347–2350, 1990.

[4] T. Watanabe. An approach to grain boundary design for strong and ductile polycrystals. *Res Mechanica*, 11(1):47–84, 1984.

[5] G. Palumbo, PJ King, PC Lichtenberger, KT Aust, and U. Erb. Grain boundary design and control for intergranular stress-corrosion resistance. *Scripta Metallurgica et Materialia(USA)*, 25(8):1775–1780, 1991.

[6] G. Palumbo, EM Lehockey, and P. Lin. Applications for grain boundary engineered materials. *JOM Journal of the Minerals, Metals and Materials Society*, 50(2):40–43, 1998.

[7] M. Kumar, A.J. Schwartz, and W.E. King. Microstructural evolution during grain boundary engineering of low to medium stacking fault energy FCC materials. *Acta materialia*, 50(10):2599–2612, 2002.

[8] M. Shimada, H. Kokawa, ZJ Wang, YS Sato, and I. Karibe. Optimization of grain boundary character distribution for intergranular corrosion resistant 304 stainless steel by twin-induced grain boundary engineering. *Acta Materialia*, 50(9):2331–2341, 2002.

[9] V. Randle and G. Owen. Mechanisms of grain boundary engineering. *Acta materialia*, 54(7):1777–1783, 2006.

[10] M. Coleman and V. Randle. Changes in interface parameters and tensile properties in copper as a consequence of iterative processing. *Metallurgical and Materials Transactions A*, 39(9):2175–2183, 2008.

[11] G. Palumbo, KT Aust, U. Erb, PJ King, AM Brennenstuhl, and PC Lichtenberger. On annealing twins and CSL distributions in FCC polycrystals. *Physica status solidi (a)*, 131(2):425–428, 1992.

[12] V. Randle. Twinning-related grain boundary engineering. *Acta Materialia*, 52(14): 4067–4081, 2004.

[13] B.W. Reed and M. Kumar. Mathematical methods for analyzing highly-twinned grain boundary networks. *Scripta materialia*, 54(6):1029–1033, 2006.

[14] R. Birringer, H. Gleiter, H.P. Klein, and P. Marquardt. Nanocrystalline materials an approach to a novel solid structure with gas-like disorder. *Physics Letters A*, 102 (8):365–369, 1984.

[15] H. Gleiter. Nanocrystalline materials. *Progress in Materials Science*, 33(4):223–315, 1989.

[16] D.H. Jeong, F. Gonzalez, G. Palumbo, K.T. Aust, and U. Erb. The effect of grain size on the wear properties of electrodeposited nanocrystalline nickel coatings. *Scripta materialia*, 44(3):493–500, 2001.

[17] H. Gleiter. Nanostructured materials: basic concepts and microstructure. *Acta materialia*, 48(1):1–29, 2000.

[18] C. Suryanarayana. Nanocrystalline materials. *International Materials Reviews*, 40 (2):41–64, 1995.

[19] M.A. Meyers, A. Mishra, and D.J. Benson. Mechanical properties of nanocrystalline materials. *Progress in Materials Science*, 51(4):427–556, 2006.

[20] C.C. Koch. *Structural nanocrystalline materials: fundamentals and applications*. Cambridge Univ. Pr., 2007.

[21] L. Lu, Y. Shen, X. Chen, L. Qian, and K. Lu. Ultrahigh strength and high electrical conductivity in copper. *Science*, 304(5669):422–426, 2004.

[22] X. Zhang, A. Misra, H. Wang, TD Shen, M. Nastasi, TE Mitchell, JP Hirth, RG Hoagland, and JD Embury. Enhanced hardening in Cu/330 stainless steel multilayers by nanoscale twinning. *Acta materialia*, 52(4):995–1002, 2004.

[23] L. Lu, X. Chen, X. Huang, and K. Lu. Revealing the maximum strength in nanotwinned copper. *Science*, 323(5914):607–610, 2009.

[24] R.J. Asaro and S. Suresh. Mechanistic models for the activation volume and rate sensitivity in metals with nanocrystalline grains and nano-scale twins. *Acta materialia*, 53(12):3369–3382, 2005.

[25] X. Zhang, O. Anderoglu, RG Hoagland, and A. Misra. Nanoscale growth twins in sputtered metal films. *Journal of the Minerals, Metals and Materials Society*, 60(9): 75–78, 2008.

[26] Y.D. Gamburg and G. Zangari. *Theory and Practice of Metal Electrodeposition*. Springer Verlag, 2011.

[27] M. Motoyama, Y. Fukunaka, T. Sakka, and Y. H. Ogata. Effect of surface pH on electrodeposited Ni films. *Journal of the Electrochemical Society*, 153:502–508, 2006.

[28] K.P. Larsen, A.A. Rasmussen, J.T. Ravnkilde, M. Ginnerup, and O. Hansen. Mems device for bending test: measurements of fatigue and creep of electroplated nickel. *Sensors and Actuators A: Physical*, 103(1-2):156–164, 2003.

[29] K. Pantleon and M.A.J. Somers. In situ investigation of the microstructure evolution in nanocrystalline copper electrodeposits at room temperature. *Journal of applied physics*, 100:114–319, 2006.

[30] K. Pantleon, A. Gholinia, and M.A.J. Somers. Quantitative microstructure characterization of self-annealed copper films with electron backscatter diffraction. *physica status solidi (a)*, 205(2):275–281, 2008.

[31] U. Klement, M. da Silva, and W. Skrotzki. On the orientations of abnormally grown grains in nanocrystalline Ni and Ni–Fe. *Journal of Microscopy*, 230(3):455–463, 2008.

[32] K. Pantleon and M.A.J. Somers. X-ray diffraction investigation of self-annealing in nanocrystalline copper electrodeposits. *Scripta materialia*, 55(4):283–286, 2006.

[33] G.D. Hibbard, U. Erb, K.T. Aust, U. Klement, and G. Palumbo. Thermal stability of nanostructured electrodeposits. In *Materials Science Forum*, volume 386, pages 387–396. Trans Tech Publ, 2002.

[34] O. Anderoglu, A. Misra, H. Wang, and X. Zhang. Thermal stability of sputtered Cu films with nanoscale growth twins. *Journal of Applied Physics*, 103:094322, 2008.

[35] CV Thompson. Structure evolution during processing of polycrystalline films. *Annual review of materials science*, 30(1):159–190, 2000.

[36] A. Bastos, S. Zaefferer, D. Raabe, and C. Schuh. Characterization of the microstructure and texture of nanostructured electrodeposited NiCo using electron backscatter diffraction (EBSD). *Acta Materialia*, 54(9):2451–2462, 2006.

[37] U. Erb. Electrodeposited nanocrystals: synthesis, properties and industrial applications. *Nanostructured Materials*, 6(5-8):533–538, 1995.

[38] G. Cao. *Nanostructures & nanomaterials: synthesis, properties & applications*. Imperial College Pr, 2004.

[39] G. Staikov and A. Milchev. *The impact of electrocrystallization on nanotechnology*. Wiley Online Library, 2007.

[40] A. Robertson, U. Erb, and G. Palumbo. Practical applications for electrodeposited nanocrystalline materials. *NanoStructured materials*, 12(5-8):1035–1040, 1999.

[41] G. Palumbo, F. Gonzalez, AM Brennenstuhl, U. Erb, W. Shmayda, and PC Lichtenberger. In-situ nuclear steam generator repair using electrodeposited nanocrystalline nickel. *Nanostructured Materials*, 9(1-8):737–746, 1997.

[42] F. Czerwinski, A. Zielinska-Lipiec, and J.A. Szpunar. Thermal instability of Ni electrodeposits applied in replication of optical recording devices. *Acta materialia*, 47(8):2553–2566, 1999.

[43] N. Kanani. *Electroplating: Basic Principles, Processes and Practice*. Elsevier Science, 2004.

[44] Jack W. Dini. *Electrodeposition: The Materials Science of Coatings and Substrates*. William Andrew, First edition, 1994.

[45] L. Bonou, M. Eyraud, R. Denoyel, and Y. Massiani. Influence of additives on Cu electrodeposition mechanisms in acid solution: direct current study supported by non-electrochemical measurements. *Electrochimica acta*, 47(26):4139–4148, 2002.

[46] J.J. Kelly, C. Tian, and A.C. West. Leveling and microstructural effects of additives for copper electrodeposition. *Journal of the Electrochemical Society*, 146:2540, 1999.

[47] L. Oniciu and L. Mureşan. Some fundamental aspects of levelling and brightening in metal electrodeposition. *Journal of applied electrochemistry*, 21(7):565–574, 1991.

[48] L. Oniciu and L. Muresan. Some fundamental aspects of levelling and brightening in metal electrodeposition. *Journal of Applied Electrochemistry*, 21(7):565–574, 1991.

[49] T. A Costavaras, M. Froment, A. Hugot-Le Goff, and C. Georgoulis. The influence of unsaturated organic molecules in the electrocrystallization of nickel. *Journal of The Electrochemical Society*, 120:867–874, 1973.

[50] M. Paunovic and M. Schlesinger. *Fundamentals of Electrochemical Deposition*. Wiley-Blackwell, 2nd edition, 2006.

[51] A.A. Rasmussen, P. Møller, and M.A.J. Somers. Microstructure and thermal stability of nickel layers electrodeposited from an additive-free sulphamate-based electrolyte. *Surface and Coatings Technology*, 200(20):6037–6046, 2006.

[52] J. Ji, W.C. Cooper, D.B. Dreisinger, and E. Peters. Surface pH measurements during nickel electrodeposition. *Journal of Applied Electrochemistry*, 25(7):642–650, 1995.

[53] E. Gomez, R. Pollina, and E. Valles. Nickel electrodeposition on different metallic substrates. *Journal of Electroanalytical Chemistry*, 386(1-2):45–56, 1995.

[54] A.A. Rasmussen, J.A.D. Jensen, A. Horsewell, and M.A.J. Somers. Microstructure in electrodeposited copper layers; the role of the substrate. *Electrochimica Acta*, 47 (1-2):67–74, 2001.

[55] K. Pantleon and M.A.J. Somers. Microstructure and texture of free-standing cu-line patterns. *Journal of electronic materials*, 33(11):1363–1372, 2004.

[56] G.A. DiBari. Nickel plating. *Plating and surface finishing*, 84:257–274, 1997.

[57] S. Fumitaka, K. Keisuke, Y. Nobira, K. Kobayakawa, and Y. Sato. Nickel electroplating bath using malic acid as a substitute agent for boric acid. *Metal Finishing*, 105 (12):34–38, 2007.

[58] O.P. Watts. Rapid nickel plating. *Transactions of American Electrochemical Society*, 29:395, 1916.

[59] H. S. Karayannis and G. Patermarakis. Effect of the Cl^- and SO_4^{-2} ions on the selective orientation and structure of Ni electrodeposits. *Electrochimica Acta*, 40(9): 1079–1092, 1995.

[60] R. Orinakova, A. Turonova, D. Kladekova, M. Galova, and R. M. Smith. Recent developments in the electrodeposition of nickel and some nickel-based alloys. *Journal of Applied Electrochemistry*, 36(9):957–972, 2006.

[61] J.P. Hoare. On the role of boric acid in the watts bath. *Journal of The Electrochemical Society*, 133(12):2491–2494, 1986.

[62] T. C. Franklin. Some mechanisms of action of additives in electrodeposition processes. *Surface and Coatings Technology*, 30(4):415–428, 1987.

[63] J. Bressan and R. Wiart. Diffusion controlled inhibition of electrodeposition: impedance measurements. *Journal of Applied Electrochemistry*, 9(5):615–621, 1979.

[64] I. Epelboin, M. Joussellin, and R. Wiart. Impedance measurements for nickel deposition in sulfate and chloride electrolytes. *Journal of Electroanalytical Chemistry and Interfacial Electrochemistry*, 119(1):61–71, 1981.

[65] Y. Nakamura, N. Kaneko, M. Watanabe, and H. Nezu. Effects of saccharin and aliphatic alcohols on the electrocrystallization of nickel. *Journal of Applied Electrochemistry*, 24(3):227–232, 1994.

[66] E.M. Oliveira, G.A. Finazzi, and I.A. Carlos. Influence of glycerol, mannitol and sorbitol on electrodeposition of nickel from a Watts bath and on the nickel film morphology. *Surface and Coatings Technology*, 200(20):5978–5985, 2006.

[67] C.C. Hu, C.Y. Lin, and T.C. Wen. Textural and electrochemical properties of watts nickel-deposited titanium electrodes. *Materials chemistry and physics*, 44(3):233–238, 1996.

[68] R. Mishra, B. Basu, and R. Balasubramaniam. Effect of grain size on the tribological behavior of nanocrystalline nickel. *Materials Science and Engineering: A*, 373(1): 370–373, 2004.

[69] AM Rashidi and A. Amadeh. The effect of current density on the grain size of electrodeposited nanocrystalline nickel coatings. *Surface and Coatings Technology*, 202(16):3772–3776, 2008.

[70] A.M. El-Sherik and U. Erb. Synthesis of bulk nanocrystalline nickel by pulsed electrodeposition. *Journal of materials science*, 30(22):5743–5749, 1995.

[71] M.J. Aus, B. Szpunar, U. Erb, A.M. El-Sherik, G. Palumbo, and K.T. Aust. Electrical resistivity of bulk nanocrystalline nickel. *Journal of applied physics*, 75(7):3632–3634, 1994.

[72] V. Darrort, M. Troyon, J. Ebothe, C. Bissieux, and C. Nicollin. Quantitative study by atomic force microscopy and spectrophotometry of the roughness and brightness of electrodeposited nickel in the presence of additives. *Thin solid films*, 265(1):52–57, 1995.

[73] R. Mishra and R. Balasubramaniam. Effect of nanocrystalline grain size on the electrochemical and corrosion behavior of nickel. *Corrosion Science*, 46(12):3019–3029, 2004.

[74] C. Gu, J. Lian, J. He, Z. Jiang, and Q. Jiang. High corrosion-resistance nanocrystalline ni coating on AZ91D magnesium alloy. *Surface and coatings technology*, 200 (18-19):5413–5418, 2006.

[75] J. Amblard, I. Epelboin, M. Froment, and G. Maurin. Inhibition and nickel electrocrystallization. *Journal of applied electrochemistry*, 9(2):233–242, 1979.

[76] N. Spyrellis, J. Amblard, M. Froment, and G Maurin. Nickel electrocrystallization–from nucleation to textures. *J. Microsc. Spectrosc. Electron.*, 12:221–230, 1987.

[77] N. Atanassov, Hr. Bozhkov, St. Vitkova, and St. Rashkov. Morphology and properties of nickel plate deposited in the presence of butynediol. *Surface Technology*, 17(4): 291–299, 1982.

[78] R. Weil and H.J. Read. Electron-microradiography of electrodeposited metals. *Journal of Applied Physics*, 21(10):1068–1068, 1950.

[79] C. Kollia, N. Spyrellis, J. Amblard, M. Froment, and G. Maurin. Nickel plating by pulse electrolysis: textural and microstructural modifications due to adsorption/desorption phenomena. *Journal of Applied Electrochemistry*, 20(6):1025–1032, 1990.

[80] E. A. Marquis, A. A. Talin, J. J. Kelly, S. H. Goods, and J. R. Michael. Effects of current density on the structure of Ni and Ni-Mn electrodeposits. *Journal of Applied Electrochemistry*, 36(6):669–676, 2006.

[81] J. Amblard, G. Maurin, D. Mercier, and N. Spyrellis. Structure multimaclee helicoïdale autour d'un axe [210] dans les depots electrolytiques de nickel. *Scripta Metallurgica*, 16(5):579–584, 1982.

[82] S. Rashkov, D. S. Stoichev, and I. Tomov. Influence of current density and temperature on the morphology and preferred orientation of electrodeposited copper coatings. *ELECTROCHIM ACTA*, 17(11):1955–1964, 1972.

[83] C.B. Nielsen, A. Horsewell, and M.J.L Ostergard. On texture formation of nickel electrodeposits. *Journal of Applied Electrochemistry*, 27(7):839–845, 1997.

[84] A.K.N. Reddy. Preferred orientations in nickel electro-deposits:: I. the mechanism of development of textures in nickel electro-deposits. *Journal of Electroanalytical Chemistry (1959)*, 6(2):141–152, 1963.

[85] J. Amblard, M. Froment, and N. Spyrellis. Origine des textures dans les depots electrolytiques de nickel. *Surface Technology*, 5(3):205–234, 1977.

[86] E. Chassaing, M. Joussellin, and R. Wiart. The kinetics of nickel electrodeposition:: Inhibition by adsorbed hydrogen and anions. *Journal of Electroanalytical Chemistry*, 157(1):7588, 1983. ISSN 0022-0728.

[87] O. Devos, A. Olivier, J. P. Chopart, O. Aaboubi, and G. Maurin. Magnetic field effects on nickel electrodeposition. *Journal of The Electrochemical Society*, 145:401, 1998.

[88] S. Spanou, E.A. Pavlatou, and N. Spyrellis. Ni/nano-TiO2 composite electrodeposits: Textural and structural modifications. *Electrochimica Acta*, 54(9):2547–2555, 2009.

[89] C. C Roth and H. Leidheiser Jr. The interaction of organic compounds with the surface during the electrodeposition of nickel. *Journal of The Electrochemical Society*, 100:553–565, 1953.

[90] C. Z Gao, Y. L Lu, S. B Yue, and H. T Wang. Effects of the compounds containing different valence sulfur on the electrocrystallization of nickel. *Transactions of the Institute of Metal Finishing*, 77:75–77, 1999.

[91] P. Sibley and P. A. Brook. The effect of addition agents on the electrical resistivity of electrodeposited nickel. *Electrodeposition and Surface Treatment*, 1(6):439–448, 1973.

[92] Aleksander Ciszewski, Szymon Posluszny, Grzegorz Milczarek, and Marek Baraniak. Effects of saccharin and quaternary ammonium chlorides on the electrodeposition of nickel from a watts-type electrolyte. *Surface and Coatings Technology*, 183(2-3): 127–133, 2004.

[93] C.C Cheng and A.C. West. Nickel deposition in the presence of coumarin. *Journal of The Electrochemical Society*, 144(9):3050–3056, 1997.

[94] J. Macheras, D. Vouros, C. Kollia, and N. Spyrellis. Nickel electro-crystallization: Influence of unsaturated organic additives on the mechanism of oriented crystal growth. *Transactions of the Institute of Metal Finishing*, 74:55–58, 1996.

[95] E. A. Pavlatou, M. Raptakis, and N. Spyrellis. Synergistic effect of 2-butyne-1, 4-diol and pulse plating on the structure and properties of nickel nanocrystalline deposits. *Surface & Coatings Technology*, 201(8):4571–4577, 2007.

[96] G. T. Rogers and K. J. Taylor. The reactions of coumarin, cinnamyl alcohol, butynediol and propargyl alcohol at an electrode on which nickel is depositing. *Electrochimica Acta*, 11:1685–1696, 1966.

[97] A. Bodnevas and J. Zahavi. Some peculiarities of cathodic behavior of brightener additives in nickel plating. *Plating and surface finishing*, 80(7):53–56, 1993.

[98] L. Mirkova, G. Maurin, M. Monev, and C. Tsvetkova. Hydrogen coevolution and permeation in nickel electroplating. *Journal of Applied Electrochemistry*, 33:93–100, 2003.

[99] P. Lejček. *Grain Boundary Segregation in Metals*. Springer Verlag, 2010.

[100] A.H. King. The geometric and thermodynamic properties of grain boundary junctions. *Interface Science*, 7(3):251–271, 1999.

[101] E.J. Mittemeijer. *Fundamentals of Materials Science*. Springer Verlag, 2010.

[102] David M. Saylor, Adam Morawiec, and Gregory S. Rohrer. Distribution of grain boundaries in magnesia as a function of five macroscopic parameters. *Acta Materialia*, 51(13):3663–3674, 2003.

[103] S.J. Dillon and G.S. Rohrer. Characterization of the grain-boundary character and energy distributions of yttria using automated serial sectioning and EBSD in the FIB. *Journal of the American Ceramic Society*, 92:1580–1585, 2009.

[104] G. Gottstein and L.S Shvindlerman. *Grain Boundary Migration in Metals: Thermodynamics, Kinetics, Applications*. CRC Press, 2nd edition, 2009.

[105] A. Brokman and RW Balluffi. Coincidence lattice model for the structure and energy of grain boundaries. *Acta Metallurgica*, 29(10):1703–1719, 1981.

[106] D.G. Brandon. The structure of high-angle grain boundaries. *Acta Metallurgica*, 14 (11):1479–1484, 1966.

[107] G. Palumbo, K.T. Aust, E.M. Lehockey, U. Erb, and P. Lin. On a more restrictive geometric criterion for special CSL grain boundaries. *Scripta materialia*, 38(11): 1685–1690, 1998.

[108] RL Fullman. Interfacial free energy of coherent twin boundaries in copper. *Journal of Applied Physics*, 22(4):448–455, 1951.

[109] G. Hasson, J.-Y. Boos, I. Herbeuval, M. Biscondi, and C. Goux. Theoretical and experimental determinations of grain boundary structures and energies: Correlation with various experimental results. *Surface Science*, 31:115–137, June 1972. ISSN 0039-6028. doi: 16/0039-6028(72)90256-7. URL `http://www.sciencedirect.com/science/article/pii/0039602872902567`.

[110] N. Bernstein and EB Tadmor. Tight-binding calculations of stacking energies and twinnability in fcc metals. *Physical Review B*, 69(9):094116, 2004.

[111] A.J. Schwartz, M. Kumar, B.L. Adams, and D.P. Field. *Electron Backscatter Diffraction in Materials Science*. Springer, 2nd edition, 2009.

[112] O. Engler and V. Randle. *Introduction to Texture Analysis: Macrotexture, Microtexture, and Orientation Mapping, Second Edition.* CRC Press, 2nd edition, 2009.

[113] S. Zaefferer. On the formation mechanisms, spatial resolution and intensity of backscatter kikuchi patterns. *Ultramicroscopy*, 107(2-3):254–266, 2007.

[114] S. I. Wright and M. M. Nowell. EBSD image quality mapping. *Microscopy and Microanalysis*, 12(01):72–84, 2005.

[115] F.J. Humphreys. Grain and subgrain characterisation by electron backscatter diffraction. *Journal of Materials Science*, 36(16):3833–3854, 2001.

[116] F. J. Humphreys. Characterisation of fine-scale microstructures by electron backscatter diffraction (EBSD). *Scripta materialia*, 51(8):771–776, 2004.

[117] D.R. Steinmetz and S. Zaefferer. Towards ultrahigh resolution EBSD by low accelerating voltage. *Materials Science and Technology*, 26(6):640–645, 2010.

[118] T.C. Isabell and V.P. Dravid. Resolution and sensitivity of electron backscattered diffraction in a cold field emission gun SEM. *Ultramicroscopy*, 67(1-4):59–68, 1997.

[119] R.A. Schwarzer. Advances in crystal orientation mapping with the SEM and TEM. *Ultramicroscopy*, 67(1):19–24, 1997.

[120] S. Zaefferer. New developments of computer-aided crystallographic analysis in transmission electron microscopy. *Journal of applied crystallography*, 33(1):10–25, 2000.

[121] J.J Fundenberger, A. Morawiec, E. Bouzy, and J.S. Lecomte. Polycrystal orientation maps from TEM. *Ultramicroscopy*, 96(2):127137, 2003.

[122] A. Darbal, K. Barmak, N.T. Nuhfer, D.J. Dingley, G. Meaden, J.R. Michael, T. Sun, B. Yao, and K.R. Coffey. Orientation imaging of nanocrystalline platinum films in the TEM. *Microscopy and Microanalysis*, 15:1232–1233, 2009.

[123] M.D. Uchic, M.A. Groeber, and Rollett A.D. automated serial sectioning methods for rapid collection of 3-d microstructure data. *Journal of the Minerals, Metals and Materials Society*, 63:25–29, 2011.

[124] N. Yao. *Focused Ion Beam Systems: Basics and Applications.* Cambridge University Press, 2007.

[125] A. Bastos, S. Zaefferer, and D. Raabe. Three-dimensional EBSD study on the relationship between triple junctions and columnar grains in electrodeposited Co-Ni films. *Journal of Microscopy*, 230(3):487–498, 2008.

[126] D.A. Porter and K.E. Easterling. *Phase Transformations in Metals and Alloys.* CRC Press, 2 edition, 1992.

[127] R. Birringer, H. Gleiter, H.P. Klein, and P. Marquardt. Nanocrystalline materials an approach to a novel solid structure with gas-like disorder. *Physics Letters A*, 102 (8):365–369, 1984.

[128] M. Ames, J. Markmann, R. Karos, A. Michels, A. Tschope, and R. Birringer. Unraveling the nature of room temperature grain growth in nanocrystalline materials. *Acta Materialia*, 56(16):4255–4266, 2008.

[129] K. Hansen and K. Pantleon. Microstructure stability of silver electrodeposits at room temperature. *Scripta Materialia*, 58(2):96–98, 2008.

[130] R.W.K. Honeycombe. *The plastic deformation of metals*. Edward Arnold London, 1968.

[131] C. Suryanarayana and C.C. Koch. Nanocrystalline materials–current research and future directions. *Hyperfine Interactions*, 130(1):5–44, 2000.

[132] G. Gottstein, L.S. Shvindlerman, and B. Zhao. Thermodynamics and kinetics of grain boundary triple junctions in metals: Recent developments. *Scripta Materialia*, 62(12):914–917, 2010.

[133] G.D. Hibbard, K.T. Aust, and U. Erb. The effect of starting nanostructure on the thermal stability of electrodeposited nanocrystalline co. *Acta materialia*, 54(9): 2501–2510, 2006.

[134] Y. Estrin, G. Gottstein, E. Rabkin, and L.S. Shvindlerman. On the kinetics of grain growth inhibited by vacancy generation. *Scripta Materialia(USA)*, 43(2):141–147, 2000.

[135] U. Klement, U. Erb, AM El-Sherik, and KT Aust. Thermal stability of nanocrystalline ni. *Materials Science and Engineering A*, 203(1-2):177–186, 1995.

[136] M. da Silva, C. Wille, U. Klement, P. Choi, and T. Al-Kassab. Electrodeposited nanocrystalline co-p alloys: Microstructural characterization and thermal stability. *Materials Science and Engineering: A*, 445:31–39, 2007.

[137] A.A. Talin, E.A. Marquis, S.H. Goods, J.J. Kelly, and M.K. Miller. Thermal stability of Ni-Mn electrodeposits. *Acta materialia*, 54(7):1935–1947, 2006.

[138] K. Lu, WD Wei, and JT Wang. Grain growth kinetics and interfacial energies in nanocrystalline Ni-P alloys. *Journal of applied physics*, 69(10):7345–7347, 1991.

[139] K. G.F Janssens, D. Olmsted, E. A Holm, S. M Foiles, S. J Plimpton, and P. M Derlet. Computing the mobility of grain boundaries. *Nature Materials*, 5(2):124–127, 2006.

[140] P. Choi, M. da Silva, U. Klement, T. Al-Kassab, and R. Kirchheim. Thermal stability of electrodeposited nanocrystalline Co-1.1 at.% P. *Acta materialia*, 53(16): 4473–4481, 2005.

[141] R. Kirchheim. Grain coarsening inhibited by solute segregation. *Acta materialia*, 50 (2):413–419, 2002.

[142] K. Pantleon and M.A.J. Somers. Interpretation of microstructure evolution during self-annealing and thermal annealing of nanocrystalline electrodeposits–a comparative study. *Materials Science and Engineering: A*, 528(1):65–71, 2010.

[143] V. Randle. Special boundaries and grain boundary plane engineering. *Scripta materialia*, 54(6):1011–1015, 2006.

[144] C.A. Schuh, M. Kumar, and W.E. King. Analysis of grain boundary networks and their evolution during grain boundary engineering. *Acta Materialia*, 51(3):687–700, 2003.

[145] P. Lin, G. Palumbo, U. Erb, and KT Aust. Influence of grain boundary character distribution on sensitization and intergranular corrosion of alloy 600. *Scripta Materialia*, 33(9):1387–1392, 1995.

[146] E.M. Lehockey and G. Palumbo. On the creep behaviour of grain boundary engineered nickel. *Materials Science and Engineering A*, 237(2):168–172, 1997.

[147] V. Randle. The coincidence site lattice and the sigma enigma. *Materials characterization*, 47(5):411–416, 2001.

[148] G.S. Rohrer, V. Randle, C.S. Kim, and Y. Hu. Changes in the five-parameter grain boundary character distribution in α-brass brought about by iterative thermomechanical processing. *Acta materialia*, 54(17):4489–4502, 2006.

[149] G.S. Rohrer, D.M. Saylor, B. El Dasher, B.L. Adams, A.D. Rollett, and P. Wynblatt. The distribution of internal interfaces in polycrystals. *Zeitschrift fur Metallkunde*, 95(4):197–214, 2004.

[150] A. King, G. Johnson, D. Engelberg, W. Ludwig, and J. Marrow. Observations of intergranular stress corrosion cracking in a grain-mapped polycrystal. *SCIENCE*, 321:382–385, 2008.

[151] DP Field, LT Bradford, MM Nowell, and TM Lillo. The role of annealing twins during recrystallization of Cu. *Acta materialia*, 55(12):4233–4241, 2007.

[152] R.L. Fullman and J.C. Fisher. Formation of annealing twins during grain growth. *Journal of Applied Physics*, 22(11):1350–1355, 1951.

[153] H. Gleiter. The formation of annealing twins. *Acta Metallurgica*, 17(12):1421–1428, 1969.

[154] M.A. Meyers and L.E. Murr. A model for the formation of annealing twins in FCC metals and alloys. *Acta Metallurgica*, 26(6):951–962, 1978.

[155] S. Mahajan, C.S. Pande, M.A. Imam, and B.B. Rath. Formation of annealing twins in FCC crystals. *Acta materialia*, 45(6):2633–2638, 1997.

[156] C. Wild, R. Kohl, N. Herres, W. Muller-Sebert, and P. Koidl. Oriented CVD diamond films: twin formation, structure and morphology. *Diamond and Related Materials*, 3(4-6):373–381, 1994.

[157] J. Wang, M. Tian, T.E. Mallouk, and M.H.W. Chan. Microtwinning in template-synthesized single-crystal metal nanowires. *Journal of Physical Chemistry B*, 108(3): 841–845, 2004.

[158] A.H. Cottrell and B.A. Bilby. A mechanism for the growth of deformation twins in crystals. *Philosophical Magazine*, 42(329):573–581, 1951.

[159] JA Venables. Deformation twinning in face-centred cubic metals. *Philosophical Magazine*, 6(63):379–396, 1961.

[160] S. Mahajan and GY Chin. Formation of deformation twins in FCC crystals. *Acta Metallurgica*, 21(10):1353–1363, 1973.

[161] M. Chen, E. Ma, K.J. Hemker, H. Sheng, Y. Wang, and X. Cheng. Deformation twinning in nanocrystalline aluminum. *Science*, 300(5623):1275, 2003.

[162] P. Haasen. How are new orientations generated during primary recrystallization. *Metallurgical and Materials Transactions A*, 24(5):1001–1015, 1993.

[163] G. Gottstein. Annealing texture development by multiple twinning in FCC crystals. *Acta Metallurgica*, 32(7):1117–1138, 1984.

[164] K.H. Song, Y.B. Chun, and S.K. Hwang. Direct observation of annealing twin formation in a Pb-base alloy. *Materials Science and Engineering: A*, 454:629–636, 2007.

[165] V.Y. Gertsman, K. Tangri, and RZ Valiev. On the grain boundary statistics in metals and alloys susceptible to annealing twinning. *Acta metallurgica et materialia*, 42(6):1785–1804, 1994.

[166] C.S. Pande and M.A. Imam. Grain growth and twin formation in boron-doped nickel polycrystals. *Materials Science and Engineering: A*, 512(1-2):82–86, 2009.

[167] I. Tomov, M. Adamik, and P.B. Barna. Texture, twinning and secondary extinction of vacuum deposited silver thin films. *Thin Solid Films*, 371(1-2):17–27, 2000.

[168] N. Atanassov, St. Vitkova, and St. Rashkov. Electrocrystallization of nickel coatings with <211> texture. *Surface Technology*, 13(3):215–223, 1981.

[169] X. W. Zhou and H. N. G. Wadley. Twin formation during the atomic deposition of copper. *Acta Materialia*, 47(3):1063–1078, 1999.

[170] S. Nakahara. Growth twins and development of polycrystallinity in electrodeposits. *Journal of Crystal Growth*, 55(2):281–290, 1981.

[171] L. M. Wang. Effect of surfactant-assistant electrodeposition in Ni matrix. *Journal of The Electrochemical Society*, 156(6):D204–D206, 2009.

[172] R. Weil. The structures of electrodeposits and the properties that depend on them. *Annual Review of Materials Science*, 19(1):165–182, 1989.

[173] J. B. de Cusminsky. The role of stacking fault energy in metal electrodeposition. *Scripta Metallurgica*, 10(12):1071–1073, 1976.

[174] N.Y.C. Yang, T.J. Headley, J.J. Kelly, and J.M. Hruby. Metallurgy of high strength Ni-Mn microsystems fabricated by electrodeposition. *Scripta Materialia*, 51(8): 761–766, 2004.

[175] B. Wu, C. Schuh, and P. Ferreira. Nanostructured Ni-Co alloys with tailorable grain size twin density. *Metallurgical and Materials Transactions A*, 36(7):1927–1936, 2005.

[176] R. Abbaschian and R.E. Reed-Hill. *Physical Metallurgy Principles*. Cengage Learning, 2008.

[177] R.W. Hinton, L.H. Schwartz, and J.B. Cohen. Effects of additives on the structure of electrodeposited silver. *Journal of The Electrochemical Society*, 110(2):103–112, 1963.

[178] S.E. Hadian and D.R. Gabe. Residual stresses in electrodeposits of nickel and nickel-iron alloys. *Surface and Coatings Technology*, 122(2-3):118–135, 1999.

[179] C. R. Hall and S. A. H. Fawzi. On the occurrence of multiply twinned particles in electrodeposited nickel films. *Philosophical magazine. A. Physics of condensed matter. Defects and mechanical properties*, 54(6):805–820, 1986.

[180] Ping Liu and Yuming Wang. Study on twin stacking faults in ultrafine nickel. *Materials & Design*, 21(3):155–157, 2000.

[181] G. Meng, Y. Shao, T. Zhang, Y. Zhang, and F. Wang. Synthesis and corrosion property of pure Ni with a high density of nanoscale twins. *Electrochimica Acta*, 2008.

[182] R.T.C. Choo, J.M. Toguri, A.M. El-Sherik, and U. Erb. Mass transfer and electrocrystallization analyses of nanocrystalline nickel production by pulse plating. *Journal of Applied Electrochemistry*, 25(4):384–403, 1995.

[183] X. Zhang, K.N. Tu, Z. Chen, Y.K. Tan, C. C. Wong, S.G. Mhaisalkar, X.M. Li, C.H. Tung, and C.K. Cheng. Pulse electroplating of copper film: A study of process and microstructure. *Journal of Nanoscience and Nanotechnology*, 8(5):2568–2574, 2008.

[184] D. Xu, W.L. Kwan, K. Chen, X. Zhang, V. Ozoliņš, and KN Tu. Nanotwin formation in copper thin films by stress/strain relaxation in pulse electrodeposition. *Applied Physics Letters*, 91:254105, 2007.

[185] T.H.V. Setty and H. Wilman. The structure of silver electrodeposited from the argentocyanide bath on to silver (110),(100) and (111) faces. *Transactions of the Faraday Society*, 51:984–995, 1955.

[186] S. Nakahara and S. Mahajan. The influence of solution pH on microstructure of electrodeposited cobalt. *Journal of the Electrochemical Society*, 127:283–288, 1980.

[187] G. Lucadamo, D. L. Medlin, N. Y. C. Yang, J. J. Kelly, and A. A. Talin. Characterization of twinning in electrodeposited Ni–Mn alloys. *Philosophical Magazine*, 85 (22):2549–2560, 2005.

[188] VY Gertsman, M. Janecek, and K. Tangri. Grain boundary ensembles in polycrystals. *Acta materialia*, 44(7):2869–2882, 1996.

[189] V.Y. Gertsman and C.H. Henager. Grain boundary junctions in microstructure generated by multiple twinning. *Interface Science*, 11(4):403–415, 2003.

[190] T. Watanabe. The impact of grain boundary character distribution on fracture in polycrystals. *Materials Science and Engineering: A*, 176(1-2):39–49, 1994.

[191] P. Lin, G. Palumbo, and KT Aust. Experimental assessment of the contribution of annealing twins to csl distributions in FCC materials. *Scripta materialia*, 36(10): 1145–1149, 1997.

[192] VY Gertsman. Coincidence site lattice theory of multicrystalline ensembles. *Acta Crystallographica Section A: Foundations of Crystallography*, 57(6):649–655, 2001.

[193] V. Randle. Mechanism of twinning-induced grain boundary engineering in low stacking-fault energy materials. *Acta materialia*, 47(15-16):4187–4196, 1999.

[194] CB Thomson and V. Randle. The effects of strain annealing on grain boundaries and secure triple junctions in nickel 200. *Journal of materials science*, 32(7):1909–1914, 1997.

[195] T. Watanabe and S. Tsurekawa. The control of brittleness and development of desirable mechanical properties in polycrystalline systems by grain boundary engineering. *Acta materialia*, 47(15-16):4171–4185, 1999.

[196] A.J. Schwartz. The potential engineering of grain boundaries through thermomechanical processing. *JOM Journal of the Minerals, Metals and Materials Society*, 50(2): 50–55, 1998.

[197] LS Shvindlerman and G. Gottstein. Unexplored topics and potentials of grain boundary engineering. *Scripta materialia*, 54(6):1041–1045, 2006.

[198] G. Gottstein and LS Shvindlerman. Grain boundary junction engineering. *Scripta materialia*, 54(6):1065–1070, 2006.

[199] T. Matteson, S. Schwarz, E. Houge, B. Kempshall, and L. Giannuzzi. Electron backscattering diffraction investigation of focused ion beam surfaces. *Journal of Electronic Materials*, 31(1):33–39, 2002.

[200] H. J Bunge and P. R Morris. *Texture analysis in materials science: mathematical methods*. Butterworths London;, 1982.

[201] R. Jenkins and R. Snyder. *Introduction to X-ray Powder Diffractometry*. Wiley-Blackwell, 1996.

[202] Th.H. de Keijser, J.I. Langford, E.J. Mittemeijer, and A.B.P. Vogels. Use of the Voigt function in a single-line method for the analysis of X-ray diffraction line broadening. *Journal of Applied Crystallography*, 15:308–314, 1982.

[203] G.K Williamson and W.H Hall. X-ray line broadening from filed aluminium and wolfram. *Acta Metallurgica*, 1(1):22–31, 1953.

[204] D.P. Field. Recent advances in the application of orientation imaging. *Ultramicroscopy*, 67(1-4):1–9, 1997.

[205] E. Mahway. *OIM user's manual*. EDAX-TSL, 2005.

[206] Standard test method for knoop and vickers hardness of materials (ASTM E384-10e2).

[207] F. Wilhelm. The orientation of high-order growth twins in diamond-type crystals. *Journal of Applied Crystallography*, 4(6):521–523, 1971.

[208] T. Ungar, A. Revesz, and A. Borbely. Dislocations and grain size in electrodeposited nanocrystalline ni determined by the modified williamson-hall and warren-averbach procedures. *Journal of applied crystallography*, 31(4):554–558, 1998.

[209] T. Ungar, I. Dragomir, ;. Ravasz, and A. Borbaly. The contrast factors of dislocations in cubic crystals: the dislocation model of strain anisotropy in practice. *Journal of Applied Crystallography*, 32(5):992–1002, 1999.

[210] T. Ungar, A. RRevesz, and A. Borbely. Dislocations and grain size in electrodeposited nanocrystalline ni determined by the modified Williamson-Hall and Warren-Averbach procedures. *Journal of Applied Crystallography*, 31(4):554–558, 1998.

[211] Robert L. Snyder, Jaroslav Fiala, and Hans J. Bunge. *Defect and Microstructure Analysis by Diffraction*. Oxford University Press, USA, March 2000. ISBN 0198501897.

[212] J. Canny. A computational approach to edge detection. *Pattern Analysis and Machine Intelligence, IEEE Transactions on*, (6):679–698, 1986.

[213] Dammers A.J. and Radelaar S. Two-dimensional computer modelling of polycrystalline film growth. *Textures and Microstructures*, 14-18:757–762, 1991.

[214] René Winand. Electrocrystallization - theory and applications. *Hydrometallurgy*, 29: 567–598, 1992.

[215] C.V. Thompson and R. Carel. Stress and grain growth in thin films. *Journal of the Mechanics and Physics of Solids*, 44(5):657–673, 1996.

[216] A.J. Haslam, S.R. Phillpot, D. Wolf, D. Moldovan, and H. Gleiter. Mechanisms of grain growth in nanocrystalline FCC metals by molecular-dynamics simulation. *Materials Science and Engineering: A*, 318(1):293–312, 2001.

[217] D. Moldovan, V. Yamakov, D. Wolf, and S.R. Phillpot. Scaling behavior of grain-rotation-induced grain growth. *Physical review letters*, 89(20):206101, 2002.

[218] A. Stukowski, J. Markmann, J. Weissmuller, and K. Albe. Atomistic origin of microstrain broadening in diffraction data of nanocrystalline solids. *Acta Materialia*, 57(5):1648–1654, 2009.

[219] S. Shekhar and A.H. King. Strain fields and energies of grain boundary triple junctions. *Acta Materialia*, 56(19):5728–5736, 2008.

[220] L.S. Shvindlerman and G. Gottstein. Cornerstones of grain structure evolution and stability: Vacancies, boundaries, triple junctions. *Journal of materials science*, 40 (4):819–839, 2005.

[221] Y. Estrin, G. Gottstein, and L.S. Shvindlerman. Intermittent self-locking of grain growth in fine-grained materials. *Scripta materialia*, 41(4):385–390, 1999.

[222] J. Kacher, I. M. Robertson, M. Nowell, J. Knapp, and K. Hattar. Study of rapid grain boundary migration in a nanocrystalline Ni thin film. *Materials Science and Engineering: A*, 528:1628–1635, 2010.

[223] F. Ebrahimi and H. Li. Grain growth in electrodeposited nanocrystalline fcc Ni–Fe alloys. *Scripta materialia*, 55(3):263–266, 2006.

[224] GD Hibbard, V. Radmilovic, KT Aust, and U. Erb. Grain boundary migration during abnormal grain growth in nanocrystalline ni. *Materials Science and Engineering: A*, 494(1-2):232–238, 2008.

[225] F.J. Humphreys and M. Hatherley. *Recrystallization and related annealing phenomena*. elsevier, 2nd. edition, 2004.

[226] H. Miura, T. Sakai, and J.J. Jonas. Variant selection of dynamically nucleated twins at triple junctions in a copper tricrystal. *Scripta materialia*, 55(2):167–170, 2006.

[227] M. Prasad, S. Suwas, and A.H. Chokshi. Microstructural evolution and mechanical characteristics in nanocrystalline nickel with a bimodal grain-size distribution. *Materials Science and Engineering: A*, 503:86–91, 2009.

[228] N. Spyrellis, J. Amblard, and G. Marin. Observation by vertical thin films of perturbation of grain formation in nickel electrodeposits by organic additives. *Oberflache Surf.*, 26(11):458–466, 1985.

[229] N. Atanassov, S. Vitkova, and S. Rashkov. Initial stages of electrocrystallization of nickel with texture $< 211>$. *C. R. Acad. Bulg. Sci.*, pages 523–526, 1980.

[230] K. Pantleon and M.A.J. Somers. Quantitative texture analysis of free-standing electrodeposited Cu-and Ni-line patterns. *Acta materialia*, 52(16):4929–4940, 2004.

[231] EC Felder, S. Nakahara, and R. Well. Effect of substrate surface conditions on the microstructure of nickel electrodeposits. *Thin Solid Films*, 84(2):197–203, 1981.

[232] G.C. Hasson and C. Goux. Interfacial energies of tilt boundaries in aluminum. experimental and theoretical determinations. *Scr. Metall.*, 5(10):889–894, 1971.

[233] D.M. Saylor, B.S. El Dasher, A.D. Rollett, and G.S. Rohrer. Distribution of grain boundaries in aluminum as a function of five macroscopic parameters. *Acta Materialia*, 52(12):3649–3655, 2004.

[234] V. Randle, M. Coleman, and M. Waterton. The role of $\sigma 9$ boundaries in grain boundary engineering. *Metallurgical and Materials Transactions A*, 42(3):582–586, 2010.

[235] A.D. Rollett and W.W. Mullins. On the growth of abnormal grains. *Scripta materialia*, 36(9):975–980, 1997.

[236] C.B. Thomson and V. Randle. Fine tuning at $\sigma 3^n$ boundaries in nickel. *Acta materialia*, 45(12):4909–4916, 1997.

[237] V. Randle, P. Davies, and B. Hulm. Grain-boundary plane reorientation in copper. *Philosophical Magazine A*, 79(2):305–316, 1999.

[238] R. E. Smallman and R.J. Bishop. *Modern physical metallurgy and materials engineering*. Butterworth-Heinemann, 1999.

[239] C. A. Schuh, T. G. Nieh, and H. Iwasaki. The effect of solid solution w additions on the mechanical properties of nanocrystalline Ni. *Acta materialia*, 51(2):431–443, 2003.

[240] I. Mizushima, P.T. Tang, Hansen H.N., and Somers M.A.J. Development of a new electroplating process for NiW alloy deposits. *Electrochim Acta*, 51:888–896, 2005.

[241] N. Zech, E. J. Podlaha, and D. Landolt. Rotating cylinder hull cell study of anomalous codeposition of binary iron-group alloys. *Journal of applied electrochemistry*, 28(11): 1251–1260, 1998.

[242] L. Wang, Y. Gao, Q. Xue, H. Liu, and T. Xu. Microstructure and tribological properties of electrodeposited Ni-Co alloy deposits. *Applied surface science*, 242 (3-4):326–332, 2005.

Appendices

Appendix A

Cross-Sectional EBSD Sample Preparation

1. Introduction:

Electron backscattered diffraction (EBSD) in scanning electron microscope (SEM) is a very powerful technique for determination of crystallite orientation and local orientation relations. This technique (also known as orientation image microscopy, OIM) is based on the detection of Kikuchi bands [1]. Kikuchi bands in electron backscattered patterns (EBSP) form in a two step process [2]: (i) incoherent scattering of the primary beam electrons (ii) elastic and coherent scattering of these electrons. EBSPs of nickel, analyzed by electrons of energy of 10 keV, originate from the top 5 nm of the surface [3]; this clearly shows how surface-sensitive the technique is. For high resolution orientation microscopy accelerating voltage of 12-20 kV is normally applied. However, in recent developments, accelerating voltage as low as 7.5 kV has been proposed as an optimized voltage for achieving higher physical resolution [4]. Accordingly, in high resolution orientation microscopy the signals originate at the very vicinity of the surface. This makes high demands on the quality and authenticity of the surface to be investigated and, hence, requires very careful sample preparation.

Sample preparation of metals for metallography and SEM analysis is normally accomplished by sampling via cutting and subsequent grinding/polishing. This preparation is associated with formation of mechanically deformed layer, comprising relatively high density of dislocation and lattice defects [5,6]. In the presence of dislocations, diffracting volume would no longer contain a single crystal lattice but a set of lattices of slightly different orientations with respect to one another, leading to a diffused EBSP and deterioration of EBSD results reliability [7].

Different parameters have been defined by commercial producers of EBSD systems for quantitative analysis of EBSP. Band contrast (BC), band slope (BS), mean angular deviation (MAD), in HKL system [8] and image quality (IQ), fit, etc. in EDAX/TSL system [9], are reflecting EBSP quality. Low EBSP quality brings about difficulties in detection of Kikuchi bands by image analysis software, resulting in higher non-indexed points (HKL system) or lower confidence index (EDAX/TSL system). All these quality parameters can indirectly indicate the relative damage of different sample preparation methods, where lower EBSP quality hints thicker damaged layer [5].

Long time colloidal silica polishing is very much recommended as the final polishing step [5,8]. In addition, chemical etching, electro-polishing, broad ion beam milling and focused ion beam (FIB) milling, are possible subsequent techniques to remove mechanically deformed layer [7,10,11]. Nowell [12] used broad ion beam milling and reported that low energy beam with high glancing angling yields the best preparation. Mateescu et.al [13] investigated EBSD sample preparation of face centered cubic (FCC) metals by Ga^+ FIB milling and reported that high quality EBSPs obtained, using ion current of $1 - 3$ nA. Koll et.al studied different preparation methods: colloidal silica polishing, electro-polishing, chemical etching and broad ion milling on silicon, steel, titanium and nickel alloys [5]. They have concluded that colloidal silica polishing is most attractive one, especially when time and cost efficiency is taken into account. The mentioned techniques for removal of mechanically deformed layer may form new artifacts or alter the microstructure. Chemical substances may react more aggressively with the grain boundaries and form undesirable grooves on the surface [7]. Long time electro-polishing results in formation of topography on the surface [6]. Broad ion beam may alter the microstructure by amorphization, heat generation and phase transformation [7]. Ion implantation, grain growth, twin formation, martensitic transformation, amorphization, redeposition, curtaining, etc. are the artifacts which may be induced by FIB milling [13–16]. On that account, a proper EBSD sample preparation needs careful consideration.

In case of electrodeposited thin films with bright and smooth surfaces, top-view EBSD analysis can be applied without any particular sample preparation. However, the film surface is not necessarily representative of whole microstructure especially when microstructure evolves with the film thickness. Thus, cross-sectional EBSD sample preparation and analysis is of high importance for thorough microstructural characterization [17,18]. Electrodeposition of thin films is very often carried out on substrates of different chemistry; this adds more to the complications of EBSD sample preparation.

The challenges of cross sectional EBSD sample preparation and suggest appropriate FIB milling parameters for proper EBSD sample preparation of electrodeposited nickel films is the main topic of this appendix.

2. Experimental

Electrodepositions of two nickel films (≈20 μm) were conducted in Watts electrolyte. The substrate of both materials was a copper sheet coated with amorphous Ni-P alloy (≈8 μm). Material "A" was made in an additive free electrolyte, applied current density of 2 A/dm^2 and investigated in as-deposited state. Material "B" was made in a electrolyte comprising 5 $mmol/dm^3$ 1,4-butynediol, applied current density of 10 A/dm^2 and subjected to thermal treatment for 30 min at $600°C$.

Sample preparation began with sampling a small piece via abrasive cutting. Samples were clamped between two brass plates with an aluminum foil protecting the film surface (schematically shown in Figure A.1). This sample holder was used for cross-sectional preparation, by means of manual grinding on SiC paper up to grade 4000. Mechanical polishing was performed for several minutes on a soft synthetic fiber polishing cloth (NAP, Struers) with diamond paste of 1 μm and lubricant Blue (Struers). Final mechanical/chemical polishing conducted with 0.04 μm colloidal silica (OP-S, Struers) on a chemically resistant synthetic fiber polishing cloth (OP-Chem, Struers) to achieve a scratch free surface.

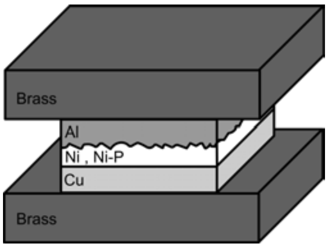

Figure A.1: Schematic sample and sample holder configuration for cross-sectional EBSD sample preparation.

For material "A", two samples were subsequently subjected to electro-polishing in an electrolyte of 0.6 dm^3 H_2SO_4 and 0.4 dm^3 distilled water applying a voltage of 1.5 V. Te time of electropolishing was either 15 s or 60 s. FIB milling with Ga^+ ions of 30 keV energy and ion currents of 0.46 nA, 0.92 nA and 2.8 nA was applied additionally on 60-seconds electropolished sample. One sample prepared by FIB milling with ion current of 0.46 nA on the colloidal silica polished sample. For all FIB milled samples, a protective platinum layer has been deposited prior to milling, Figure A.4b. Platinum deposition and FIB milling were carried out in dual beam FIB-SEM, Helios Nanolab™ 600 from FEI, equipped with an EBSD system from Oxford Instruments HKL Technology with a Nordlys II camera. FIB milling was applied parallel to electrodeposition growth direction and EBSD data acquisition conducted in the same microscope afterwards by acceleration voltage of 15 kV, electron probe current of 5.5 nA and step size of 50 nm. Preparation methods applied for material “A” are summarized in Table A.1. Data evaluation was carried out with the Channel5 software from Oxford Instruments HKL Technology and no cleaning was applied. Ion channeling imaging was performed, using ion density of 3.45 C/m^2 in the same microscope.

Table A.1: Preparation methods applied for cross sectional EBSD sample preparation of material “A”.

Sample Name	Mechanical Polishing	Electro-polishing time		FIB milling , ion current		
		15 sec	60 sec	0.46 nA	0.92 nA	2.8 nA
A1	✓					
A2	✓	✓				
A3	✓		✓			
A4	✓		✓	✓		
A5	✓		✓		✓	
A6	✓		✓			✓
A7	✓			✓		

For material “B” after finishing with colloidal silica polishing the samples were prepared by FIB milling with Ga^+ ions of energy of 30 keV and ion currents of 0.46 nA, 0.92 nA, 2.8 nA and 6.5 nA. A protective Pt layer has been deposited prior to FIB milling,Figure A.4b. Some of samples exposed to additional 2 min FIB milling with Ga^+ ions of 5 keV energy and ion current of 85 pA. A dual beam FIB-SEM, Helios Nanolab™ 600 from FEI, equipped with an EBSD system from EDAX-TSL and Hikari camera was used for FIB milling and EBSD data acquisition. EBSD measurements were performed by electron probe current of 5.5 nA, acceleration voltage of 12 kV or 7.5 kV and step size of 50 nm. OIM TSL5 was used for quantification and analysis of the EBSD results. The details of various preparation methods and used primary electron beam accelerating voltage for material “B” is summarized in Table A.2. Ion channeling imaging was conducted with ion density of 0.90 C/m^2 in the same microscope.

Table A.2: Preparation methods applied for cross sectional EBSD sample preparation of material “B” and accelerating voltage used for EBSD data acquisition.

Sample	Mech.	FIB mill, ion current and accelerating voltage					EBSD, accelerating voltage	
Name	Polish	0.46nA 30kV	0.92nA 30kV	2.8nA 30kV	6.5nA 30kV	85pA 5kV	12kV	7.5kV
B1	✓	✓					✓	
B2	✓		✓				✓	
B3	✓			✓			✓	
B4	✓				✓		✓	
B5	✓	✓						✓
B6	✓				✓			✓
B7	✓	✓				✓		✓
B8	✓				✓	✓		✓

3. Results:

3.1 Material "A"

The BC maps of material "A" prepared with different methods A1-A6 (Table A.1) are shown in Figure A.2. It can be seen in Figure A.2a that, sole colloidal silica polishing without any subsequent treatment, reveals a columnar microstructure in which there are fine circular crystallites inside the columnar grains. Applying electropolishing for 15 seconds, a columnar microstructure is revealed with no circular crystallites inside the columns, Figure A.2b. Longer electropolishing time, 60 seconds, shows a columnar microstructure Figure A.2c similar to shortly electropolished sample. However, growth twins are not straight and they look wavy; in addition, the BC changes within a single columnar grain ,Figure A.2c. For the electropolished samples, the backscattered electron signal at the Ni/Ni-P interface is lost; this is shown by a white boxes on Figure A.2c. The longer the electropolishing time the bigger the size of the no signal region at the Ni/Ni-P interface. Figure A.3a shows SEM secondary electron image of 60-seconds electropolished sample. The prepared edge is rounded and cross section does not make right angle with film surface after electropolishing. The topography formed due to electropolishing on the nickel thin film is visible too. The BC variation within the column in Figure A.2c is in accordance with the topography of surface visible in Figure A.3a. Schematic representation of 3-dimensional geometry of an electropolished sample is shown in Figure A.3b. Sample preparation by FIB milling reveals a columnar microstructure, in which the whole cross section is visible and growth twins are straight, Figures A.2d, A.2e, and A.2f. FIB milled samples show no significant variation of BC within the columns.

Figure A.4a shows channeling ion image of sample A7, region marked by 'MP' is where preparation is stopped after colloidal silica polishing and region marked by 'FIB' is where ≈750 nm from the mechanically prepared surface is removed by FIB milling. It is clear that region 'FIB' has columnar microstructure whereas region 'MP' exhibits relatively small columns encompassing circular crystallites. Schematic representation of 3-dimensional geometry of sample after FIB milling is shown in Figure A.4b. One can easily see the similarity between the BC map shown in FigureA.2a and the channeling ion image micrograph of region called 'MP'. Likewise BC map of sample A7, shown on Figure A.4a by 'FIB' is similar to what is shown for FIB milled sample earlier in Figure A.2d and for sake of brevity is not represented here. Average BC, average BS and fraction of non-indexed points for different preparation methods are reported in Table A.3. Since a rather strong <211> fiber texture has been determined from X-ray diffraction, grains having the <211> crystallographic direction aligned parallel (maximum 10° deviation) to the growth direction of the nickel film were quantified from the EBSD maps too. The EBSD data close to the

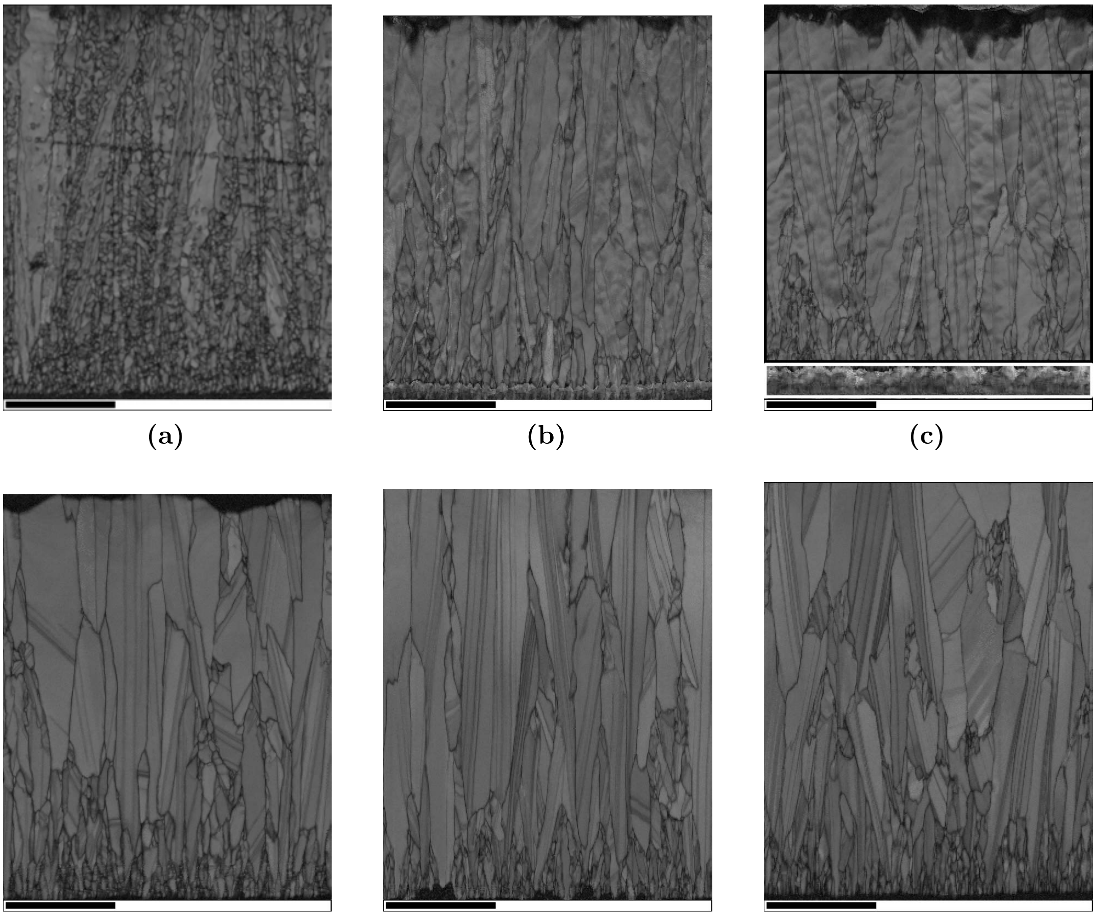

(a) (b) (c)

(d) (e) (f)

Figure A.2: Band contrast maps of samples prepared with different methods (a) A1 colloidal silica polishing only; (b) A2 electropolished for 15 seconds, (c) A3 electropolished for 60 seconds; no signal region is enclosed by a white box, the solid box indicates where quantification for all the maps were applied; (d) A4, (e) A5, (f) A6 FIB milled with 0.46 nA 0.92 nA and 2.8 nA respectively. The scale bar for all maps is $5\mu m$.

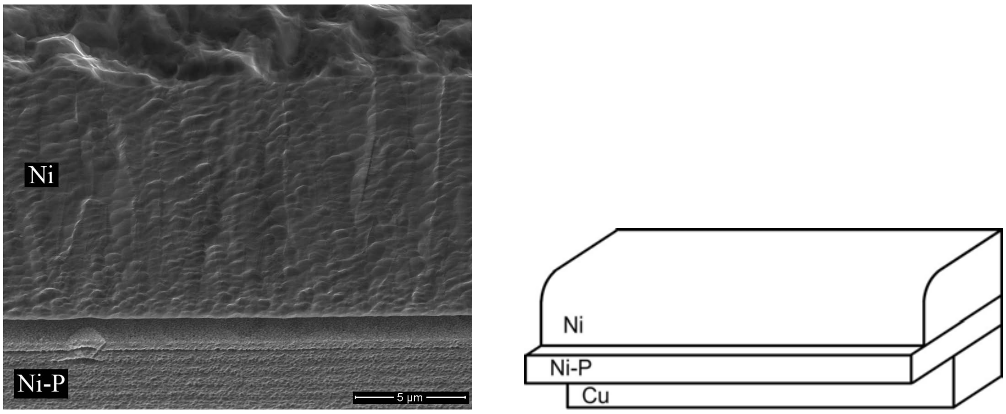

(a) (b)

Figure A.3: (a) SEM secondary electron image of sample electropolished for 60 seconds, A3. (b) Schematic representation of 3-dimensional geometry of electropolished samples.

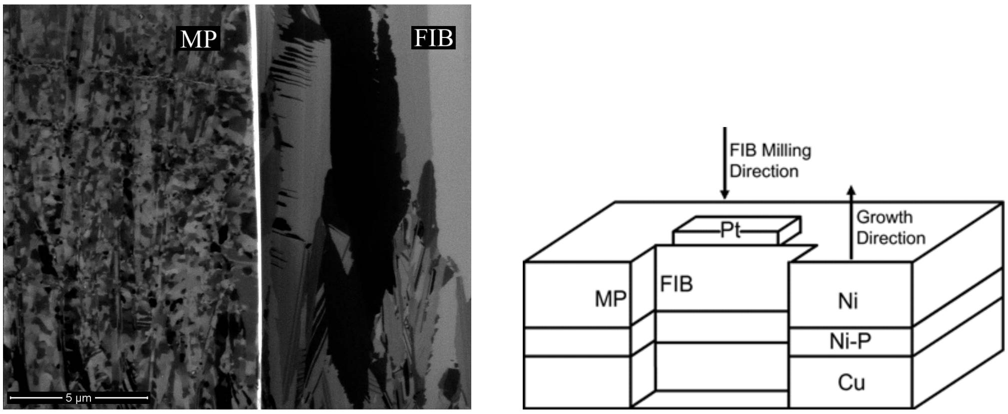

(a) **(b)**

Figure A.4: (a) Channeling ion image of the sample A7, region marked by 'MP' is where preparation is stopped after colloidal silica polishing, and region marked by 'FIB' is the FIB milled surface. (b) Schematic representation of 3-dimensional geometry of FIB milled sample A7. Regions 'MP' and 'FIB' are representative of what is shown in (a).

Ni/Ni-P and on top of nickel film of electropolished samples is not available; thus for sake of valid comparison, quantification for all the EBSD results is carried out on a rectangle of size $15\mu m \times 13\mu m$ (78300 data points) shown by solid box on Figure A.2c ($\approx 2\mu m$ above the Ni/Ni-P interface).

From Table A.3 it is evident that by electropolishing (A2 and A3) average BC and BS increases and fraction of non-indexed points decreases in comparison with colloidal silica polished sample (A1). FIB milling with at ion current of 0.46 nA (A4) brings about higher average BC and BS in comparison with mechanical polishing (A1) but the increase does not reach to the level of electropolishing (A2 and A3). Ion current of 0.92 nA and 2.8 nA for FIB milling (A5 and A6) results in decrease of average BC, BS and increase of fraction of non-indexed points, in comparison with 0.46 nA milled sample (A4). Applying low current FIB milling on colloidal silica polished sample and on an electropolished sample (A7 and A4 respectively) brings about no significant difference in average BC, average BS and non-indexed fraction of the maps.

Table A.3: Average BC, average BS and fraction of non-indexed points for different preparation methods for material "A".

	A1	A2	A3	A4	A5	A6	A7
Ave. BC	83.10	92.96	96.37	88.86	92.21	89.29	89.46
Ave. BS	179.22	228.51	237.34	197.78	147.27	140.10	203.63
Non-indexed fraction (%)	26.08	7.51	5.27	7.30	18.50	30.80	7.38
Fraction of <211> fiber texture (%)	41.7	54.8	57.3	50.7	42.4	25.4	43.6

3.2 Material "B"

EBSD data acquisition was applied by measuring 1200 points of one particular grain oriented such that <310> crystallographic direction was parallel to electrodeposition direction. Average IQ of EBSPs measured after different FIB milling preparation methods, is tabulated in Table A.4. One can clearly see that notable variation in ion current, B1-4, brought about no significant difference between average IQ of BESPs (minimum ion current: 0.46 nA - maximum ion current 6.5 nA). Acquiring EBSD data with electron acceleration voltage of 7.5 kV still shows no significant difference in IQ, between FIB milling with ion current of 0.46 nA and 6.5 nA, B5 and B6. Prepared sites of interest with 0.46 nA and 6.5 nA ion current were subjected to additional 5 keV Ga^+ ions at glancing angle of 4°. This extra step decreased the average IQ in both cases, comparing IQ of B5 with B7 and B6 with B8. It is notable that, different setting has been applied for measuring with 12 kV (samples B1-4) and 7.5 kV (samples B5-8). Thus the values reported for samples B1-4 are only comparable to each other, likewise B5-8.

Table A.4: Average IQ of EBSPs measured after different FIB milling preparation methods for material "B".

	B1	B2	B3	B4	B5	B6	B7	B8
Ave. IQ	3876	3833	3925	3832	7085	7134	6665	6455

Figure A.5 shows orientation map, IQ map and ion channeling image of a location on cross-section of matereial "B". Three grains are indicated by number 1, 2 and 3 on the orientation map and channeling ion image. Grain No.1 is <17 7 1> oriented and grains No.2 and 3 are <310> oriented in respect with film growth direction, sown by an arrow on the legend of Figure A.5a. It can clearly be seen from the ion channeling image (Figure A.5c) that grain No.2 and 3 FIB milled very smoothly while the portion of microstructure below the grain No.1 milled with formation of surface relief; that is reflected in IQ map too (Figure A.5b).

4. Discussion:

The starting steps of EBSD sample preparation are similar to metallographic sample preparation; cutting, grinding and mechanical polishing. The subsequent step(s), e.g. electropolishing and FIB milling, aim to remove the remained mechanically deformed layer of mechanical polishing. Colloidal silica polishing utilizes simultaneous mechanical and chemical removal of the material [8]. In order to remove the deformed layer by colloidal silica the effect of chemical removal should be more pronounced than mechanical. That is why occasionally corrosive substances are mixed with colloidal silica to enhance the chemical effect [19]. In regular metallographic preparation, the sample is mounted in a

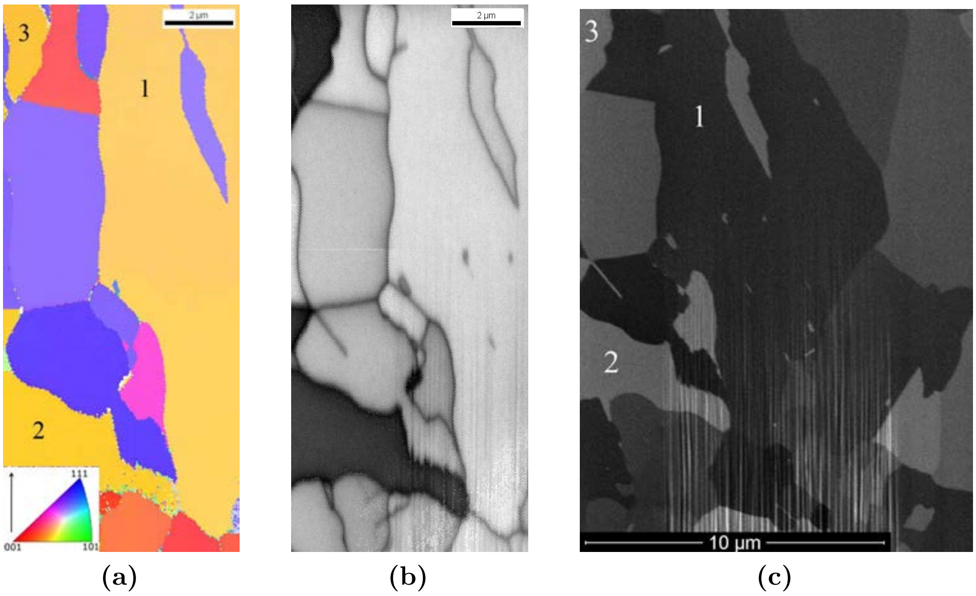

Figure A.5: (a) Orientation map color coded in relation with film growth direction shown by an arrow, (b) IQ map of the EBSD measurements; (c) ion channeling image of the same location with lower magnification; Three grains with close crystallographic orientation are indicated on orientation map and shown on channeling ion image too.

polymeric embedding mess. Metals are more reactive than polymer, thus metallic part encounters both mechanical and chemical removal while the polymeric part bears only the mechanical removal. Assuming similar hardness of the embedding polymer and the metallic sample, a slight height difference starts to form by colloidal silica polishing, especially in presence of right corrosive substances. This brings about less mechanical contact on the metal and relatively more chemical removal. In the correct conditions after some time, metallic sample bears only chemical removal which yields no deformation layer.

For electropolishing and FIB milling, the mechanically polished samples in an embedding mess must be taken off which is problematic. More than that, 3-dimentional characterization with EBSD (3D-EBSD) requires two free surfaces [20]; while for embedded samples there is only one free surface. Thus in this work, the samples were clamped between two brass plates with screws, and easily taken off after preparation. Aluminum foil, copper substrate and brass plates react faster than the nickel film with colloidal silica. Hence, nickel film always bears mechanical removal of colloidal silica. Additionally, rather fast reaction of aluminum foil results in formation of gaps between film surface and the foil. Thus very long colloidal silica polishing was not applicable. Accordingly, it is found impossible to prepare a reliable EBSD sample free of deformation layer regardless of the time of mechanical polishing in the used set-up (compare Figure A.2a with Figure A.2b–A.2f). Even though no extra corrosive substance was added to colloidal silica, still one can imagine that it is extremely hard to find a proper substance to react faster with nickel than all the other metals in the preparation system. Very similar issue arises when electropolishing is applied. Electropolishing is also based on chemical reaction of a corrosive substance and the metallic sample. Electropolishing is time dependent process and certain time is needed to assure the removal of mechanically deformed layer. Since Ni-P reacts slower than nickel, Ni-P substrate steaks out after electropolishing. This impedes proper EBSD measurements at Ni/Ni-P interface, where Ni-P shadows the signals from reaching the detector. Longer electropolishing ensures removal of the deformation layer but that yields bigger region with no signal at the interface. In addition, the edge of cross section is in contact from two sides with electropolishing electrolyte and reacts faster than the cross section. So a sharp prepared edge starts to round which is disadvantageous for a proper EBSD measurement too. The used electropolishing system also made some topography on the surface, and that is one of the main drawbacks of electropolishing [6] especially when high resolution orientation microscopy is intended. Loss of the Ni/Ni-P interface information, rounding of the edge and formation of surface topography, all deter a proper whole cross-sectional EBSD measurements. Accordingly neither colloidal silica polishing nor electropolishing is a good choice for cross sectional sample preparation of the multi-layer samples.

Broad ion beam is traditionally used for sample preparation parallel to the sample surface and is not very suitable for cross-sectional sample preparation. Difference in sputtering rate of Ni, Ni-P and Cu potentially causes further problems. Thus, it has not been tested experimentally in this work.

Figure A.2a (colloidal silica polished) and Figure A.2f (high current FIB milled) show two different microstructures. The band slop and fraction of non-indexed points hint that there is thicker damaged layer on high current FIB milled sample, in comparison with the colloidal silica polished sample. Observing the microstructures revealed by electropolishing, it is evident that the true microstructure is FIB prepared one. Thus, EBSP quality on its own can be a misleading measure for validity of sample preparation of different routines. It is more important to assure the result of analysis represents the true microstructure but not the artifacts of sample preparation. In this case, for the FIB milled sample the fraction of non-indexed points can be reduced by applying different cleaning procedures and assigning the non-indexed point orientation, according to their neighbors. That brings about relatively acceptable EBSD maps.

Damaged layer of FIB milling preparation methods can be compared based on EBSPs quality indicators such as BC, BS, IQ, etc. BC maps reveal microstructural features better than BS graphically, however based on the results tabulated in Table 3, BS provides better correlation with FIB ion current and non-indexed fraction. FIB milling of the sample A4-6 was conducted on electropolished sample to assure the milling is not inside the deformation layer. Applying FIB milling directly on the colloidal silica polished sample brought about very similar result to the sample prepared by FIB milling of electropolished sample. Thus, electropolishing can simply be eschewed and one can conduct FIB milling such to assure the mechanically deformed layer is removed. The thickness of mechanically deformed layer is dependent both on mechanical polishing conditions and strength of the sample itself. The deformation layer thickness is smaller for the samples with higher strength and vice versa.

Material “A” was prepared by different ion currents, ranging from 0.46 nA to 2.8 nA. This is close to the range suggested by Mateescu et.al to be suitable for EBSD sample preparation of FCC metals [13]. They have reported that lower ion current (0.1 nA) is problematic in terms of time of preparation and redeposition of sputtered atoms back to the surface; and higher ion current results in more lattice defects. Looking at material “A” FIB milling preparation results tabulated in Table A.3 it is evident that by increase of ion current of FIB milling the average band slope decreases and fraction of non-indexed points increases. Lower EBSP quality and higher non-indexed points hints to formation more lattice defects and bigger damaged layer. This conclusion is not valid for material “B”, compare IQ of samples B1-B4 in Table A.2, where increase of ion current even up to 6.5 nA did not change the EBSPs quality notably. By lowering electron accelerating voltage from 12 kV down to 7.5 kV, smaller depth from the surface has been probed by EBSD analysis. But still no significant difference was seen between the sample prepared with 6.5 nA and 0.46 nA, B5 and B6 at Table A.2. This concludes that the damaged layer is extremely thin in this particular case even when the surface is prepared with high ion current. The different behavior of materials “A” and “B” stems from their different crystallographic orientation with respect to incident ion beam. Sputtering of the atoms is very much dependent on the crystallographic orientation [21][22]. Channeling directions for incoming ions, sputter differently from non-channeling directions [21] and few degrees difference in orientation changes ion-atom interaction drastically [23]. This fact is also shown in Figure A.5 where three grains with slight difference in orientation in respect with incident ions, sputter very differently. For all three grains there is less than 5° deviations from <310> pole, that is why they look with rather similar colors in orientation map. Grain 1 which is slightly off <310> pole does not sputter as smooth as grain 2 and 3, which are on exact <310> pole. Accordingly the quality of FIB milled surfaces for EBSD analysis in dependent on crystallographic orientation in respect with incident ion beam. Generally higher ion current decreases EBSP quality by formation of thicker damaged layer but the thickness of damaged layer is orientation dependent. Thus, it is wise strategy

to use higher current for fast removal of the mechanically deformed layer (rough milling) and then use low current milling to remove the damaged layer rough milling.
Orientation microscopy is significantly enhanced by use of better EBSD detectors and using more powerful computers and algorithm for EBSPs analysis [24]. In addition, it has been pointed by Steinmetz and Zaefferer that lowering electron energy plays a major role for high resolution orientation microscopy [4]. By lowering the accelerating voltage, interaction volume lessens in size, hence, surface lattices which are more prone to be defective due to preparation, contribute more to the forming EBSPs. Thus, avoiding any lattice defect is highly crucial for low energy EBSD analysis. Si is more prone to amorphization than metals [11] and low kV milling (2 and 5 kV) after normal 30 kV FIB milling has shown a notable increase in EBSP quality [11,25]. This idea has been tested by applying 5 kV FIB milling with low glancing angle of 4° for the samples prepared with 0.46 nA and 6.5 nA. In both cases low kV FIB milling lowered the EBSP quality, hence, induced more damages to crystal lattices; most probably due to gallium ion implantation. Here again by alteration of crystallographic orientation this behavior may alter. In general, for compounds or stochiometric intermetallics which are prone to amorphization [11] low kV milling improves EBSP quality; that may not be true for pure metals. As mentioned earlier, FIB milling quality is dependent on orientation, thus further investigation is needed to clarify whether low kV milling can benefit high resolution orientation microscopy of certain orientations of metallic materials or not.

5. Conclusions:

- Colloidal silica polishing is not a good choice for cross sectional sample preparation if the chemical removal is less pronounced than the mechanical removal.

- Electropolishing brings about rounding of the sharp edges of the sample and formation of surface relieves. Thus, it is not a good choice for cross-sectional sample preparation of multi-layered samples.

- EBSP quality on its own can be a misleading measure for validity of sample preparation. It is more important to assure the result of analysis represents the true microstructure but not the artifacts of sample preparation.

- Damaged layer of FIB milling preparation methods can be compared based on EBSPs quality indicators; in HKL system Band Slope (BS) provides better correlation with FIB ion current and non-indexed fraction.

- The quality of EBSP after FIB milling, is dependent on the crystallographic orientation in respect with incident ion beam.
- Generally higher ion current decreases EBSP quality by formation of thicker damaged layer but the thickness of damaged layer is orientation dependent.
- For a specific crystallographic that has been tested, the EBSP quality decreased due to low kV FIB milling.
- The optimal preparation routine is final polishing with colloidal silica and removal of the mechanically deformed layer (in this case 750 nm) of the prepared surface by FIB milling. The time efficient method is to apply rough milling (high current) first and then apply a gentle milling (low current ≈ 0.5 nA).

References

[1] A. J. Schwartz, M. Kumar, B. L. Adams, and D. P. Field, Electron Backscatter Diffraction in Materials Science, 2nd ed. Springer, 2009.

[2] S. Zaefferer, On the formation mechanisms, spatial resolution and intensity of backscatter Kikuchi patterns, Ultramicroscopy, vol. 107, No. 2-3, 254-266, 2007.

[3] V. Randle and O. Engler, Introduction to texture analysis: macrotexture, microtexture and orientation mapping. CRC Press, 2000.

[4] D. R. Steinmetz and S. Zaefferer, Towards ultrahigh resolution EBSD by low accelerating voltage, Materials Science and Technology, vol. 26, No. 6, 640-645, 2010.

[5] L. Koll, P. Tsipouridis, and E. A. Werner, Preparation of metallic samples for electron backscatter diffraction and its influence on measured misorientation, Journal of Microscopy.

[6] G. L. Wynick and C. J. Boehlert, Use of electropolishing for enhanced metallic specimen preparation for electron backscatter diffraction analysis, Materials Characterization, vol. 55, No. 3, 190-202, 2005.

[7] S. I. Wright and M. M. Nowell, EBSD Image Quality Mapping, Microscopy and Microanalysis, vol. 12, No. 1, 72-84, 2005.

[8] H. K. L. Channel5 Users Manual, 2001, HKL Technology, Danbury, CT.

[9] E. Mahway, OIM users manual, EDAX-TSL, New Jersey, 2005.

[10] S. Zaefferer, P. Romano, and F. Friedel, EBSD as a tool to identify and quantify bainite and ferrite in low-alloyed Al-TRIP steels, Journal of Microscopy, vol. 230, No. 3, 499-508, 2008.

[11] T. Matteson, S. Schwarz, E. Houge, B. Kempshall, and L. Giannuzzi, Electron backscattering diffraction investigation of focused ion beam surfaces, Journal of Electronic

Materials, vol. 31, No. 1, 33-39, 2002.

[12] M. M. Nowell, Ion beam preparation of passivated copper integrated circuit structures for electron backscatter diffraction/orientation imaging microscopy analysis, Journal of Electronic Materials, vol. 31, No. 1, 23-32, 2002.

[13] N. Mateescu, M. Ferry, W. Xu, and J. M. Cairney, Some factors affecting EBSD pattern quality of Ga^+ ion-milled face centred cubic metal surfaces, Materials Chemistry and Physics, vol. 106, No. 1, 142-148, 2007.

[14] L. A. Giannuzzi and F. A. Stevie, Introduction to focused ion beams: instrumentation, theory, techniques and practice. Springer, 2005.

[15] W. Voegeli, K. Albe, and H. Hahn, Simulation of grain growth in nanocrystalline nickel induced by ion irradiation, Nuclear Inst. and Methods in Physics Research, B, vol. 202, 230-235, 2003.

[16] S. Olliges, P. Gruber, A. Bardill, D. Ehrler, H. D. Carstanjen, and R. Spolenak, Converting polycrystals into single crystals - Selective grain growth by high-energy ion bombardment, Acta Materialia, vol. 54, No. 20, 5393-5399, 2006.

[17] A. Bastos, S. Zaefferer, D. Raabe, and C. Schuh, Characterization of the microstructure and texture of nanostructured electrodeposited NiCo using electron backscatter diffraction (EBSD), Acta Materialia, vol. 54, No. 9, 2451-2462, 2006.

[18] K. Pantleon, A. Gholinia, and M. A. J. Somers, Quantitative microstructure characterization of self-annealed copper films with electron backscatter diffraction, physica status solidi (a), vol. 205, No. 2, 275-281, 2008.

[19] G. G. E. Seward, S. Celotto, D. J. Prior, J. Wheeler, and R. C. Pond, In situ SEM-EBSD observations of the hcp to bcc phase transformation in commercially pure titanium, Acta Materialia, vol. 52, No. 4, 821-832, 2004.

[20] S. Zaefferer, S. I. Wright, and D. Raabe, Three-Dimensional Orientation Microscopy in a Focused Ion BeamScanning Electron Microscope: A New Dimension of Microstructure Characterization, Metallurgical and Materials Transactions A, vol. 39, No. 2, 374-389, 2008.

[21] B. W. Kempshall, S. M. Schwarz, B. I. Prenitzer, L. A. Giannuzzi, R. B. Irwin, and F. A. Stevie, Ion channeling effects on the focused ion beam milling of Cu, Journal of Vacuum Science & Technology B: Microelectronics and Nanometer Structures, vol. 19, No. 3, 749-754, 2001.

[22] U. Wendt and G. Nolze, Correlation between crystal orientation, channeling contrast and topography during FIB milling of Cu studied by FIB, EBSD, SEM, and AFM, Praktische Metallographie, vol. 44, No. 5, 236238, 2007.

[23] Y. Yahiro, K. Kaneko, T. Fujita, W.J. Moon, and Z. Horita, Crystallographic orien-

tation contrast associated with Ga+ ion channelling for Fe and Cu in focused ion beam method, J Electron Microsc., vol. 53, No. 5, 571-576, 2004.
[24] V. Randle, Applications of electron backscatter diffraction to materials science: status in 2009, Journal of Materials Science, vol. 44, No. 16, 4211-4218, 2009.
[25] J. Michael and L. Giannuzzi, Improved EBSD Sample Preparation Via Low Energy Ga^+ FIB Ion Milling, Microscopy and Microanalysis, vol. 13, No. 2, 926-927, 2007.

Appendix B

OIM Data Acquisition Parameters

It is noted [1] that the effective resolution is affected by the microscope and by noise in the EBSP (therefore the pattern quality). By increase of acquisition time per EBSP, the signal to noise ratio in the pattern increases, hence, the the effective resolution improves. Even though long acquisition time is theoretically beneficial, in practice the stability of microscope, formation of thick carbon contamination layer, and other technical issues encourages limiting the acquisition time and conducting the measurements as fast as possible. Accordingly, it is necessary to optimize the acquisition settings of OIM data acquisition to minimize the time without deterring the resolution. The optimization required acquiring OIM data at different conditions. In order to exclude the effect of carbon contamination on the resolution, twin lamellae with fixed thickness enveloped in columnar grains were chosen for the study. Thus, different measurements were conducted on the different locations of a single columnar grain which possessed nano-twins.

Some preliminary studies had shown that accelerating voltage of 12 kV, probe current of 1.4 nA, and acquisition time per EBSP of 40 s^{-1} provided a good compromise between the resolution and acquisition time of the used microscope[1].

The acquisition time of a map is the function of step size squared, hence, it is of high importance to determine the maximum step size which can be applied without losing the microstructural features. Using the mentioned settings and varying the step size from 15 nm to 40 nm, it was found out that step size of 40 nm is not acceptable and step size of 15 – 30 nm provides almost identical information, Figure B.1.

In the next step, the probe current was systematically increased from 1.4 to 2.7 and 5.5 nA and accordingly the acquisition time per EBSP was increased from 40 to 60 and 80 s^{-1} respectively. It was found out that for step size of 20 nm the increase of probe current to

---

[1] It is worth mentioning that acquisition time per EBSP of 40 s^{-1} is interpreted as 40 fps (frame per second) in TSL/EDAX nomenclatures.

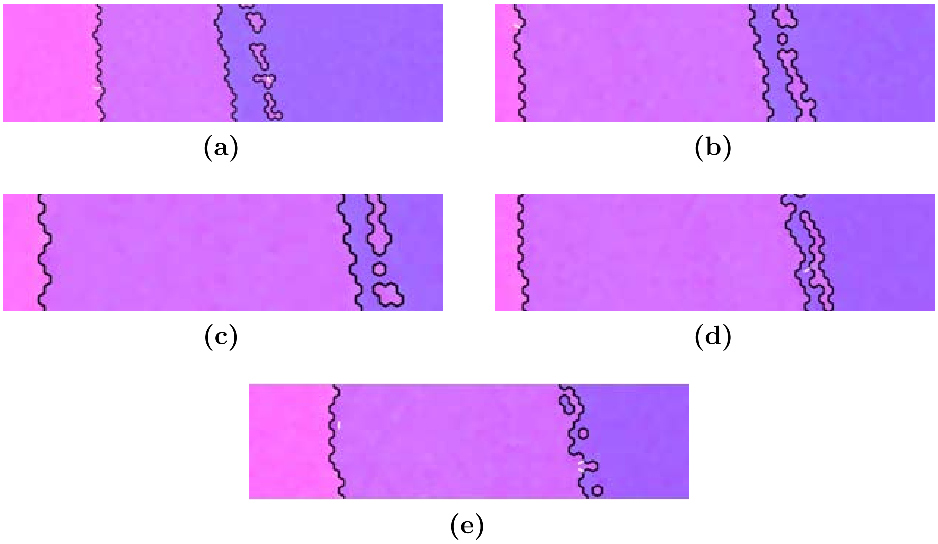

Figure B.1: Orientation map obtained at accelerating voltage of 12 kV, probe current of 1.4 nA, and acquisition time per EBSP of 40 s^{-1} and step size of (a) 15 nm, (b) 20 nm, (c) 25 nm, (d) 30 nm, and (e) 40 nm.

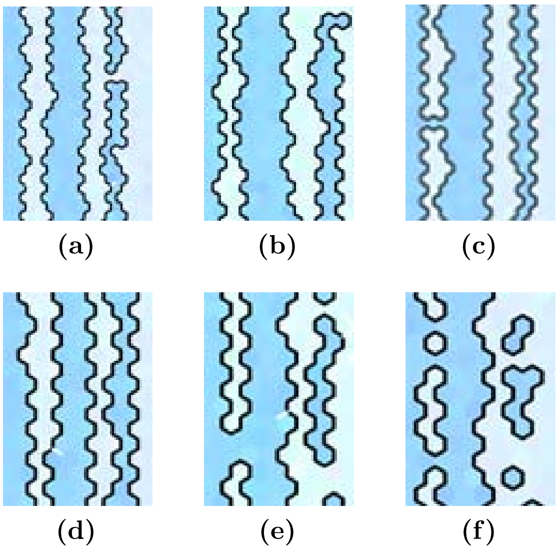

Figure B.2: Orientation map obtained at accelerating voltage of 12 kV. (a) step size of 20 nm, probe current of 1.4 nA and acquisition time per EBSP of 40 s^{-1}; (b) step size of 20 nm, probe current of 2.7 nA and acquisition time per EBSP of 60 s^{-1}; (c) step size of 20 nm, probe current of 5.5 nA and acquisition time per EBSP of 80 s^{-1}; (d) step size of 30 nm, probe current of 1.4 nA and acquisition time per EBSP of 40 s^{-1}; (e) step size of 30 nm, probe current of 2.7 nA and acquisition time per EBSP of 60 s^{-1}; (f) step size of 30 nm, probe current of 5.5 nA and acquisition time per EBSP of 80 s^{-1}.

5.5 nA does not alter the obtained OIM data (compare Figures B.2a, B.2b, and B.2c); whereas, using step size of 30 nm, only probe current of 1.4 nA and acquisition time per EBSP of 40 s^{-1} provides an acceptable map (compare Figures B.2d, B.2e, B.2f). It is noted that using step size of 20 nm and acquisition time per EBSP of 80 s^{-1} has only a slightly longer acquisition time than that of using step size of 30 nm and acquisition time per EBSP of 40 s^{-1} (the difference between the two is only 11%).

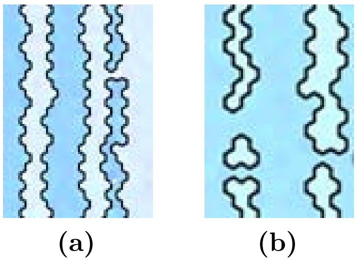
(a) (b)

Figure B.3: Orientation map obtained at step size of 20 nm and probe current of 5.5 nA. (a) accelerating voltage of 12 kV acquisition time per EBSP of 40 s^{-1}; (b) accelerating voltage of 20 kV acquisition time per EBSP of 120 s^{-1}.

By fixing probe current to 5.5 nA the effect of accelerating voltage is studied. Increase of accelerating voltage, facilitate a faster measurement but due to increase of electron/matter interaction volume the physical resolution decreases. As shown in Figures B.3, increase of accelerating voltage from 12 to 20 kV and increasing the acquisition time per EBSP from 80 s^{-1} to 120 s^{-1} the obtained map is not acceptable in terms of resolving the twin lamellae[2]. Increase of accelerating voltage to a value larger than 12 kV had a negative influence on the resolution generally. The effect of lowering voltage is mentioned in Appendix F, but in here it suffice to point out that lowering voltage from 15 to 7.5 kV is associated with a 15 fold increase in acquisition time [2].
Thus, the optimal conditions for OIM measurement was: step size of 20 nm, acquisition time per EBSP of 80 s^{-1}, probe current of 5.5 nA, and accelerating voltage of 12 kV.

References

[1] F.J. Humphreys: "Characterisation of fine-scale microstructures by electron backscatter diffraction", Scr. Mater., 51, 771-776, 2004.
[2] D. R. Steinmetz and S. Zaefferer, "Towards ultrahigh resolution EBSD by low accelerating voltage", Materials Science and Technology, 26, 640-645, 2010.

---

[2] Note that the Figure B.2a and B.3a are identical and for ease of comparison is shown twice.

Appendix C

OIM Maps Cleaning Procedures

The determination of orientation of the grains in OIM is based on detection of Kikuchi bands. At the vicinity of grain boundaries, the detected EBSP is composed of the Kikuchi bands of two neighboring grains. Since the detected bands belong to two differently oriented grains, the automatically determined orientation of the data points close to the boundaries is normally associated with error. This is shown for an orientation map in Figure C.1b, in which erroneously indexed data points are visible at the boundaries. Thus, it is essential to clean this errors from the map.

There is no particular solution for cleaning the OIM data and it is rather case dependent. Thus, the commercially available OIM data analysis softwares provide different routines and it is the user finding a proper cleaning procedure.

Using OIM 5™ software, different methods of cleaning were tested and confidence index (CI) standardization and grain dilation were found suitable procedures for the studied samples in this dissertation.

In CI standardization, the CI of every point in the map within a recognized grain is assigned to the highest CI value found in that grain. Figure C.1a shows the CI map of the as-measured data, and after applying CI standardization the CI map changes to the Figure C.1c. It is notable that in the vicinity of the boundaries in the as measured data, the erroneously indexed data points and correctly indexed data points, both are of low CI; And after CI standardization only the erroneously indexed data points remain of low CI. Thus, by CI standardization the correctly indexed points belonging to a same grain are grouped together and the erroneously indexed data points are singled out. By disregarding the data points with CI value below 0.1 in the data analysis, only reliable data points are taken into account. In addition, it is a common practice to assign an orientation of the data points belonging to no grain. This can be accomplished by grain dilation routine. In this routine, the orientation of the data points which do not belong to any grain is changed to the orientation of the majority of neighboring points belonging to a same grain. The result of applying this routine is shown in Figure C.1d, in which all of the erroneous data points in the as-measured data are cleaned.

It is worth emphasizing that grain dilation routine is associated with alteration of orientation of the data points in the map, hence, it must be applied cautiously. For this reason, grain dilation was applied only in a single iteration and the number of altered data points was checked; if that exceeded 6% of total number of data points, then this cleanup is disregarded and only grain CI standardization was applied. Note that after cleaning the maps, data points with CI larger than 0.1 were studied only.

Both (CI) standardization and grain dilation require definition of a grain which is the minimum number of connected points with misorientations of less than a certain value between them. In other words, these cleaning routines require (1) minimum number of data points clustered together and (2) the maximum allowed misorientation between the data points in that cluster. In the successful cleaning procedure shown in Figure C.1d, the minimum number of data points were 4 and maximum allowed misorientation was 5°. This choice owes to experimenting with different definition of the two parameters. The dissatisfactory orientation map obtained using maximum allowed misorientation of 15° is shown in Figure C.1f, in which erroneously indexed data points are not cleaned and instead low angle grain boundaries (marked by white lines) are added to the map.

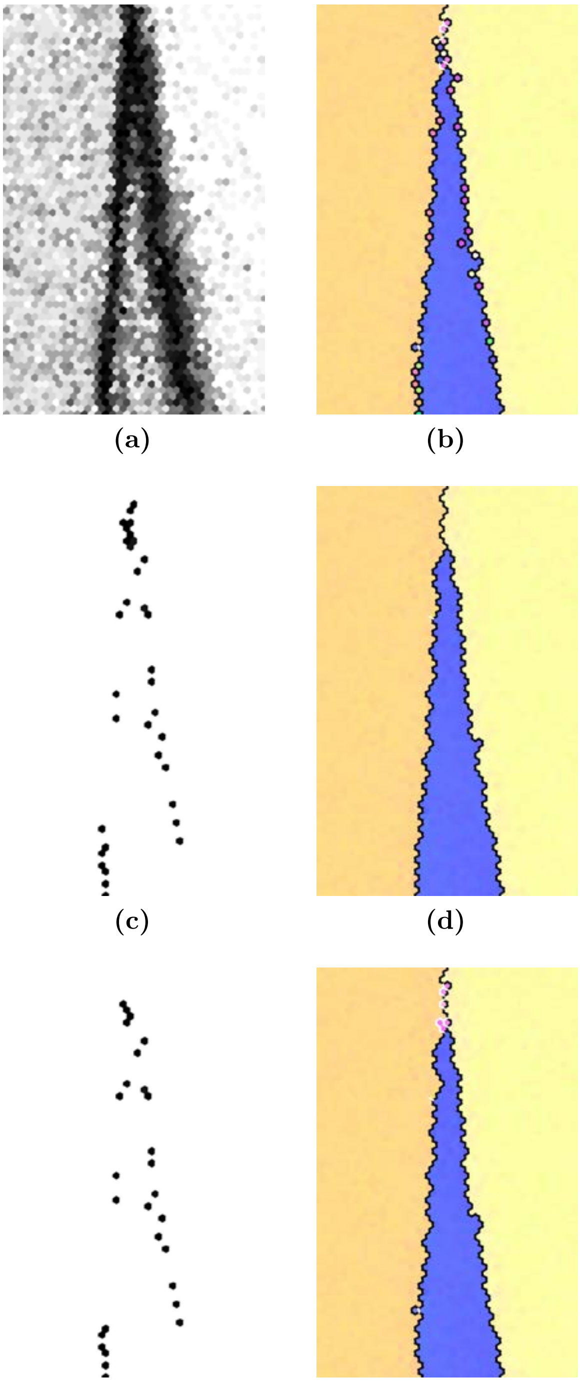

(a) (b) (c) (d) (e) (f)

Figure C.1: (a) Confidence index map of as-measured data; (b) Orientation map of as-measured data; (c) Confidence index map after CI standardization, maximum allowed misorientation of 5°; (d) Orientation map after grain dilation, maximum allowed misorientation of 5°; (e) Confidence index map after CI standardization, maximum allowed misorientation of 15°; (e) Orientation map after grain dilation, maximum allowed misorientation of 15°; In all the cleaned map the minimum number of data points considered as a grain is 4. In the orientation maps high angle grain boundaries are in black and low angle grain boundaries in white.

Appendix D

MATLAB® Scripts for OIM Data Analysis

```
% lets start in a fresh world: clear matrix, command window and figures
clear all
clc
clf
close all
% here I will read the 9 data which has been entered in the input file, the description is in input file:
Input_File_name='input.txt';
fid = fopen(Input_File_name);
Input_file_data=textscan(fid, '%s %s %s %f %f %f %f %f %f %f','delimiter','\n');
fclose(fid);
AsMeas_file_name=char(Input_file_data{1,1});
Cleaned_file_name=char(Input_file_data{1,2});
Cleaned_Data_File=char(Input_file_data{1,3});
CI_min=Input_file_data{1,4};
Map_Cut=Input_file_data{1,5};
Sub_Thick=Input_file_data{1,6};
New_Grains_check=Input_file_data{1,7};
Calc_Size=Input_file_data{1,8};
Num_line_intercept=Input_file_data{1,9};
% in order to avoid a messy working directory I make another directory to
% put the subsets and results in
directory_maker=['!mkdir ' Cleaned_Data_File '_folder'];
eval(directory_maker)
Main_Directory=cd;
Working_Directory=[Cleaned_Data_File '_folder'];
% I want to know the number of lines in the header
fid = fopen(AsMeas_file_name);
Header_line_number=0;
flag=0;
while flag==0
    LineCell=textscan(fid,'%s',1,'delimiter','\n');
    LineString=char(LineCell{1,1});
```

```
    if strncmp(LineString,'#',1)==1
        Header_line_number=Header_line_number+1;
    else
        flag=1;
    end
end
fclose(fid);
% Now I know the number of lines in header
% lets save the whole header in a string, first I need to read the header
% with text scan
fid = fopen(AsMeas_file_name);
LineCell=textscan(fid,'%s',Header_line_number,'delimiter','\n');
fclose(fid);
% now I save all the header in a file called Ang_Header.txt in the working
% directpry
cd(Working_Directory);
fid = fopen('Ang_Header.txt', 'wt');
for i=1:Header_line_number
    fprintf(fid,'%s\n' ,char(LineCell{1,1}{i,1}));
end
fclose(fid);
cd(Main_Directory);
% import all data of the ang files into the MTRX_data, and read thickness from coloumn ↩
    5 and CI from column 7 .
% here I readthe data from ang file.
% note the corrected files did not behave fine with importdata so I read it
% with textscan
fid = fopen(AsMeas_file_name);
Ang_as_MEas_Cell=textscan(fid, '%f %f %f %f %f %f %f %f %f %f','HeaderLines',↩
    Header_line_number);
fclose(fid);
MTRX_data= [Ang_as_MEas_Cell{1,1:10}];
All_Y_Map=MTRX_data(:,5);
All_CI_Map=MTRX_data(:,7);
lengthTH=size(All_Y_Map,1);
Step_Size_micron=MTRX_data(2,4)-MTRX_data(1,4);
X_size_map_micron=MTRX_data(size(MTRX_data,1),4);
Y_size_map_micron=MTRX_data(size(MTRX_data,1),5);
% I want to avarage all the CI values with same thickness. in TSL if there
% is no soulution then the CI will be -1. we don't want to put that into averaging.
% a defined number of counted points with the same thickness value and
% CIThickness is average of the CI and specific Thickness
CIThickness=0;
counter=0;
Map_Y_Num=0;
for i=1:(size(All_Y_Map,1)-1)
    if All_Y_Map(i)==All_Y_Map(i+1)
        if All_CI_Map(i)==-1
            All_CI_Map(i)=0;
        end
    CIThickness=CIThickness+All_CI_Map(i);
    counter=counter+1;
    else
        Map_Y_Num=Map_Y_Num+1;
        TH_CI(Map_Y_Num,1)=All_Y_Map(i);
```

```
        TH_CI(Map_Y_Num,2)=CIThickness/counter;
        counter=0;
        CIThickness=0;
    end
end
map_X_Num=counter;
% TH_CI is a matrix with a value for Y of the map and single CI average value for
% that Y.
% here I plot that matrix
figure;
axes('fontsize',15);
plot(TH_CI(:,2),TH_CI(:,1),'-k.');
ylabel('Distance from bottom of the map (m)', 'fontsize',15)
xlabel('Average CI value', 'fontsize',15)
hold on
% here I want to find the cutoff, basically that is the last Y of the map
% which its average CI value is below indicated minimum acceptable CI and
% the next thickness is higher than that.
flag=0;
nominate=0;
for i=2:Map_Y_Num/2
    if TH_CI(i,2)>CI_min && TH_CI(i-1,2)<CI_min
        if flag==0
            First_Thickness=TH_CI(i,1);
            flag=1;
        end
        nominate=TH_CI(i,1);
    end
end
% this just puts the line on the plot
% -------------------------
verticalline=[0 nominate ;0.6 nominate];
plot (verticalline(:,1),verticalline(:,2),'-k');
hold on;
note_on_plot=num2str(nominate);
text (0.63,nominate+0.1,note_on_plot,'FontSize',15);
% -------------------------
% similar as before, this time for the the other end of the map
nominate2=max(TH_CI(:,1));
for i=(int32(Map_Y_Num/2)):Map_Y_Num
    if TH_CI(i,2)<CI_min && TH_CI(i-1,2)>CI_min
        nominate2=TH_CI(i,1);
    end
end
% ---------------
 verticalline=[0 nominate2 ;0.6 nominate2];
 plot (verticalline(:,1),verticalline(:,2),'-k');
 hold on;
 note_on_plot=num2str(nominate2);
 text (0.63,nominate2+0.1,note_on_plot,'FontSize',15);
% ------------
% till now I figure out where the map starts and where it finishes, now I want to cut the map
% into smaller Subsets.provided that at the input file you have indicated
% that you want Subseting
```

```
% here if figure out where in the matrix the interface starts:start_cut and
% where it finishes:end_cut
    fid = fopen(Cleaned_file_name);
    Ang_cleaned_Cell=textscan(fid, '%f %f %f %f %f %f %f %f %f %f','HeaderLines',↩
        Header_line_number);
    fclose(fid);
    MTRX_data= [Ang_cleaned_Cell{1,1:10}];
    start_cut=0;
    for i=1:(size(All_Y_Map,1)-1)
        if double(MTRX_data(i,5))==nominate
            start_cut=i+1;
        end
        if double(MTRX_data(i,5))< (nominate+Sub_Thick)
            end_cut=i;
        end
    end
    Cut_length_Num=end_cut-start_cut+1;
 % so far I figure out what is the Cut_length_Num in the matrix
 % now I have to get x and Y from 0 to end of cut from the same dimention
 % of the  ang file
    Proper_X_Y=MTRX_data(1:Cut_length_Num,4:5);
    Num_Slice=ceil((nominate2-nominate)/Sub_Thick);
    Marrix_End_Num=size(MTRX_data,1);
 if Map_Cut==1
% it is written with try and catch which is not good and should be improved, ↩
    nevertheless it works
    for i=1:Num_Slice
        try
            Cut_start=start_cut+(double(i-1)*Cut_length_Num);
            Cut_end=start_cut+(double((i))*Cut_length_Num)-1;
            A=MTRX_data(Cut_start:Cut_end,1:10);
            A(1:Cut_length_Num,4:5)=Proper_X_Y;
        catch

            flag=0;
            while flag==0
                if MTRX_data(Cut_start,4)>Step_Size_micron
                    Cut_start=Cut_start+1;
                else
                    flag=1;
                end
            end
            A=MTRX_data(Cut_start:Marrix_End_Num,1:10);
        end
        cd(Working_Directory);
        dlmwrite(['SliceTemp_' num2str(i) '.txt'],A,'delimiter', '\t','newline', 'pc');
        % this is for combining the header and data
        text_ang=['!copy Ang_Header.txt+SliceTemp_' num2str(i) '.txt ' ↩
            Cleaned_file_name '_Slice_' num2str(i) '.ang'];
        % this is for deleting the remaining file
        text_clean= ['!del SliceTemp_' num2str(i) '.txt'];
        eval(text_ang)
        eval(text_clean);
        cd(Main_Directory);
```

```
    end
end
% lets delete the ang_header file
    cd(Working_Directory);
    eval('!del Ang_Header.txt')
    cd(Main_Directory);
% here I want to look into number of new grains in each subsets.
if New_Grains_check==1
    % now I have to find the number of header lines in the cleaned data
    % file
    fid = fopen(Cleaned_Data_File);
    Header_line_number_cleaned=0;
    flag=0;
    while flag==0
     LineCell=textscan(fid,'%s',1,'delimiter','\n');
     LineString=char(LineCell{1,1});
        if strncmp(LineString,'#',1)==1
            Header_line_number_cleaned=Header_line_number_cleaned+1;
        else
            flag=1;
        end
    end
    fclose(fid);
    %I will read the rest of grain data file into cells
    fid = fopen(Cleaned_Data_File);
    GrainID_MTRX=textscan(fid, '%s %f %f %f %f %f %f %f %f %f %s','HeaderLines',↩
        Header_line_number_cleaned);
    fclose(fid);
    % ok now it is the time to seprate the grain ID according to Subsets
    % which have been made
    Marrix_End_Num=size(GrainID_MTRX{1,9},1);
    Cut_start=0;
    Cut_end=0;
    for k=1:Num_Slice
            Cut_start=start_cut+(double(k-1)*Cut_length_Num);
            Cut_end=start_cut+(double((k))*Cut_length_Num)-1;
        if Cut_end<Marrix_End_Num
            GrainID_Sliced(:,k)=GrainID_MTRX{1,9}(Cut_start:Cut_end);
        else
            GrainID_Sliced(1:Marrix_End_Num-Cut_start,k)=GrainID_MTRX{1,9}(Cut_start:↩
                Marrix_End_Num-1);
        end
    end
    % so now I know grain ID but there are many times repeated so I want to
    % have one of each
    for i=1:Num_Slice
        MTRX_UNI=unique(GrainID_Sliced(:,i));
        Grain_ID_Single([1:size(MTRX_UNI,1)],i)=MTRX_UNI;
    end
    % lets compare and find comon grains between a layer and all
    % previous ones
    Compare_ref=Grain_ID_Single(:,1);
    Compare_ref=nonzeros(Compare_ref);
    New_grains(1,1)=size(nonzeros(Grain_ID_Single(:,1)),1);
    for i=1:Num_Slice-1
```

```
        Common_Grains=size(intersect(Compare_ref,nonzeros(Grain_ID_Single(:,i+1))),1);
        Slice_grain_number=size(nonzeros(Grain_ID_Single(:,i+1)),1);
        New_grains(i+1,1)=Slice_grain_number-Common_Grains;
        Compare_ref=union(Compare_ref,Grain_ID_Single(:,i+1));
        Compare_ref=nonzeros(Compare_ref);
    end
    counter=0;
    for i=1:size(Grain_ID_Single,2)
          counter=size((find(Grain_ID_Single(:,i))),1);
          Grain_Number(1,i)=counter;
    end
   % so far I found the number of new grains and garins in each slice but that has to
   % be converted into number of new grains per surface size

   % I want to do two different things first find number of new grains in
   % slected area, second: the portion of new grains to total number of grains

   % for relative number: new grains to total number of grains:
   New_Grain_Relative=New_grains./Grain_Number';

   % this scales the number of new grains over the area
   New_grains_scaled=New_grains/(X_size_map_micron*Sub_Thick);

   % the thickness of each subset is the same except the last one, here we fix
   % the last subset size
  New_grains_scaled((size(New_grains_scaled,1)),1)=New_grains_scaled((size(↩
      New_grains_scaled,1)),1)*Sub_Thick/(GrainID_MTRX{1,5}(Marrix_End_Num)-↩
      GrainID_MTRX{1,5}(Cut_start));
end

if Calc_Size==1
    Marrix_End=size(GrainID_MTRX{1,9},1);
    Cut_start=0;
    Cut_end=0;
    for k=1:Num_Slice
            Cut_start=start_cut+(double(k-1)*Cut_length_Num);
            Cut_end=start_cut+(double((k))*Cut_length_Num)-1;
        if Cut_end>Marrix_End
            Cut_length_Num=ceil(Cut_length_Num*(Marrix_End-Cut_start)/(Cut_end-↩
                Cut_start));
        end
        for i=1:Num_line_intercept
            line_coeff=i/(Num_line_intercept+1);
            line_of_interest=Cut_start+ceil(Cut_length_Num*line_coeff);
            line_grainsID=GrainID_MTRX{1,9}(line_of_interest:line_of_interest+map_X_Num↩
                );
            line_grainsID_uni=unique(line_grainsID);
            line_grainsID_num=size(line_grainsID_uni,1);
            Intercept_size(1,i)=(X_size_map_micron)/line_grainsID_num;
        end
        Intercept_size_Average(k,1)=(sum(Intercept_size))/Num_line_intercept;
    end

end
```

```
 % here I write a text file where all the results are
 % and it is easy to be loaded it to matlab or any where else

 %first I want to delete the file with exact name if it is exist.
 cd(Working_Directory);
 Result_File_name=[Cleaned_file_name '_Results.txt'];
 if exist(Result_File_name,'file')==2
     text_clean= ['!del ' Result_File_name];
     eval(text_clean);
 end
 cd(Main_Directory);
 % file deleted lets make the result
 % here is just making the result txt file
 Result_Start=nominate;
 for i=1:Num_Slice
     REsult_start=nominate+double(i-1)*Sub_Thick;
     REsult_End=nominate+double(i)*Sub_Thick;
     if nominate+double(i)*Sub_Thick>nominate2
         REsult_End=nominate2;
     end
     REsult_Mean=((REsult_start+REsult_End)/2)-nominate;
     REsult_TExt_start=num2str(REsult_start);
     REsult_TExt_End=num2str(REsult_End);
     REsult_TExt_Mean=num2str(REsult_Mean);
     Result_Text=[REsult_TExt_start blanks(9) REsult_TExt_End blanks(9) ↩
         REsult_TExt_Mean];
      if Calc_Size==1
         REsult_Intercept_size_Average=num2str(Intercept_size_Average(i,1));
     end
     if New_Grains_check==1
         REsult_TExt_New_grains=num2str(New_grains_scaled(i,1));
         New_Grain_Relative_TXT=num2str(New_Grain_Relative(i,1));
         Result_Text=[REsult_TExt_start blanks(9) REsult_TExt_End blanks(9) ↩
             REsult_TExt_Mean blanks(9) REsult_TExt_New_grains blanks(9) ↩
             New_Grain_Relative_TXT];
     end

     if Calc_Size==1
         Result_Text=[REsult_TExt_start blanks(9) REsult_TExt_End blanks(9) ↩
             REsult_TExt_Mean blanks(9) REsult_TExt_New_grains blanks(9) ↩
             New_Grain_Relative_TXT blanks(9) REsult_Intercept_size_Average];
     end
     cd(Working_Directory);
     Result_File_name=[Cleaned_file_name '_Results.txt'];
     fid=fopen(Result_File_name,'at');
     fprintf(fid,'%s\n' ,Result_Text);
     fclose(fid);
     cd(Main_Directory);
 end

%lets plot the results
  cd(Working_Directory);
  Results_MTRX = dlmread(Result_File_name, '');
  cd(Main_Directory);
```

```
    if New_Grains_check==1
    figure
        axes('fontsize',15);
        bar(Results_MTRX(1:Num_Slice-1,3),Results_MTRX(1:Num_Slice-1,4),1,'facecolor'↩
            ,[0.35,0.35,0.35])
        xlabel('Distance from practical interface ( m)', 'fontsize',15)
        ylabel('Number of new crystallites in submap (1/ m^2)', 'fontsize',15)

        figure
        axes('fontsize',15);
        bar(Results_MTRX(1:Num_Slice-1,3),Results_MTRX(1:Num_Slice-1,5),1,'facecolor'↩
            ,[0.35,0.35,0.35])
        xlabel('Distance from practical interface ( m)', 'fontsize',15)
        ylabel('Relative number of new crsytallites', 'fontsize',15)
    end

    if Calc_Size==1
         figure
         axes('fontsize',15);
         bar(Results_MTRX(1:Num_Slice-1,3),Results_MTRX(1:Num_Slice-1,6),1,'facecolor'↩
             ,[0.35,0.35,0.35])
         xlabel('Distance from practical interface ( m)', 'fontsize',15)
         ylabel('Average horizental intercept length ( m)', 'fontsize',15)
end
```

Appendix E

Ion Channeling Image, A Destructive Technique

Ion channeling imaging is a destructive technique and is associated with alteration of the microstructure. Figure E.1 shows two consecutive ion channeling images of the surface of an electrodeposited nickel film. Figure E.1b is the FIB image made right after the Figure E.1a. Comparison between Figure E.1a and E.1b clearly shows that some of the crystallites have sputtered more than their neighbors and a pronounced topography has formed after first channeling ion imaging. Sputtering rate of different crystallite orientations in respect to incoming ions is different and consequently ion channeling imaging of a smooth surface yields formation of topography. More than formation of surface topography due to channeling ion imaging, grain growth may occur as well. Figure E.2a shows the channeling ion image of an electrodeposited nickel film on top of an amorphous Ni-P layer. Fig.4b is made from the same sample but at higher magnification and dwell time for imaging. A comparison between Figure E.2a (ion density of imaging 6.59 C/m^2) and Figure E.2b (ion density of imaging 22.4 C/m^2) clearly indicates that the microstructure is heavily altered after imaging by 3.4 time higher ion density and finer grains (closer to Ni-P) are grown more than large grain. The darker grains in black and white image grow, thus, easy channeling directions grow at the expense of their neighbors. For the purpose of imaging, exposure to FIB must be kept as limited as possible to hinder microstructure alterations. Simulation of grain growth induced by ion irradiation in nano-crystalline nickel has shown that smaller grains grow more due to FIB induced grain growth [1]. This phenomenon, makes resolving the microstructure of nano-crystalline materials, possessing fine grains, more noteworthy where in one hand higher ion density improves ion channeling images quality and in the other hand increases the chance of microstructure alteration and grain growth. Thus, ion density has to be optimized to achieve high resolution images.

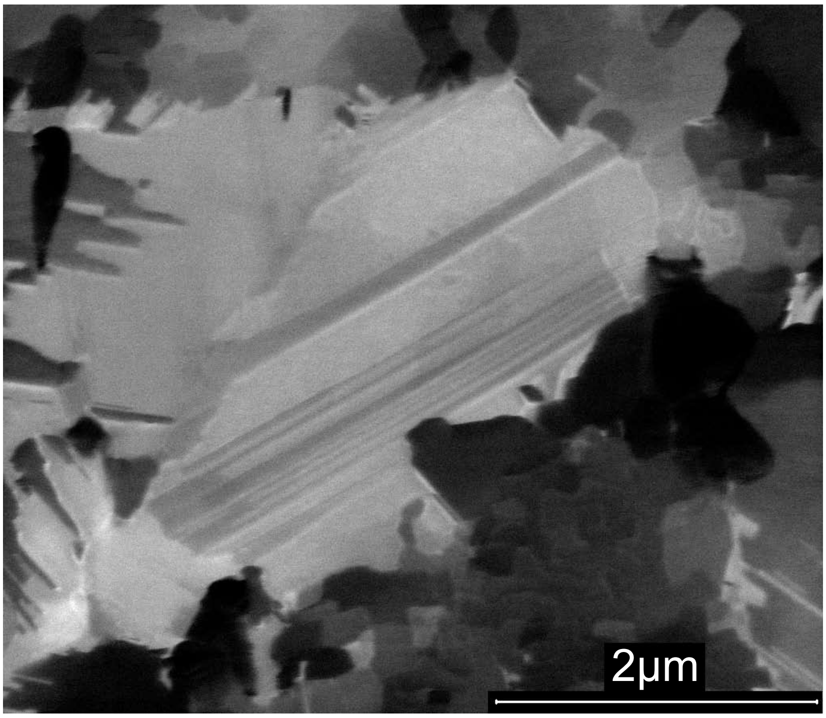

(a)

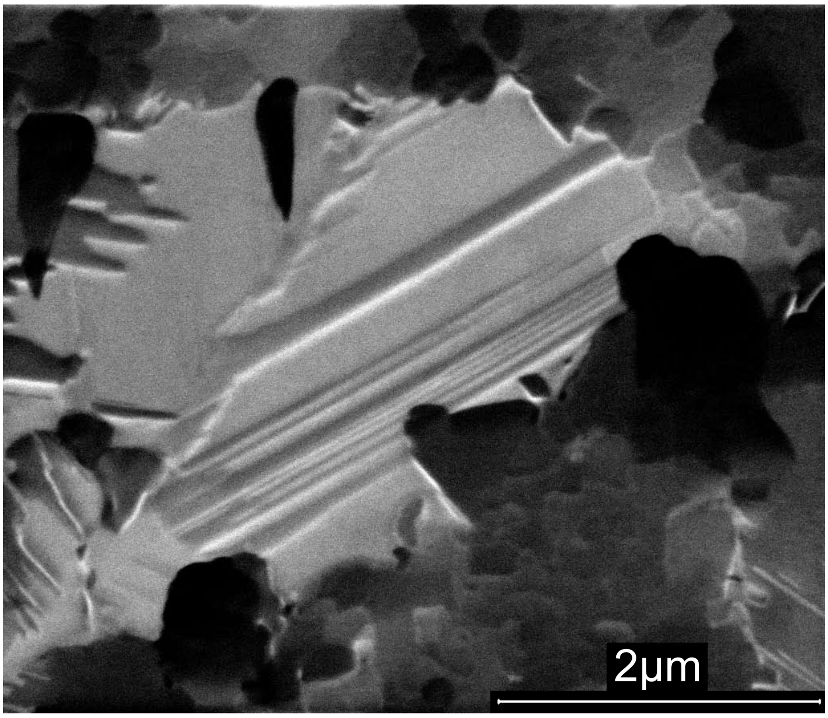

(b)

Figure E.1: Two consecutive channeling ion images, (a) 1st micrograph (b) the 2nd micrograph.

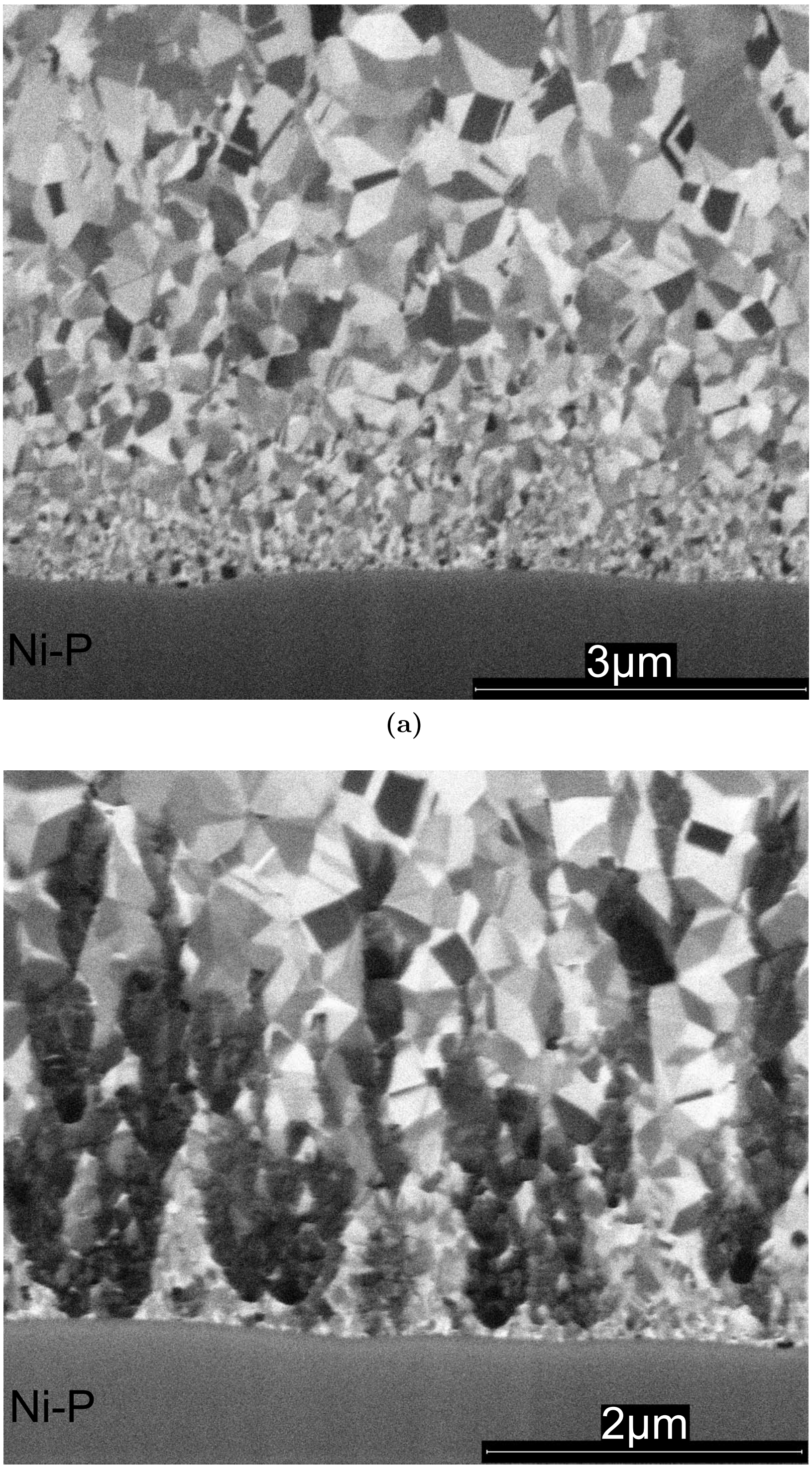

(a)

(b)

Figure E.2: channeling ion image of an electrodeposited nickel film. (a) micrograph is made by ion density of 6.59 C/m^2 and (b) ion density of 22.40 C/m^2. Note the growth of darker grains.

More than sputtering and grain growth which mentioned earlier, channeling contrast imagining is associated with gallium ion implantation which causes phase formation, introduction of micro strain, etc. [2]. All of these deter OIM measurement reliability, if supplementation of OIM and ion channeling imaging is intended. Accordingly for supplementing the two techniques it is wise strategy to conduct OIM measurements first and apply channeling ion imaging with optimized ion density afterwards.

References

[1] W. Voegeli, K. Albe, and H. Hahn, "Simulation of grain growth in nanocrystalline nickel induced by ion irradiation," Nuclear Inst. and Methods in Physics Research, 202, 230-235, 2003.

[2] D. Kiener, C. Motz, M. Rester, M. Jenko, and G. Dehm, "FIB damage of Cu and possible consequences for miniaturized mechanical tests," Materials Science & Engineering A, 459, 262-272, 2007.

Appendix F

High Resolution OIM

It is shown [1] that by lowering the accelerating voltage the physical resolution of OIM improves. This owes to the fact that electron/matter interaction volume decreases by lowering the accelerating voltage. A lower accelerating voltage also brings about a decrease in total number of backscattered electrons. In addition, the the energy of backscattered electrons decreases, hence, fewer electrons have sufficient energy to transmit through the thin Al coating of the EBSD detector [1]. As the number of electrons detected by the EBSD detector decreases the longer acquisition time per EBSP is required. It is reported [1] that lowering accelerating voltage from 15 to 7.5 requires a 15 fold increase acquisition time per ESBP.

Based on these pieces of information, high resolution OIM in SEM of nano-crystalline samples was attempted using accelerating voltage of 7.5 kV. In one hand, the best contrast between the Kikuchi bands and the background is a function of accelerating voltage [1] and in the other hand, highest intensity is not dependent on accelerating voltage. Thus by lowering the accelerating voltage, the working distance should be optimized. In the used microscope, working distance of 8 mm is optimum to achieve highest intensity and it is found that at accelerating voltage of 7.5 kV, the optimal working distance is 10 mm. Using these parameters, step size of 15 nm and the maximum rate of indexing was 16 EBPS per second was attempted. Figure F.1a shows the orientation map of a as-measured OIM data. Cleaning the map by CI standardization and limiting the minimum acceptable CI to 0.1, Figure F.1b, 47% of the map is indexed. It is noted that, larger grains in the microstructure are revealed and the excluded points (shown in white in Figure F.1b) belong to finer grains of microstructure.

Even though half of the map is indexed correctly, no meaningful assessment of the boundaries can be obtained. Furthermore the obtained data is biased by the size of the grains, i.e. most the acceptable data points on Figure F.1b belong to larger grains. These makes

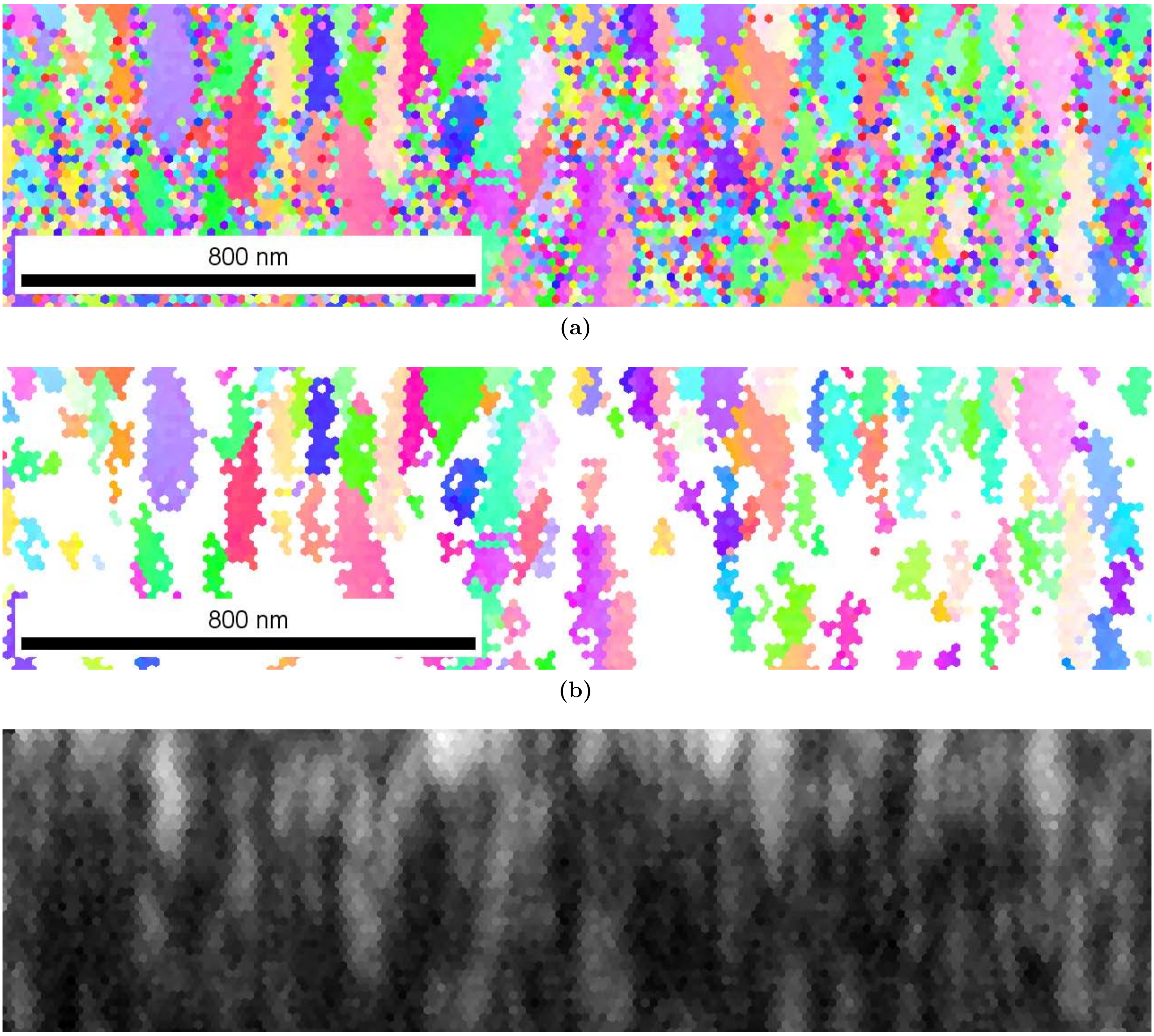

(a)

(b)

(c)

Figure F.1: (a) Orientation map of as-measured OIM data, without any cleaning (b) Orientation map after CI standardization and limiting the minimum acceptable CI to 0.1. (c) IQ map.

the results of little practical use, and resolving finer grains of microstructure is necessary is analysis of the grain boundaries is intended. Lowering the accelerating voltage and step size, as well as increase in acquisition time may help. But these cannot be applied readily. The IQ map shown in Figure F.1c, clarifies that at the top of the map, where the data acquisition has started, the EBSP quality is higher and as data acquisition progress, the quality of the EBSPs decreases. This is due to formation of amorphous carbon layer on the analyzing surface. It is noted that (i) high resolution microscopy requires decreasing the step size which results in denser data grid of the analyzed area. (ii) a low indexing rate the electron beam remains at a point for a long time. These two, bring about a thicker carbon contamination layer on the surface. As data acquisition progress the carbon layers thickens and the quality of the EBSP decreases. Lowering the accelerating voltage, and hence, increasing the acquisition time worsens carbon contamination effect.

References

[1] D. R. Steinmetz and S. Zaefferer, “Towards ultrahigh resolution EBSD by low accelerating voltage”, Materials Science and Technology, 26, 640645, 2010.

Appendix G

OIM/Ion Channeling Imaging; Supplementary Techniques

1. Introduction:

Controlled synthesis of materials such that microstructure possesses many twin lamellae in nano scale range (nano-twinned microstructure) improves mechanical properties like strength and ductility without deterioration of physical properties like conductivity and thermal stability [1]. Accordingly, characterization of nano-twined microstructures in terms of twin size, twin spacing, orientation relation, etc. is of high importance. Nano-twinned microstructure with very small twin spacing (few to a couple tens of nm) of low stacking fault materials, like copper and stainless steel, has been synthesized, and analyzed by TEM [1-3]. Nano-twins in materials with relatively higher stacking fault energy, e.g. nickel, have relatively larger size and spacing such that characterization by other techniques like ion channeling imaging and orientation image microscopy (OIM) in SEM becomes favorable. Both of these techniques have easier sample preparation and provide larger analysis area in comparison with TEM. OIM-in-SEM, equally known as electron backscattered diffraction (EBSD), is also advantageous technique to TEM in terms of ease in orientation relation analysis and boundary characterization. EBSD is a very powerful technique for microstructure characterization which is based on determination of crystallite orientation by analysis of Kikuchi bands in electron backscattered pattern (EBSP). Kikuchi bands form in a two step process: (i) incoherent scattering of the primary beam electrons (ii) elastic and coherent scattering of incoherently scattered electrons [4]. By detection and analysis of Kikuchi bands, orientation of diffracting crystallite can be determined and by scanning an area, the internal structure (grain size, grain orientation, grain boundary character, phase distribution, etc.) and microtexture can be obtained [5,6]. More than orientation, the perfection of crystal lattices in diffracting volume can be assessed by analysis of image quality (IQ), a parameter describing the quality of a diffraction pattern [7]. When diffracting volume contains two or more adjacent crystallites, the resulting EBSP is a superposition of the patterns associated with each of crystallites. Thus, IQ is lower at the vicinity of crystallites boundaries in comparison with interior of each crystallite [7].

The spacial resolution of EBSD technique has been continuously improved in the past years, and it is dependent on microscope, material, accelerating voltage, etc. [8-10]. The EBSD resolution is asymmetrical due to 70° tilt which is commonly applied for the data acquisition. Parallel to tilt axis resolution is the best and in direction perpendicular to tilt axis is the worst [11]. The effective resolution of EBSD for iron using 15 kV accelerating voltage was reported 30 nm and 90 nm in the mentioned directions, respectively [4]. Effective resolution of EBSD has been successfully improved by lowering accelerating voltage to 7.5kV [10], however that requires special sample preparation, extremely stable microscope, enhanced detectors, etc.

Focused ion beam (FIB) microscope has been extensively used in the semiconductor industry from the time it is commercialized (1980s) onward [12,13]. FIB has four main capabilities: milling, imaging, deposition and implantation [13]. Milling is based on elastic ion-atom collision where ions knock off the surface atoms. This capability has been used extensively in materials science for sample preparation and micro-machining. In contrast, imaging is based on inelastic ion-atom collision and it is not as widely used as milling. Inelastic collision causes emission of secondary electron (SE), secondary ions (SI), X-ray, etc [13]. By rastering focused ions beam on a material and detection of emitted SEs or SIs, FIB images are made [13]. Ion-induced SE emission is dependent on surface topography, chemical composition and orientation of crystallites [14]. A FIB-SE-image in which contrast is solely based on crystallite orientation, is known as ion channeling image and has been used for microstructural characterization [15,16]. Since ion-induced SE emission varies profoundly with orientation of crystallites, high contrast ion channeling images can be made [17,18]. When the direction of incident ions comes close to the direction of crystallographic dense planes (channeling direction), ions are deflected between rows of atoms, hence, follow an oscillatory trajectory along the channeling direction. This results in strong reduction of SE emission [19]. Thus, crystallites with their channeling direction parallel to the incident ion beam look relatively dark in ion channeling image. Similarly, less channeling directions looks relatively bright in ion channeling image [14]. The size and shape of the beam intensity profile on the sample, and sputtering rate of the sample determine the imaging resolution which in modern FIB systems is about 10 nm [14]. In addition to SE emission, sputtering, grain growth, martensitic transformation, etc. may occur due to ion channeling imaging [20-23].

In a dual beam (FIB/SEM) it is possible to combine the capabilities of both microscopes. Combination of OIM and serial sectioning by FIB milling, provides 3-dimentional characterization of microstructure (3D-EBSD) [24,25] which is an emerging technique [26]. However, except few cases [27,28], ion channeling imaging and EBSD have been rarely combined. Microstructural characterization by both techniques is even less utilized [16]. Since both ion channeling imaging and OIM are orientation dependent techniques, they can be used supplementarily. For nano-twins characterization, ion channeling imaging provides higher resolution images for quantitative analysis and OIM provides the orientation information. The aim of this appendix is to demonstrate the importance of applying ion channeling imaging and OIM analysis on exact same location for an extensive microstructural characterization of nano-twinned materials.

2. Experimental:

2.1 Materials and sample preparation:

Analyzed samples are electrodeposited nickel thin films possess nano-twins in their microstructure. For sample preparation, small pieces were cut out of synthesized material via abrasive cutting. Samples were subjected to cross-sectional preparation, by manual grinding on SiC paper up to grade 4000. Mechanical polishing was performed for several minutes on a soft synthetic fiber polishing cloth (NAP, Struers) with diamond paste of 1 μm. Final mechanical/chemical polishing conducted with 0.04 μm colloidal silica (OP-S, Struers) on a chemically resistant synthetic fiber polishing cloth (OP-Chem, Struers) to achieve a scratch free surface. Then, samples ultra sonically cleaned with ethanol and dried. Further preparation is conducted in dual beam FIB-SEM, Helios Nanolab™ 600 from FEI, by removal of ≈750 nm of the mechanically prepared cross-section via FIB milling. Ga^+ ions of energy of 30 keV were used for milling in a two step process as follows. First ≈700 nm is removed by current of 2.8 nA (rough milling); secondly ≈50 nm is removed by current of 0.46 nA. Smooth and artifact free surface is prepared in this manner.

To study the surface of a thin films, mechanical grinding and polishing was not applied; and only FIB milling is conducted in the same two step process explained, such to remove all the existing topography on the surface.

2.2 Orientation image microscopy:

OIM measurements were carried out in the mentioned microscope, equipped with an EBSD system from EDAX-TSL and Hikari camera. EBSD measurements were performed by electron probe current of 5.5 nA, acceleration voltage of 12 kV and step size of 20, 25 or 30 nm. OIM 5™ software was used for quantification and analysis of the EBSD results. Final represented EBSD maps were cleaned by routines available in OIM 5™ software as follows. First: confidence index (CI) of every point in the map within a recognized grain is assigned to the highest confidence index CI value found in that grain (a grain was defined as a region consisting of at least four connected points with misorientations of less than 5° and CI above 0.1). Second: orientation of a point which does not belong to any grains is changed to the orientation of majority of neighboring points belonging to a same grain. To characterize boundaries of microstructure, four parameters are calculated using OIM 5™ software: (1) Average intercept length is obtained by passing 5 lines vertically in orientation map, and averaging the intercept length; intercept is where point to point misorientation is larger than 15°. (2) Fraction of low angle grain boundaries (point to point misorientation 2-15°). (3) Fraction of high angle grain boundaries (point to point misorientation above 15°), and (4) Fraction of $\Sigma 3$ boundaries (point to point misorientation 60°/<111>).

2.3 Ion channeling imaging:

Microstructural characterization by ion channeling imaging is applied in the same microscope mentioned earlier. High resolution images were made with Ga^+ ions of energy of 30 keV at ion density of 7.17, 3.38 and 1.08 C/m^2. Ion density is calculated by the following formula:

$$\text{Ion density} = \frac{I \times t}{A}$$

Where I is beam current in amps; t, the time for scanning whole area of interest in seconds; A, the size of area of interest in m^2.

In order to calculate twin lamella width, the number of pixels in vertical direction of image counted and then converted to length in terms of nm. Then according to twin boundary angle in respect with vertical direction of image, twin lamella width in direction perpendicular to twin boundary in the image is calculated. In order to avoid alteration of microstructure, EBSD measurement always conducted first and then ion channeling imaging is applied.

2.4 EBSD map correction:

Orientation map was compared with ion channeling image to find out whether all fine twin lamellae present in the latter are indexed correctly in the former or not. In case of a non-indexed twin lamella, its position was located on IQ map in OIM 5™ software. Then orientation of the points forming non-indexed twin lamella was changed to a new orientation, using a home written MATLAB® scripts (the scripts are provided in Appendix H). Thus, a new EBSD data file is made which twin lamella was present. Two different methods were applied for obtaining the new orientation. Method (i): An arbitrary orientation is assigned with two conditions for misorientation to neighboring grain: (a) exceeds 15° and (b) does not satisfy 60°/<111>. Method (ii) In case, some data points on the as-measured map were indexed correctly, then the average orientation of correctly indexed points is used as the orientation of wrongly indexed points. In case no single correct orientation was existed, the average orientation of nearest similarly oriented crystallite in the map is chosen as orientation of wrongly indexed points.

3. Results:

3.1. Nano-twins characterization:

Figure G.1a shows orientation map, IPF color coded in respect with film growth direction. At the top of the orientation map a relatively thick twin lamella is revealed. Observing IQ map, presence of fine twin lamellae in the microstructure approximately parallel to the resolved twin is evident, Figure G.1b. Number of twin lamellae is counted 15 in IQ map. Size estimation in terms of twin lamella width is inapplicable from IQ map data. Ion channeling imaging of the same location, Figure G.1c, provides similar microstructure characteristics to IQ map. However, the contrast and resolution in the former is higher than that in the latter.

The average twin lamella width in vertical direction of the ion channeling image is 38±17 nm. Consequently, the average twin lamella width in direction perpendicular to the twin boundaries in ion channeling image, is 27±12 nm (minimum 18 nm). In addition, better estimation of number of twin lamellae is obtained in comparison with IQ map. Ion channeling image makes clear that some twin lamellae recognized as single one in IQ map, are actually two very closely positioned twin lamellae. Thus, number of twin lamellae in ion channeling image is 18, and twin lamella density is 5.13/μm in direction perpendicular to twin boundaries.

3.2. EBSD data correction:

Figure G.2a shows orientation map, color coded in respect with film growth direction; $\Sigma 3$ boundaries are shown by black lines. It is evident that there is a pattern in orientation relation between neighboring crystallites. Crystallites mark by ‘A’,‘C’ , and ‘E’ have similar orientation; likewise crystallites ‘B’,‘D’, and ‘F’. Based on the orientation map shown in Figure G.2a, average intercept length, fraction of low and high angle grain boundaries and $\Sigma 3$ boundaries fraction are obtained and listed in Table G.1. IQ map and

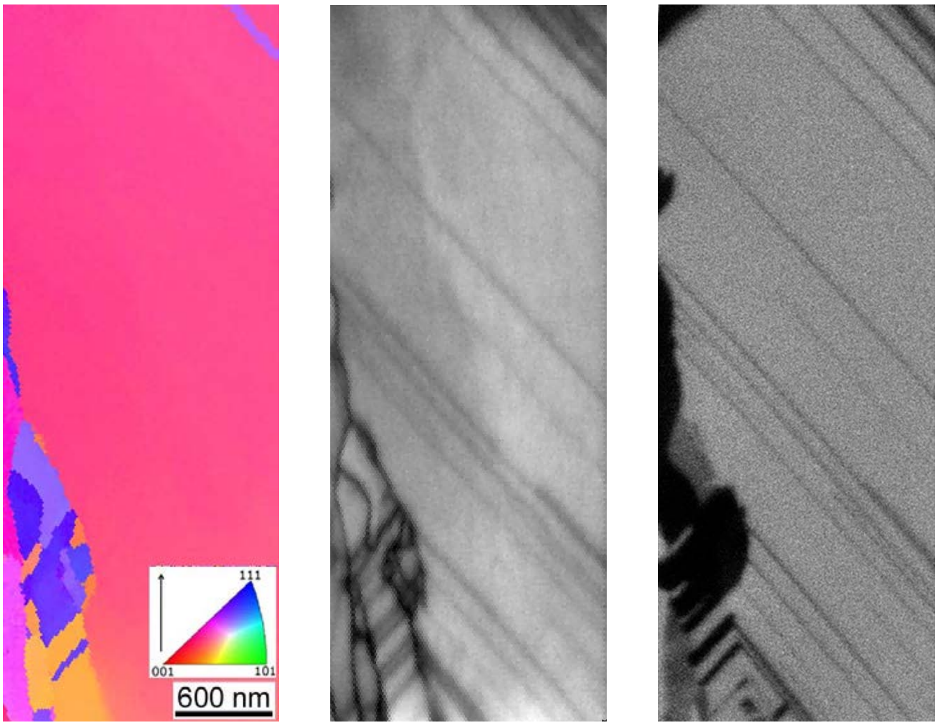

(a) (b) (c)

Figure G.1: Cross section of one and the same location in a nano-twinned microstructure investigated with different methods: (a) Orientation map color coded in relation with film growth direction shown by an arrow; (b) EBSD IQ map; (c) ion channeling image; Step size of EBSD measurement is 20 nm and the ion density applied or ion channeling image is 7.17 C/m^2.

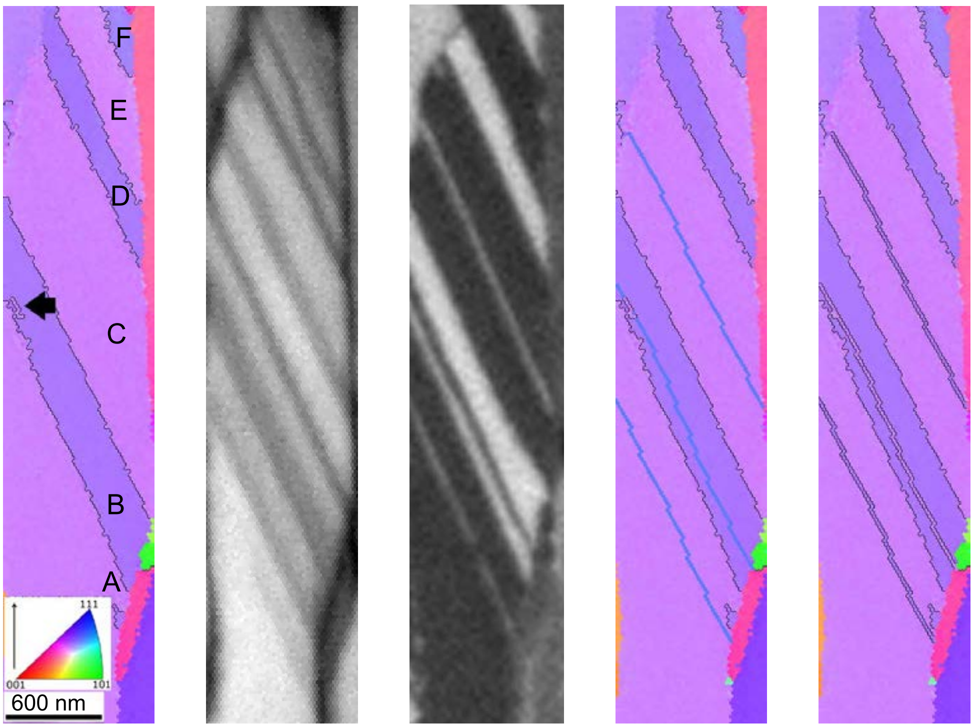

(a) (b) (c) (d) (e)

Figure G.2: Cross section of one and the same location in a nano-twinned microstructure investigated with different methods: (a) Orientation map color coded in relation with film growth direction shown by an arrow, $\Sigma 3$ boundaries are shown by black lines; (b) EBSD IQ map; (c) ion channeling image; (d) same as (a) after correction using method (i); (e) same as (a) after correction using method (ii). Step size of EBSD measurement is 25 nm and the ion density applied or ion channeling image is 3.38 C/m2.

ion channeling image of the same location, Figure G.2b and G.2c reveal the same pattern; visible as dark and bright contrast in channeling ion image. IQ map and more clearly high contrast ion channeling image, reveal presence of three nano-twins which are not indexed correctly in orientation map (Figure G.2a). By correcting the map such to reflect presence of these nano-twins more accurate results can be achieved. Using method (i) of correction, EBSD data was corrected, shown in Figure G.2d and boundary characterizing parameters calculated accordingly, Table G.1. Using method (ii) of correction, the average orientation of 5 correctly indexed data points, to the left of arrow in Figure G.2a, is assigned to the rest of wrongly indexed points. Due to the existing pattern of crystallite orientation and similarity of gray value in channeling ion image, it is assumed that the orientation of the nano-twin within crystallite 'A' is similar to average orientation of crystallite 'B'. Likewise, orientation of nano-twin within crystallite 'C' assumed as similar to average orientation of crystallite 'B'. Corrected orientation map is shown in Figure G.2e and boundary characterizing parameters are tabulated in Table G.1. Generally, by applying map correction average intercept length decreases and fraction of high angle grain boundaries increases, Table G.1. There is no difference in results listed in Table G.1 between correction methods (i) and (ii) other than fraction of Σ3 boundaries.

Table G.1: Quantitative result for analysis of size (Average intercept length) and the boundaries for different maps shown in Figure G.2. 'Non-corrected data', 'Corrected by method (i)' and 'Corrected by method (ii)' respectively correspond to Figures G.2a, G.2d, and G.2e.

	Average intercept length (nm)	High angle boundary length fraction (%)	Low angle boundary length fraction (%)	Σ3 boundary fraction (%)
Non-corrected data	335	81.7	18.3	52.2
Corrected by method (i)	198	88.9	11.1	32.7
Corrected by method (ii)	198	88.9	11.1	70.1

3.3. Ion channeling imaging, boundary determination:

Figure G.3a shows orientation map, IPF color coded in respect with film growth direction; High angle grain boundaries are shown in orientation map by gray lines. Evidently it is easy to distinguish between neighboring grains. However it is extremely hard to distinguish between the same neighboring grains in ion channeling image, Figure G.3b. The grain marked as 'G' in orientation map, Figure G.3a, is totally invisible in ion channeling image, Figure G.3b. Apparently, ion channeling image may not provide the contrast needed to distinguish between two crystallites with totally different orientations.

Figure G.4a shows ion channeling image in which regions marked as 'A', 'B' and 'C' have

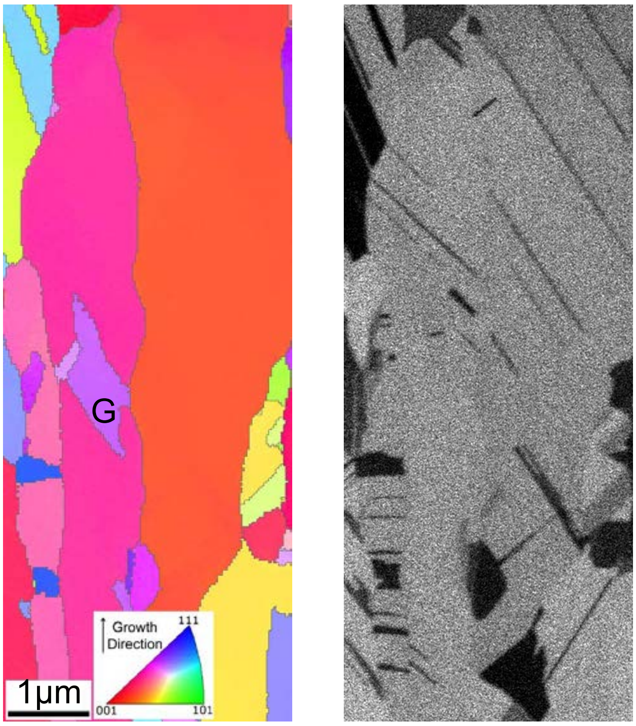

(a) **(b)**

Figure G.3: Cross section of a same location in a nano-twinned microstructure investigated with different methods: (a) Orientation map color coded in relation with film growth direction shown by an arrow; high angle boundaries are shown by gray lines; (b) ion channeling image. Step size of EBSD measurement is 30 nm and the ion density applied or ion channeling image is 1.08 C/m^2.

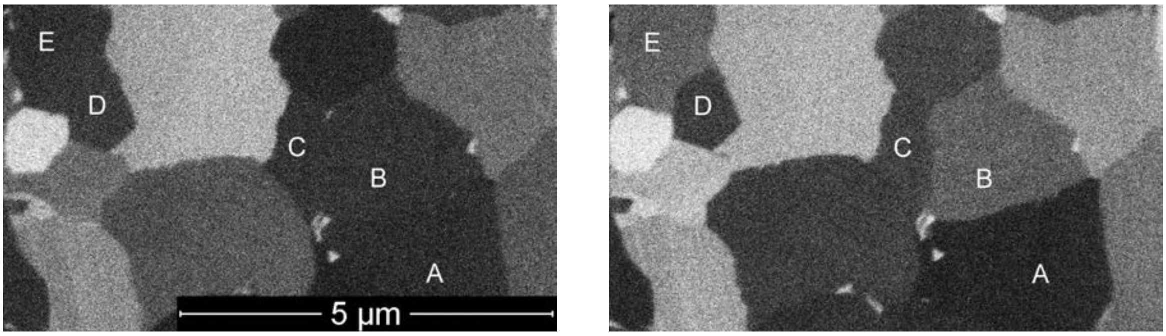

(a) **(b)**

Figure G.4: (a) Ion channeling image of surface of an electrodeposited thin film; (b) ion channeling image of the same location as (b) but made after 2° tilt.

very similar gray value, presumably belong to a single grain; regions marked as 'D' and 'E' look alike in black and white image too. Ion channeling image obtained at very same location but with 2° tilt in respect to Figure G.4a, clearly shows that each region is actually a single grains, Figure G.4b. Thus, an ion channeling image on its own can be misleading for microstructural characterization and making different images by changing tilting angle may provide better information.

4. Discussion:

As shown in Figure G.1 resolving nano-twins of nickel, ≈ 27 nm, in terms of orientation cannot be easily achieved. As mentioned earlier, EBSD resolution parallel to tilt axis is the best [11]. That means, mounting the sample such to have the finest crystallite dimension in the maximum resolution direction, provides highest resolution possible. In practice the direction of nano-twins is not known, hence, to achieve highest resolution possible, at least two consecutive measurements must be applied, which is cumbersome and yet fully resolving finest nano-twins, 18 nm in width, cannot be taken as granted. As shown in Figure G.1 and G.2, IQ map provides rough estimation about twin lamella number and spacing, which cannot be achieved in the orientation map. However, since there is no sharp contrast change in IQ map, it is essentially vague in terms of twin lamella width. More important than that, closely positioned twin lamellae cannot be distinguished independent of step size. IQ map provides only an indication of presence of different crystallites in diffraction volume, but not the number of those. Ion channeling imaging is a fast technique which strongly clarifies presence of twin lamellae and provides an estimation of their width. Twin lamella width can be estimated in direction perpendicular to twin boundaries in the channeling ion image. However, the actual twin width must be calculated in direction perpendicular to twin boundary plane. As shown schematically in Figure G.5, AB is perpendicular to twin boundary however, since AB is not perpendicular to twin boundary plane, the width in AB direction is overestimated. Based on ion channeling image alone the crystallographic directions are not known thus actual twin lamella width cannot be calculated. However, when it is combined with EBSD, it is possible to achieve this. For instance, the twin lamella at the top Figure G.1 is (10 8 19) oriented and that of adjacent points on the other side of the boundary is $(2\ \overline{13}\ \overline{3})$. Nickel has FCC crystal, and most probably twin boundary plane is of $\{111\}$ family type [29]. For (10 8 19) and $(2\ \overline{13}\ \overline{3})$ pair, twin boundary plane is $(1\overline{1}1)$ or $(\overline{1}1\overline{1})$ [30]. Thus, the calculated twin lamella width in vertical direction of channeling ion image (38 nm in [10 8 19] crystallographic direction) can be converted to twin width in $[1\overline{1}1]$ direction. From simple geometry it follows that average actual twin width is 20 nm. This clearly shows how OIM and ion channeling imaging supplement each other mutually for better microstructural characterization.

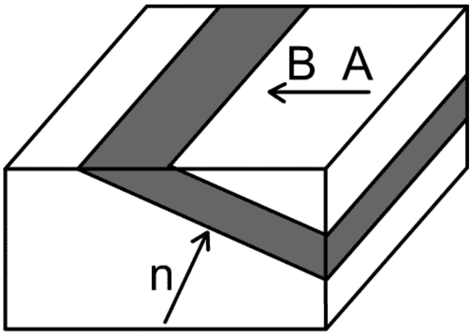

Figure G.5: Schematic representation of twin lamella width overestimation in AB direction. AB is perpendicular to twin boundary but it is not perpendicular to twin boundary plane (n is plane normal).

It is shown that, nano-twines can be characterized in terms of number, density, and width. If more detailed information is needed about boundaries in the microstructure e.g. boundary fraction, length intercept, etc. it is fairly easy to obtain those from EBSD data (commercially available softwares do these routinely). Presence of nano-twins in microstructure which are not resolved in orientation map brings about inaccurate boundary characterization, see Table G.1. Even though EBSD is the most established technique for orientation relations analysis, for nano-crystalline materials (grain size below 100 nm) where EBSD resolution is inadequate, orientation mapping in TEM has been applied in recent years [31,32]. However, supplementing ion channeling imaging wrongly indexed EBSD data points in nano-twinned microstructures can be recognized, and map correction can be applied. In general, one must be very critical about assigning new orientation to EBSD data, where correct orientation is not measured. Method (i) of correction is a conservative method with two condition: misorientation to neighboring grain: (a) exceeds 15° and (b) does not satisfy 60°/<111>. The second condition is just to differentiate between method (i) and (ii). The first condition is rely on the fact that twin boundaries in ion channeling image are sharply straight and that cannot be a low angle grain boundary in electrodeposited materials to the best of author knowledge. This correction brings about better accordance between orientation map and ion channeling image. Thus, boundaries can be characterized more accurately, in terms of average intercept length, high angle and low angle boundary fraction. The weakness of this method is that fraction of $\Sigma3$ boundaries is underestimated. Since, importance of fraction of low Σ boundaries on the material properties cannot be neglected [33,34] and nano-twinned microstructures has high fraction of low Σ boundaries, it is favorable to estimate $\Sigma3$ fraction as close to its actual value as possible. To achieve this, one must rely on some assumptions in order to estimate the average orientation of wrongly indexed data points. In case of sample with repeated twins, the pattern of orientation repetition, strongly hints to the orientation of the non-resolved twins, and applying method (ii) of correction is fairly safe. Thus, $\Sigma3$ boundaries fraction after correction method (ii), 1.3 fold increase, is a better estimation. Since the orientation of twin is not known, it is better to use the obtained $\Sigma3$ boundary fraction from the corrected data, as upper limit of $\Sigma3$ boundary fraction.

One must remember that, if map correction is applied incautiously base on weak assumptions, it deteriorate authenticity and accuracy of the results.

Ion channeling imaging has a great potential for fast high resolution imaging but there are some limitations too. SE emission coefficient of two neighboring grains with totally different crystallographic orientations may be similar, hence, indivisible in black and white image [18]. This occasionally inhibits proper microstructure characterization, see Figure G.4. Easy channeling directions look dark in ion channeling images [18]. By tilting, crystallites may come close or go away from easy channeling direction in respect with incident ion beam and become brighter or darker, respectively [20]. As shown in Figure G.4, 2° tilting may change the contrast drastically. This can be utilized for better characterization of microstructure and better supplementation of EBSD results. However, one should keep in mind that ion channeling imaging is a destructive technique and repeated imaging is associated with alteration of the microstructure. Sputtering rate of different crystallite orientations in respect to incoming ions is different [28] and consequently ion channeling imaging of a smooth surface yields formation of topography. More than that, due to channeling ion imaging, grain growth may occur. Easy channeling directions grow at the expense of their neighbors. FIB induced grain growth has been proposed as a tool for deliberate microstructure manipulation [23,35,36]. However, for the purpose of imaging, exposure to FIB must be kept as limited as possible to hinder microstructure alterations. Simulation of grain growth induced by ion irradiation in nano-crystalline nickel has shown that smaller grains grow more due to FIB induced grain growth [22]. This phenomenon, makes resolving the microstructure of nano-crystalline materials, possessing fine grains, more noteworthy where in one hand higher ion density improves ion channeling images quality and in the other hand increases the chance of microstructure alteration and grain growth. Thus, ion density has to be optimized to achieve high resolution images.

It is very well established that 3-dimensional analysis of microstructure provides valuable information about real grain size, grain shape, etc. This has been achieved by combination of FIB milling and FIB imaging capabilities (3D-FIB tomography) [37]. 3D-EBSD is superior to 3D-FIB tomography, since it provides additional information like orientation variation in depth, grain boundary character, etc. [24,38]. As argued, supplementing ion channeling imaging to 2D-EBSD provides better microstructural analysis. This can be extended to the 3rd dimension effectively, since both techniques have been used in practice for 3D characterization. The sequence of FIB milling, 2D-EBSD and ion channeling imaging in principle provides better internal characterization than 3D-EBSD.

5. Conclusions:

- Nickel nano-twins of ≈27 nm are challenging to be fully resolved orientation-wise using OIM in SEM.
- Image quality data provides semi-quantitative data on number of nano-twins, but the IQ maps cannot to be used for quantifying the width of nano-twins.
- Ion channeling image resolution is higher than OIM in SEM which makes quantification of the width of nano-twins of ≈27 nm possible.
- Supplementing the OIM data and ion channeling image, the twin width in normal direction to the twin boundary plane can be obtained.
- The non-resolved nano-twins in orientation map can be located based on ion channeling image; then using some correction methods the quantification accuracy of the boundary related parameters can be improved.
- Ion channeling image on its own can be misleading method for quantification of boundary related parameters and it is best to be supplemented with OIM in SEM.

References

[1] L. Lu, Y. Shen, X. Chen, L. Qian, and K. Lu, “Ultrahigh Strength and High Electrical Conductivity in Copper” Science, vol. 304, No. 5669, 422-426, 2004.

[2] X. Zhang et al., “Enhanced hardening in Cu/330 stainless steel multilayers by nanoscale twinning” Acta Materialia, vol. 52, No. 4, 995-1002, 2004.

[3] O. Anderoglu, A. Misra, H. Wang, and X. Zhang, “Thermal stability of sputtered Cu films with nanoscale growth twins” Journal of Applied Physics, vol. 103, No. 9, 094322-6, 2008.

[4] S. Zaefferer, “On the formation mechanisms, spatial resolution and intensity of backscatter Kikuchi patterns” Ultramicroscopy, vol. 107, No. 2-3, 254-266, 2007.

[5] A. J. Schwartz, M. Kumar, B. L. Adams, and D. P. Field, Electron Backscatter Diffraction in Materials Science, 2nd ed. Springer, 2009.

[6] V. Randle and O. Engler, Introduction to texture analysis: macrotexture, microtexture and orientation mapping. CRC Press, 2000.

[7] S. I. Wright and M. M. Nowell, "EBSD Image Quality Mapping" Microscopy and Microanalysis, vol. 12, No. 1, 72-84, 2005.

[8] F. J. Humphreys, "Grain and subgrain characterisation by electron backscatter diffraction" Journal of Materials Science, vol. 36, No. 16, 3833-3854, 2001.

[9] F. J. Humphreys, "Characterisation of fine-scale microstructures by electron backscatter diffraction (EBSD)" Scripta materialia, vol. 51, No. 8, 771-776, 2004.

[10] D. R. Steinmetz and S. Zaefferer, "Towards ultrahigh resolution EBSD by low accelerating voltage" Materials Science and Technology, vol. 26, No. 6, 640645, 2010.

[11] T. C. Isabell and V. P. Dravid, "Resolution and sensitivity of electron backscattered diffraction in a cold field emission gun SEM" Ultramicroscopy, vol. 67, No. 1-4, 59-68, 1997.

[12] D. Kiener, C. Motz, M. Rester, M. Jenko, and G. Dehm, "FIB damage of Cu and possible consequences for miniaturized mechanical tests" Materials Science & Engineering A, vol. 459, No. 1-2, 262-272, 2007.

[13] N. Yao, Focused Ion Beam Systems: Basics and Applications, Reissue. Cambridge University Press, 2011.

[14] C. A. Volkert and A. M. Minor, "Focused Ion Beam Microscopy and Micromachining" MRS bulletin, vol. 32, 2007.

[15] R. E. Franklin, E. C. G. Kirk, J. R. A. Cleaver, and H. Ahmed, "Channelling ion image contrast and sputtering in gold specimens observed in a high-resolution scanning ion microscope" Journal of Materials Science Letters, vol. 7, No. 1, 39-41, 1988.

[16] A. Bastos, S. Zaefferer, D. Raabe, and C. Schuh, "Characterization of the microstructure and texture of nanostructured electrodeposited NiCo using electron backscatter diffraction (EBSD)" Acta Materialia, vol. 54, No. 9, 2451-2462, 2006.

[17] J. Gupta, J. M. E. Harper, J. L. Mauer IV, P. G. Blauner, and D. A. Smith, "Focused ion beam imaging of grain growth in copper thin films" Applied Physics Letters, vol. 61, No. 6, 663-665, 1992.

[18] Y. Yahiro, K. Kaneko, T. Fujita, W.-J. Moon, and Z. Horita, "Crystallographic orientation contrast associated with Ga^+ ion channelling for Fe and Cu in focused ion beam method" J Electron Microsc (Tokyo), vol. 53, No. 5, 571-576, 2004.

[19] K. Wang, P. Garoche, and L. Dumoulin, "Focused ion beam imaging of grains in Al-Li-Cu quasicrystal" Journal of Physics: Condensed Matter, vol. 10, p. 3479-3488, 1998.

[20] L. A. Giannuzzi and F. A. Stevie, Introduction to focused ion beams: instrumentation, theory, techniques and practice. Springer, 2005.

[21] N. Mateescu, M. Ferry, W. Xu, and J. M. Cairney, "Some factors affecting EBSD pattern quality of Ga^+ ion-milled face centred cubic metal surfaces" Materials Chemistry

and Physics, vol. 106, No. 1, 142-148, 2007.

[22] W. Voegeli, K. Albe, and H. Hahn, “Simulation of grain growth in nanocrystalline nickel induced by ion irradiation” Nuclear Inst. and Methods in Physics Research, B, vol. 202, 230-235, 2003.

[23] S. Olliges, P. Gruber, A. Bardill, D. Ehrler, H. D. Carstanjen, and R. Spolenak, “Converting polycrystals into single crystals - Selective grain growth by high-energy ion bombardment” Acta Materialia, vol. 54, No. 20, 5393-5399, 2006.

[24] S. Zaefferer, S. I. Wright, and D. Raabe, “Three-Dimensional Orientation Microscopy in a Focused Ion BeamScanning Electron Microscope: A New Dimension of Microstructure Characterization” Metallurgical and Materials Transactions A, vol. 39, No. 2, 374-389, 2008.

[25] A. Bastos, S. Zaefferer, and D. Raabe, “Three-dimensional EBSD study on the relationship between triple junctions and columnar grains in electrodeposited Co-Ni films” Journal of Microscopy, vol. 230, No. 3, 487-498, 2008.

[26] V. Randle, “Applications of electron backscatter diffraction to materials science: status in 2009” Journal of Materials Science, vol. 44, No. 16, 4211-4218, 2009.

[27] D. L. Barr and W. L. Brown, “Contrast formation in focused ion beam images of polycrystalline aluminum” Journal of Vacuum Science & Technology B: Microelectronics and Nanometer Structures, vol. 13, 2580-2583, 1995.

[28] U. Wendt and G. Nolze, “Correlation between crystal orientation, channeling contrast and topography during FIB milling of Cu studied by FIB, EBSD, SEM, and AFM” Praktische Metallographie, vol. 44, No. 5, 236-238, 2007.

[29] D. G. Brandon, B. Ralph, S. Ranganathan, and M. S. Wald, “A field ion microscope study of atomic configuration at grain boundaries” Acta Metallurgica, vol. 12, No. 7, 813-821, 1964.

[30] F. Wilhelm, “The orientation of high-order growth twins in diamond-type crystals” Journal of Applied Crystallography, vol. 4, No. 6, 521-523, 1971.

[31] J. J. Fundenberger, A. Morawiec, E. Bouzy, and J. S. Lecomte, “Polycrystal orientation maps from TEM” Ultramicroscopy, vol. 96, No. 2, 127-137, 2003.

[32] A. Darbal et al., “Orientation Imaging of Nanocrystalline Platinum Films in the TEM” Microscopy and Microanalysis, vol. 15, No. 2, 1232-1233, 2009.

[33] P. Lin, G. Palumbo, U. Erb, and K. T. Aust, “Influence of grain boundary character distribution on sensitization and intergranular corrosion of alloy 600” Scripta Materialia, vol. 33, No. 9, 1387-1392, 1995.

[34] G. Palumbo, E. Lehockey, and P. Lin, “Applications for grain boundary engineered materials” JOM Journal of the Minerals, Metals and Materials Society, vol. 50, No. 2,

40-43, Feb. 1998.

[35] R. Spolenak, L. Sauter, and C. Eberl, “Reversible orientation-biased grain growth in thin metal films induced by a focused ion beam” Scripta Materialia, vol. 53, No. 11, 1291-1296, 2005.

[36] C. M. Park and J. A. Bain, “Focused-ion-beam induced grain growth in magnetic materials for recording heads” Journal of Applied Physics, vol. 91, 6830-6832, 2002.

[37] B. Inkson, “3D determination of grain shape in a FeAl-based nanocomposite by 3D FIB tomography” Scripta Materialia, vol. 45, No. 7, 753-758, 2001.

[38] S. J. Dillon and G. S. Rohrer, “Characterization of the Grain-Boundary Character and Energy Distributions of Yttria Using Automated Serial Sectioning and EBSD in the FIB” Journal of the American Ceramic Society, vol. 92, No. 7, 1580-1585, 2009.

Appendix H

MATLAB® Scripts for OIM Map Correction

```
% correct the the EBSD maps
% the idea is to have as-measured ang file which should be corrected

% what is needed? set(s)of selected points in text files to get the x,y of
% and orientation to assign that with.

%  lets start in a fresh world: clear matrix, command window and figures
clear all
clc
clf
close all

% here I will read the data which has been entered in the input file, the description ↩
    is in description file:
Input_File_name='input.txt';
fid = fopen(Input_File_name);
Input_file_data=textscan(fid, '%s %f %f %f %f','delimiter',' ');
fclose(fid);

AsMeas_file_name=char(Input_file_data{1,1}(1))
Num_Correct_File=Input_file_data{1,2}(1);
selected_points_files=Input_file_data{1,1}(2:end)
CI_Correction_Flag=Input_file_data{1,3}(1);
orientation_matrix=[Input_file_data{1,2}(2:end) Input_file_data{1,3}(2:end) ↩
    Input_file_data{1,4}(2:end)];
% lets convert degrees to radian
orientation_radian=(pi/180).*orientation_matrix;
correction_matrix=[orientation_radian Input_file_data{1,5}(2:end)];

first_run_flag=1;
for k=1:Num_Correct_File
    if first_run_flag==1
        % I want to know the number of lines in the header of ang file
```

```
        fid = fopen(AsMeas_file_name)
        Ang_Header_line_number=0;
        flag=0;
        while flag==0
        LineCell=textscan(fid,'%s',1,'delimiter','\n');
        LineString=char(LineCell{1,1});
            if strncmp(LineString,'#',1)==1
                Ang_Header_line_number=Ang_Header_line_number+1;
            else
            flag=1;
            end
        end
        fclose(fid);

        % Now I know the number of lines in header
        % lets save the whole header in a string, first I need to read the header
        % with text scan
        fid = fopen(AsMeas_file_name);

        LineCell=textscan(fid,'%s',Ang_Header_line_number,'delimiter','\n');
        fclose(fid);

        % lets start with the header of the ang file
        % now I save all the header in a file called Ang_Header.txt in the working
        % directpry
        fid = fopen('Ang_Header.txt', 'wt');
        for i=1:Ang_Header_line_number
            fprintf(fid,'%s\n' ,char(LineCell{1,1}{i,1}));
        end
        fclose(fid);
        first_run_flag=0;
    end

        % so lets read the rest of txt file into matrix Ang_as_MEas_MTRX

    fid = fopen(AsMeas_file_name);
    Ang_as_MEas_Cell=textscan(fid, '%f %f %f %f %f %f %f %f %f %f','HeaderLines',↩
        Ang_Header_line_number);
    fclose(fid);
    % since only X and Y are important I only work with those two in the
    % XY_matrix
    Ang_XY_MTRX=[Ang_as_MEas_Cell{1,4} Ang_as_MEas_Cell{1,5}];

    % I want to know the number of lines in the header of txt points-to-be-corrected ↩
        file
    selected_points_file_name=char(selected_points_files(k,1))
    fid = fopen(selected_points_file_name)
    TXT_Header_line_number=0;
    flag=0;
    while flag==0
         LineCell=textscan(fid,'%s',1,'delimiter','\n');
         LineString=char(LineCell{1,1});
         if strncmp(LineString,'#',1)==1
             TXT_Header_line_number=TXT_Header_line_number+1;
         else
```

```
         flag=1;
     end
 end
    fclose(fid);

% so lets read the rest of txt file into matrix Data_points_MTRX
fid = fopen(selected_points_file_name);
Data_points_Cell=textscan(fid,'Red RGB(255 0 0), %f %f','HeaderLines',↩
    TXT_Header_line_number,'delimiter',',');
fclose(fid);
Data_points_XY_MTRX=[Data_points_Cell{1,1} Data_points_Cell{1,2}];

% here I find in the position of data points in the as measured ang file
number_of_data_points=size(Data_points_XY_MTRX,1);
size_of_ang_file=size(Ang_XY_MTRX,1);

flag=1;
position_in_ang=[];
% number of digits does not work between selected and ang file, so I
% once try lower floor and the next time ceiling. let's start with floor
for i=1:number_of_data_points
    flag=1;
    counter=0;
    while flag==1
        counter=counter+1;
        if round(Data_points_XY_MTRX(i,1)*100)==floor(Ang_XY_MTRX(counter,1)*100) ↩
           && round(Data_points_XY_MTRX(i,2)*100)==floor(Ang_XY_MTRX(counter,2)↩
            *100)
            flag=0;
            position_in_ang=[position_in_ang;counter];
        end
        if counter==size_of_ang_file
            flag=0;
        end
    end
end
% lets change the orientation n the as measured file to what has been
% defined in the input file, this is floor part
for i=1:size(position_in_ang,1)
    Ang_as_MEas_Cell{1,1}(position_in_ang(i,1))=correction_matrix(k,1);
    Ang_as_MEas_Cell{1,2}(position_in_ang(i,1))=correction_matrix(k,2);
    Ang_as_MEas_Cell{1,3}(position_in_ang(i,1))=correction_matrix(k,3);
    if CI_Correction_Flag==1
        Ang_as_MEas_Cell{1,7}(position_in_ang(i,1))=correction_matrix(k,4);
    end
end

    % number of digits does not work between selected and ang file, so I
% once try lower floor and the next time ceiling. let's co ceiling
for i=1:number_of_data_points
    flag=1;
    counter=0;
    while flag==1
        counter=counter+1;
```

```
        if round(Data_points_XY_MTRX(i,1)*100)==ceil(Ang_XY_MTRX(counter,1)*100) &&↩
             round(Data_points_XY_MTRX(i,2)*100)==ceil(Ang_XY_MTRX(counter,2)*100)
            flag=0;
            position_in_ang=[position_in_ang;counter];
        end
        if counter==size_of_ang_file
            flag=0;
        end
    end
end
% lets change the orientation n the as measured file to what has been
% defined in the input file, this is ceiling
for i=1:size(position_in_ang,1)
    Ang_as_MEas_Cell{1,1}(position_in_ang(i,1))=correction_matrix(k,1);
    Ang_as_MEas_Cell{1,2}(position_in_ang(i,1))=correction_matrix(k,2);
    Ang_as_MEas_Cell{1,3}(position_in_ang(i,1))=correction_matrix(k,3);
    if CI_Correction_Flag==1
        Ang_as_MEas_Cell{1,7}(position_in_ang(i,1))=correction_matrix(k,4);
    end
end

%--------------
    for i=1:number_of_data_points
    flag=1;
    counter=0;
    while flag==1
        counter=counter+1;
        if round(Data_points_XY_MTRX(i,1)*100)==floor(Ang_XY_MTRX(counter,1)*100) ↩
           && round(Data_points_XY_MTRX(i,2)*100)==ceil(Ang_XY_MTRX(counter,2)↩
            *100)
            flag=0;
            position_in_ang=[position_in_ang;counter];
        end
        if counter==size_of_ang_file
            flag=0;
        end
    end
end
% lets change the orientation n the as measured file to what has been
% defined in the input file, this is ceiling
for i=1:size(position_in_ang,1)
    Ang_as_MEas_Cell{1,1}(position_in_ang(i,1))=correction_matrix(k,1);
    Ang_as_MEas_Cell{1,2}(position_in_ang(i,1))=correction_matrix(k,2);
    Ang_as_MEas_Cell{1,3}(position_in_ang(i,1))=correction_matrix(k,3);
    if CI_Correction_Flag==1
        Ang_as_MEas_Cell{1,7}(position_in_ang(i,1))=correction_matrix(k,4);
    end
end
%-----------------------
    for i=1:number_of_data_points
    flag=1;
    counter=0;
    while flag==1
        counter=counter+1;
```

```
            if round(Data_points_XY_MTRX(i,1)*100)==ceil(Ang_XY_MTRX(counter,1)*100) &&↩
                 round(Data_points_XY_MTRX(i,2)*100)==floor(Ang_XY_MTRX(counter,2)*100)
                flag=0;
                position_in_ang=[position_in_ang;counter];
            end
            if counter==size_of_ang_file
                flag=0;
            end
        end
    end
    %lets change the orientation n the as measured file to what has been
    %defined in the input file , this is ceiling
    for i=1:size(position_in_ang,1)
        Ang_as_MEas_Cell{1,1}(position_in_ang(i,1))=correction_matrix(k,1);
        Ang_as_MEas_Cell{1,2}(position_in_ang(i,1))=correction_matrix(k,2);
        Ang_as_MEas_Cell{1,3}(position_in_ang(i,1))=correction_matrix(k,3);
        if CI_Correction_Flag==1
            Ang_as_MEas_Cell{1,7}(position_in_ang(i,1))=correction_matrix(k,4);
        end
    end
    %-----------------------

    % it is time to reconstruct the edited file
    % i Want to use dlmwrite to make the matrix of ang and it works with ang so
    % I convert the cell to matrix in here
    Ang_Edited_MTRX=[Ang_as_MEas_Cell{1,1:10}];
    dlmwrite([AsMeas_file_name '_edited.txt'],Ang_Edited_MTRX,'delimiter', '\t','↩
        newline', 'pc');
    % this is for combining the header and data
    text_ang=['!copy Ang_Header.txt+' AsMeas_file_name '_edited.txt ' AsMeas_file_name ↩
        '_' num2str(k) '.ang'];
    eval(text_ang);
    % this for cleaniing the txt file made by dlmwrite
    clean_text=['!del ' AsMeas_file_name '_edited.txt'];
    eval(clean_text);
    AsMeas_file_name=[AsMeas_file_name '_' num2str(k) '.ang']
end
% this is for deleting the header file
eval('!del Ang_Header.txt')
```